

Near-field radiative heat transfer with hyperbolic metamaterials

Vom Promotionsausschuss der
Technischen Universität Hamburg
zur Erlangung des akademischen Grades
Doktor-Ingenieur (Dr.-Ing.)
genehmigte Dissertation

von
SLAWA LANG

aus
PAWLODAR

2018



Gutachter / Prof. Dr. Manfred Eich
Reviewers: Prof. Dr. Christian Schuster
PD Dr. Svend-Age Biehs

Tag der mündlichen Prüfung / 13.07.2018
Day of oral examination: July 13, 2018

DOI: 10.15480/882.2064

Handle: 11420/2068

2019

Abstract

Near-field radiative heat transfer is the increased heat flux between closely spaced bodies. It is caused by thermal photons tunneling the gap between the bodies and can surpass the blackbody radiation limit by orders of magnitude. This thesis analyzes aspects of near-field heat flux. In particular, we look at the effects of hyperbolic media and hyperbolic metamaterials – materials with extreme anisotropy. Metamaterials are artificial structures which, concerning electromagnetic radiation, resemble homogeneous materials.

First, we find that thermal radiation inside hyperbolic media is very strong and radiative heat fluxes can be larger than solid heat fluxes, which are sustained by phonons and electrons instead of photons, even at room temperature. The spectral distribution and temperature dependences of radiation inside hyperbolic media are fundamentally different from Planck's blackbody counterparts. Second, the near-field heat flux between hyperbolic media is particularly strong and the penetration depth of the

radiation into the media is large compared with materials using other mechanisms to achieve a strong near-field effect. Third, a new technique to measure near-field radiative heat fluxes is presented. Our dynamic technique is more convenient than conventional steady-state techniques and allowed us to measure heat fluxes 16 times above the blackbody value at a gap of around 150 nm.

The scientific and technical insights of this thesis should help realizing thermal management and energy harvesting systems based on near-field effects and hyperbolic metamaterials.

Contents

1	Introduction and background	1
1.1	Near-field radiative heat transfer	2
1.2	Hyperbolic materials and metamaterials	8
1.3	Thesis outline	16
2	Thermal radiation calculations	19
2.1	Notations	22
2.2	Transfer-matrix method	26
2.3	Green's functions in presence of uniaxial media .	31
2.3.1	Green's functions in homogeneous uniaxial media	33
2.3.2	Green's functions for uniaxial medium–vacuum halfspaces	42
2.3.3	Green's functions for multilayer systems .	45

2.4	Density of states and thermal power flow	47
2.4.1	Energy density and density of states . . .	47
2.4.2	Power flow	53
2.5	Thermal radiation inside uniaxial materials . . .	59
2.5.1	Energy density and density of states . . .	59
2.5.2	Power flow	73
2.6	Radiative heat flux in vacuum	88
2.6.1	Thermal emission into vacuum	88
2.6.2	Radiative heat flux through vacuum gap .	95
3	Thermal radiation inside hyperbolic media	101
3.1	Thermal radiation inside nondispersive HMs . . .	106
3.1.1	Energy density and density of states . . .	106
3.1.2	Power flow	114
3.2	Thermal radiation inside dispersive HMs	119
3.2.1	Energy density and density of states . . .	126
3.2.2	Power flow	131
3.2.3	Thermal conductivity in hyperbolic materials	141

4	Near-field heat flux and its penetration depth in HMs	146
4.1	Far-field thermal emission from hyperbolic media	149
4.2	Near-field heat flux between hyperbolic media . . .	152
4.3	Penetration depth in hyperbolic media	163
5	Dynamic measurement of near-field heat transfer	174
5.1	Sample preparation and characterization	178
5.1.1	Sample preparation	178
5.1.2	Gap size measurement	180
5.2	Dynamic measuring technique	184
5.3	Modeling and fitting	187
5.3.1	1-dimensional model	187
5.3.2	2-dimensional model	198
5.4	Measurement results	202
5.5	Discussion of new dynamic technique	206
6	Conclusions and outlook	210
A	Thermal properties derived from mode counting	216
A.1	Density of states and heat flux	216
A.2	Graphical derivation of heat flux formula	222

B	Additional information on the near-field measurements	225
B.1	Spacers contribution to heat flux	225
B.2	Optical properties of BK7 and fused silica glass .	232
B.3	300 nm and 150 nm gaps	235
C	Physical and mathematical relations	240
C.1	Effective permittivity of layered structures	240
C.2	Dispersion relation of surface waves	242
C.3	Mathematical relations	245
	Bibliography	246
	List of Figures	266
	List of Tables	270

Chapter 1

Introduction and background

Metamaterials promise interesting applications in optics by utilizing new phenomena [1]. They are nanostructured materials and their variety and quality are improving due to advancing nanofabrication techniques. Metamaterials can have properties unseen in nature and thus exhibit new phenomena like negative refraction. One type of metamaterials are hyperbolic metamaterials (HMMs) [2,3]. HMMs are extremely anisotropic and possess a very large density of electromagnetic states.

This thesis analyzes the effects of HMMs on thermal radiation. In particular, we look at the radiative heat transfer inside HMMs and the near-field heat flux between HMMs. The near-field ef-

fect is the increase of radiative heat flux when the distance of the bodies exchanging heat becomes less than a few micrometers [4, 5]. The physical origin is tunneling of thermal photons. Although solid conduction is usually dominant around room temperature, radiation can be non-negligible in nanostructures due to the near-field effect. Understanding and managing near-field heat fluxes gains more and more importance in nowadays nanoelectronics. Furthermore, the effect may allow improving thermophotovoltaic (TPV) systems [6].

The near-field effect has been verified experimentally [7–9]. However, it remains very challenging to observe the strong or extreme near field where heat fluxes surpass the blackbody heat flux by orders of magnitude. The variety of experiments extends only to few different geometries and is far from the variety of solid conductivity measurement techniques. New near-field measuring methods could simplify practical measurements and allow novel characterizations e. g. of dynamic processes.

1.1 Near-field radiative heat transfer

Heat can be transported via conduction, convection and radiation [10, 11]. The key properties of thermal radiation are comprised in Max Planck’s blackbody theory [11, 12] which is summarized at the beginning of Chapter 3. Together with Kirchhoff’s law (of thermal radiation) which says that emissivity of a body is equal to its absorptivity [10, 11] the blackbody theory

allows to solve most thermal radiation problems. Only the absorptivity and the wave propagation must be calculated which are pure electrodynamic problems [13, 14] that can be solved numerically or sometimes even analytically.

In recent years, nanoscale radiative heat transfer has attracted a lot of attention because of Polder and van Hove's prediction on the possibility to observe heat fluxes at subwavelength distances which are several orders of magnitude larger than those obtained by the blackbody theory [4, 5, 15]. This behavior is not predictable with the blackbody theory and Kirchhoff's law. Theoretical investigations focus on mechanisms leading to particularly strong near-field heat fluxes, e. g. surface [16] and hyperbolic modes [17, 18] which are further analyzed in Chapter 4. Moreover, numerical techniques are developed to be able to make predictions for complex geometries [19].

Recent experimental results have confirmed the theoretical predictions [7–9, 20, 21]. Both hot and cold body temperatures and the power flow are measured once the experimental system has reached a steady-state. Almost all experiments feature a tip-plane [8, 20], a sphere-plane [9] or a plane-plane geometry [7, 21]. More information on near-field experiments is available in Chapter 5.

Let us now have a closer look at the near-field effect. Fig. 1.1a shows a hotter and a colder body separated by a uniform vacuum gap of width l . They exchange heat via electromagnetic radiation.

In the far field, when l is larger than the thermal wavelengths, the heat flux can only depend on l due to a viewing effect. That is the finite-sized cold body catches only a particular solid angle of the radiation emitted by the finite-sized hot body. With increasing l the solid angle decreases and the heat flux goes down. The wavelength of maximal thermal radiation at room temperature of $T = 300$ K is around $10\ \mu\text{m}$. This is the approximate boundary between far and near field.

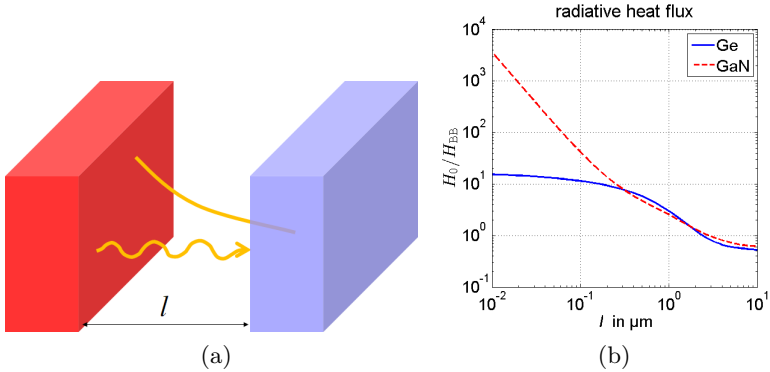


Figure 1.1: Radiative heat transfer in the near field. (a) A hot and a cold body at distance l exchange heat via electromagnetic radiation. Propagating waves transport heat over arbitrary distances. Evanescent waves decay exponentially away from the surface and can only transport energy over very short distances. (b) Heat transfer coefficient (HTC) H_0 in a uniform vacuum gap of width l at $T = 300$ K. The hot and cold halfspaces are identical and consist of bulk Ge or bulk GaN. The HTC is normalized to the HTC between blackbodies H_{BB} .

In the near field things change. To see that the heat flux between two identical halfspaces separated by a vacuum gap l is plotted in Fig. 1.1b. Actually the heat transfer coefficient (HTC) H_0 – the heat flux normalized to the temperature difference of hot and cold body – normalized to the HTC between blackbodies H_{BB} is plotted. H_{BB} does not depend on the gap size l . The halfspaces are germanium (Ge) or gallium nitride (GaN). Details on the calculation and the optical properties are provided in Section 4.2.

Halfspaces show no viewing effect and thus the heat flux is constant for larger l . It is below the blackbody value because as absorptivity is limited to $[0, 1]$ so is the emissivity. And the emissivity is the ratio of emitted radiation vs. blackbody radiation (and in general frequency and direction dependent). Thus, no body can emit or absorb more than a blackbody.

With decreasing l the heat flux increases and surpasses the blackbody limit. It can then saturate to a rather small value as for the case of Ge, or continue increasing to values several orders of magnitude above the blackbody limit as for GaN. The reasons for these characteristics will be discussed in Section 4.2.

Despite its complexity concerning analytical, numerical and experimental treatment, the explanation for the near-field effect is rather simple [4, 5]. Vacuum supports different kinds of electromagnetic modes [13]: propagating and evanescent modes [4], illustrated in Fig. 1.1a. Propagating modes are waves transporting energy over large distances. They can be represented by

plane waves with purely real wavevectors \mathbf{k} . Evanescent modes are typically observed at interfaces and have fields decaying exponentially away from the interface. The normal k -vector component becomes imaginary. A simple example is total internal reflection [14]. Due to boundary conditions the fields in the optically thinner medium are not zero but decay exponentially away from the interface [14].

In the far field only propagating modes contribute to the radiative heat transfer. The evanescent waves decay so fast that they do not reach from one body to the other body. The blackbody uses all propagating modes the most effective way, which is why it sets an upper limit. When the distance l becomes small the evanescent waves do reach the other body and allow energy to be transported across the gap. Quantum mechanically thermal photons tunnel through the gap. The smaller the gap l the better and the more evanescent modes can transport the heat. The origin of frustrated total internal reflection is the same [22].

The increased radiative heat transfer in the near-field regime might be used for different applications [4,5]. Examples are near-field imaging [20, 23–25], touchless cooling [26, 27], nanoscale thermal management by heat flux rectification [28–30], amplification [31] and storage [32, 33], and near-field thermophotovoltaics (nTPV) [7, 34–38].

Thermal far-field emission can be measured and information on the emitting material / structure extracted from the spectra. However, the spatial resolution is limited to roughly half the

free space wavelength by diffraction [13]. When a nanosize tip is brought close to the surface of a hot body the thermal near field is scattered into the far field where it can be measured [20, 25]. This way the spatial resolution is increased. Furthermore, information only contained in the near field can be obtained. An example would be the existence of surface modes, which we will discuss in the context of near-field heat transfer. A similar idea is to illuminate the sample from outside (and scatter with a tip) instead of heating it [24]. Measuring the heat flux from sample to tip can also provide valuable information about a sample surface [8, 23].

Good thermal management is crucial for nowadays nanoelectronics. The integrated components become smaller and smaller and produce more and more heat. Most of the thermal management is realized with solid-state conduction. Nevertheless, with decreasing size radiation gains importance because of the near-field effect. In addition, some effects like rectification [28–30] can be better realized using radiative or even near-field radiative concepts [5].

Finally, nTPV is a special type of thermophotovoltaics (TPV). TPV is similar to photovoltaics but the radiation is provided by a thermal emitter not by the sun [6, 39]. Different to photovoltaics, TPV systems are not limited by the Shockley–Queisser limit [40]. The emitter can be optimized to emit radiation only at frequencies slightly above the band gap of the photovoltaic cell [41]. The energy to heat the emitter can be waste heat or

solar radiation, resulting in waste heat recovery or solar TPV. For TPV / nTPV applications it is desirable to have large heat fluxes which are quasi-monochromatic at the band gap frequency of the thermophotovoltaic cell. Thus, output power of TPV devices could be increased with the help of the near-field effect [4,5,7,35–37]. Alternatively, the operation temperature can be reduced without losing output power, hence diminishing thermal stability problems. As we will see, spectral control of the near-field heat flux is also possible to some degree. So nTPV efficiencies may become very large.

1.2 Hyperbolic materials and metamaterials

Hyperbolic media (HMs) are, in the first place, optically anisotropic media, more precisely they are uniaxial [2,3]. We restrict ourselves to nonmagnetic hyperbolic media which is the typical case [2, 3] and assume without loss of generality that the optical axis is oriented in z -direction (\parallel -direction). The relative permittivity tensor ϵ then reads

$$\epsilon = \begin{pmatrix} \epsilon_{\perp} & 0 & 0 \\ 0 & \epsilon_{\perp} & 0 \\ 0 & 0 & \epsilon_{\parallel} \end{pmatrix}. \quad (1.1)$$

Within such uniaxial materials so-called ordinary modes (OMs)

and extraordinary modes (EMs) (sometimes also called s- and p-polarized modes) exist and satisfy the dispersion relations [42]

$$\frac{k_{\perp}^2}{\epsilon_{\perp}} + \frac{k_{\parallel}^2}{\epsilon_{\parallel}} = \frac{\omega^2}{c^2}, \quad (\text{OM}) \quad (1.2)$$

$$\frac{k_{\perp}^2}{\epsilon_{\parallel}} + \frac{k_{\parallel}^2}{\epsilon_{\perp}} = \frac{\omega^2}{c^2}, \quad (\text{EM}) \quad (1.3)$$

where $k_{\perp} = |\mathbf{k}_{\perp}|$ (k_{\parallel}) is the wavevector component perpendicular (parallel) to the optical axis. ω is the angular frequency and c the vacuum speed of light.

First, we notice that OMs do not sense the anisotropy of the material because the electric field is perpendicular to the optical axis [42]. The isofrequency contour – the set of all real k -vectors

$$\mathbf{k} = \begin{pmatrix} \mathbf{k}_{\perp} \\ k_{\parallel} \end{pmatrix} = \begin{pmatrix} k_x \\ k_y \\ k_{\parallel} \end{pmatrix} \quad (1.4)$$

satisfying (1.2) for a fixed ω – is a sphere if $\epsilon_{\perp} > 0$ or empty otherwise. Isofrequency contours display only propagating modes with real \mathbf{k} . Evanescent modes are ignored.

In usual dielectric uniaxial media the principal constants ϵ_{\perp} and ϵ_{\parallel} are both positive and the isofrequency surfaces of EMs defined by relation (1.3) are ellipsoids, as illustrated in Fig. 1.2a. In the isotropic case, $\epsilon_{\parallel} = \epsilon_{\perp}$, the ellipsoids reduce to spheres as for OMs.

On the other hand, when $\{\epsilon_{\parallel} < 0 \text{ and } \epsilon_{\perp} > 0\}$ or $\{\epsilon_{\parallel} > 0 \text{ and } \epsilon_{\perp} < 0\}$ the isofrequency surfaces of the EMs are two- or one-sheeted hyperboloids [2, 43], see Fig. 1.2. Thus the name “hyperbolic” medium (HM). The first class of such uniaxial media is called hyperbolic medium of type I while the second one HM of type II [43]. So hyperbolic materials are extremely anisotropic materials with dielectric (positive permittivity) and metallic (negative permittivity) behavior at the same time.

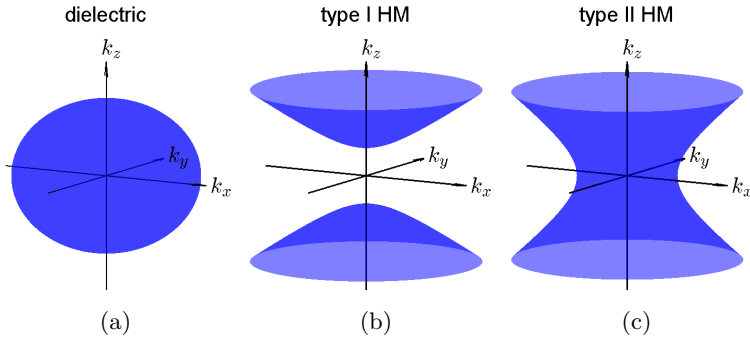


Figure 1.2: Isofrequency contours of extraordinary modes in uniaxial media. (a) Dielectric materials, $\epsilon_{\perp} > 0$ and $\epsilon_{\parallel} > 0$, feature an ellipsoid of revolution (spheroid), (b) type I hyperbolic materials, $\epsilon_{\perp} > 0$ and $\epsilon_{\parallel} < 0$, feature a hyperboloid of revolution of two sheets (elliptic hyperboloid), (c) type II hyperbolic materials, $\epsilon_{\perp} < 0$ and $\epsilon_{\parallel} > 0$, feature a hyperboloid of revolution of one sheet (hyperbolic hyperboloid).

Of course both ϵ_{\perp} and ϵ_{\parallel} can also be negative. In such uniaxial metallic-like materials no propagating modes exist. With

“metallic” we refer to the optical property of having negative permittivity which is typical for metals in the visible and infrared (i. e. for frequencies below the metal’s plasma frequency [44]). But other non-metal materials, like the phonon-polaritonic materials gallium nitride (GaN) and silicon carbide (SiC) [45, 46], can exhibit a negative permittivity as well.

HMs do exist in nature [3, 47, 48]. But these materials are hyperbolic only in limited and non-adjustable frequency ranges. Early known examples are calcite (CaCO_3) and hexagonal boron nitride (hBN) [3, 47]. More recently, materials were found which exhibit hyperbolic behavior in all kinds of spectral regions including the visible and near-infrared [47].

Initially, the hyperbolic characteristic has been obtained with metamaterials [43]. Metamaterials are structures with feature sizes much smaller than the wavelength [1]. Electromagnetic waves behave like in a homogeneous medium, however, a homogeneous medium with unique properties rarely or not at all found in nature [1]. A famous example are metamaterials with a negative effective refractive index [1].

Hyperbolic metamaterials (HMMS) can be realized with two types of structures [3, 47]. Both types are visualized in Fig. 1.3. On the one hand, multilayer HMMS (mHMMS) are periodic multilayer structures with alternating dielectric and metallic layers [49–51]. On the other hand, nanowire HMMS (wHMMS) consist of a periodic arrangement of metallic wires immersed into a dielectric host medium [52, 53].

According to the effective medium theory (EMT) [1, 54, 55], the effective permittivity of a mHMM is given by [42, 54]

$$\epsilon_{\perp} = f_m \epsilon_m + (1 - f_m) \epsilon_d, \quad (1.5)$$

$$\epsilon_{\parallel} = \left(\frac{f_m}{\epsilon_m} + \frac{(1 - f_m)}{\epsilon_d} \right)^{-1} = \frac{\epsilon_m \epsilon_d}{(1 - f_m) \epsilon_m + f_m \epsilon_d} \quad (1.6)$$

and for a wHMM it is given by [54]

$$\epsilon_{\perp} = \epsilon_d \frac{(1 + f_m) \epsilon_m + (1 - f_m) \epsilon_d}{(1 - f_m) \epsilon_m + (1 + f_m) \epsilon_d}, \quad (1.7)$$

$$\epsilon_{\parallel} = f_m \epsilon_m + (1 - f_m) \epsilon_d, \quad (1.8)$$

where f_m is the volume filling fraction of the “metallic” component. ϵ_d (ϵ_m) is the permittivity of the isotropic dielectric (metallic) filling material.

EMT gives reliable results if the unit-cell size Λ of the underlying structure is much smaller than the effective wavelength [55–57]. Remember, the dominant free space wavelength of thermal blackbody radiation is about 10 μm at room temperature 300 K. Consequently, nanometer sized HMMs should behave as effective media. But the wavelength inside the HMM is $\frac{2\pi}{k}$ with $k = |\mathbf{k}|$. And as we have seen, the k -vector can take on very large values. For larger k -vectors it is therefore expected that the EMT provides inaccurate results.

To exemplify this, Fig. 1.3c shows the isofrequency contour of a multilayer structure with the parameters given in the figure

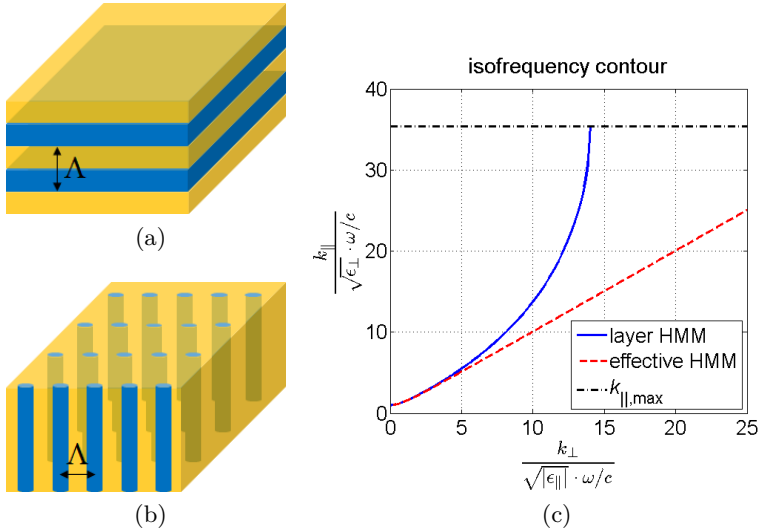


Figure 1.3: Hyperbolic metamaterials (HMMs) and their isofrequency contours. The schematics show (a) a layer HMM and (b) a wire HMM. The isofrequency contours (c) of hyperbolic modes of a bilayer HMM and the corresponding effective HMM agree well for small k values but differ for larger values. The assumed permittivities of the layers are 2 and -1, the angular frequency $\omega \approx 188.4 \cdot 10^{12} \text{ s}^{-1}$. The periodicity is $\Lambda = 200 \text{ nm}$ with equal layer thicknesses. Thus, the effective permittivities are $\epsilon_{\perp} = 0.5$ and $\epsilon_{\parallel} = -4$. The maximal k_{\parallel} of the layer HMM is $k_{\parallel, \max} = \frac{\pi}{\Lambda}$ and is also marked.

caption. The contour of the effective medium is a hyperbola. Inside the real multilayer Bloch waves exist [58], the dispersion of which is plotted. For the calculation the transfer-matrix method

(TMM) is used, see Section 2.2. For smaller k the EMT is in good agreement with the real isofrequency contour. But for larger k both differ and the real one reaches the limit $\frac{\pi}{\Lambda}$ at the edge of the first Brillouin zone.

The existence of a maximal wavenumber, k_{\max} , is the most important characteristic that the EMT misses [2, 3, 55, 57]. It limits the number of propagating modes to a finite value and thus has significant consequences, as we will see in this thesis. For an ideal HM k_{\max} is infinite so that the density of electromagnetic states (DOS) diverges [59, 60]. However, for any real structure k_{\max} is a finite quantity. Still the DOS of HMMs is much larger than the one of dielectrics [2, 3].

If Λ denotes the unit-cell size of our HM (Fig. 1.3) then $k_{\parallel, \max} = \frac{\pi}{\Lambda}$ or $k_{\perp, \max} = \frac{\pi}{\Lambda}$ depending on the concrete structure. For example, for a multilayer structure with layers perpendicular to the \parallel -axis the edge of the first Brillouin zone gives $k_{\parallel, \max} = \frac{\pi}{\Lambda}$, whereas for a nanowire structure with nanowires along the \parallel -axis the edge of the first Brillouin zone gives $k_{\perp, \max} = \frac{\pi}{\Lambda}$.

In natural HMs there might be different length scales which determine their hyperbolic behavior. Nonetheless, we think that it is reasonable to assume that the main length scale is again given by the unit-cell size which is in this case determined by the interatomic spacing, i. e. $\Lambda \approx 1 \text{ \AA} = 0.1 \text{ nm}$.

If no further information is available or tedious calculations should be avoided, independent of the structure both maximum wave-

numbers are approximately related by

$$\frac{k_{\perp,\max}^2}{\epsilon_{\parallel}} + \frac{k_{\parallel,\max}^2}{\epsilon_{\perp}} = \frac{\omega^2}{c^2}, \quad (1.9)$$

and because $k_{\perp/\parallel,\max} \gg \frac{\omega}{c}$ the relation simplifies to $k_{\perp,\max} \approx \sqrt{\left|\frac{\epsilon_{\parallel}}{\epsilon_{\perp}}\right|} k_{\parallel,\max}$.

Note that like natural HMs HMMs are also hyperbolic only in certain frequency regions. Further, Kramers–Kronig relations forbid negative permittivities without dissipation [14, 44]. So real HMs / HMMs are characterized by the real parts of the permittivities having opposite signs, $\Re(\epsilon_{\perp})\Re(\epsilon_{\parallel}) < 0$.

The effect of the huge density of states on thermal (near-field) radiation inside and between HMs / HMMs will be discussed in this thesis. But HMMs can be utilized for more applications [2, 3].

HMMs can show negative refraction [49, 52]. To understand this one has to remember that the energy is generally propagating not in the direction of \mathbf{k} , as in vacuum, but in the direction of the group velocity $\mathbf{c}_g = \nabla_{\mathbf{k}}\omega(\mathbf{k})$ [14]. \mathbf{c}_g is by definition perpendicular to the isofrequency surface and for large wavenumbers inside HMMs it is even nearly perpendicular to \mathbf{k} . Using negative refraction spatial filters and planar lenses can be realized [2, 3].

An extension of the idea are hyperlenses [61]. Normally, imaging with light is limited by diffraction. The reason is that the k -values of the imaging (propagating) modes are limited to $\frac{\omega}{c}$ (or

a single-digit multiple thereof depending on the refractive index of the lenses). Larger Fourier components, which are a characteristic of very small nanostructures, correspond to evanescent modes and are not contributing to the far field [61]. The idea of the hyperlens is to transform the evanescent modes to propagating modes. This is done e. g. with a curved HMM brought in close proximity to the object. Inside the HMM the high- k modes are not evanescent but propagating. Due to the curvature they magnify the object attributes from the smaller inner surface of the curved HMM, where the object is situated, to the larger outer surface. With the increased surface in real space the k -vectors in reciprocal space are decreased, till they correspond to modes propagating in air and can be further imaged [2, 3, 61]. The previous concepts rely on the different directions of \mathbf{k} and \mathbf{c}_g for hyperbolic modes. Nevertheless, also the enormous DOS of HMMs can be employed e. g. to enhance spontaneous emission [50, 55, 56]. The dependence of emitted power on the environment into which is emitted is known as Purcell effect [2, 3, 55, 56]. The more modes exist the more is emitted. The enhancement leads to a reduction of the lifetime / increase of the decay rate of fluorescent molecules [2, 3, 50].

1.3 Thesis outline

After the introduction, the thesis starts with the calculation of thermal radiation properties, in particular the heat flux and the

energy density. For that fluctuational electrodynamics [62] is combined with the fluctuation-dissipation theorems [63]. This approach is widely used and, different from blackbody theory plus Kirchhoff's law, can predict effects like near-field heat transfer. For the calculations Green's functions [64] are required and multilayers can be treated numerically with the help of the transfer-matrix method (TMM) [42] which is briefly introduced.

Chapter 3 analyzes thermal radiation inside hyperbolic media. First, an idealized lossless and dispersionless HM is investigated to obtain the properties of "hyperbolic blackbody" radiation. It is compared to Planck's blackbody radiation which is thermal radiation in vacuum or air. Second, more realistic HMs are considered and the radiative heat flux compared with solid conduction. Except for the last Section 3.2.3, the HMs in this chapter are assumed to be lossless because treating losses is very complicated, as we will see during the derivation.

At the beginning of Chapter 4 we take a brief look at the far-field thermal emission characteristics of HMMs. Then, the near-field radiative heat transfer is discussed. Particular attention is paid to two mechanisms yielding strong heat fluxes: surface modes and hyperbolic modes. Finally, we show that the penetration depth of near-field heat flux into the colder body is very different for these two kinds of modes.

An experimental verification of the near-field effect is presented in Chapter 5. For that a new, dynamic measuring technique is developed. It measures the temperature transient as a response

to a step input power function and extracts the gap conductance from the transients. Gaps as small as ≈ 150 nm are realized over cm^2 -sized areas and near-field heat fluxes ≈ 16 times higher than the blackbody limit are measured.

The thesis concludes with a summary and an outlook.

The work presented here has been carried out at the Institute of Optical and Electronic Materials at Hamburg University of Technology (TUHH). Besides group members, valued colleagues Svend-Age Biehs and Maria Tschikin from Carl von Ossietzky University in Oldenburg, Germany, Philippe Ben-Abdallah from Institut d'Optique, CNRS in Palaiseau, France, Sean Molesky and Zubin Jacob from University of Alberta in Edmonton, Canada, and Michael Störmer from Helmholtz-Zentrum Geesthacht in Geesthacht, Germany, who we cooperated with, contributed to the work.

Results from this thesis have already been published and content of this thesis is copied from our publications [41, 65–68] and its supplemental information. Reproduced with permission from Appl. Phys. Lett. 104, 121903 (2014), J. Quant. Spectrosc. Radiat. Transf. 158, 17 (2015), Phys. Rev. Lett. 115, 174301 (2015), Nat. Commun. 7, 11809 (2016) and Sci. Rep. 7, 13916 (2017). Copyright 2014 AIP Publishing LLC, 2014 Elsevier Ltd. and 2015 American Physical Society. Being part of this work citations from these papers will not be made visible via quotation marks.

Chapter 2

Thermal radiation calculations

This chapter provides the mathematical and physical background for the calculations of thermal radiation. All formulas later used to analyze the radiation inside and in vicinity of hyperbolic media are derived here. The results together with illustrative examples are discussed in the next chapters.

We restrict ourselves to nonmagnetic uniaxial media [42] with

the optical axis oriented in z -direction (\parallel -direction):

$$\boldsymbol{\epsilon} = \begin{pmatrix} \epsilon_{\perp} & 0 & 0 \\ 0 & \epsilon_{\perp} & 0 \\ 0 & 0 & \epsilon_{\parallel} \end{pmatrix}, \quad (2.1)$$

$$\boldsymbol{\mu} = \begin{pmatrix} 1 & 0 & 0 \\ 0 & 1 & 0 \\ 0 & 0 & 1 \end{pmatrix} = \mathbb{1}. \quad (2.2)$$

$\boldsymbol{\epsilon}$ and $\boldsymbol{\mu}$ are the relative permittivity and permeability tensors. Furthermore, nonlocal and nonlinear effects are ignored.

The fundamental framework for the calculations of thermal radiation is fluctuational electrodynamics [15,62]. The idea is rather simple: As usual, the electrodynamics is governed by Maxwell's equations [13,14]

$$\nabla \times \mathbf{E} = i\omega\mathbf{B} - \mathbf{M} = i\omega\mu_0\boldsymbol{\mu}\mathbf{H} - \mathbf{M} \quad (2.3)$$

$$\nabla \times \mathbf{H} = -i\omega\mathbf{D} + \mathbf{J} = -i\omega\epsilon_0\boldsymbol{\epsilon}\mathbf{E} + \mathbf{J}. \quad (2.4)$$

We use the $e^{-i\omega t}$ time dependence here. However, the electric current sources \mathbf{J} (and possible magnetic current sources \mathbf{M}) are stochastic, fluctuating sources instead of deterministic ones, resulting from fluctuations on a microscopical scale. Thus, the fields created by the sources are also fluctuating. We focus on thermal fluctuations as we want to analyze thermal radiation. Other fluctuations are e.g. zero-point fluctuations [69] which cause Casimir forces even at zero temperature.

As there is no preferred direction the ensemble averages of all quantities $\langle \mathbf{J} \rangle$, $\langle \mathbf{E} \rangle$ etc. is 0. The correlation of sources is given by the fluctuation-dissipation theorem of the second kind and the correlation of fields at thermal equilibrium by the fluctuation-dissipation theorem of the first kind [62,63].

Knowing the source properties and the electrodynamic behavior we can calculate average values for the energy density and the power flux which are then the thermal energy density and the radiative heat flux [70]. The next sections follow this approach and derive the energy density and heat flux for a few particular setups comprising hyperbolic media.

An important tool for the calculations are Green's functions [13, 64]. They relate the fields to the sources. Whether the sources and fields are deterministic or fluctuating plays no role, Green's functions are universal and will be used extensively.

This chapter starts with introducing some mathematical and physical notations, followed by a short introduction to the transfer-matrix method (TMM) in Section 2.2. This numerical technique allows calculating the electromagnetic fields inside a multilayer system. Then, Green's functions for some setups are obtained. The setups are a homogeneous uniaxial medium, an interface between a uniaxial medium halfspace and a vacuum halfspace, and a more general layered system. The Green's functions are needed for the computation of the radiative thermal energy density U and radiative heat flux Φ in the mentioned setups. But first, the general expressions for U and Φ are derived.

The formulas for Φ for the different setups are the main results of this chapter. Inside hyperbolic media also the energy density and the related density of states loom large.

2.1 Notations

Before starting with the calculations a few conventions and mathematical relationships are presented. Furthermore, the symbols for physical quantities and abbreviations are given.

Vectors are defined as column vectors and have x -, y - and z -components, e. g.

$$\mathbf{a} = \begin{pmatrix} a_x \\ a_y \\ a_z \end{pmatrix}. \quad (2.5)$$

The components of a matrix are depicted as $A_{lm} = (\mathbf{A})_{lm}$ ($l, m = x, y, z$) where

$$\mathbf{A} = \begin{pmatrix} A_{xx} & A_{xy} & A_{xz} \\ A_{yx} & A_{yy} & A_{yz} \\ A_{zx} & A_{zy} & A_{zz} \end{pmatrix}. \quad (2.6)$$

The following mathematical symbols and operations will be used throughout the thesis:

- i: imaginary unit, $i^2 = -1$.
- \mathbf{e}_l : unit vector of Cartesian coordinate system ($l = x, y, z$).
- $\mathbb{1}$: unit dyad or identity matrix.

δ_{lm} : Kronecker delta, $\delta_{lm} = \begin{cases} 1 & \text{if } l = m \\ 0 & \text{if } l \neq m \end{cases}$.

ξ_{lmn} : Levi-Civita symbol,

$\xi_{lmn} = \begin{cases} +1 & \text{if } (l, m, n) \text{ is even permutation of } (1, 2, 3)/(x, y, z) \\ -1 & \text{if } (l, m, n) \text{ is uneven permutation of } \dots \\ 0 & \text{if } l = m \text{ or } l = n \text{ or } m = n \end{cases}$.

$\Re(\circ)$: real part of a scalar / vector / matrix.

$\Im(\circ)$: imaginary part of a scalar / vector / matrix.

$(\circ)^*$: complex conjugate of a scalar / vector / matrix.

$(\circ)^{-1}$: inverse of a scalar / matrix.

$(\circ)^H$: conjugate transpose of a vector / matrix.

$(\circ)^T$: transpose of a vector / matrix.

$|\circ|$: absolute value of a scalar or Euclidean norm of a vector,
 $|\mathbf{a}| = \sqrt{\mathbf{a}^H \mathbf{a}}$.

$\|\circ\|$: absolute value of a real scalar or Euclidean norm of a real vector, $\|\mathbf{a}\| = \sqrt{\mathbf{a}^T \mathbf{a}}$.

With complex numbers this is strictly speaking not an absolute value / Euclidean norm but just an operation.

$\arg(\circ)$: argument of a complex number z , $\arg(|z|e^{i\varphi}) = \varphi$.

$\text{sgn}(\circ)$: sign function, $\text{sgn}(x) = x/|x|$.

$\text{diag}(\circ)$: diagonal matrix with elements given in brackets.

$\text{Tr}(\circ)$: trace of a matrix, $\text{Tr}(\mathbf{A}) = \sum_l A_{ll}$.

$(\circ)!$: factorial, $x! = \prod_{l=1}^x l$ ($x \in \mathbb{N}$), $0! = 1$.

$\text{expm}(\circ)$: matrix exponential, $\text{expm}(\mathbf{Z}) = \sum_{l=0}^{\infty} \frac{1}{l!} \mathbf{Z}^l$.

$\Gamma(\circ)$: gamma function, $\Gamma(z) = \int_0^{\infty} x^{z-1} e^{-x} dx$ ($\Re(z) > 0$).

$\zeta(\circ)$: Riemann zeta function, $\zeta(z) = \sum_{l=1}^{\infty} \frac{1}{l^z}$.

$\langle \circ \rangle$: ensemble average (or expected value) of a stochastic quantity.

$(\circ) \cdot (\circ)$: scalar product of two real vectors,

$$\mathbf{a} \cdot \mathbf{b} = \mathbf{a}^T \mathbf{b} = \sum \sum_{l,m} \delta_{lm} a_l b_m = \text{Tr}(\mathbf{a}\mathbf{b}^T).$$

With complex vectors this is strictly speaking not a scalar product but just an operation.

$(\circ) \times (\circ)$: cross product of two vectors,

$$\mathbf{a} \times \mathbf{b} = \sum \sum \sum_{\substack{l=x,y,z \\ m=x,y,z \\ n=x,y,z}} \xi_{lmn} \mathbf{e}_l a_m b_n.$$

$(\circ) \otimes (\circ)$: tensor product, for vectors $\mathbf{a} \otimes \mathbf{b} = \mathbf{a}\mathbf{b}^T$.

∇ : gradient operator, $\nabla = \left(\frac{\partial}{\partial x}, \frac{\partial}{\partial y}, \frac{\partial}{\partial z} \right)^T$.

$\nabla \cdot (\circ)$: divergence of a vector field. Applied to matrices the operation is performed column wise yielding a row vector.

$\nabla \times (\circ)$: curl of a vector field. Applied to matrices the operation is performed column wise yielding a matrix.

The physical constants and symbols in this thesis are:

c : vacuum speed of light, $c \approx 299792458 \text{ m s}^{-1}$.

μ_0 : vacuum permeability, $\mu_0 = 4\pi \cdot 10^{-7} \text{ V s A}^{-1} \text{ m}^{-1}$.

ϵ_0 : vacuum permittivity,

$$\epsilon_0 = \frac{1}{c^2 \mu_0} \approx 8.854188 \cdot 10^{-12} \text{ A s V}^{-1} \text{ m}^{-1}.$$

\hbar : reduced Planck constant, $\hbar \approx 1.0545718 \cdot 10^{-34} \text{ J s}$.

k_B : Boltzmann constant, $k_B \approx 1.38064852 \cdot 10^{-23} \text{ J K}^{-1}$.

σ_B : Stefan–Boltzmann constant,

$$\sigma_B = \frac{\pi^2 k_B^4}{60 \hbar^3 c^2} \approx 5.6704 \cdot 10^{-8} \text{ W m}^{-2} \text{ K}^{-4}.$$

- f : temporal frequency.
 ω : temporal angular frequency, $\omega \equiv 2\pi f$.
 T : absolute temperature.

Finally, here is a summary of abbreviations introduced throughout the thesis:

- 1D: 1-dimensional.
2D: 2-dimensional.
BB: blackbody.
DOS: density of states.
EM (pl. EMs): extraordinary mode.
EMT: effective medium theory.
ENZ: epsilon-near-zero.
FDTD: finite-difference time-domain (method).
HM (pl. HMs): hyperbolic medium.
HMM (pl. HMMs): hyperbolic metamaterial.
HTC (pl. HTCs): heat transfer coefficient.
LDOS: local density of states.
mHMM: multilayer HMM.
MIR: mid infrared.
NIR: near infrared.
nTPV: near-field thermophotovoltaic(s).
OM (pl. OMs): ordinary mode.
PD (pl. PDs): penetration depth.
sHTC (pl. sHTCs): spectral heat transfer coefficient.
TMM: transfer-matrix method.

TPS: transient plane source.

TPV: thermophotovoltaic(s).

UM (pl. UMs): uniaxial medium.

wHMM: nanowire HMM.

2.2 Transfer-matrix method

The transfer-matrix method (TMM) is a numerical technique to calculate the electromagnetic fields in a multilayer system [42, 58]. The method works with plane, monochromatic waves. All other possible electromagnetic solutions can be expanded into plane waves if necessary.

In each layer there is a forward and a backward running wave, as shown in Fig. 2.1. Multiple for- or backward traveling waves coming from multiple reflections can be summed up to a single wave. The waves can be characterized by the tangential field, in case of p-polarized light it is the solely tangential magnetic field H . The electric field can be easily concluded knowing ω and the tangential component of the wavevector k_{\perp} which is consistent in all layers and basically represents the propagation angle w. r. t. the z -axis. For s-polarization one would choose the solely tangential electric field E not H .

Following Fig. 2.1, the TMM combines the fields representing the two waves at different z -positions via matrices. E.g. the

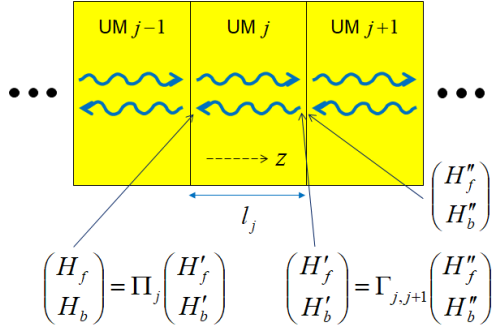


Figure 2.1: Visualization of the transfer-matrix method (TMM). Matrices combine fields of forward (subscript “f”) and backward (subscript “b”) propagating waves at different positions in a layered system. The layer thicknesses are l_j . The dashed arrow shows the orientations of the optical axes of the uniaxial materials (UMs) which are all along the z -axis.

fields at both ends of layer j with thickness l_j are combined by

$$\Pi_j = \begin{pmatrix} e^{-ik_{z,j}l_j} & 0 \\ 0 & e^{ik_{z,j}l_j} \end{pmatrix}. \quad (2.7)$$

Replacing l_j by another distance one can access any location inside the layer. $k_{z,j}$ is the longitudinal wavevector component

in layer j [42]

$$k_{z,j}^s = \sqrt{\frac{\omega^2}{c^2} \epsilon_{\perp,j} - k_{\perp}^2}, \quad (2.8)$$

$$k_{z,j}^p = \sqrt{\frac{\omega^2}{c^2} \epsilon_{\perp,j} - k_{\perp}^2 \frac{\epsilon_{\perp,j}}{\epsilon_{\parallel,j}}}. \quad (2.9)$$

The superscripts s and p stand for the s- and p-polarization and we assumed the optical axes of all layer media to be oriented along the z -direction.

When the layers in Fig. 2.1 constitute the metallic and dielectric layers of a HMM the assumption of anisotropy is superfluous, as most layer materials are isotropic. Nevertheless, it should be noted that HMMs can also be realized with anisotropic constituents. However, the layers in Fig. 2.1 can be natural HMs or HMMs treated as effective media as well. In which case the uniaxiality is needed. An example of a layered structure with itself hyperbolic layers are hypercrystals. They combine HMs with dielectrics or metals and obtain structure properties comprising features of both HMs and photonic crystals [71].

The matrix

$$\Gamma_{j,j+1} = \frac{1}{t_{j,j+1}} \begin{pmatrix} 1 & r_{j,j+1} \\ r_{j,j+1} & 1 \end{pmatrix} \quad (2.10)$$

combines the fields at both sides of the interface between layers j and $j + 1$ and ensures continuity of tangential electric and magnetic fields. The reflection and transmission coefficients from

layer j to $j + 1$ are

$$r_{j,j+1}^s = \frac{\mu_{j+1}k_{z,j}^s - \mu_j k_{z,j+1}^s}{\mu_{j+1}k_{z,j}^s + \mu_j k_{z,j+1}^s}, \quad (2.11)$$

$$r_{j,j+1}^p = \frac{\epsilon_{\perp,j+1}k_{z,j}^p - \epsilon_{\perp,j}k_{z,j+1}^p}{\epsilon_{\perp,j+1}k_{z,j}^p + \epsilon_{\perp,j}k_{z,j+1}^p}, \quad (2.12)$$

$$t_{j,j+1}^{s/p} = 1 + r_{j,j+1}^{s/p}. \quad (2.13)$$

The relative permeabilities of the (magnetically isotropic) layers μ_j , seen in Eq. (2.11), are in our cases all 1 as mentioned before.

With the matrices for the inside of a layer Π_j and the interface between two layers $\Gamma_{j,j+1}$ the fields at two arbitrary locations in a multilayer stack can be combined by a single matrix. This single matrix is simply the product of the individual matrices.

Now, either the fields of both waves are known at one z -position. Then the fields at any other location can be obtained via multiplication with the corresponding matrix (or its inverse). Or the fields of two waves are known, however at different positions. Then, still the unknown fields at the two spots can be calculated. There are two equations with two unknowns and the matrix elements are the coefficients in the equations.

A particularly important combination of both cases is the reflection from a multilayer. Imagine a stack of N layers where layers 1 and N are actually halfspaces. The matrix connecting the fields in the two halfspaces (more precisely at their boundaries)

is

$$\Gamma_{1,N} = \Gamma_{1,2} \prod_{j=2}^{N-1} \Pi_j \Gamma_{j,j+1}. \quad (2.14)$$

If a plane wave incident from halfspace 1 hits the structure there will be a total reflected wave. With a normalized incident field strength 1 and no incident wave from the other side, the mathematical connection of fields looks as

$$\begin{pmatrix} 1 \\ r_{1,N} \end{pmatrix} = \Gamma_{1,N} \begin{pmatrix} t_{1,N} \\ 0 \end{pmatrix}. \quad (2.15)$$

Consequently, the total transmission and reflection coefficients of the layered structure are

$$t_{1,N} = \frac{1}{[\Gamma_{1,N}]_{11}}, \quad (2.16)$$

$$r_{1,N} = [\Gamma_{1,N}]_{21} t_{1,N} = \frac{[\Gamma_{1,N}]_{21}}{[\Gamma_{1,N}]_{11}}. \quad (2.17)$$

From here on, one can calculate the normalized fields at any position by multiplying the corresponding matrix by $\begin{pmatrix} t_{1,N} & 0 \end{pmatrix}^T$, or the inverse of the matrix governing the other part of the multilayer by $\begin{pmatrix} 1 & r_{1,N} \end{pmatrix}^T$.

For further reading and the derivations of the presented formulas, please refer to Ref. [58]. It also shows how periodic multilayers in which Bloch waves propagate can be treated with TMM. Note that the TMM and the formulas are not limited to propagating waves. Evanescent and lossy waves are covered as

well, and thus, the materials can be lossless or lossy dielectrics or metals.

2.3 Green's functions in presence of uniaxial media

Green's functions \mathbf{G} allow obtaining the electric and magnetic fields at any location for any source distribution via [64]

$$\begin{aligned} \mathbf{E}(\mathbf{r}) &= i\omega\mu_0 \iiint_V \mathbf{G}^{\text{EE}}(\mathbf{r}, \mathbf{r}') \mathbf{J}(\mathbf{r}') d^3r' \\ &+ i\omega\epsilon_0 \iiint_V \mathbf{G}^{\text{EH}}(\mathbf{r}, \mathbf{r}') \mathbf{M}(\mathbf{r}') d^3r', \end{aligned} \quad (2.18)$$

$$\begin{aligned} \mathbf{H}(\mathbf{r}) &= i\omega\mu_0 \iiint_V \mathbf{G}^{\text{HE}}(\mathbf{r}, \mathbf{r}') \mathbf{J}(\mathbf{r}') d^3r' \\ &+ i\omega\epsilon_0 \iiint_V \mathbf{G}^{\text{HH}}(\mathbf{r}, \mathbf{r}') \mathbf{M}(\mathbf{r}') d^3r'. \end{aligned} \quad (2.19)$$

Basically, Green's functions are the fields (at any observation point \mathbf{r}) for a point source at \mathbf{r}' . V is the volume of the considered structure containing the source currents. There are four Green's functions connecting electric and magnetic current sources to electric and magnetic fields.

We will have a look at Green's functions for three different setups, illustrated in Fig. 2.2. The first one is a homogeneous uni-

axial medium which can be simply dielectric or else hyperbolic. The second setup limits the uniaxial medium to a halfspace. The other half of the space is simply vacuum. Finally, we look at Green's functions for a general multilayer stack.

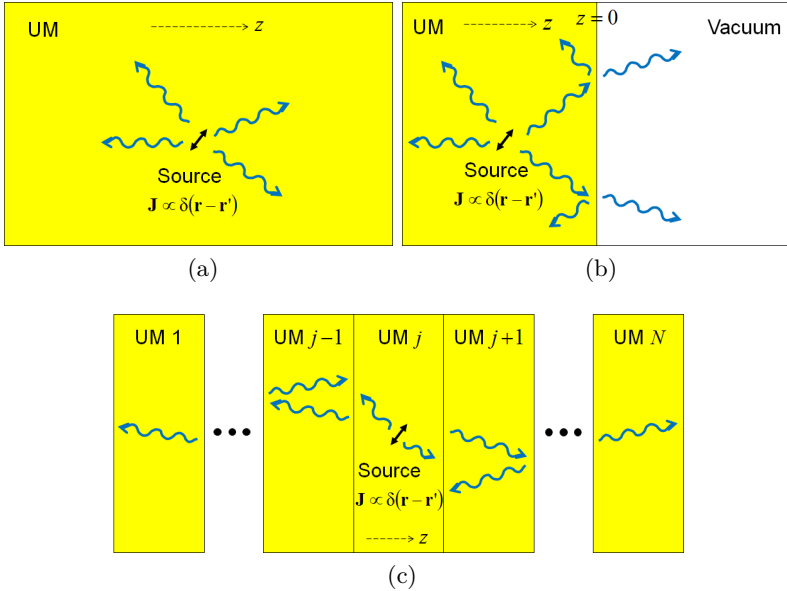


Figure 2.2: Illustration of the setups for which Green's functions are evaluated. (a) homogeneous uniaxial medium (UM), (b) halfspaces of UM and vacuum with the source in the UM, (c) multilayer stack of N uniaxial media (UM 1 and N are halfspaces). The dashed arrows show the orientations of the optical axes of the UMs which are all along the z -axis.

2.3.1 Green's functions in homogeneous uniaxial media

The electric and magnetic Green's dyadic functions for a uniaxial medium can be written as [72]

$$\mathbf{G}^{\text{EE}}(\mathbf{r}, \mathbf{r}') = \left[\frac{c^2}{\omega^2 \epsilon_{\perp}} \nabla \otimes \nabla + \epsilon_{\parallel} \boldsymbol{\epsilon}^{-1} \right] g_e(\mathbf{r} - \mathbf{r}') - \mathbb{F}(\mathbf{r} - \mathbf{r}') \quad (2.20)$$

and

$$\mathbf{G}^{\text{HH}}(\mathbf{r}, \mathbf{r}') = \left[\frac{c^2}{\omega^2} \nabla \otimes \nabla + \epsilon_{\perp} \mathbb{1} \right] g_o(\mathbf{r} - \mathbf{r}') + \epsilon_{\perp} \mathbb{F}(\mathbf{r} - \mathbf{r}'). \quad (2.21)$$

The scalar Green's functions for the ordinary and extraordinary modes are given by ($\mathbf{x} \equiv \mathbf{r} - \mathbf{r}'$)

$$g_{o/e}(\mathbf{x}) = \frac{1}{4\pi} \frac{e^{i\frac{\omega}{c}\sqrt{\epsilon_{\perp}}x_{o/e}}}{x_{o/e}}, \quad (2.22)$$

where

$$x_e^2 = \frac{\epsilon_{\parallel}}{\epsilon_{\perp}} (\mathbf{x} \times \mathbf{e}_{\parallel})^2 + (\mathbf{x} \cdot \mathbf{e}_{\parallel})^2 \quad \text{and} \quad x_o^2 = x^2 := |\mathbf{x}|^2. \quad (2.23)$$

Here \mathbf{e}_{\parallel} is the unit vector parallel to the optical axis, i. e. in our case $\mathbf{e}_{\parallel} = \mathbf{e}_z$.

Moreover, we can split the dyad \mathbb{F} into its extraordinary and

ordinary part [72]

$$\mathbb{F}(\mathbf{x}) = \epsilon_{\parallel} \mathbb{F}_e(\mathbf{x}) - \mathbb{F}_o(\mathbf{x}) \quad (2.24)$$

where

$$\mathbb{F}_e(\mathbf{x}) = \iiint_{-\infty}^{\infty} \frac{e^{i\mathbf{k}\cdot\mathbf{x}}}{\mathbf{k}\cdot\boldsymbol{\epsilon}\cdot\mathbf{k} - \frac{\omega^2}{c^2}\epsilon_{\perp}\epsilon_{\parallel}} \frac{(\mathbf{k}\times\mathbf{e}_{\parallel})\otimes(\mathbf{k}\times\mathbf{e}_{\parallel})}{(\mathbf{k}\times\mathbf{e}_{\parallel})^2} \frac{d^3k}{(2\pi)^3} \quad (2.25)$$

and

$$\mathbb{F}_o(\mathbf{x}) = \iiint_{-\infty}^{\infty} \frac{e^{i\mathbf{k}\cdot\mathbf{x}}}{k^2 - \frac{\omega^2}{c^2}\epsilon_{\perp}} \frac{(\mathbf{k}\times\mathbf{e}_{\parallel})\otimes(\mathbf{k}\times\mathbf{e}_{\parallel})}{(\mathbf{k}\times\mathbf{e}_{\parallel})^2} \frac{d^3k}{(2\pi)^3}. \quad (2.26)$$

These expressions can now be brought into a form which is much more convenient for further calculations. To this end, we make a Fourier expansion of the scalar Green's functions (by Fourier transforming the differential equations governing $g_{o/e}$, see Ref. [72]):

$$\begin{aligned} g_e(\mathbf{x}) &= \epsilon_{\perp} \iiint_{-\infty}^{\infty} \frac{e^{i\mathbf{k}\cdot\mathbf{x}}}{\mathbf{k}\cdot\boldsymbol{\epsilon}\cdot\mathbf{k} - \frac{\omega^2}{c^2}\epsilon_{\perp}\epsilon_{\parallel}} \frac{d^3k}{(2\pi)^3} \\ &= \frac{\epsilon_{\perp}}{\epsilon_{\parallel}} \iiint_{-\infty}^{\infty} e^{i\mathbf{k}_{\perp}\cdot\mathbf{x}_{\perp}} \int_{-\infty}^{\infty} \frac{e^{ik_{\parallel}x_{\parallel}}}{(k_{\parallel} - k_{\parallel}^e)(k_{\parallel} + k_{\parallel}^e)} \frac{dk_{\parallel}}{2\pi} \frac{d^2k_{\perp}}{(2\pi)^2}, \end{aligned} \quad (2.27)$$

$$\begin{aligned}
g_o(\mathbf{x}) &= \iiint_{-\infty}^{\infty} \frac{e^{i\mathbf{k}\cdot\mathbf{x}}}{k^2 - \frac{\omega^2}{c^2}\epsilon_{\perp}} \frac{d^3k}{(2\pi)^3} \\
&= \iint_{-\infty}^{\infty} e^{i\mathbf{k}_{\perp}\cdot\mathbf{x}_{\perp}} \int_{-\infty}^{\infty} \frac{e^{ik_{\parallel}x_{\parallel}}}{(k_{\parallel} - k_{\parallel}^o)(k_{\parallel} + k_{\parallel}^o)} \frac{dk_{\parallel}}{2\pi} \frac{d^2k_{\perp}}{(2\pi)^2}.
\end{aligned} \tag{2.28}$$

Taking the poles for outgoing solutions into account in the residue theorem we can integrate over k_{\parallel} and express the scalar Green's functions as

$$g_e(\mathbf{x}) = \frac{\epsilon_{\perp}}{\epsilon_{\parallel}} \iint_{-\infty}^{\infty} e^{i\mathbf{k}_{\perp}\cdot\mathbf{x}_{\perp}} \frac{ie^{ik_{\parallel}^e|x_{\parallel}|}}{2k_{\parallel}^e} \frac{d^2k_{\perp}}{(2\pi)^2} \equiv \frac{\epsilon_{\perp}}{\epsilon_{\parallel}} \hat{I}_e, \tag{2.29}$$

$$g_o(\mathbf{x}) = \iint_{-\infty}^{\infty} e^{i\mathbf{k}_{\perp}\cdot\mathbf{x}_{\perp}} \frac{ie^{ik_{\parallel}^o|x_{\parallel}|}}{2k_{\parallel}^o} \frac{d^2k_{\perp}}{(2\pi)^2} \equiv \hat{I}_o, \tag{2.30}$$

introducing the integral operators

$$\hat{I}_e = \iint_{-\infty}^{\infty} \frac{d^2k_{\perp}}{(2\pi)^2} e^{i\mathbf{k}_{\perp}\cdot\mathbf{x}_{\perp}} \frac{ie^{ik_{\parallel}^e|x_{\parallel}|}}{2k_{\parallel}^e}, \tag{2.31}$$

$$\hat{I}_o = \iint_{-\infty}^{\infty} \frac{d^2k_{\perp}}{(2\pi)^2} e^{i\mathbf{k}_{\perp}\cdot\mathbf{x}_{\perp}} \frac{ie^{ik_{\parallel}^o|x_{\parallel}|}}{2k_{\parallel}^o}, \tag{2.32}$$

where the components of the wavevectors parallel to the optical axis are defined as

$$k_{\parallel}^e = \sqrt{\frac{\omega^2}{c^2}\epsilon_{\perp} - k_{\perp}^2 \frac{\epsilon_{\perp}}{\epsilon_{\parallel}}} \quad \text{and} \quad k_{\parallel}^o = \sqrt{\frac{\omega^2}{c^2}\epsilon_{\perp} - k_{\perp}^2}. \tag{2.33}$$

We have used the quantities $x_{\parallel} = \mathbf{e}_{\parallel} \cdot \mathbf{x} = z - z'$ and $\mathbf{x}_{\perp} = \mathbf{x} - x_{\parallel} \mathbf{e}_{\parallel}$. $\mathbf{k}_{\perp} = (k_x \ k_y \ 0)^T$ is the part of the wavevector perpendicular to \mathbf{e}_{\parallel} and $k_{\perp}^2 = \|\mathbf{k}_{\perp}\|^2 = k_x^2 + k_y^2$. Outgoing waves are propagating away from the source. The sign of $k_{\parallel}^{e/o}$ must be chosen such that the plane wave $\propto e^{ik_{\parallel}x_{\parallel}}$ propagates in positive x_{\parallel} -direction (because this is the direction away from the source). “Propagation” refers to the energy flow, not the phase which can propagate in a different direction.

Now, we further introduce a polarization basis by defining

$$\mathbf{a}_s^{e/o} \equiv \frac{\mathbf{k}^{e/o} \times \mathbf{e}_{\parallel}}{\|\mathbf{k}^{e/o} \times \mathbf{e}_{\parallel}\|} = \frac{1}{k_{\perp}} \begin{pmatrix} k_y \\ -k_x \\ 0 \end{pmatrix} \quad (2.34)$$

and

$$\mathbf{a}_p^{e/o} \equiv \frac{\mathbf{a}_s^{e/o} \times \mathbf{k}^{e/o}}{\|\mathbf{a}_s^{e/o} \times \mathbf{k}^{e/o}\|} = \frac{1}{k_{\perp} k^{e/o}} \begin{pmatrix} \mp k_x k_{\parallel}^{e/o} \\ \mp k_y k_{\parallel}^{e/o} \\ k_{\perp}^2 \end{pmatrix} \quad (2.35)$$

where it is assumed that $k_{\parallel}^{e/o}$ is real. This basis accompanied by the wavevector

$$\mathbf{k}^{e/o} = \begin{pmatrix} k_x \\ k_y \\ \pm k_{\parallel}^{e/o} \end{pmatrix} \quad (2.36)$$

with $k^{e/o2} = \|\mathbf{k}^{e/o}\|^2 = k_{\parallel}^{e/o2} + k_{\perp}^2$ forms a complete orthogonal

basis for real $k_{\parallel}^{e/o}$ with the completeness relation

$$\mathbf{a}_s^{e/o} \otimes \mathbf{a}_s^{e/o} + \mathbf{a}_p^{e/o} \otimes \mathbf{a}_p^{e/o} + \frac{\mathbf{k}^{e/o} \otimes \mathbf{k}^{e/o}}{k^{e/o2}} = \mathbb{1}. \quad (2.37)$$

The undetermined signs in $\mathbf{k}^{e/o}$ and $\mathbf{a}_p^{e/o}$ are chosen depending on the observation point. The first choice is for $x_{\parallel} > 0$, the halfspace in which waves propagate in positive x_{\parallel} -direction (thus k_{\parallel} -component of $\mathbf{k}^{e/o}$ must be positive); the second choice for $x_{\parallel} < 0$, the halfspace in which waves propagate in negative x_{\parallel} -direction (thus k_{\parallel} -component must be negative).

If the wavevector component k_{\parallel} becomes complex, as in dissipative media or for evanescent modes, the above introduced vectors $\mathbf{a}_p^{e/o}$ and $\mathbf{k}^{e/o}$ are not orthogonal to each other anymore ($\mathbf{a}_s^{e/o}$ remains orthogonal to both). However, relation (2.37) remains valid and the vectors still form a basis.

From the definition of $\mathbf{a}_s^{e/o}$ it follows that $\mathbf{a}_s^e = \mathbf{a}_s^o \equiv \mathbf{a}_s$ and that (independent of k_{\parallel})

$$\frac{(\mathbf{k} \times \mathbf{e}_{\parallel}) \otimes (\mathbf{k} \times \mathbf{e}_{\parallel})}{(\mathbf{k} \times \mathbf{e}_{\parallel})^2} = \mathbf{a}_s \otimes \mathbf{a}_s. \quad (2.38)$$

This last relation allows us to rewrite the dyad \mathbb{F} . We find the expressions

$$\mathbb{F}_e = \frac{1}{\epsilon_{\parallel}} \hat{J}_e [\mathbf{a}_s \otimes \mathbf{a}_s], \quad (2.39)$$

$$\mathbb{F}_o = \hat{J}_o [\mathbf{a}_s \otimes \mathbf{a}_s]. \quad (2.40)$$

Finally, using the expansions for g_e and g_o together with the definition of the polarization bases and the completeness relation, we can bring the electric and magnetic Green's dyad in the final form. We obtain

$$\begin{aligned} \mathbf{G}^{\text{EE}} &= \mathbf{G}_o^{\text{EE}} + \mathbf{G}_e^{\text{EE}} \\ &= \hat{I}_o [\mathbf{a}_s \otimes \mathbf{a}_s] + \hat{I}_e [\mathbf{a}_p^e \otimes \mathbf{a}_p^e + B \mathbf{k}^e \otimes \mathbf{k}^e + C \mathbf{e}_\parallel \otimes \mathbf{e}_\parallel] \end{aligned} \quad (2.41)$$

and

$$\mathbf{G}^{\text{HH}} = \mathbf{G}_o^{\text{HH}} + \mathbf{G}_e^{\text{HH}} = \hat{I}_o [\epsilon_\perp \mathbf{a}_p^o \otimes \mathbf{a}_p^o] + \hat{I}_e [\epsilon_\perp \mathbf{a}_s \otimes \mathbf{a}_s] \quad (2.42)$$

introducing the anisotropy coefficients

$$B \equiv \frac{\frac{\omega^2}{c^2} \epsilon_\parallel - k^{e2}}{k^{e2} \frac{\omega^2}{c^2} \epsilon_\parallel} \quad \text{and} \quad C \equiv \frac{\epsilon_\perp}{\epsilon_\parallel} - 1. \quad (2.43)$$

Remembering the definition of the \hat{I} operators Green's functions (2.41) and (2.42) are represented here as a superposition of ordinary and extraordinary plane monochromatic waves.

Note, that due to the second derivation in Eqs. (2.20) and (2.21) with respect to x_\parallel the nabla operator ∇ not only provides an $\mathbf{i}\mathbf{k}^{e/o}$ but we additionally obtain the two singular terms [73]

$$\begin{aligned} \mathbf{G}_{\text{sing}}^{\text{EE}} &= \frac{1}{\epsilon_\parallel} \frac{c^2}{\omega^2} \hat{I}_e [2ik_\parallel^e] \mathbf{e}_\parallel \otimes \mathbf{e}_\parallel \delta(x_\parallel) \\ &= -\frac{1}{\epsilon_\parallel} \frac{c^2}{\omega^2} \mathbf{e}_\parallel \otimes \mathbf{e}_\parallel \delta(\mathbf{x}), \end{aligned} \quad (2.44)$$

$$\begin{aligned}
\mathbf{G}_{\text{sing}}^{\text{HH}} &= \frac{c^2}{\omega^2} \hat{I}_o \left[2i k_{\parallel}^o \right] \mathbf{e}_{\parallel} \otimes \mathbf{e}_{\parallel} \delta(x_{\parallel}) \\
&= -\frac{c^2}{\omega^2} \mathbf{e}_{\parallel} \otimes \mathbf{e}_{\parallel} \delta(\mathbf{x}),
\end{aligned} \tag{2.45}$$

where we have introduced the Dirac delta function

$$\delta(\mathbf{x}) \equiv \iiint_{-\infty}^{\infty} e^{\pm i \mathbf{k} \cdot \mathbf{x}} \frac{d^3 k}{(2\pi)^3}. \tag{2.46}$$

For the calculation of the heat flux these terms do not contribute since in this case $\mathbf{x} \neq \mathbf{0}$ (i. e. $\mathbf{r} \neq \mathbf{r}'$) as will be seen later. On the other hand, these terms do also not contribute to the density of states when neglecting losses, since in this case these terms are purely real. Therefore, we will neglect these terms in the following.

With the expressions for the electric and magnetic Green's dyad and $\mathbf{k}^{e/o} \times \mathbf{a}_p^{e/o} = k^{e/o} \mathbf{a}_s$ it can be easily proven that

$$\mathbf{G}^{\text{HH}} = -\frac{c^2}{\omega^2} \nabla \times \mathbf{G}^{\text{EE}} \times \nabla'. \tag{2.47}$$

Remembering Maxwell's equations the hybrid Green's functions are found to be [72]

$$\mathbf{G}^{\text{HE}} = \frac{1}{i\omega\mu_0} \nabla \times \mathbf{G}^{\text{EE}}, \tag{2.48}$$

$$\mathbf{G}^{\text{EH}} = \frac{-1}{i\omega\epsilon_0} \epsilon^{-1} \nabla \times \mathbf{G}^{\text{HH}}. \tag{2.49}$$

As can be seen later, \mathbf{G}^{EH} is not needed for the materials under

consideration, so we focus on \mathbf{G}^{HE} here. However, \mathbf{G}^{EH} can be calculated the same way and due to reciprocity $\mathbf{G}^{\text{EH}}(\mathbf{r}, \mathbf{r}') = \frac{\mu_0}{\epsilon_0} \mathbf{G}^{\text{HE}T}(\mathbf{r}, \mathbf{r}')$ holds [72].

We find

$$\begin{aligned}
 \mathbf{G}^{\text{HE}} &= \mathbf{G}_o^{\text{HE}} + \mathbf{G}_e^{\text{HE}} \\
 &= \frac{\hat{I}_o}{\omega\mu_0} [(\mathbf{k}^o \times \mathbf{a}_s) \otimes \mathbf{a}_s] + \frac{\hat{I}_e}{\omega\mu_0} \left[(\mathbf{k}^e \times \mathbf{a}_p^e) \otimes \mathbf{a}_p^e \right. \\
 &\quad \left. + B(\mathbf{k}^e \times \mathbf{k}^e) \otimes \mathbf{k}^e + C(\mathbf{k}^e \times \mathbf{e}_{\parallel}) \otimes \mathbf{e}_{\parallel} \right] \\
 &= \frac{\hat{I}_o}{\omega\mu_0} \left[-k^o \mathbf{a}_p^o \otimes \mathbf{a}_s \right] + \frac{\hat{I}_e}{\omega\mu_0} \left[k^e \mathbf{a}_s \otimes \mathbf{a}_p^e + C k_{\perp} \mathbf{a}_s \otimes \mathbf{e}_{\parallel} \right].
 \end{aligned} \tag{2.50}$$

Obviously, for an electric source the electric field of ordinary modes is polarized along \mathbf{a}_s and the magnetic field of ordinary modes along \mathbf{a}_p^o . However, although the magnetic field of extraordinary modes is polarized along \mathbf{a}_s their electric field is not polarized purely in \mathbf{a}_p^e -direction but has also components in \mathbf{k}^e -direction. Indeed, in uniaxial, nonmagnetic materials only for ordinary modes electric fields \mathbf{E} / \mathbf{D} , magnetic fields \mathbf{H} / \mathbf{B} and wavevector \mathbf{k}^o form an orthogonal set of vectors (orthogonal assuming real \mathbf{k}). For extraordinary modes only electric displacement field \mathbf{D} , magnetic fields \mathbf{H} / \mathbf{B} and wavevector \mathbf{k}^e are orthogonal which can be seen from the corresponding Green's

function

$$\begin{aligned} \mathbf{G}^{\text{DE}} = \mathbf{G}_o^{\text{DE}} + \mathbf{G}_e^{\text{DE}} = \epsilon_0 \boldsymbol{\epsilon} \mathbf{G}^{\text{EE}} = \epsilon_0 \hat{I}_o [\epsilon_{\perp} \mathbf{a}_s \otimes \mathbf{a}_s] \\ + \epsilon_0 \hat{I}_e \left[\frac{k^{e2}}{\epsilon_{\parallel} \frac{\omega^2}{c^2}} \mathbf{a}_p^e \otimes \left(\text{diag}(\epsilon_{\parallel}, \epsilon_{\parallel}, \epsilon_{\perp}) \mathbf{a}_p^e \right) \right] \end{aligned} \quad (2.51)$$

or directly from Maxwell's equations.

Furthermore, by definition \mathbf{E} , \mathbf{H} and (complex) Poynting vector $\mathbf{S} = \frac{1}{2} \mathbf{E} \times \mathbf{H}^*$ are also orthogonal. For extraordinary modes neither \mathbf{E} and \mathbf{D} nor \mathbf{S} and \mathbf{k}^e are parallel but point in different directions.

As a final remark, let us look at the polarization state. Propagating modes in a lossless medium have real wavevectors $\mathbf{k}^{e/o}$. \mathbf{a}_s and $\mathbf{a}_p^{e/o}$ are also real. Electric and magnetic fields are linearly polarized and in-phase.

When $\mathbf{k}^{e/o}$ becomes complex, as for evanescent modes or in dissipative materials, the situation changes. \mathbf{a}_s is still real. So \mathbf{E} of ordinary modes and \mathbf{H} of extraordinary modes are linearly polarized. But because $\mathbf{a}_p^{e/o}$ is complex, electric field of extraordinary modes and magnetic field of ordinary modes are elliptically polarized.

The modes used here have solely real tangential wavevectors \mathbf{k}_{\perp} . It is as if they are excited by light impinging from a lossless medium on an interface with the uniaxial medium under consideration. They should not be confused with modes which have a $\mathbf{k}^{e/o}$ that can be split into a real direction and a complex amplitude. Such modes represent a different basis with different

properties. E. g. in the isotropic case \mathbf{E} and \mathbf{H} are both linearly polarized but not in-phase.

As will be seen later, the setups under consideration are all 1-dimensional and infinitely extended in the transverse direction. Hence, all problems exhibit a translational symmetry in transverse direction and modes with real transverse wavevectors \mathbf{k}_\perp are a rational choice for our mode basis. Complex \mathbf{k}_\perp lead to different field amplitudes along the transverse direction which is difficult to interpret in a system with translational symmetry. So our choice of basis is not only a consequence of the derivation but will allow a physical interpretation of the thermal radiation equations.

Please notice that we use the names “ordinary” and “extraordinary” for the two fundamental polarization states throughout the thesis independent of the material, to keep it consistent. For isotropic materials the states are usually called “s- and p-polarized” instead. For lossy materials some people could expect another mode basis (with complex \mathbf{k}_\perp) when talking of ordinary and extraordinary modes.

2.3.2 Green’s functions for uniaxial medium–vacuum halfspaces

To calculate the emission from a uniaxial halfspace we need Green’s functions \mathbb{G}^{EE} and \mathbb{G}^{HE} for the setup shown in Fig. 2.2b. We restrict ourselves to sources in the uniaxial medium ($r'_\parallel =$

$z' < 0$) and are interested only in the fields in the vacuum ($r_{\parallel} = z > 0$).

The emitted waves, derived in the previous section, are now partially reflected and partially transmitted at the $z = 0$ interface. The tangential wavevector \mathbf{k}_{\perp} and of course the frequency are preserved. Green's functions become (only for $r'_{\parallel} < 0$ and $r_{\parallel} > 0$)

$$\begin{aligned} \mathbf{G}_{\text{vac}}^{\text{EE}}(\mathbf{r}, \mathbf{r}') &= \mathbf{G}_{\text{o,vac}}^{\text{EE}} + \mathbf{G}_{\text{e,vac}}^{\text{EE}} = \hat{I}_{\text{o,vac}} [t^{\text{s}} \mathbf{a}_{\text{s}} \otimes \mathbf{a}_{\text{s}}] \\ &+ \frac{\hat{I}_{\text{e,vac}}}{\omega/c} \left[t^{\text{p}} k^{\text{e}} \mathbf{a}_{\text{p}}^{\text{vac}} \otimes \mathbf{a}_{\text{p}}^{\text{e}} + t^{\text{p}} C k_{\perp} \mathbf{a}_{\text{p}}^{\text{vac}} \otimes \mathbf{e}_{\parallel} \right] \end{aligned} \quad (2.52)$$

and

$$\begin{aligned} \mathbf{G}_{\text{vac}}^{\text{HE}}(\mathbf{r}, \mathbf{r}') &= \mathbf{G}_{\text{o,vac}}^{\text{HE}} + \mathbf{G}_{\text{e,vac}}^{\text{HE}} = \frac{\hat{I}_{\text{o,vac}}}{c\mu_0} \left[-t^{\text{s}} \mathbf{a}_{\text{p}}^{\text{vac}} \otimes \mathbf{a}_{\text{s}} \right] \\ &+ \frac{\hat{I}_{\text{e,vac}}}{\omega\mu_0} \left[t^{\text{p}} k^{\text{e}} \mathbf{a}_{\text{s}} \otimes \mathbf{a}_{\text{p}}^{\text{e}} + t^{\text{p}} C k_{\perp} \mathbf{a}_{\text{s}} \otimes \mathbf{e}_{\parallel} \right], \end{aligned} \quad (2.53)$$

where the \hat{I} operators must be redefined to

$$\hat{I}_{\text{e,vac}} = \iint_{-\infty}^{\infty} \frac{d^2 k_{\perp}}{(2\pi)^2} e^{i\mathbf{k}_{\perp} \cdot \mathbf{x}_{\perp}} \frac{ie^{-ik_{\parallel}^{\text{e}} r'_{\parallel}} e^{ik_{\parallel}^{\text{vac}} r_{\parallel}}}{2k_{\parallel}^{\text{e}}}, \quad (2.54)$$

$$\hat{I}_{\text{o,vac}} = \iint_{-\infty}^{\infty} \frac{d^2 k_{\perp}}{(2\pi)^2} e^{i\mathbf{k}_{\perp} \cdot \mathbf{x}_{\perp}} \frac{ie^{-ik_{\parallel}^{\text{o}} r'_{\parallel}} e^{ik_{\parallel}^{\text{vac}} r_{\parallel}}}{2k_{\parallel}^{\text{o}}}, \quad (2.55)$$

and a new \mathbf{a}_p

$$\mathbf{a}_p^{\text{vac}} \equiv \frac{\mathbf{a}_s \times \mathbf{k}^{\text{vac}}}{\|\mathbf{a}_s \times \mathbf{k}^{\text{vac}}\|} = \frac{c}{k_\perp \omega} \begin{pmatrix} -k_x k_\parallel^{\text{vac}} \\ -k_y k_\parallel^{\text{vac}} \\ k_\perp^2 \end{pmatrix} \quad (2.56)$$

as well as the component of the wavevector parallel to the optical axis / z -axis in the vacuum

$$k_\parallel^{\text{vac}} = \sqrt{\frac{\omega^2}{c^2} - k_\perp^2} \quad (2.57)$$

are introduced. We further used the fact that $k^{\text{vac}} = \|\mathbf{k}^{\text{vac}}\| = \frac{\omega}{c}$ and

$$\mathbf{G}_{\text{vac}}^{\text{HE}} = \frac{1}{i\omega\mu_0} \nabla \times \mathbf{G}_{\text{vac}}^{\text{EE}}, \quad (2.58)$$

$$\mathbf{G}_{\text{vac}}^{\text{EE}} = \frac{-1}{i\omega\epsilon_0} \nabla \times \mathbf{G}_{\text{vac}}^{\text{HE}}. \quad (2.59)$$

The derivation of \mathbf{G}_{vac} is fairly simple. The field that is solely tangential – E for ordinary modes and H for extraordinary modes – remains solely tangential in all layers. It must only be modified by the transmission coefficient $t^{s/p}$ which is depicted in Eqs. (2.11)–(2.13) and the propagation in the vacuum must be taken into account in the \hat{I}_{vac} . The remaining fields are calculated via (2.58) and (2.59) which are basically Maxwell's equations in vacuum.

In the vacuum the fields are polarized as expected. For s-polar-

ization E is along \mathbf{a}_s and H along $\mathbf{a}_p^{\text{vac}}$, for p-polarization it's vice versa. Whereas the left vectors in the tensor products in \mathbb{G}_{vac} become vectors from the vacuum (or more generally from the observed medium), the right vectors remain vectors from inside the uniaxial medium (or more generally from the emitting medium). This is no surprise as the right vectors are later multiplied by the source and the source orientation in the emitting medium is crucial. The left vectors represent the polarization in the observation medium and thus, are adjusted to it.

2.3.3 Green's functions for multilayer systems

Extending the setup to a multilayer stack works similar to the introduction of an interface. Assume the emitter is still located in the left halfspace ($r'_{\parallel} = z' < 0$) the boundary of which is at $z = 0$. And the observation is in one of the layers ($r_{\parallel} = z > 0$). Green's functions are derived and look similar to (2.52) and (2.53) except for two differences.

First, the observation medium is not vacuum but the medium of observed layer j . Therefore, the wavevector components parallel to the optical axis / z -axis are now

$$k_{\parallel,j}^e = \sqrt{\frac{\omega^2}{c^2} \epsilon_{\perp,j} - k_{\perp}^2 \frac{\epsilon_{\perp,j}}{\epsilon_{\parallel,j}}} \quad \text{and} \quad k_{\parallel,j}^o = \sqrt{\frac{\omega^2}{c^2} \epsilon_{\perp,j} - k_{\perp}^2}. \quad (2.60)$$

Similarly $\mathbf{a}_{p,j}^{e/o}$ must be introduced which replace $\mathbf{a}_p^{\text{vac}}$.

Second, in addition to the forward (in positive z -direction) prop-

agating wave, there is a backward propagating wave whose $k_{\parallel,j}^{e/o}$ component has the opposite sign. The amplitudes of these waves are not altered by transmission coefficients $t^{s/p}$ but by four coefficients, two for ordinary / s-polarized modes and two for extraordinary / p-polarized ones, each time one for the forward and one for the backward wave. The normalized coefficients can be calculated numerically with the TMM, as explained at the end of Section 2.2. Related methods like the numerically more stable scattering-matrix method [74] can be used as well. Or for simple geometries the coefficients can be calculated analytically.

We refrain from writing down the equations for \mathbb{G} as the approach is clear, albeit writing down all equations is cumbersome. The situation is alike when the emitter is located in one of the layers with finite thickness, as shown in Fig. 2.2c, and not in the halfspace. The only difference is: In each observation layer there will be two pairs of forward and backward propagating waves [74]. One pair comes from the wave emitted from the source in positive direction and one from the wave emitted in negative direction. When the emitter is located in the left halfspace, the wave emitted to the left will never reach and thus influence the multilayers. This is why in this case there is only one forward and backward wave in each layers. Again, the normalized amplitudes can be calculated e. g. with the TMM, where each pair is treated separately. For more details and equations we refer the reader to Ref. [74].

2.4 Thermal energy density, density of states and thermal power flow

2.4.1 Energy density and density of states

From Poynting's theorem [13]

$$-\nabla \cdot (\mathbf{E} \times \mathbf{H}) = \mathbf{E} \cdot \frac{\partial \mathbf{D}}{\partial t} + \mathbf{H} \cdot \frac{\partial \mathbf{B}}{\partial t} + \mathbf{J} \cdot \mathbf{E} \quad (2.61)$$

the rate of change of the energy density U inside an anisotropic medium is given by [13]

$$\frac{\partial U}{\partial t} = \frac{\partial U^E}{\partial t} + \frac{\partial U^H}{\partial t} = \mathbf{E} \cdot \frac{\partial \mathbf{D}}{\partial t} + \mathbf{H} \cdot \frac{\partial \mathbf{B}}{\partial t}. \quad (2.62)$$

Following the reasoning of Ref. [75] we concentrate on the electric part (the magnetic part can be treated analogously) and integrate it over time to obtain the energy density. Using the Fourier representations

$$\mathbf{E}(t) = \int_{-\infty}^{\infty} \mathbf{E}(\omega) e^{-i\omega t} \frac{d\omega}{2\pi}, \quad (2.63)$$

$$\mathbf{D}(t) = \int_{-\infty}^{\infty} \mathbf{D}(\omega) e^{-i\omega t} \frac{d\omega}{2\pi} \quad (2.64)$$

with respect to time we have (Einstein's summation convention)

$$U^E = \int_{-\infty}^t \iint_{-\infty}^{\infty} E_{\alpha}(\omega)(-i\omega')D_{\alpha}(\omega')e^{-i(\omega+\omega')t'} \frac{d\omega'}{2\pi} \frac{d\omega}{2\pi} dt', \quad (2.65)$$

assuming that the fields at $t = -\infty$ vanish so that the energy density also vanishes, i. e. $U(t = -\infty) = 0$. The time integration can be carried out and using the relation $\mathbf{D}(\omega) = \epsilon_0 \epsilon(\omega) \mathbf{E}(\omega)$ the expression for the energy density can be brought into the form

$$\begin{aligned} U^E &= \frac{\epsilon_0}{2} \iint_{-\infty}^{\infty} \left[\frac{E_{\alpha}(\omega) \epsilon_{\alpha\beta}(\omega') E_{\beta}(\omega') \omega'}{\omega + \omega'} \right. \\ &\quad \left. + \frac{E_{\alpha}(\omega) \epsilon_{\alpha\beta}(\omega') E_{\beta}(\omega') \omega'}{\omega + \omega'} \right] e^{-i(\omega+\omega')t} \frac{d\omega'}{2\pi} \frac{d\omega}{2\pi} \\ &= \frac{\epsilon_0}{2} \iint_{-\infty}^{\infty} \left[-\frac{E_{\alpha}(\omega) \epsilon_{\alpha\beta}^*(\omega') E_{\beta}^*(\omega') \omega'}{\omega - \omega'} \right. \\ &\quad \left. + \frac{E_{\alpha}^*(\omega') \epsilon_{\alpha\beta}(\omega) E_{\beta}(\omega) \omega}{\omega - \omega'} \right] e^{-i(\omega-\omega')t} \frac{d\omega'}{2\pi} \frac{d\omega}{2\pi} \end{aligned} \quad (2.66)$$

Here the following property was used: Since $\mathbf{E}(t)$ is real its Fourier transform obeys the relation $\mathbf{E}(-\omega) = \mathbf{E}^*(\omega)$. The same holds for ϵ and Green's functions \mathbf{G} .

Now, since we are interested in the properties of the thermal electric field in equilibrium, we can make use of the fluctuation-

dissipation theorem (of the first kind) [63]

$$\begin{aligned} & \langle E_\alpha(\mathbf{r}, \omega) E_\beta^*(\mathbf{r}', \omega') \rangle \\ & = 4\pi\omega\mu_0 \tilde{\mathcal{U}}(\omega, T) \delta(\omega - \omega') \Im \left(\mathbb{G}_{\alpha\beta}^{\text{EE}}(\mathbf{r}, \mathbf{r}'; \omega) \right) \end{aligned} \quad (2.67)$$

where \mathbb{G}^{EE} is the electrical Green's dyadic, and

$$\tilde{\mathcal{U}}(\omega, T) = \frac{\hbar\omega}{2} \coth \left(\frac{\hbar\omega}{2k_{\text{B}}T} \right) \quad (2.68)$$

is the mean energy of a harmonic oscillator in thermal equilibrium at temperature T including zero-point fluctuations [69]. It is common and in many cases allowed to neglect the small zero-point energy and use the term

$$\mathcal{U}(\omega, T) = \tilde{\mathcal{U}}(\omega, T) - \frac{\hbar\omega}{2} = \frac{\hbar\omega}{e^{\frac{\hbar\omega}{k_{\text{B}}T}} - 1} \quad (2.69)$$

instead of $\tilde{\mathcal{U}}$. However, this should only be done when no integration over negative frequencies is performed any more. Otherwise one loses the property of $\tilde{\mathcal{U}}$ being an even function of ω and obtains wrong results.

The fluctuation-dissipation theorem (2.67) comprises the fact that fields at different frequencies are uncorrelated. This is because thermal fluctuations are (wide-sense) stationary stochastic processes, so as one would assume they don't change their properties over time.

Now we make the assumption that we have no losses at the obser-

vation point \mathbf{r} , i. e. the permittivity tensor has real components. Losses at other locations are allowed and influence Green's functions. A discussion about energy density at locations with losses can be found at the end of this subsection. By means of relation (2.67) we can determine the ensemble mean of the electrical energy density in equilibrium. We obtain

$$\begin{aligned} \langle U^E(\mathbf{r}) \rangle &= \frac{1}{2} \int_{-\infty}^{\infty} \lim_{\omega' \rightarrow \omega} \frac{\epsilon_{\alpha\beta}(\omega)\omega - \epsilon_{\alpha\beta}(\omega')\omega'}{\omega - \omega'} \\ &\quad \cdot \frac{2\omega}{c^2} \tilde{\mathcal{U}}(\omega, T) \Im \left(\mathbb{G}_{\alpha\beta}^{EE}(\mathbf{r}, \mathbf{r}; \omega) \right) \frac{d\omega}{2\pi}. \end{aligned} \quad (2.70)$$

Note that the transpose of Green's dyadic is given by $\mathbb{G}^{EE^T}(\mathbf{r}, \mathbf{r}') = \mathbb{G}^{EE}(\mathbf{r}', \mathbf{r}) = \mathbb{G}^{EE}(\mathbf{r}, \mathbf{r}')$ [64, 72].

Finally, we arrive at (neglecting the zero-point energy)

$$\langle U^E \rangle = \int_0^{\infty} \frac{2\omega}{c^2} \frac{d(\epsilon_{\alpha\beta}(\omega)\omega)}{d\omega} \mathcal{U}(\omega, T) \Im \left(\mathbb{G}_{\alpha\beta}^{EE}(\mathbf{r}, \mathbf{r}; \omega) \right) \frac{d\omega}{2\pi}. \quad (2.71)$$

Similarly for the magnetic part we find

$$\langle U^H \rangle = \int_0^{\infty} \frac{2\omega}{c^2} \frac{d(\mu_{\alpha\beta}(\omega)\omega)}{d\omega} \mathcal{U}(\omega, T) \Im \left(\mathbb{G}_{\alpha\beta}^{HH}(\mathbf{r}, \mathbf{r}; \omega) \right) \frac{d\omega}{2\pi}. \quad (2.72)$$

The integration has been restricted to solely positive frequencies as the whole integrand is a real, even function.

In the following we refrain from always writing expected value

$\langle \circ \rangle$ of a quantity. Nevertheless, the reader should remember that we deal with fluctuating quantities and present their expected values. From these expressions for U we can now read off the spectral energy density of the fields in thermal equilibrium as

$$u(\mathbf{r}; \omega) = \frac{\omega}{\pi c^2} \mathcal{U}(\omega, T) \left[\frac{d(\epsilon_{\alpha\beta}(\omega)\omega)}{d\omega} \Im \left(\mathbf{G}_{\alpha\beta}^{\text{EE}}(\mathbf{r}, \mathbf{r}; \omega) \right) + \frac{d(\mu_{\alpha\beta}(\omega)\omega)}{d\omega} \Im \left(\mathbf{G}_{\alpha\beta}^{\text{HH}}(\mathbf{r}, \mathbf{r}; \omega) \right) \right]. \quad (2.73)$$

If we define the local density of states (LDOS) $D(\mathbf{r}, \omega)$ by the relation [76]

$$u(\mathbf{r}; \omega) = \mathcal{U}(\omega, T) D(\mathbf{r}, \omega), \quad (2.74)$$

i. e.

$$U = \int_0^\infty u(\mathbf{r}; \omega) d\omega = \int_0^\infty \mathcal{U}(\omega, T) D(\mathbf{r}, \omega) d\omega, \quad (2.75)$$

we find

$$D(\omega) = \frac{\omega}{\pi c^2} \left[\frac{d(\epsilon_{\alpha\beta}(\omega)\omega)}{d\omega} \Im \left(\mathbf{G}_{\alpha\beta}^{\text{EE}}(\mathbf{r}, \mathbf{r}; \omega) \right) + \frac{d(\mu_{\alpha\beta}(\omega)\omega)}{d\omega} \Im \left(\mathbf{G}_{\alpha\beta}^{\text{HH}}(\mathbf{r}, \mathbf{r}; \omega) \right) \right]. \quad (2.76)$$

Or since $\mathbf{G}^{\text{EE}}(\mathbf{r}, \mathbf{r})$ and $\mathbf{G}^{\text{HH}}(\mathbf{r}, \mathbf{r})$ are symmetric

$$D(\omega) = \frac{\omega}{\pi c^2} \Im \text{Tr} \left[\frac{d(\boldsymbol{\epsilon}\omega)}{d\omega} \mathbf{G}^{\text{EE}}(\mathbf{r}, \mathbf{r}; \omega) + \frac{d(\boldsymbol{\mu}\omega)}{d\omega} \mathbf{G}^{\text{HH}}(\mathbf{r}, \mathbf{r}; \omega) \right]. \quad (2.77)$$

This relation holds for any anisotropic medium without dissipation. For dispersionless anisotropic materials this relation can be further simplified to

$$D(\omega) = \frac{\omega}{\pi c^2} \Im \text{Tr} \left[\boldsymbol{\epsilon} \mathbf{G}^{\text{EE}}(\mathbf{r}, \mathbf{r}; \omega) + \boldsymbol{\mu} \mathbf{G}^{\text{HH}}(\mathbf{r}, \mathbf{r}; \omega) \right]. \quad (2.78)$$

In the limit of an isotropic body this trace formula reduces to the well-known trace formula for the local density of states [76].

At the end, let us comment on materials with dissipation. The applied assumption of negligible losses only holds for the material at the observation point \mathbf{r} . At other locations losses will of course influence Green's functions, however, do not impact the validity of the presented formalism. Even more, there must be some losses in the system to emit thermal radiation. Though, the losses can be arbitrary small. Besides that, when we talk of no losses we only refer to the spectral regions of interest, namely the near, mid and parts of the far infrared. In regions irrelevant for thermal radiation dissipation can exist, in principle allowing normal dispersion even in the infrared [14].

Defining the energy density inside a lossy medium is complicated for several reasons. Poynting's theorem (2.61) relates three quantities: the power flux $\mathbf{E} \times \mathbf{H}$, the energy density and the dissipated heat. Energy density and dissipation are encoded in the complex $\boldsymbol{\epsilon}$. Unfortunately, in general it is impossible to separately express the energy density and the evolved heat as functions of (complex) permittivity [77]. But energy density without

dissipation is what we are looking for.

Next, in thermal equilibrium the total dissipated heat should vanish. Dissipation is compensated by emission [75]. To model the emission one would need to introduce fluctuating sources, as done in the following subsection. As will be shown, these sources are point sources. The fields and thus the energy density diverge at point sources, which are located in the lossy medium.

By employing particular models for the material behavior one can avoid the problems and calculate an energy density [75]. Here, we keep the materials universal and refrain from dealing with the complicated problem of energy density inside dissipative materials. Admittedly, the restriction to lossless materials is problematic when analyzing HMs or HMMs which feature at least some dissipation. Nonetheless, our study of energy densities inside idealized lossless HMs in Chapter 3 is an important step towards the understanding of thermal radiation inside real HMs.

2.4.2 Power flow

Deriving the general formula for the radiative heat flux is very similar to the derivation of the thermal energy density.

In Poynting's theorem (2.61) there appears the term $\nabla \cdot (\mathbf{E} \times \mathbf{H})$.

Thus, one can consider

$$\mathbf{S} = \mathbf{E} \times \mathbf{H} \tag{2.79}$$

as the power flux. \mathbf{S} is called Poynting vector [13].

Using the Fourier representation of $\mathbf{E}(t)$ (2.63) and $\mathbf{H}(t)$ (equivalent equation) we arrive at the expression

$$\mathbf{S} = \iint_{-\infty}^{\infty} \mathbf{E}(\omega) \times \mathbf{H}(\omega') e^{-i(\omega+\omega')t} \frac{d\omega'}{2\pi} \frac{d\omega}{2\pi}. \quad (2.80)$$

Furthermore, we know that since we consider nonmagnetic materials the fluctuating thermal fields \mathbf{E} and \mathbf{H} are produced solely by fluctuating electric currents \mathbf{J} :

$$\mathbf{E}(\mathbf{r}; \omega) = i\omega\mu_0 \iiint_V \mathbf{G}^{\text{EE}}(\mathbf{r}, \mathbf{r}'; \omega) \mathbf{J}(\mathbf{r}'; \omega) d^3r', \quad (2.81)$$

$$\mathbf{H}(\mathbf{r}; \omega) = i\omega\mu_0 \iiint_V \mathbf{G}^{\text{HE}}(\mathbf{r}, \mathbf{r}'; \omega) \mathbf{J}(\mathbf{r}'; \omega) d^3r'. \quad (2.82)$$

This yields

$$\begin{aligned} \mathbf{S}(\mathbf{r}; t) = & \mu_0^2 \iint_{-\infty}^{\infty} \iiint_V \iiint_V \iiint_V e^{-i(\omega-\omega')t} \omega\omega' [\mathbf{G}^{\text{EE}}(\mathbf{r}, \mathbf{r}'; \omega) \mathbf{J}(\mathbf{r}'; \omega)] \\ & \times [\mathbf{G}^{\text{HE}*}(\mathbf{r}, \mathbf{r}''; \omega') \mathbf{J}^*(\mathbf{r}''; \omega')] d^3r'' d^3r' \frac{d\omega'}{2\pi} \frac{d\omega}{2\pi} \end{aligned} \quad (2.83)$$

where we have used the Fourier transform property $\mathbf{J}(-\omega) = \mathbf{J}^*(\omega)$ and same for \mathbf{G} .

Before we can make use of the fluctuation-dissipation theorem

(of the second kind) [62, 70]

$$\begin{aligned} & \langle J_\alpha(\mathbf{r}, \omega) J_\beta^*(\mathbf{r}', \omega') \rangle \\ & = 4\pi\omega\epsilon_0\tilde{\mathcal{U}}(\omega, T)\delta(\omega - \omega')\Im[\epsilon_{\alpha\beta}(\omega)]\delta(\mathbf{r} - \mathbf{r}'), \end{aligned} \quad (2.84)$$

we have to assume that the emitting parts of the system are held in local thermal equilibrium at a given temperature T . Moreover, we define the heat flux of interest Φ , and its spectral counterpart $\phi(\omega)$, as the power flux along the optical axis / z -axis and rewrite it as

$$\begin{aligned} \Phi & = \langle S_{\parallel} \rangle = \langle S_z \rangle = \int_0^\infty \phi(\omega) d\omega \\ & = \mu_0^2 \int_{-\infty}^\infty \int_V \int_V \int_V \int_V \omega\omega' e^{-i(\omega-\omega')t} \xi_{\alpha\beta z} \left\langle \left(\mathbf{G}^{\text{EE}}(\mathbf{r}, \mathbf{r}'; \omega) \mathbf{J}(\mathbf{r}'; \omega) \right)_\alpha \right. \\ & \quad \left. \left(\mathbf{G}^{\text{HE}*}(\mathbf{r}, \mathbf{r}''; \omega') \mathbf{J}^*(\mathbf{r}''; \omega') \right)_\beta \right\rangle d^3r'' d^3r' \frac{d\omega'}{2\pi} \frac{d\omega}{2\pi} \\ & = \mu_0^2 \int_{-\infty}^\infty \int_V \int_V \int_V \int_V \omega\omega' e^{-i(\omega-\omega')t} \xi_{\alpha\beta z} \left\langle \mathbf{G}_{\alpha\gamma}^{\text{EE}}(\mathbf{r}, \mathbf{r}'; \omega) J_\gamma(\mathbf{r}'; \omega) \right. \\ & \quad \left. \mathbf{G}_{\beta\eta}^{\text{HE}*}(\mathbf{r}, \mathbf{r}''; \omega') J_\eta^*(\mathbf{r}''; \omega') \right\rangle d^3r'' d^3r' \frac{d\omega'}{2\pi} \frac{d\omega}{2\pi}. \end{aligned} \quad (2.85)$$

The fluctuation-dissipation theorem (2.84) comprises not only the fact that the sources at different frequencies are uncorrelated, which is due to the stationarity of the thermal processes, but that sources at different locations are uncorrelated as well.

That is a direct consequence of locality. Locality which manifests itself as ϵ and μ being independent of the wavevector \mathbf{k} means: A reaction of the material to a field at one location does not influence the reaction at another location. In such a medium the thermal fluctuations at different spots cannot influence each other. Furthermore, the spatial non-correlation means that the sources are point-like sources. Watch out, here we are talking about the sources. The fields can be correlated as fields at different locations can be created by the same source.

There is a fluctuation-dissipation theorem (of the second kind) for magnetic sources [63, 70]

$$\begin{aligned} & \langle M_\alpha(\mathbf{r}, \omega) M_\beta^*(\mathbf{r}', \omega') \rangle \\ &= 4\pi\omega\mu_0\tilde{\mathcal{U}}(\omega, T)\delta(\omega - \omega')\Im[\mu_{\alpha\beta}(\omega)]\delta(\mathbf{r} - \mathbf{r}'). \end{aligned} \quad (2.86)$$

But because we take $\mu = \mathbb{1}$ and thus $\Im(\mu) = 0$, it only tells us that there are no magnetic sources, as stated above. (If there are, magnetic and electric sources are uncorrelated [70].)

Now, the fluctuation-dissipation theorem (2.84) simplifies the heat flux expression to

$$\begin{aligned} \Phi &= \int_{-\infty}^{\infty} \frac{2\omega^3\mu_0}{c^2}\tilde{\mathcal{U}}(\omega, T) \iiint_V \xi_{\alpha\beta\gamma} \mathbf{G}_{\alpha\gamma}^{\text{EE}}(\mathbf{r}, \mathbf{r}'; \omega) \\ & \quad \Im[\epsilon_{\gamma\eta}(\omega)] \mathbf{G}_{\beta\eta}^{\text{HE}*}(\mathbf{r}, \mathbf{r}'; \omega) d^3r' \frac{d\omega}{2\pi}. \end{aligned} \quad (2.87)$$

We assumed that the emitting volume is in local thermal equi-

librium at temperature T . As can be checked easily the Fourier transform property $\mathbb{G}(-\omega) = \mathbb{G}^*(\omega)$ is valid for the whole integrand. That allows us to eliminate the integration over negative frequencies (neglecting the zero-point energy)

$$\begin{aligned}
\Phi &= 2\Re \int_0^\infty \frac{2\omega^3 \mu_0}{c^2} \mathcal{U}(\omega, T) \iiint_V \xi_{\alpha\beta z} \mathbb{G}_{\alpha\gamma}^{\text{EE}}(\mathbf{r}, \mathbf{r}'; \omega) \\
&\quad \Im [\epsilon_{\gamma\eta}(\omega)] \mathbb{G}_{\beta\eta}^{\text{HE}*}(\mathbf{r}, \mathbf{r}'; \omega) d^3 r' \frac{d\omega}{2\pi} \\
&= 2\Re \int_0^\infty \frac{2\omega^3 \mu_0}{c^2} \mathcal{U}(\omega, T) \iiint_V \xi_{\alpha\beta z} \left(\mathbb{G}^{\text{EE}}(\mathbf{r}, \mathbf{r}'; \omega) \right. \\
&\quad \left. \Im [\epsilon(\omega)] \mathbb{G}^{\text{HEH}}(\mathbf{r}, \mathbf{r}'; \omega) \right)_{\alpha\beta} d^3 r' \frac{d\omega}{2\pi}
\end{aligned} \tag{2.88}$$

providing a general expression for the heat flux.

Now, we limit the emitting part of the structure to the half-space $z' < 0$ and determine the heat flux along the z -axis at a position $z \geq 0$. Further simplifications are possible if we write Green's functions as spatial Fourier transforms with respect to the coordinates perpendicular to the optical axis:

$$\mathbb{G}(\mathbf{r}, \mathbf{r}') = \iint_{-\infty}^{\infty} \mathbb{G}(\mathbf{r}, z', \mathbf{k}'_{\perp}) e^{-i\mathbf{k}'_{\perp} \cdot \mathbf{r}'_{\perp}} \frac{d^2 k'_{\perp}}{(2\pi)^2}, \tag{2.89}$$

as we have done in Section 2.3. Then we obtain

$$\begin{aligned}
\Phi &= 2\Re \int_0^\infty \frac{2\omega^3 \mu_0}{c^2} \mathcal{U}(\omega, T) \int_{-\infty}^0 \iint_{-\infty}^\infty \xi_{\alpha\beta z} \left(\iint_{-\infty}^\infty \iint_{-\infty}^\infty \right. \\
&\quad \mathbf{G}^{\text{EE}}(\mathbf{r}, z', \mathbf{k}'_\perp; \omega) \Im[\boldsymbol{\epsilon}(\omega)] \mathbf{G}^{\text{HEH}}(\mathbf{r}, z', \mathbf{k}''_\perp; \omega) \\
&\quad \left. e^{-i(\mathbf{k}'_\perp - \mathbf{k}''_\perp) \cdot \mathbf{r}'_\perp} \frac{d^2 k''_\perp}{(2\pi)^2} \frac{d^2 k'_\perp}{(2\pi)^2} \right)_{\alpha\beta} d^2 r'_\perp dz' \frac{d\omega}{2\pi} \\
&= 2\Re \int_0^\infty \frac{2\omega^3 \mu_0}{c^2} \mathcal{U}(\omega, T) \int_{-\infty}^0 \xi_{\alpha\beta z} \left(\iint_{-\infty}^\infty \iint_{-\infty}^\infty \right. \\
&\quad \mathbf{G}^{\text{EE}}(\mathbf{r}, z', \mathbf{k}'_\perp; \omega) \Im[\boldsymbol{\epsilon}(\omega)] \mathbf{G}^{\text{HEH}}(\mathbf{r}, z', \mathbf{k}''_\perp; \omega) \\
&\quad \left. (2\pi)^2 \delta(\mathbf{k}'_\perp - \mathbf{k}''_\perp) \frac{d^2 k''_\perp}{(2\pi)^2} \frac{d^2 k'_\perp}{(2\pi)^2} \right)_{\alpha\beta} dz' \frac{d\omega}{2\pi} \\
&= 2\Re \int_0^\infty \frac{2\omega^3 \mu_0}{c^2} \mathcal{U}(\omega, T) \int_{-\infty}^0 \iint_{-\infty}^\infty \xi_{\alpha\beta z} \left(\mathbf{G}^{\text{EE}}(\mathbf{r}, z', \mathbf{k}'_\perp; \omega) \right. \\
&\quad \left. \Im[\boldsymbol{\epsilon}(\omega)] \mathbf{G}^{\text{HEH}}(\mathbf{r}, z', \mathbf{k}'_\perp; \omega) \right)_{\alpha\beta} \frac{d^2 k'_\perp}{(2\pi)^2} dz' \frac{d\omega}{2\pi}
\end{aligned} \tag{2.90}$$

using the Dirac delta identity

$$\iint_{-\infty}^\infty e^{\pm i \mathbf{k}'_\perp \cdot \mathbf{r}'_\perp} d^2 r'_\perp = (2\pi)^2 \delta(\mathbf{k}'_\perp). \tag{2.91}$$

Finally, we make use of the rotational symmetry (around the

optical axis) of the problems under consideration

$$\begin{aligned}
\Phi &= 2\Re \int_0^\infty \frac{2\omega^3 \mu_0}{c^2} \mathcal{U}(\omega, T) \iint_{-\infty}^\infty \int_{-\infty}^0 \xi_{\alpha\beta z} \left(\mathbf{G}^{\text{EE}}(\mathbf{r}, z', \mathbf{k}'_\perp; \omega) \right. \\
&\quad \left. \Im[\boldsymbol{\epsilon}(\omega)] \mathbf{G}^{\text{HEH}}(\mathbf{r}, z', \mathbf{k}'_\perp; \omega) \right)_{\alpha\beta} dz' \frac{d^2 k'_\perp}{(2\pi)^2} \frac{d\omega}{2\pi} \\
&= 2\Re \int_0^\infty \frac{2\omega^3 \mu_0}{c^2} \mathcal{U}(\omega, T) \int_0^\infty \int_{-\infty}^0 \xi_{\alpha\beta z} \left(\mathbf{G}^{\text{EE}}(\mathbf{r}, z', k'_\perp; \omega) \right. \\
&\quad \left. \Im[\boldsymbol{\epsilon}(\omega)] \mathbf{G}^{\text{HEH}}(\mathbf{r}, z', k'_\perp; \omega) \right)_{\alpha\beta} dz' k'_\perp \frac{dk'_\perp}{2\pi} \frac{d\omega}{2\pi}.
\end{aligned} \tag{2.92}$$

Note that for deriving Eq. (2.92) no material restrictions have been assumed. So this expression is valid for dissipative and dispersive materials.

2.5 Thermal radiation inside uniaxial materials

2.5.1 Energy density and density of states

The thermal energy density inside a lossless uniaxial medium (UM) will be derived in this section. To this end, the medium is put in a cavity with opaque walls at constant temperature T [11], as shown in Fig. 2.3b. The cavity acts as a heat bath. In thermal equilibrium the radiations absorbed and emitted by

the cavity compensate each other, the fields become equilibrated and the energy density inside the UM is constant.

The cavity can show locally different energy densities. First, there can be evanescent waves reaching from the cavity walls into the UM. Second, there can be interferences creating resonator modes. To avoid these cavity effects we let the size of the cavity approach infinity. That resembles the situation in Fig. 2.3a where the whole space is filled with the homogeneous UM.

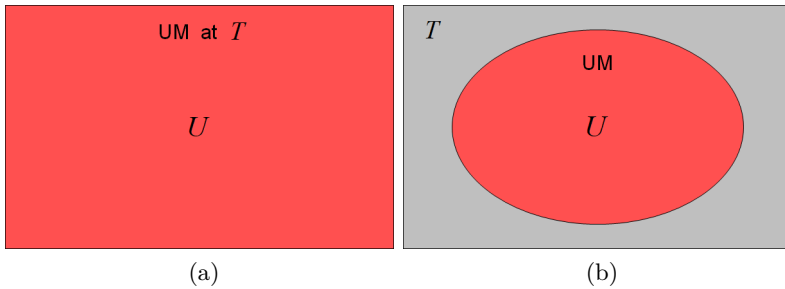


Figure 2.3: Illustration of the setups for which the thermal energy density U inside uniaxial media is evaluated. (a) homogeneous uniaxial medium (UM) at temperature T , (b) large cavity at temperature T filled with UM. Both setups (a) and (b) yield the same energy density.

Alternatively to the cavity walls in the infinite, one can also imagine a situation with no cavity. A perfect lossless space will show no thermal radiation as without absorption there is also no emission. However, even the smallest dissipation, as it is present

in every material, changes the situation. Introducing dissipation and letting it approach zero yield the same energy density as the infinite cavity [76].

The limit formation reduces to finding the limit of Green's functions as losses approach zero. As they are continuous w. r. t. permittivity we simply use Green's dyadics for the lossless bulk uniaxial medium.

For lossless and nonmagnetic uniaxial media, using the material properties from Eqs. (2.1) and (2.2) and Green's functions derived in Section 2.3.1, we find for the ordinary modes

$$\begin{aligned} \text{Tr} \left[\mathbf{G}_o^{\text{HH}}(\mathbf{r}, \mathbf{r}', \omega) \right] &= \text{Tr} \left[\boldsymbol{\epsilon} \mathbf{G}_o^{\text{EE}}(\mathbf{r}, \mathbf{r}', \omega) \right] \\ &= \epsilon_{\perp} g_o(\mathbf{r}, \mathbf{r}', \omega) = \epsilon_{\perp} \hat{I}_o, \end{aligned} \quad (2.93)$$

$$\text{Tr} \left[\frac{d\boldsymbol{\epsilon}}{d\omega} \mathbf{G}_o^{\text{EE}}(\mathbf{r}, \mathbf{r}', \omega) \right] = \frac{d\epsilon_{\perp}}{d\omega} g_o(\mathbf{r}, \mathbf{r}', \omega) = \frac{d\epsilon_{\perp}}{d\omega} \hat{I}_o \quad (2.94)$$

and for the extraordinary modes

$$\begin{aligned} \text{Tr} \left[\mathbf{G}_e^{\text{HH}}(\mathbf{r}, \mathbf{r}', \omega) \right] &= \text{Tr} \left[\boldsymbol{\epsilon} \mathbf{G}_e^{\text{EE}}(\mathbf{r}, \mathbf{r}', \omega) \right] \\ &= \epsilon_{\parallel} g_e(\mathbf{r}, \mathbf{r}', \omega) = \epsilon_{\perp} \hat{I}_e, \end{aligned} \quad (2.95)$$

$$\text{Tr} \left[\frac{d\boldsymbol{\epsilon}}{d\omega} \mathbf{G}_e^{\text{EE}}(\mathbf{r}, \mathbf{r}', \omega) \right] = \frac{d\epsilon_{\perp}}{d\omega} \hat{I}_e - \frac{d(\epsilon_{\perp}/\epsilon_{\parallel})}{d\omega} \hat{I}_e \frac{k_{\perp}^2}{\omega^2/c^2}, \quad (2.96)$$

where $\hat{I}_{e/o}$ are given in Eqs. (2.31) and (2.32). The frequency derivative $\frac{d(\boldsymbol{\epsilon}\omega)}{d\omega}$ in the expression for the density of states (2.77) is expanded to $\boldsymbol{\epsilon} + \omega \frac{d\boldsymbol{\epsilon}}{d\omega}$ using the product rule. Please be reminded of our no loss assumption which strongly restricts the

dispersion $\frac{d\epsilon}{d\omega}$ due to Kramers–Kronig relations [14]. But as explained previously we will still have a look at energy density inside (hypothetic) lossless, dispersive HMs in Section 3.2.1, a vital step towards real HMs.

Here the following properties were utilized:

$$\text{Tr} [\mathbf{a}_s \otimes \mathbf{a}_s] = 1, \quad (2.97)$$

$$\text{Tr} [\boldsymbol{\epsilon} \mathbf{a}_s \otimes \mathbf{a}_s] = \epsilon_{\perp}, \quad (2.98)$$

$$\text{Tr} [\mathbf{a}_p^o \otimes \mathbf{a}_p^o] = 1, \quad (2.99)$$

$$\text{Tr} [\boldsymbol{\epsilon} \mathbf{a}_p^e \otimes \mathbf{a}_p^e] = \frac{\epsilon_{\perp} k_{\parallel}^{e2} + \epsilon_{\parallel} k_{\perp}^2}{k^{e2}}, \quad (2.100)$$

$$\text{Tr} [\boldsymbol{\epsilon} \mathbf{k}^e \otimes \mathbf{k}^e] = \epsilon_{\perp} k_{\perp}^2 + \epsilon_{\parallel} k_{\parallel}^{e2}, \quad (2.101)$$

$$\text{Tr} [\boldsymbol{\epsilon} \mathbf{e}_{\parallel} \otimes \mathbf{e}_{\parallel}] = \epsilon_{\parallel}, \quad (2.102)$$

$$\text{Tr} \left[\frac{d\boldsymbol{\epsilon}}{d\omega} \mathbf{a}_s \otimes \mathbf{a}_s \right] = \frac{d\epsilon_{\perp}}{d\omega}, \quad (2.103)$$

$$\text{Tr} \left[\frac{d\boldsymbol{\epsilon}}{d\omega} \mathbf{a}_p^e \otimes \mathbf{a}_p^e \right] = \frac{\frac{d\epsilon_{\perp}}{d\omega} k_{\parallel}^{e2} + \frac{d\epsilon_{\parallel}}{d\omega} k_{\perp}^2}{k^{e2}}, \quad (2.104)$$

$$\text{Tr} \left[\frac{d\boldsymbol{\epsilon}}{d\omega} \mathbf{k}^e \otimes \mathbf{k}^e \right] = \frac{d\epsilon_{\perp}}{d\omega} k_{\perp}^2 + \frac{d\epsilon_{\parallel}}{d\omega} k_{\parallel}^{e2}, \quad (2.105)$$

$$\text{Tr} \left[\frac{d\boldsymbol{\epsilon}}{d\omega} \mathbf{e}_{\parallel} \otimes \mathbf{e}_{\parallel} \right] = \frac{d\epsilon_{\parallel}}{d\omega}. \quad (2.106)$$

Furthermore, it is important to note that in lossless materials $k_{\parallel}^{e/o}$ is either purely real which corresponds to propagating modes or purely imaginary which corresponds to evanes-

cent modes. Except for the last term in Eq. (2.96) all dependences look similar. The upcoming calculations will however demonstrate that because for hyperbolic materials ordinary and extraordinary modes are fundamentally different their contributions to the density of states are too.

Combining everything in the limit $\mathbf{r}' \rightarrow \mathbf{r}$ we obtain the density of ordinary states (using $\frac{dk_{\parallel}^{\circ}}{dk_{\perp}} = -\frac{k_{\perp}}{k_{\parallel}^{\circ}}$):

$$\begin{aligned}
 D^{\circ}(\omega) &= \frac{\omega}{\pi c^2} \Im \operatorname{Tr} \left[\epsilon \mathbf{G}_o^{\text{EE}}(\mathbf{r}, \mathbf{r}; \omega) + \omega \frac{d\epsilon}{d\omega} \mathbf{G}_o^{\text{EE}}(\mathbf{r}, \mathbf{r}; \omega) \right. \\
 &\quad \left. + \mathbf{G}_o^{\text{HH}}(\mathbf{r}, \mathbf{r}; \omega) \right] \\
 &= \frac{\omega}{\pi c^2} \Im \left[2\epsilon_{\perp} \hat{I}_o \right] + \frac{\omega^2}{\pi c^2} \Im \left[\frac{d\epsilon_{\perp}}{d\omega} \hat{I}_o \right] \\
 &= \frac{\omega}{\pi c^2} \left(2\epsilon_{\perp} + \omega \frac{d\epsilon_{\perp}}{d\omega} \right) \Im \left[\hat{I}_o \right] \\
 &= \frac{\omega}{\pi c^2} \left(2\epsilon_{\perp} + \omega \frac{d\epsilon_{\perp}}{d\omega} \right) \Im \left[\iint_{-\infty}^{\infty} \frac{i}{2k_{\parallel}^{\circ}} \frac{d^2 k_{\perp}}{(2\pi)^2} \right] \\
 &= \frac{\omega}{\pi c^2} \left(2\epsilon_{\perp} + \omega \frac{d\epsilon_{\perp}}{d\omega} \right) \int_{k_{\parallel}^{\circ} \in \mathbb{R}} \frac{k_{\perp}}{2k_{\parallel}^{\circ}} \frac{dk_{\perp}}{2\pi} \\
 &= \frac{\omega}{\pi c^2} \left(\epsilon_{\perp} + \frac{\omega}{2} \frac{d\epsilon_{\perp}}{d\omega} \right) \int_{k_{\parallel}^{\circ} \in \mathbb{R}} \frac{dk_{\parallel}^{\circ}}{2\pi}.
 \end{aligned} \tag{2.107}$$

Thanks to the anisotropy the extraordinary modes have an ad-

ditional term (using $\frac{dk_{\parallel}^e}{dk_{\perp}} = -\frac{\epsilon_{\perp}}{\epsilon_{\parallel}} \frac{k_{\perp}}{k_{\parallel}^e}$):

$$\begin{aligned}
 D^e(\omega) &= \frac{\omega}{\pi c^2} \Im \operatorname{Tr} \left[\epsilon \mathbf{G}_e^{\text{EE}}(\mathbf{r}, \mathbf{r}; \omega) + \omega \frac{d\epsilon}{d\omega} \mathbf{G}_e^{\text{EE}}(\mathbf{r}, \mathbf{r}; \omega) \right. \\
 &\quad \left. + \mathbf{G}_e^{\text{HH}}(\mathbf{r}, \mathbf{r}; \omega) \right] \\
 &= \frac{\omega}{\pi c^2} \Im \left[2\epsilon_{\perp} \hat{I}_e \right] \\
 &\quad + \frac{\omega^2}{\pi c^2} \Im \left[\frac{d\epsilon_{\perp}}{d\omega} \hat{I}_e - \frac{d(\epsilon_{\perp}/\epsilon_{\parallel})}{d\omega} \hat{I}_e \frac{k_{\perp}^2}{\omega^2/c^2} \right] \\
 &= \frac{\omega}{\pi c^2} \left(2\epsilon_{\perp} + \omega \frac{d\epsilon_{\perp}}{d\omega} \right) \Im \left[\hat{I}_e \right] \\
 &\quad - \frac{\omega^2}{\pi c^2} \frac{d(\epsilon_{\perp}/\epsilon_{\parallel})}{d\omega} \Im \left[\hat{I}_e \frac{k_{\perp}^2}{\omega^2/c^2} \right] \\
 &= \frac{\omega}{\pi c^2} \left(2\epsilon_{\perp} + \omega \frac{d\epsilon_{\perp}}{d\omega} \right) \int_{k_{\parallel}^e \in \mathbb{R}} \frac{k_{\perp}}{2k_{\parallel}^e} \frac{dk_{\perp}}{2\pi} \\
 &\quad - \frac{\omega^2}{\pi c^2} \frac{d(\epsilon_{\perp}/\epsilon_{\parallel})}{d\omega} \int_{k_{\parallel}^e \in \mathbb{R}} \frac{k_{\perp}}{2k_{\parallel}^e} \frac{k_{\perp}^2}{\omega^2/c^2} \frac{dk_{\perp}}{2\pi} \\
 &= \pm \frac{\omega}{\pi c^2} \left(\epsilon_{\perp} + \frac{\omega}{2} \frac{d\epsilon_{\perp}}{d\omega} \right) \frac{\epsilon_{\parallel}}{\epsilon_{\perp}} \int_{k_{\parallel}^e \in \mathbb{R}} \frac{dk_{\parallel}^e}{2\pi} \\
 &\quad \mp \frac{\omega^2}{2\pi c^2} \frac{d(\epsilon_{\perp}/\epsilon_{\parallel})}{d\omega} \frac{\epsilon_{\parallel}}{\epsilon_{\perp}} \int_{k_{\parallel}^e \in \mathbb{R}} \left(\epsilon_{\parallel} - \frac{\epsilon_{\parallel}}{\epsilon_{\perp}} \frac{k_{\parallel}^{e2}}{\omega^2/c^2} \right) \frac{dk_{\parallel}^e}{2\pi}
 \end{aligned}$$

$$\begin{aligned}
&= \pm \frac{\omega}{\pi c^2} \left(\epsilon_{\parallel} + \frac{\omega}{2} \frac{d\epsilon_{\parallel}}{d\omega} \right) \int_{k_{\parallel}^{e/o} \in \mathbb{R}} \frac{dk_{\parallel}^e}{2\pi} \\
&\mp \frac{\omega^2}{2\pi c^2} \frac{d(\epsilon_{\parallel}/\epsilon_{\perp})}{d\omega} \int_{k_{\parallel}^{e/o} \in \mathbb{R}} \frac{k_{\parallel}^{e2}}{\omega^2/c^2} \frac{dk_{\parallel}^e}{2\pi}.
\end{aligned} \tag{2.108}$$

When the bounds of integration are given by $k_{\parallel}^{e/o} \in \mathbb{R}$ it means the integration shall be performed from the lowest to the highest positive value of the integral variable satisfying this condition. The sign in Eq. (2.108) will be chosen according to the dispersion of the uniaxial medium. Here, the density of states (DOS) is identical to the local density of states (LDOS), it means it does not depend on location \mathbf{r} .

The above formulas reveal an interesting feature. Evanescent modes (with imaginary $k_{\parallel}^{e/o}$) do not contribute to the thermal energy density in the lossless limit. This is not surprising considering the following explanation: In the lossless limit the fluctuating current sources are infinitely weak. However, there are infinitely many of them since we analyze a bulk material without boundaries. Infinitely many propagating modes with infinitely small intensities add up to a finite value at the observation position. Evanescent modes decay exponentially such that only a limited number of sources contribute to the energy at the observation point. A finite number of infinitely weak modes has zero contribution. This is true for all analyzed cases.

Dielectric uniaxial media

For dielectric media with $\epsilon_{\perp} > 0$ and $\epsilon_{\parallel} > 0$ the largest normal wavevector $k_{\parallel}^{e/o}$ for propagating modes is $\frac{\omega}{c} \sqrt{\epsilon_{\perp}}$, so that we have

$$\begin{aligned}
 D_{\text{D}}^{\text{o}}(\omega) &= \frac{\omega}{\pi c^2} \left(\epsilon_{\perp} + \frac{\omega}{2} \frac{d\epsilon_{\perp}}{d\omega} \right) \int_{k_{\parallel}^{\text{o}} \in \mathbb{R}} \frac{dk_{\parallel}^{\text{o}}}{2\pi} \\
 &= \frac{\omega}{\pi c^2} \left(\epsilon_{\perp} + \frac{\omega}{2} \frac{d\epsilon_{\perp}}{d\omega} \right) \int_0^{\frac{\omega}{c} \sqrt{\epsilon_{\perp}}} \frac{dk_{\parallel}^{\text{o}}}{2\pi} \\
 &= \frac{\omega^2}{\pi^2 c^3} \left(\epsilon_{\perp} + \frac{\omega}{2} \frac{d\epsilon_{\perp}}{d\omega} \right) \frac{\sqrt{\epsilon_{\perp}}}{2},
 \end{aligned} \tag{2.109}$$

and similarly

$$\begin{aligned}
 D_{\text{D}}^{\text{e}}(\omega) &= \frac{\omega}{\pi c^2} \left(\epsilon_{\parallel} + \frac{\omega}{2} \frac{d\epsilon_{\parallel}}{d\omega} \right) \int_{k_{\parallel}^{\text{e}} \in \mathbb{R}} \frac{dk_{\parallel}^{\text{e}}}{2\pi} \\
 &\quad - \frac{\omega^2}{2\pi c^2} \frac{d(\epsilon_{\parallel}/\epsilon_{\perp})}{d\omega} \int_{k_{\parallel}^{\text{e}} \in \mathbb{R}} \frac{k_{\parallel}^{\text{e}2}}{\omega^2/c^2} \frac{dk_{\parallel}^{\text{e}}}{2\pi} \\
 &= \frac{\omega}{\pi c^2} \left(\epsilon_{\parallel} + \frac{\omega}{2} \frac{d\epsilon_{\parallel}}{d\omega} \right) \int_0^{\frac{\omega}{c} \sqrt{\epsilon_{\perp}}} \frac{dk_{\parallel}^{\text{e}}}{2\pi} \\
 &\quad - \frac{\omega^2}{2\pi c^2} \frac{d(\epsilon_{\parallel}/\epsilon_{\perp})}{d\omega} \int_0^{\frac{\omega}{c} \sqrt{\epsilon_{\perp}}} \frac{k_{\parallel}^{\text{e}2}}{\omega^2/c^2} \frac{dk_{\parallel}^{\text{e}}}{2\pi}
 \end{aligned}$$

$$\begin{aligned}
&= \frac{\omega^2}{\pi^2 c^3} \left(\epsilon_{\parallel} + \frac{\omega}{2} \frac{d\epsilon_{\parallel}}{d\omega} - \epsilon_{\perp} \frac{\omega}{6} \frac{d(\epsilon_{\parallel}/\epsilon_{\perp})}{d\omega} \right) \frac{\sqrt{\epsilon_{\perp}}}{2} \\
&= \frac{\omega^2}{\pi^2 c^3} \left(\epsilon_{\parallel} + \frac{\omega}{3} \frac{d\epsilon_{\parallel}}{d\omega} + \frac{\epsilon_{\parallel}}{\epsilon_{\perp}} \frac{\omega}{6} \frac{d\epsilon_{\perp}}{d\omega} \right) \frac{\sqrt{\epsilon_{\perp}}}{2}.
\end{aligned} \tag{2.110}$$

In the dispersionless case the formulas further reduce to

$$D_{\text{D}}^{\text{o}}(\omega) = \frac{\omega^2}{\pi^2 c^3} \frac{\epsilon_{\perp} \sqrt{\epsilon_{\perp}}}{2} \tag{2.111}$$

and

$$D_{\text{D}}^{\text{e}}(\omega) = \frac{\omega^2}{\pi^2 c^3} \frac{\epsilon_{\parallel} \sqrt{\epsilon_{\perp}}}{2}. \tag{2.112}$$

These are the expressions for the density of states of dielectric uniaxial media which were already derived by Eckhardt [78], for instance.

Note that in case of normal dispersion ($\frac{d\epsilon_{\perp}}{d\omega} > 0$, $\frac{d\epsilon_{\parallel}}{d\omega} > 0$) the density of states is always positive and is increased due to the dispersion. Anomalous dispersion is discussed in Section 3.2.

Setting $\epsilon_{\perp} = \epsilon_{\parallel} = 1$ yields the well-known vacuum density of states

$$D_{\text{BB}}^{\text{s}}(\omega) = D_{\text{BB}}^{\text{p}}(\omega) = \frac{\omega^2}{2\pi^2 c^3}. \tag{2.113}$$

Instead of ordinary and extraordinary modes we rather talk about s- and p-polarization. Multiplied by $\mathcal{U}(\omega, T)$, it gives Planck's blackbody spectral energy density [10–12, 14].

Metallic media

A lossless metallic medium with $\epsilon_{\perp} < 0$ and $\epsilon_{\parallel} < 0$ supports no propagating modes at all. As evanescent modes do not contribute to the densities of states, they vanish

$$D_{\text{M}}^{\circ}(\omega) = D_{\text{M}}^{\text{e}}(\omega) = 0. \quad (2.114)$$

Hyperbolic media of type I

For type I hyperbolic media the permittivities are $\epsilon_{\parallel} < 0$ and $\epsilon_{\perp} > 0$. For such a medium the ordinary modes behave as in a dielectric medium (k_{\parallel}° is a real number and $k_{\parallel}^{\circ} \in [0, \frac{\omega}{c} \sqrt{\epsilon_{\perp}}]$ for $k_{\perp} \in [0, \frac{\omega}{c} \sqrt{\epsilon_{\perp}}]$), so that

$$D_{\text{I}}^{\circ}(\omega) = D_{\text{D}}^{\circ}(\omega) = \frac{\omega^2}{\pi^2 c^3} \left(\epsilon_{\perp} + \frac{\omega}{2} \frac{d\epsilon_{\perp}}{d\omega} \right) \frac{\sqrt{\epsilon_{\perp}}}{2}. \quad (2.115)$$

On the other hand, for the extraordinary modes k_{\parallel}^{e} is a real number for any $k_{\perp} \in [0, \infty]$. Therefore, to get a finite solution we introduce a cutoff wavenumber $k_{\perp, \text{max}}$ or $k_{\parallel, \text{max}}$, as discussed in Section 1.2, connected via

$$k_{\parallel, \text{max}} = \sqrt{\frac{\omega^2}{c^2} \epsilon_{\perp} - k_{\perp, \text{max}}^2 \frac{\epsilon_{\perp}}{\epsilon_{\parallel}}}. \quad (2.116)$$

The density of extraordinary modes is

$$\begin{aligned}
D_{\text{I}}^{\text{e}}(\omega) &= -\frac{\omega}{\pi c^2} \left(\epsilon_{\parallel} + \frac{\omega}{2} \frac{d\epsilon_{\parallel}}{d\omega} \right) \int_{k_{\parallel}^{\text{e}} \in \mathbb{R}} \frac{dk_{\parallel}^{\text{e}}}{2\pi} \\
&\quad + \frac{\omega^2}{2\pi c^2} \frac{d(\epsilon_{\parallel}/\epsilon_{\perp})}{d\omega} \int_{k_{\parallel}^{\text{e}} \in \mathbb{R}} \frac{k_{\parallel}^{\text{e}2}}{\omega^2/c^2} \frac{dk_{\parallel}^{\text{e}}}{2\pi} \\
&= -\frac{\omega}{\pi c^2} \left(\epsilon_{\parallel} + \frac{\omega}{2} \frac{d\epsilon_{\parallel}}{d\omega} \right) \int_{\frac{\omega}{c}\sqrt{\epsilon_{\perp}}}^{k_{\parallel, \text{max}}} \frac{dk_{\parallel}^{\text{e}}}{2\pi} \\
&\quad + \frac{\omega^2}{2\pi c^2} \frac{d(\epsilon_{\parallel}/\epsilon_{\perp})}{d\omega} \int_{\frac{\omega}{c}\sqrt{\epsilon_{\perp}}}^{k_{\parallel, \text{max}}} \frac{k_{\parallel}^{\text{e}2}}{\omega^2/c^2} \frac{dk_{\parallel}^{\text{e}}}{2\pi} \\
&= \frac{\omega}{\pi^2 c^2} \left(|\epsilon_{\parallel}| - \frac{\omega}{2} \frac{d\epsilon_{\parallel}}{d\omega} + \frac{\omega}{6} \frac{d(\epsilon_{\parallel}/\epsilon_{\perp})}{d\omega} \frac{k_{\parallel, \text{max}}^2}{\omega^2/c^2} \right) \frac{k_{\parallel, \text{max}}}{2} \\
&\quad - \frac{\omega^2}{\pi^2 c^3} \left(|\epsilon_{\parallel}| - \frac{\omega}{2} \frac{d\epsilon_{\parallel}}{d\omega} + \epsilon_{\perp} \frac{\omega}{6} \frac{d(\epsilon_{\parallel}/\epsilon_{\perp})}{d\omega} \right) \frac{\sqrt{\epsilon_{\perp}}}{2} \\
&= \frac{\omega}{\pi^2 c^2} \left[\frac{|\epsilon_{\parallel}|}{2} + \frac{\omega}{12} \frac{d\epsilon_{\parallel}}{d\omega} \left(\frac{k_{\parallel, \text{max}}}{\sqrt{\epsilon_{\perp}}\omega/c} + 2 \right) \left(\frac{k_{\parallel, \text{max}}}{\sqrt{\epsilon_{\perp}}\omega/c} - 1 \right) \right. \\
&\quad \left. + \frac{|\epsilon_{\parallel}|}{\epsilon_{\perp}} \frac{\omega}{12} \frac{d\epsilon_{\perp}}{d\omega} \left(\frac{k_{\parallel, \text{max}}^2}{\epsilon_{\perp}\omega^2/c^2} + \frac{k_{\parallel, \text{max}}}{\sqrt{\epsilon_{\perp}}\omega/c} + 1 \right) \right] \\
&\quad \left(k_{\parallel, \text{max}} - \frac{\omega}{c} \sqrt{\epsilon_{\perp}} \right).
\end{aligned} \tag{2.117}$$

The last representation makes clear that in case of normal dis-

person ($\frac{d\epsilon_{\perp}}{d\omega} > 0$, $\frac{d\epsilon_{\parallel}}{d\omega} > 0$) the density of states is always positive and is increased due to the dispersion because $k_{\parallel, \max} > \frac{\omega}{c} \sqrt{\epsilon_{\perp}}$.

Without dispersion the density of states is given by

$$D_1^o(\omega) = \frac{\omega^2}{\pi^2 c^3} \frac{\epsilon_{\perp} \sqrt{\epsilon_{\perp}}}{2}, \quad (2.118)$$

$$D_1^e(\omega) = \frac{\omega}{\pi^2 c^2} \frac{|\epsilon_{\parallel}|}{2} \left(k_{\parallel, \max} - \frac{\omega}{c} \sqrt{\epsilon_{\perp}} \right). \quad (2.119)$$

Hyperbolic media of type II

For type II hyperbolic media the permittivities are $\epsilon_{\parallel} > 0$ and $\epsilon_{\perp} < 0$. For such a medium k_{\parallel}^o has a vanishing real part for all $k_{\perp} \in [0, \infty]$. This means that there exist no propagating ordinary modes. It follows that

$$D_{\text{II}}^o(\omega) = D_{\text{M}}^o(\omega) = 0. \quad (2.120)$$

Since k_{\parallel}^e is a real number for any $k_{\perp} \in [\frac{\omega}{c} \sqrt{\epsilon_{\parallel}}, \infty]$ we again introduce a cutoff wavenumber $k_{\parallel, \max}$ and obtain for extraordinary

modes

$$\begin{aligned}
D_{\Pi}^e(\omega) &= \frac{\omega}{\pi c^2} \left(\epsilon_{\parallel} + \frac{\omega}{2} \frac{d\epsilon_{\parallel}}{d\omega} \right) \int_{k_{\parallel}^e \in \mathbb{R}} \frac{dk_{\parallel}^e}{2\pi} \\
&\quad - \frac{\omega^2}{2\pi c^2} \frac{d(\epsilon_{\parallel}/\epsilon_{\perp})}{d\omega} \int_{k_{\parallel}^e \in \mathbb{R}} \frac{k_{\parallel}^{e2}}{\omega^2/c^2} \frac{dk_{\parallel}^e}{2\pi} \\
&= \frac{\omega}{\pi c^2} \left(\epsilon_{\parallel} + \frac{\omega}{2} \frac{d\epsilon_{\parallel}}{d\omega} \right) \int_0^{k_{\parallel, \max}} \frac{dk_{\parallel}^e}{2\pi} \\
&\quad - \frac{\omega^2}{2\pi c^2} \frac{d(\epsilon_{\parallel}/\epsilon_{\perp})}{d\omega} \int_0^{k_{\parallel, \max}} \frac{k_{\parallel}^{e2}}{\omega^2/c^2} \frac{dk_{\parallel}^e}{2\pi} \\
&= \frac{\omega}{\pi^2 c^2} \left(\epsilon_{\parallel} + \frac{\omega}{2} \frac{d\epsilon_{\parallel}}{d\omega} - \frac{\omega}{6} \frac{d(\epsilon_{\parallel}/\epsilon_{\perp})}{d\omega} \frac{k_{\parallel, \max}^2}{\omega^2/c^2} \right) \frac{k_{\parallel, \max}}{2} \\
&= \frac{\omega}{\pi^2 c^2} \left[\frac{\epsilon_{\parallel}}{2} + \frac{\omega}{12} \frac{d\epsilon_{\parallel}}{d\omega} \left(\frac{k_{\parallel, \max}^2}{|\epsilon_{\perp}| \omega^2/c^2} + 3 \right) \right. \\
&\quad \left. + \frac{\epsilon_{\parallel}}{|\epsilon_{\perp}|} \frac{\omega}{12} \frac{d\epsilon_{\perp}}{d\omega} \frac{k_{\parallel, \max}^2}{|\epsilon_{\perp}| \omega^2/c^2} \right] k_{\parallel, \max}.
\end{aligned} \tag{2.121}$$

Again, in case of normal dispersion ($\frac{d\epsilon_{\perp}}{d\omega} > 0$, $\frac{d\epsilon_{\parallel}}{d\omega} > 0$) the density of states is always positive and is increased due to the dispersion because $k_{\parallel, \max} > 0$.

For completeness let us notice that in this case the outgoing waves, introduced in Section 2.3 to obtain Eqs. (2.31) and (2.32), actually possess negative k_{\parallel}^e . Hence, after performing a simple

$k_{\parallel}^e = -k_{\parallel}^e$ substitution, an additional minus in the equation for D_{II}^e was introduced.

Finally, with vanishing dispersion

$$D_{\text{II}}^e(\omega) = \frac{\omega}{\pi^2 c^2} \frac{\epsilon_{\parallel}}{2} k_{\parallel, \max}. \quad (2.122)$$

In the typical hyperbolic cases where $k_{\parallel, \max} \gg \frac{\omega}{c} \sqrt{|\epsilon_{\perp}|}$ the $k_{\parallel, \max}^3$ terms dominate and the total spectral density of states is dominated by its extraordinary part and becomes proportional to $k_{\parallel, \max}^3$ [59, 60]:

$$\begin{aligned} D_{\text{I}}^e(\omega) \approx D_{\text{II}}^e(\omega) &\approx \frac{k_{\parallel, \max}^3}{12\pi^2} \frac{1}{|\epsilon_{\perp}|^2} \left(|\epsilon_{\perp}| \frac{d\epsilon_{\parallel}}{d\omega} + |\epsilon_{\parallel}| \frac{d\epsilon_{\perp}}{d\omega} \right) \\ &= \frac{k_{\parallel, \max}^3}{12\pi^2} \left| \frac{\epsilon_{\parallel}}{\epsilon_{\perp}} \right| \left(\frac{1}{|\epsilon_{\parallel}|} \frac{d\epsilon_{\parallel}}{d\omega} + \frac{1}{|\epsilon_{\perp}|} \frac{d\epsilon_{\perp}}{d\omega} \right). \end{aligned} \quad (2.123)$$

If no dispersion is present the approximation reads

$$D_{\text{I}}^e(\omega) \approx D_{\text{II}}^e(\omega) = \frac{\omega}{\pi^2 c^2} \frac{\epsilon_{\parallel}}{2} k_{\parallel, \max}. \quad (2.124)$$

Here, the spectral density of states is linear in frequency and linear in $k_{\parallel, \max}$ or $k_{\perp, \max} \approx k_{\parallel, \max} \sqrt{\left| \frac{\epsilon_{\parallel}}{\epsilon_{\perp}} \right|}$ resp.

In Appendix A.1 we show, with the example of a type II hyperbolic medium, that the density of states can also be derived via simple mode counting in k -space. This is another way to obtain the results for the DOS without using fluctuational electrodynamics.

2.5.2 Power flow

Like for the calculation of the energy density / density of states, instead of considering a cavity emitting via an opening into a material identical to the filling material as in Fig. 2.4b, we consider a homogeneous, infinitely extended medium. In that case the total heat flux would be 0 at all positions because there are equally strong fluxes in forward and backward direction. Therefore, we limit the emitting part to the halfspace $z' < 0$ and determine the heat flux along the optical axis at a position $z \geq 0$. This situation is shown in Fig. 2.4a and equivalent to the cavity case when boundary and size effects are not present.

Now, we come to the concrete uniaxial medium whose Green's functions were presented in Section 2.3.1. Note that the form of Green's dyadics in Eqs. (2.41) and (2.50) is exactly as desired in Eq. (2.89), so we can easily continue our calculation of the heat flux. Inserting the dyadics in Eq. (2.92) yields

$$\Phi = 2\Re \int_0^\infty \frac{2\omega^3 \mu_0}{c^2} \mathcal{U}(\omega, T) \int_0^\infty \int_{-\infty}^0 \xi_{\alpha\beta z} \left(\mathbf{G}^{\text{EE}}(\mathbf{r}, z', k_\perp; \omega) \right. \\ \left. \Im [\boldsymbol{\epsilon}(\omega)] \mathbf{G}^{\text{HEH}}(\mathbf{r}, z', k_\perp; \omega) \right)_{\alpha\beta} dz' k_\perp \frac{dk_\perp}{2\pi} \frac{d\omega}{2\pi}$$

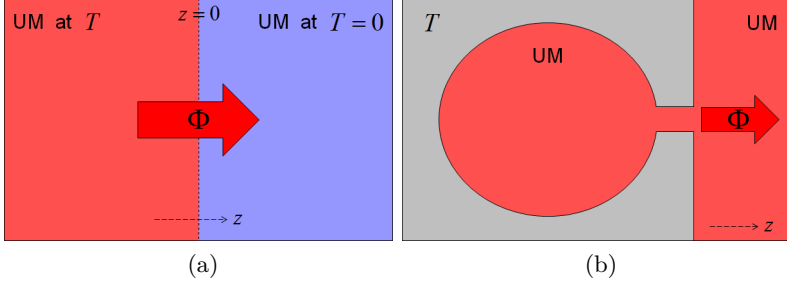


Figure 2.4: Illustration of the setups for which the thermal power flux Φ inside uniaxial media is evaluated. (a) homogeneous uniaxial medium (UM) with a halfspace at temperature T and the other one at $T = 0$ K, (b) large cavity at temperature T filled with UM and emitting via an opening into the UM. The dashed arrow shows the orientation of the optical axis of the UM which is along the z -axis. Both setups (a) and (b) yield the same power flux.

$$\begin{aligned}
&= 2\Re \int_0^\infty \frac{2\omega^3 \mu_0}{c^2} \mathcal{U}(\omega, T) \int_0^\infty \int_{-\infty}^0 \xi_{\alpha\beta z} \left(\left\{ \frac{ie^{ik_{\parallel}^o x_{\parallel}}}{2k_{\parallel}^o} [\mathbf{a}_s \otimes \mathbf{a}_s] \right. \right. \\
&\quad \left. \left. + \frac{ie^{ik_{\parallel}^e x_{\parallel}}}{2k_{\parallel}^e} [\mathbf{a}_p^e \otimes \mathbf{a}_p^e + B\mathbf{k}^e \otimes \mathbf{k}^e + C\mathbf{e}_{\parallel} \otimes \mathbf{e}_{\parallel}] \right\} \right. \\
&\quad \left. \left\{ \Im[\epsilon_{\perp}] \mathbf{1} + \Im[\epsilon_{\parallel} - \epsilon_{\perp}] \mathbf{e}_{\parallel} \otimes \mathbf{e}_{\parallel} \right\} \left\{ \frac{-ie^{-ik_{\parallel}^{o*} x_{\parallel}}}{2\omega \mu_0 k_{\parallel}^{o*}} [-k^{o*} \mathbf{a}_s \otimes \mathbf{a}_p^{o*}] \right. \right. \\
&\quad \left. \left. + \frac{-ie^{-ik_{\parallel}^{e*} x_{\parallel}}}{2\omega \mu_0 k_{\parallel}^{e*}} [k^{e*} \mathbf{a}_p^{e*} \otimes \mathbf{a}_s + C^* k_{\perp} \mathbf{e}_{\parallel} \otimes \mathbf{a}_s] \right\} \right)_{\alpha\beta} dz' k_{\perp} \frac{dk_{\perp}}{2\pi} \frac{d\omega}{2\pi}
\end{aligned}$$

$$\begin{aligned}
&= 2\Re \int_0^\infty \frac{\omega^2}{2c^2} \mathcal{U}(\omega, T) \int_0^\infty \int_{-\infty}^0 \xi_{\alpha\beta z} \left(\Im[\epsilon_\perp] \frac{e^{-2\Im[k_\parallel^o](z-z')}}{|k_\parallel^o|^2} \right. \\
&\quad \left[-k^{o*}(\mathbf{a}_s^T \mathbf{a}_s) \mathbf{a}_s \otimes \mathbf{a}_p^{o*} \right] + \Im[\epsilon_\perp] \frac{e^{-2\Im[k_\parallel^e](z-z')}}{|k_\parallel^e|^2} \\
&\quad \left[k^{e*}(\mathbf{a}_p^{eT} \mathbf{a}_p^{e*}) \mathbf{a}_p^e \otimes \mathbf{a}_s + Bk^{e*}(\mathbf{k}^{eT} \mathbf{a}_p^{e*}) \mathbf{k}^e \otimes \mathbf{a}_s \right. \\
&\quad + Ck^{e*}(\mathbf{e}_\parallel^T \mathbf{a}_p^{e*}) \mathbf{e}_\parallel \otimes \mathbf{a}_s + C^* k_\perp (\mathbf{a}_p^{eT} \mathbf{e}_\parallel) \mathbf{a}_p^e \otimes \mathbf{a}_s \\
&\quad \left. + BC^* k_\perp (\mathbf{k}^{eT} \mathbf{e}_\parallel) \mathbf{k}^e \otimes \mathbf{a}_s + |C|^2 k_\perp (\mathbf{e}_\parallel^T \mathbf{e}_\parallel) \mathbf{e}_\parallel \otimes \mathbf{a}_s \right] \\
&\quad + \Im[\epsilon_\parallel - \epsilon_\perp] \frac{e^{-2\Im[k_\parallel^e](z-z')}}{|k_\parallel^e|^2} \left[k^{e*}(\mathbf{a}_p^{eT} \mathbf{e}_\parallel) (\mathbf{e}_\parallel^T \mathbf{a}_p^{e*}) \mathbf{a}_p^e \otimes \mathbf{a}_s \right. \\
&\quad + Bk^{e*}(\mathbf{k}^{eT} \mathbf{e}_\parallel) (\mathbf{e}_\parallel^T \mathbf{a}_p^{e*}) \mathbf{k}^e \otimes \mathbf{a}_s + Ck^{e*}(\mathbf{e}_\parallel^T \mathbf{e}_\parallel) (\mathbf{e}_\parallel^T \mathbf{a}_p^{e*}) \mathbf{e}_\parallel \otimes \mathbf{a}_s \\
&\quad + C^* k_\perp (\mathbf{a}_p^{eT} \mathbf{e}_\parallel) (\mathbf{e}_\parallel^T \mathbf{e}_\parallel) \mathbf{a}_p^e \otimes \mathbf{a}_s + BC^* k_\perp (\mathbf{k}^{eT} \mathbf{e}_\parallel) (\mathbf{e}_\parallel^T \mathbf{e}_\parallel) \mathbf{k}^e \otimes \mathbf{a}_s \\
&\quad \left. + |C|^2 k_\perp (\mathbf{e}_\parallel^T \mathbf{e}_\parallel) (\mathbf{e}_\parallel^T \mathbf{e}_\parallel) \mathbf{e}_\parallel \otimes \mathbf{a}_s \right] \Bigg)_{\alpha\beta} dz' k_\perp \frac{dk_\perp}{2\pi} \frac{d\omega}{2\pi}
\end{aligned}$$

$$\begin{aligned}
&= \Re \int_0^\infty \frac{\omega^2}{c^2} \mathcal{U}(\omega, T) \int_0^\infty \xi_{\alpha\beta z} \left(\Im[\epsilon_\perp] \frac{e^{-2\Im[k_\parallel^{\text{o}}]z}}{2\Im[k_\parallel^{\text{o}}]|k_\parallel^{\text{o}}|^2} \left[-k^{\text{o}*} \mathbf{a}_s \otimes \mathbf{a}_p^{\text{o}*} \right] \right. \\
&\quad + \Im[\epsilon_\perp] \frac{e^{-2\Im[k_\parallel^{\text{e}}]z}}{2\Im[k_\parallel^{\text{e}}]|k_\parallel^{\text{e}}|^2} \left[k^{\text{e}*} \frac{|k_\parallel^{\text{e}}|^2 + k_\perp^2}{|k^{\text{e}}|^2} \mathbf{a}_p^{\text{e}} \otimes \mathbf{a}_s \right. \\
&\quad + iBk_\perp 2\Im[k_\parallel^{\text{e}}] \mathbf{k}^{\text{e}} \otimes \mathbf{a}_s + Ck_\perp \mathbf{e}_\parallel \otimes \mathbf{a}_s + C^* \frac{k_\perp^2}{k^{\text{e}}} \mathbf{a}_p^{\text{e}} \otimes \mathbf{a}_s \\
&\quad \left. + BC^* k_\perp k_\parallel^{\text{e}} \mathbf{k}^{\text{e}} \otimes \mathbf{a}_s + |C|^2 k_\perp \mathbf{e}_\parallel \otimes \mathbf{a}_s \right] + \Im[\epsilon_\parallel - \epsilon_\perp] \frac{e^{-2\Im[k_\parallel^{\text{e}}]z}}{2\Im[k_\parallel^{\text{e}}]|k_\parallel^{\text{e}}|^2} \\
&\quad \left[\frac{k_\perp^2}{k^{\text{e}}} \mathbf{a}_p^{\text{e}} \otimes \mathbf{a}_s + Bk_\parallel^{\text{e}} k_\perp \mathbf{k}^{\text{e}} \otimes \mathbf{a}_s + Ck_\perp \mathbf{e}_\parallel \otimes \mathbf{a}_s + C^* \frac{k_\perp^2}{k^{\text{e}}} \mathbf{a}_p^{\text{e}} \otimes \mathbf{a}_s \right. \\
&\quad \left. + BC^* k_\perp k_\parallel^{\text{e}} \mathbf{k}^{\text{e}} \otimes \mathbf{a}_s + |C|^2 k_\perp \mathbf{e}_\parallel \otimes \mathbf{a}_s \right] \Big)_{\alpha\beta} k_\perp \frac{dk_\perp}{2\pi} \frac{d\omega}{2\pi}.
\end{aligned} \tag{2.125}$$

The heat flux along the optical axis (z -direction) is searched for, so only the xy and yx -components of the matrices are needed. With the relations

$$\left(\mathbf{a}_s \otimes \mathbf{a}_p^{\text{o}*} \right)_{xy} - \left(\mathbf{a}_s \otimes \mathbf{a}_p^{\text{o}*} \right)_{yx} = -\frac{k_\parallel^{\text{o}*}}{k^{\text{o}*}}, \tag{2.126}$$

$$\left(\mathbf{a}_p^{\text{e}} \otimes \mathbf{a}_s \right)_{xy} - \left(\mathbf{a}_p^{\text{e}} \otimes \mathbf{a}_s \right)_{yx} = \frac{k_\parallel^{\text{e}}}{k^{\text{e}}}, \tag{2.127}$$

$$\left(\mathbf{k}^{\text{e}} \otimes \mathbf{a}_s \right)_{xy} - \left(\mathbf{k}^{\text{e}} \otimes \mathbf{a}_s \right)_{yx} = -k_\perp, \tag{2.128}$$

$$\left(\mathbf{e}_\parallel \otimes \mathbf{a}_s \right)_{xy} - \left(\mathbf{e}_\parallel \otimes \mathbf{a}_s \right)_{yx} = 0 \tag{2.129}$$

and

$$\begin{aligned}\Re[k_{\parallel}^e]2\Im[k_{\parallel}^e] &= \frac{1}{2i} (k_{\parallel}^{e2} - k_{\parallel}^{e2*}) \\ &= \Im[k_{\parallel}^{e2}] = \frac{\omega^2}{c^2} \Im[\epsilon_{\perp}] - k_{\perp}^2 \Im\left[\frac{\epsilon_{\perp}}{\epsilon_{\parallel}}\right],\end{aligned}\quad (2.130)$$

$$\Re[k_{\parallel}^o]2\Im[k_{\parallel}^o] = \frac{1}{2i} (k_{\parallel}^{o2} - k_{\parallel}^{o2*}) = \Im[k_{\parallel}^{o2}] = \frac{\omega^2}{c^2} \Im[\epsilon_{\perp}] \quad (2.131)$$

we obtain

$$\begin{aligned}\Phi &= \Re \int_0^{\infty} \frac{\omega^2}{c^2} \mathcal{U}(\omega, T) \int_0^{\infty} \left(\Re[k_{\parallel}^o] \frac{c^2}{\omega^2} \frac{e^{-2\Im[k_{\parallel}^o]z}}{|k_{\parallel}^o|^2} k_{\parallel}^{o*} \right. \\ &\quad + \frac{\Im[\epsilon_{\perp}] \Re[k_{\parallel}^e]}{\frac{\omega^2}{c^2} \Im[\epsilon_{\perp}] - k_{\perp}^2 \Im\left[\frac{\epsilon_{\perp}}{\epsilon_{\parallel}}\right]} \frac{e^{-2\Im[k_{\parallel}^e]z}}{|k_{\parallel}^e|^2} \left[\frac{|k_{\parallel}^e|^2 + k_{\perp}^2}{|k^e|^2} \frac{k^{e*} k_{\parallel}^e}{k^e} \right. \\ &\quad \left. \left. - i B k_{\perp}^2 2\Im[k_{\parallel}^e] + C^* \frac{k_{\perp}^2 k_{\parallel}^e}{k^{e2}} - B C^* k_{\perp}^2 k_{\parallel}^e \right] + \frac{\Im[\epsilon_{\parallel} - \epsilon_{\perp}] \Re[k_{\parallel}^e]}{\frac{\omega^2}{c^2} \Im[\epsilon_{\perp}] - k_{\perp}^2 \Im\left[\frac{\epsilon_{\perp}}{\epsilon_{\parallel}}\right]} \right. \\ &\quad \left. \frac{e^{-2\Im[k_{\parallel}^e]z}}{|k_{\parallel}^e|^2} \left[\frac{k_{\perp}^2 k_{\parallel}^e}{k^{e2}} - B k_{\parallel}^e k_{\perp}^2 + C^* \frac{k_{\perp}^2 k_{\parallel}^e}{k^{e2}} - B C^* k_{\perp}^2 k_{\parallel}^e \right] \right) k_{\perp} \frac{dk_{\perp}}{2\pi} \frac{d\omega}{2\pi}\end{aligned}$$

$$\begin{aligned}
&= \Re \int_0^\infty \frac{\omega^2}{c^2} \mathcal{U}(\omega, T) \int_0^\infty \left(\Re[k_{\parallel}^{\circ}] \frac{c^2}{\omega^2} \frac{e^{-2\Im[k_{\parallel}^{\circ}]z}}{|k_{\parallel}^{\circ}|^2} k_{\parallel}^{\circ*} \right. \\
&\quad + \frac{\Re[k_{\parallel}^e]}{\frac{\omega^2}{c^2} - k_{\perp}^2 \Im\left[\frac{\epsilon_{\perp}}{\epsilon_{\parallel}}\right] / \Im[\epsilon_{\perp}]} \frac{e^{-2\Im[k_{\parallel}^e]z}}{|k_{\parallel}^e|^2} \left[\frac{|k_{\parallel}^e|^2 + k_{\perp}^2}{|k^e|^2} \frac{k^{e*} k_{\parallel}^e}{k^e} \right. \\
&\quad \left. \left. - i B k_{\perp}^2 2\Im[k_{\parallel}^e] + C^* \frac{k_{\perp}^2 k_{\parallel}^e}{k^{e2}} - B C^* k_{\perp}^2 k_{\parallel}^e + \left(\frac{\Im[\epsilon_{\parallel}]}{\Im[\epsilon_{\perp}]} - 1 \right) \right. \right. \\
&\quad \left. \left. \left\{ \frac{k_{\perp}^2 k_{\parallel}^e}{k^{e2}} - B k_{\perp}^2 k_{\parallel}^e + C^* \frac{k_{\perp}^2 k_{\parallel}^e}{k^{e2}} - B C^* k_{\perp}^2 k_{\parallel}^e \right\} \right] \right) k_{\perp} \frac{dk_{\perp}}{2\pi} \frac{d\omega}{2\pi}.
\end{aligned} \tag{2.132}$$

Substituting

$$B = \frac{1}{k^{e2}} - \frac{c^2}{\omega^2 \epsilon_{\parallel}} \quad , \quad C = \frac{\epsilon_{\perp}}{\epsilon_{\parallel}} - 1, \tag{2.133}$$

$$\Im \left[\frac{\epsilon_{\perp}}{\epsilon_{\parallel}} \right] = \frac{\Im[\epsilon_{\perp} \epsilon_{\parallel}^*]}{|\epsilon_{\parallel}|^2} = \frac{\Im[\epsilon_{\perp}] \Re[\epsilon_{\parallel}] - \Re[\epsilon_{\perp}] \Im[\epsilon_{\parallel}]}{|\epsilon_{\parallel}|^2}, \tag{2.134}$$

$$\Re \left[\frac{k^{e*} k_{\parallel}^e}{k^e} \right] = \frac{\Re \left[(k_{\parallel}^{e2*} + k_{\perp}^2) k_{\parallel}^e \right]}{|k^e|^2} = \frac{|k_{\parallel}^e|^2 + k_{\perp}^2}{|k^e|^2} \Re[k_{\parallel}^e], \tag{2.135}$$

$$\begin{aligned}
\Im \left[k_{\parallel}^{e2} \right] &= \frac{\omega^2}{c^2} \Im[\epsilon_{\perp}] - k_{\perp}^2 \Im \left[\frac{\epsilon_{\perp}}{\epsilon_{\parallel}} \right] \\
&= \frac{\omega^2}{c^2} \Im[\epsilon_{\perp}] - k_{\perp}^2 \frac{\Im[\epsilon_{\perp}] \Re[\epsilon_{\parallel}] - \Re[\epsilon_{\perp}] \Im[\epsilon_{\parallel}]}{|\epsilon_{\parallel}|^2},
\end{aligned} \tag{2.136}$$

$$\begin{aligned}
\left(|k_{\parallel}^e|^2 + k_{\perp}^2\right)^2 - |k^e|^4 &= \left(|k_{\parallel}^e|^2 + k_{\perp}^2\right)^2 - |k_{\parallel}^e|^2 + k_{\perp}^2|^2 \\
&= 2k_{\perp}^2 \left(|k_{\parallel}^e|^2 - \Re[k_{\parallel}^e{}^2]\right)
\end{aligned} \tag{2.137}$$

and further simplifying results in

$$\begin{aligned}
\Phi &= \int_0^{\infty} \frac{\omega^2}{c^2} \mathcal{U}(\omega, T) \int_0^{\infty} \left(\Re[k_{\parallel}^o]^2 \frac{c^2}{\omega^2} \frac{e^{-2\Im[k_{\parallel}^o]z}}{|k_{\parallel}^o|^2} \right. \\
&\quad + \frac{\Re[k_{\parallel}^e]}{\frac{\omega^2}{c^2} - k_{\perp}^2} \frac{\Re[\epsilon_{\parallel}] - \Re[\epsilon_{\perp}] \Im[\epsilon_{\parallel}] / \Im[\epsilon_{\perp}]}{|\epsilon_{\parallel}|^2} \frac{e^{-2\Im[k_{\parallel}^e]z}}{|k_{\parallel}^e|^2} \left\{ \frac{|k_{\parallel}^e|^2 + k_{\perp}^2}{|k^e|^2} \Re \left[\frac{k^{e*} k_{\parallel}^e}{k^e} \right] \right. \\
&\quad \left. + 2k_{\perp}^2 \Im[k_{\parallel}^e] \Im \left[\frac{1}{k^e} - \frac{c^2}{\omega^2 \epsilon_{\parallel}} \right] \right. \\
&\quad \left. \left. + k_{\perp}^2 \frac{c^2}{\omega^2} \Re \left[\frac{k_{\parallel}^e}{\epsilon_{\parallel}} \left(C^* \frac{\Im[\epsilon_{\parallel}]}{\Im[\epsilon_{\perp}]} + \frac{\Im[\epsilon_{\parallel}]}{\Im[\epsilon_{\perp}]} - 1 \right) \right] \right\} \right) k_{\perp} \frac{dk_{\perp}}{2\pi} \frac{d\omega}{2\pi} \\
&= \int_0^{\infty} \mathcal{U}(\omega, T) \int_0^{\infty} \left(\frac{\Re[k_{\parallel}^o]^2}{|k_{\parallel}^o|^2} e^{-2\Im[k_{\parallel}^o]z} \right. \\
&\quad + \frac{\Re[k_{\parallel}^e]}{|k_{\parallel}^e|^2} \frac{e^{-2\Im[k_{\parallel}^e]z}}{1 - \frac{k_{\perp}^2}{\omega^2/c^2} \frac{\Re[\epsilon_{\parallel}] - \Re[\epsilon_{\perp}] \Im[\epsilon_{\parallel}] / \Im[\epsilon_{\perp}]}{|\epsilon_{\parallel}|^2}} \left\{ \frac{\left(|k_{\parallel}^e|^2 + k_{\perp}^2\right)^2}{|k^e|^4} \Re[k_{\parallel}^e] \right. \\
&\quad + \frac{2k_{\perp}^2 \Im[k_{\parallel}^e]}{|k^e|^4 \omega^2 / c^2 |\epsilon_{\parallel}|^2} \left[|k^e|^4 \Im[\epsilon_{\parallel}] - \frac{\omega^2}{c^2} |\epsilon_{\parallel}|^2 \Im[k_{\parallel}^e{}^2] \right] \\
&\quad \left. \left. - \frac{k_{\perp}^2}{\omega^2/c^2} \frac{1}{|\epsilon_{\parallel}|^2} \Re \left[k_{\parallel}^e (\epsilon_{\parallel}^* - \epsilon_{\perp}^* \frac{\Im[\epsilon_{\parallel}]}{\Im[\epsilon_{\perp}]}) \right] \right\} \right) k_{\perp} \frac{dk_{\perp}}{2\pi} \frac{d\omega}{2\pi}
\end{aligned}$$

$$\begin{aligned}
&= \int_0^\infty \mathcal{U}(\omega, T) \int_0^\infty \left(\frac{\Re[k_{\parallel}^{\circ}]^2}{|k_{\parallel}^{\circ}|^2} e^{-2\Im[k_{\parallel}^{\circ}]z} \right. \\
&\quad + \frac{\Re[k_{\parallel}^{\text{e}}]}{|k_{\parallel}^{\text{e}}|^2} \frac{e^{-2\Im[k_{\parallel}^{\text{e}}]z}}{1 - \frac{k_{\perp}^2}{\omega^2/c^2} \frac{\Re[\epsilon_{\parallel}] - \Re[\epsilon_{\perp}]\Im[\epsilon_{\parallel}]/\Im[\epsilon_{\perp}]}{|\epsilon_{\parallel}|^2}} \left\{ \frac{(|k_{\parallel}^{\text{e}}|^2 + k_{\perp}^2)^2}{|k^{\text{e}}|^4} \Re[k_{\parallel}^{\text{e}}] \right. \\
&\quad + \frac{2k_{\perp}^2}{\omega^2/c^2} \frac{\Im[\epsilon_{\parallel}]}{|\epsilon_{\parallel}|^2} \Im[k_{\parallel}^{\text{e}}] - \frac{k_{\perp}^2}{\omega^2/c^2} \frac{\Re[\epsilon_{\parallel}] - \Re[\epsilon_{\perp}]\Im[\epsilon_{\parallel}]/\Im[\epsilon_{\perp}]}{|\epsilon_{\parallel}|^2} \Re[k_{\parallel}^{\text{e}}] \\
&\quad - \frac{2k_{\perp}^2 \Im[k_{\parallel}^{\text{e}}] \omega^2}{|k^{\text{e}}|^4 c^2} \Im[\epsilon_{\perp}] \\
&\quad \left. \left[1 - \frac{k_{\perp}^2}{\omega^2/c^2} \frac{\Re[\epsilon_{\parallel}] - \Re[\epsilon_{\perp}]\Im[\epsilon_{\parallel}]/\Im[\epsilon_{\perp}]}{|\epsilon_{\parallel}|^2} \right] \right\} k_{\perp} \frac{dk_{\perp}}{2\pi} \frac{d\omega}{2\pi} \\
&= \int_0^\infty \mathcal{U}(\omega, T) \int_0^\infty \left(\frac{\Re[k_{\parallel}^{\circ}]^2}{|k_{\parallel}^{\circ}|^2} e^{-2\Im[k_{\parallel}^{\circ}]z} + \frac{\Re[k_{\parallel}^{\text{e}}]}{|k_{\parallel}^{\text{e}}|^2} e^{-2\Im[k_{\parallel}^{\text{e}}]z} \right. \\
&\quad \left\{ \frac{(|k_{\parallel}^{\text{e}}|^2 + k_{\perp}^2)^2}{|k^{\text{e}}|^4} \Re[k_{\parallel}^{\text{e}}] + \frac{2k_{\perp}^2}{\omega^2/c^2} \frac{\Im[\epsilon_{\parallel}]}{|\epsilon_{\parallel}|^2} \Im[k_{\parallel}^{\text{e}}] \right. \\
&\quad - \frac{2k_{\perp}^2}{\omega^2/c^2} \frac{\omega^4}{|k^{\text{e}}|^4} \Im[\epsilon_{\perp}] \Im[k_{\parallel}^{\text{e}}] + \frac{k_{\perp}^2}{\omega^2/c^2} \frac{\Re[\epsilon_{\parallel}] - \Re[\epsilon_{\perp}]\Im[\epsilon_{\parallel}]/\Im[\epsilon_{\perp}]}{|\epsilon_{\parallel}|^2} \\
&\quad \left. \left. \Re[k_{\parallel}^{\text{e}}] \left[\frac{(|k_{\parallel}^{\text{e}}|^2 + k_{\perp}^2)^2}{|k^{\text{e}}|^4} - 1 \right] + \frac{2k_{\perp}^2}{\omega^2/c^2} \frac{\Im[\epsilon_{\parallel}]}{|\epsilon_{\parallel}|^2} \Im[k_{\parallel}^{\text{e}}] \right\} \right) k_{\perp} \frac{dk_{\perp}}{2\pi} \frac{d\omega}{2\pi} \\
&\quad \left. \frac{1 - \frac{k_{\perp}^2}{\omega^2/c^2} \frac{\Re[\epsilon_{\parallel}] - \Re[\epsilon_{\perp}]\Im[\epsilon_{\parallel}]/\Im[\epsilon_{\perp}]}{|\epsilon_{\parallel}|^2}}{1 - \frac{k_{\perp}^2}{\omega^2/c^2} \frac{\Re[\epsilon_{\parallel}] - \Re[\epsilon_{\perp}]\Im[\epsilon_{\parallel}]/\Im[\epsilon_{\perp}]}{|\epsilon_{\parallel}|^2}} \right\} k_{\perp} \frac{dk_{\perp}}{2\pi} \frac{d\omega}{2\pi}
\end{aligned}$$

$$\begin{aligned}
&= \int_0^\infty \mathcal{U}(\omega, T) \int_0^\infty \left(\frac{\Re[k_\parallel^o]^2}{|k_\parallel^o|^2} e^{-2\Im[k_\parallel^o]z} + \frac{\Re[k_\parallel^e]^2}{|k_\parallel^e|^2} e^{-2\Im[k_\parallel^e]z} \right. \\
&\quad \left\{ \frac{(|k_\parallel^e|^2 + k_\perp^2)^2}{|k^e|^4} + \frac{2k_\perp^2}{\omega^2/c^2} \frac{\Im[k_\parallel^e]}{\Re[k_\parallel^e]} \left[\frac{\Im[\epsilon_\parallel]}{|\epsilon_\parallel|^2} - \frac{\omega^4}{c^4} \frac{\Im[\epsilon_\perp]}{|k^e|^4} \right] \right. \\
&\quad \left. + \frac{k_\perp^2}{\omega^2/c^2} \frac{\Re[\epsilon_\parallel] - \Re[\epsilon_\perp] \Im[\epsilon_\parallel] / \Im[\epsilon_\perp]}{|\epsilon_\parallel|^2} \right. \\
&\quad \left. \left. \frac{1 - \frac{k_\perp^2}{\omega^2/c^2} \frac{\Re[\epsilon_\parallel] - \Re[\epsilon_\perp] \Im[\epsilon_\parallel] / \Im[\epsilon_\perp]}{|\epsilon_\parallel|^2}}{1 - \frac{k_\perp^2}{\omega^2/c^2} \frac{\Re[\epsilon_\parallel] - \Re[\epsilon_\perp] \Im[\epsilon_\parallel] / \Im[\epsilon_\perp]}{|\epsilon_\parallel|^2}} \right] \right. \\
&\quad \left. \left[\frac{2k_\perp^2}{|k^e|^4} \left(|k_\parallel^e|^2 - \Re[k_\parallel^{e2}] \right) + \frac{2k_\perp^2}{\omega^2/c^2} \frac{\Im[\epsilon_\parallel]}{|\epsilon_\parallel|^2} \frac{\Im[k_\parallel^e]}{\Re[k_\parallel^e]} \right] \right\} k_\perp \frac{dk_\perp}{2\pi} \frac{d\omega}{2\pi}.
\end{aligned} \tag{2.138}$$

In the isotropic case where $\epsilon_\parallel = \epsilon_\perp$ and thus $k^{e2} = \frac{\omega^2}{c^2} \epsilon_\perp$ the formula significantly simplifies to

$$\begin{aligned}
\Phi &= \int_0^\infty \mathcal{U}(\omega, T) \int_0^\infty \left(\frac{\Re[k_\parallel^o]^2}{|k_\parallel^o|^2} e^{-2\Im[k_\parallel^o]z} \right. \\
&\quad \left. + \frac{\Re[k_\parallel^e]^2}{|k_\parallel^e|^2} e^{-2\Im[k_\parallel^e]z} \frac{(|k_\parallel^e|^2 + k_\perp^2)^2}{\frac{\omega^4}{c^4} |\epsilon_\perp|^2} \right) k_\perp \frac{dk_\perp}{2\pi} \frac{d\omega}{2\pi}.
\end{aligned} \tag{2.139}$$

Interestingly, we see an extra term for the extraordinary modes in expression (2.139) which has no ordinary counterpart. Even in the isotropic case where $k_\parallel^e = k_\parallel^o$ ordinary and extraordinary modes contribute differently to the heat flux. In this case there is actually no optical axis. Yet, we take the heat flux direction as an outstanding \parallel -axis and use it to define the two fundamental polarization states, usually called s- and p-polarized instead of

ordinary and extraordinary.

The reason for the extra term is the different polarization states. As discussed in Section 2.3.1 we employ a mode basis with real \mathbf{k}_\perp which fits to our translationally symmetric problems. The electric field of s-polarized (ordinary) modes is linearly polarized whereas for p-polarized (extraordinary) modes it is elliptically polarized. The sources of thermal radiation are electric ones and they excite the different polarizations differently. When losses vanish the situation changes. Evanescent modes with imaginary $k_\parallel^{e/o}$ do not contribute to the heat flux. S- and p-polarized propagating modes with real $k_\parallel^{e/o}$ contribute equally because the extra term $\frac{(k_\parallel^e + k_\perp^2)^2}{c^4 \epsilon_\perp^2}$ becomes 1.

So far the calculation was performed for a general nonmagnetic uniaxial material. Hereinafter, we want to look at lossless materials. We do that because we want to follow the same route with the power flow as with the energy density. Moreover, handling thermal power flows inside lossy materials is similarly complicated as handling energy densities. There is no fundamental problem with defining the power flux but it diverges if no additional restrictions are introduced. The explanation for that is all modes contribute to the heat flow and there are infinitely many of them. On the other side, with vanishing losses a clear differentiation between propagating and evanescent modes is possible and only propagating modes transport heat – as expected and proved below. And the density of propagating modes is always

limited, restricting the radiative heat flux to finite values.

To get the heat flux in lossless materials we have to find the limit as the imaginary parts of the permittivities approach 0 equally fast ($\Im[\epsilon_{\parallel}], \Im[\epsilon_{\perp}] \rightarrow 0$ and $\frac{\Im[\epsilon_{\parallel}]}{\Im[\epsilon_{\perp}]} \rightarrow a = \text{const.}$). In that case $k_{\parallel}^{e/o}$ becomes purely real or purely imaginary. As seen in Eq. (2.138) purely imaginary $k_{\parallel}^{e/o}$ do not contribute to the heat flux. Physically it means only propagating modes with real $k_{\parallel}^{e/o}$ support the radiative heat flux, no evanescent modes. So limiting the integration to $k_{\parallel}^{e/o} \in \mathbb{R}$ makes the heat flux in lossless media

$$\begin{aligned}
 \Phi &= \int_0^{\infty} \mathcal{U}(\omega, T) \left(\int_{k_{\parallel}^o \in \mathbb{R}} \frac{k_{\parallel}^{o2}}{k_{\parallel}^{o2}} k_{\perp} \frac{dk_{\perp}}{2\pi} + \int_{k_{\parallel}^e \in \mathbb{R}} \frac{k_{\parallel}^{e2}}{k_{\parallel}^{e2}} \left\{ \frac{(k_{\parallel}^{e2} + k_{\perp}^2)^2}{k^{e4}} \right. \right. \\
 &\quad \left. \left. + \frac{\frac{k_{\perp}^2}{\omega^2/c^2} \frac{\epsilon_{\parallel} - \epsilon_{\perp} a}{\epsilon_{\parallel}^2}}{1 - \frac{k_{\perp}^2}{\omega^2/c^2} \frac{\epsilon_{\parallel} - \epsilon_{\perp} a}{\epsilon_{\parallel}^2}} \frac{2k_{\perp}^2 (k_{\parallel}^{e2} - k_{\perp}^2)}{k^{e4}} \right\} k_{\perp} \frac{dk_{\perp}}{2\pi} \right) \frac{d\omega}{2\pi} \\
 &= \int_0^{\infty} \mathcal{U}(\omega, T) \left(\int_{k_{\parallel}^o \in \mathbb{R}} k_{\perp} \frac{dk_{\perp}}{2\pi} + \int_{k_{\parallel}^e \in \mathbb{R}} k_{\perp} \frac{dk_{\perp}}{2\pi} \right) \frac{d\omega}{2\pi}.
 \end{aligned} \tag{2.140}$$

The bounds of integration can be determined very easily using Eq. (2.33).

The integral kernels (integrands without the always appearing $\mathcal{U}(\omega, T) \frac{k_{\perp}}{(2\pi)^2}$ term) can be interpreted as transmission coefficients or transmission probabilities [22, 79]. In the lossless case,

it is one for all propagating modes inside the uniaxial medium ($k_{\parallel}^{o/e}$ is purely real) and zero ($k_{\parallel}^{o/e}$ is purely imaginary) otherwise. Hence, the heat flux is the larger the more propagating transversal modes are supported by the medium [22, 79].

Dispersion influences the heat flux via material properties (permittivities) varying with frequency. But it does not manifest itself in an own $\frac{d\epsilon}{d\omega}$ term as for the density of states. The integral over k_{\perp} is the area of the isofrequency contour projected onto the plane normal to the direction of heat flux (\parallel -direction). Therefore, the spectral heat flux is proportional to the projection area [80]. Appendix A.2 features a simple, graphical derivation.

Dielectric uniaxial media

In the anisotropic dielectric case, $\epsilon_{\parallel} > 0$ and $\epsilon_{\perp} > 0$, the k_{\perp} leading to real $k_{\parallel}^{e/o}$ is in the interval $[0, \frac{\omega}{c}\sqrt{\epsilon_{\perp}}]$ for ordinary modes and in $[0, \frac{\omega}{c}\sqrt{\epsilon_{\parallel}}]$ for extraordinary modes.

So the radiative heat flux by ordinary modes is

$$\begin{aligned}\Phi_{\text{D}}^{\text{o}} &= \int_0^{\infty} \mathcal{U}(\omega, T) \int_0^{\frac{\omega}{c}\sqrt{\epsilon_{\perp}}} k_{\perp} \frac{dk_{\perp}}{2\pi} \frac{d\omega}{2\pi} \\ &= \int_0^{\infty} \mathcal{U}(\omega, T) \frac{\epsilon_{\perp}}{8\pi^2} \frac{\omega^2}{c^2} d\omega\end{aligned}\tag{2.141}$$

and by extraordinary modes

$$\begin{aligned}\Phi_{\text{D}}^{\text{e}} &= \int_0^{\infty} \mathcal{U}(\omega, T) \int_0^{\frac{\omega}{c} \sqrt{\epsilon_{\parallel}}} k_{\perp} \frac{dk_{\perp}}{2\pi} \frac{d\omega}{2\pi} \\ &= \int_0^{\infty} \mathcal{U}(\omega, T) \frac{\epsilon_{\parallel}}{8\pi^2} \frac{\omega^2}{c^2} d\omega.\end{aligned}\quad (2.142)$$

With $\epsilon_{\perp} = \epsilon_{\parallel} = 1$ we obtain Planck's blackbody law [11]

$$\Phi_{\text{BB}}^{\text{s}} = \Phi_{\text{BB}}^{\text{p}} = \int_0^{\infty} \mathcal{U}(\omega, T) \frac{\omega^2}{8\pi^2 c^2} d\omega. \quad (2.143)$$

Instead of ordinary and extraordinary modes we rather talk about s- and p-polarization here.

Metallic media

A lossless metallic medium ($\epsilon_{\perp} < 0$ and $\epsilon_{\parallel} < 0$) supports no propagating modes. As evanescent modes do not contribute to the heat fluxes, they vanish

$$\Phi_{\text{M}}^{\text{o}} = \Phi_{\text{M}}^{\text{e}} = 0. \quad (2.144)$$

Hyperbolic media of type I

For type I hyperbolic media the permittivities are $\epsilon_{\parallel} < 0$ and $\epsilon_{\perp} > 0$. As in the dielectric case the ordinary heat flux is

$$\Phi_{\text{I}}^{\circ} = \Phi_{\text{D}}^{\circ} = \int_0^{\infty} \mathcal{U}(\omega, T) \frac{\epsilon_{\perp}}{8\pi^2} \frac{\omega^2}{c^2} d\omega. \quad (2.145)$$

However, the extraordinary modes possess real parallel k -vector components even for much larger k_{\perp} . The cutoff $k_{\perp, \text{max}}$, already introduced during the derivation of the energy density, limits the number of propagating modes resulting in

$$\begin{aligned} \Phi_{\text{I}}^{\circ} &= \int_0^{\infty} \mathcal{U}(\omega, T) \int_0^{k_{\perp, \text{max}}} k_{\perp} \frac{dk_{\perp}}{2\pi} \frac{d\omega}{2\pi} \\ &= \int_0^{\infty} \mathcal{U}(\omega, T) \frac{1}{8\pi^2} k_{\perp, \text{max}}^2 d\omega. \end{aligned} \quad (2.146)$$

Hyperbolic media of type II

Finally, for the hyperbolic type II case with $\epsilon_{\parallel} > 0$ and $\epsilon_{\perp} < 0$ no propagating ordinary modes with real k_{\parallel}° exist making the heat flux

$$\Phi_{\text{II}}^{\circ} = \Phi_{\text{M}}^{\circ} = 0. \quad (2.147)$$

For the extraordinary modes we again use a cutoff and obtain

$$\begin{aligned}\Phi_{\text{II}}^e &= \int_0^\infty \mathcal{U}(\omega, T) \int_{\frac{\omega}{c}\sqrt{\epsilon_{\parallel}}}^{k_{\perp, \max}} k_{\perp} \frac{dk_{\perp}}{2\pi} \frac{d\omega}{2\pi} \\ &= \int_0^\infty \mathcal{U}(\omega, T) \frac{1}{8\pi^2} \left(k_{\perp, \max}^2 - \frac{\omega^2}{c^2} \epsilon_{\parallel} \right) d\omega.\end{aligned}\tag{2.148}$$

In the typical hyperbolic cases $k_{\perp, \max} \gg \frac{\omega}{c}\sqrt{|\epsilon_{\parallel}|}$ holds. The heat flux is dominated by extraordinary modes and approximately

$$\Phi_{\text{II}}^e \approx \Phi_{\text{I}}^e = \int_0^\infty \mathcal{U}(\omega, T) \frac{1}{8\pi^2} k_{\perp, \max}^2 d\omega.\tag{2.149}$$

Here, the spectral heat flux is quadratic in $k_{\perp, \max}$ or $k_{\parallel, \max} \approx k_{\perp, \max} \sqrt{\left| \frac{\epsilon_{\perp}}{\epsilon_{\parallel}} \right|}$ resp. and not directly dependent on frequency (only via dispersion and thermal occupation of states $\mathcal{U}(\omega, T)$).

We have checked in Appendix A.1, with the example of a type II hyperbolic medium, that the same results can be obtained by calculating the energy flow using the density of states together with the group velocity. So also the heat flux can be obtained without using fluctuational electrodynamics.

2.6 Radiative heat flux in vacuum

After having derived the thermal energy density and heat flux inside uniaxial media, in particular inside hyperbolic media – the results will be analyzed and discussed in Chapter 3 – we look at the radiative heat flux inside vacuum. Two setups are considered: First, a halfspace emitting into vacuum. Second, two halfspaces separated by a uniform vacuum gap exchanging heat through the gap.

2.6.1 Thermal emission into vacuum

The setup under consideration is presented in Fig. 2.5. A uniaxial medium halfspace at temperature T emits into vacuum. As for all configurations, the optical axis of the medium is oriented along the z -axis and orthogonal to the interface.

The procedure to derive the heat flux is the same as in Section 2.5.2. The only difference are Green's functions. Now, we have to take the ones introduced in Section 2.3.2.

So the heat flux in the vacuum is

$$\Phi_{\text{vac}} = 2\Re \int_0^\infty \frac{2\omega^3 \mu_0}{c^2} \mathcal{U}(\omega, T) \int_0^\infty \int_{-\infty}^0 \xi_{\alpha\beta z} \left(\mathbf{G}_{\text{vac}}^{\text{EE}}(\mathbf{r}, z', k_\perp; \omega) \right. \\ \left. \Im [\boldsymbol{\epsilon}(\omega)] \mathbf{G}_{\text{vac}}^{\text{HE}^H}(\mathbf{r}, z', k_\perp; \omega) \right)_{\alpha\beta} dz' k_\perp \frac{dk_\perp}{2\pi} \frac{d\omega}{2\pi}$$

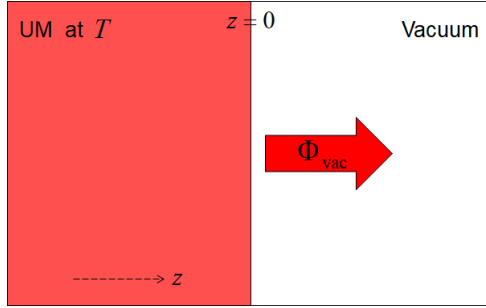


Figure 2.5: Illustration of the setup for which the thermal power flux into vacuum Φ_{vac} is evaluated. Halfspace of uniaxial medium (UM) at temperature T emits into vacuum. The dashed arrow shows the orientation of the optical axis of the UM which is along the z -axis.

$$\begin{aligned}
&= 2\Re \int_0^\infty \frac{2\omega^3 \mu_0}{c^2} \mathcal{U}(\omega, T) \int_0^\infty \int_{-\infty}^0 \xi_{\alpha\beta z} \left(\left\{ \frac{\text{ie}^{-ik_{\parallel}^o r'_{\parallel}} \text{e}^{ik_{\parallel}^{\text{vac}} r_{\parallel}}}{2k_{\parallel}^o} \right. \right. \\
&\quad \left. \left[t^s \mathbf{a}_s \otimes \mathbf{a}_s \right] + \frac{\text{ie}^{-ik_{\parallel}^e r'_{\parallel}} \text{e}^{ik_{\parallel}^{\text{vac}} r_{\parallel}}}{2k_{\parallel}^e \omega / c} \left[t^p k^e \mathbf{a}_p^{\text{vac}} \otimes \mathbf{a}_p^e \right. \right. \\
&\quad \left. \left. + t^p C k_{\perp} \mathbf{a}_p^{\text{vac}} \otimes \mathbf{e}_{\parallel} \right] \right\} \left\{ \Im[\epsilon_{\perp}] \mathbf{1} + \Im[\epsilon_{\parallel} - \epsilon_{\perp}] \mathbf{e}_{\parallel} \otimes \mathbf{e}_{\parallel} \right\} \\
&\quad \left\{ \frac{-\text{ie}^{ik_{\parallel}^{o*} r'_{\parallel}} \text{e}^{-ik_{\parallel}^{\text{vac}*} r_{\parallel}}}{2c\mu_0 k_{\parallel}^{o*}} \left[-t^{s*} \mathbf{a}_s \otimes \mathbf{a}_p^{\text{vac}*} \right] + \frac{-\text{ie}^{ik_{\parallel}^{e*} r'_{\parallel}} \text{e}^{-ik_{\parallel}^{\text{vac}*} r_{\parallel}}}{2\omega\mu_0 k_{\parallel}^{e*}} \right. \\
&\quad \left. \left[t^{p*} k^{e*} \mathbf{a}_p^{e*} \otimes \mathbf{a}_s + t^{p*} C^* k_{\perp} \mathbf{e}_{\parallel} \otimes \mathbf{a}_s \right] \right\} \Bigg)_{\alpha\beta} dz' k_{\perp} \frac{dk_{\perp}}{2\pi} \frac{d\omega}{2\pi}
\end{aligned}$$

$$\begin{aligned}
&= \Re \int_0^\infty \frac{\omega^3}{c^2} \mathcal{U}(\omega, T) \int_0^\infty \int_{-\infty}^0 \xi_{\alpha\beta z} \left(\Im[\epsilon_\perp] \frac{e^{2\Im[k_\parallel^o]z'} e^{-2\Im[k_\parallel^{\text{vac}}]z}}{c|k_\parallel^o|^2} \right. \\
&\quad |t^s|^2 \left[-(\mathbf{a}_s^T \mathbf{a}_s) \mathbf{a}_s \otimes \mathbf{a}_p^{\text{vac}*} \right] + \Im[\epsilon_\perp] \frac{e^{2\Im[k_\parallel^e]z'} e^{-2\Im[k_\parallel^{\text{vac}}]z}}{\frac{\omega^2}{c} |k_\parallel^e|^2} \\
&\quad |t^p|^2 \left[|k^e|^2 (\mathbf{a}_p^e{}^T \mathbf{a}_p^{e*}) \mathbf{a}_p^{\text{vac}} \otimes \mathbf{a}_s + C k_\perp k^{e*} (\mathbf{e}_\parallel^T \mathbf{a}_p^{e*}) \mathbf{a}_p^{\text{vac}} \otimes \mathbf{a}_s \right. \\
&\quad \left. + C^* k_\perp k^e (\mathbf{a}_p^e{}^T \mathbf{e}_\parallel) \mathbf{a}_p^{\text{vac}} \otimes \mathbf{a}_s + |C|^2 k_\perp^2 (\mathbf{e}_\parallel^T \mathbf{e}_\parallel) \mathbf{a}_p^{\text{vac}} \otimes \mathbf{a}_s \right] \\
&\quad + \Im[\epsilon_\parallel - \epsilon_\perp] \frac{e^{2\Im[k_\parallel^e]z'} e^{-2\Im[k_\parallel^{\text{vac}}]z}}{\frac{\omega^2}{c} |k_\parallel^e|^2} |t^p|^2 \left[|k^e|^2 (\mathbf{a}_p^e{}^T \mathbf{e}_\parallel) (\mathbf{e}_\parallel^T \mathbf{a}_p^{e*}) \right. \\
&\quad \mathbf{a}_p^{\text{vac}} \otimes \mathbf{a}_s + |C|^2 k_\perp^2 (\mathbf{e}_\parallel^T \mathbf{e}_\parallel) (\mathbf{e}_\parallel^T \mathbf{e}_\parallel) \mathbf{a}_p^{\text{vac}} \otimes \mathbf{a}_s \\
&\quad \left. + C k_\perp k^{e*} (\mathbf{e}_\parallel^T \mathbf{e}_\parallel) (\mathbf{e}_\parallel^T \mathbf{a}_p^{e*}) \mathbf{a}_p^{\text{vac}} \otimes \mathbf{a}_s \right. \\
&\quad \left. + C^* k_\perp k^e (\mathbf{a}_p^e{}^T \mathbf{e}_\parallel) (\mathbf{e}_\parallel^T \mathbf{e}_\parallel) \mathbf{a}_p^{\text{vac}} \otimes \mathbf{a}_s \right] \Big)_{\alpha\beta} dz' k_\perp \frac{dk_\perp}{2\pi} \frac{d\omega}{2\pi} \\
&= \Re \int_0^\infty \frac{\omega^3}{c^2} \mathcal{U}(\omega, T) \int_0^\infty \xi_{\alpha\beta z} \left(\Im[\epsilon_\perp] \frac{e^{-2\Im[k_\parallel^{\text{vac}}]z}}{c 2\Im[k_\parallel^o] |k_\parallel^o|^2} |t^s|^2 [-1] \right. \\
&\quad \mathbf{a}_s \otimes \mathbf{a}_p^{\text{vac}*} + \Im[\epsilon_\perp] \frac{e^{-2\Im[k_\parallel^{\text{vac}}]z}}{\frac{\omega^2}{c} 2\Im[k_\parallel^e] |k_\parallel^e|^2} |t^p|^2 \left[|k^e|^2 \frac{|k_\parallel^e|^2 + k_\perp^2}{|k^e|^2} \right. \\
&\quad \left. + C k_\perp^2 + C^* k_\perp^2 + |C|^2 k_\perp^2 \right] \mathbf{a}_p^{\text{vac}} \otimes \mathbf{a}_s \\
&\quad + \Im[\epsilon_\parallel - \epsilon_\perp] \frac{e^{-2\Im[k_\parallel^{\text{vac}}]z}}{\frac{\omega^2}{c} 2\Im[k_\parallel^e] |k_\parallel^e|^2} |t^p|^2 \left[|k^e|^2 \frac{k_\perp^2}{|k^e|^2} \right. \\
&\quad \left. + C k_\perp^2 + C^* k_\perp^2 + |C|^2 k_\perp^2 \right] \mathbf{a}_p^{\text{vac}} \otimes \mathbf{a}_s \Big)_{\alpha\beta} k_\perp \frac{dk_\perp}{2\pi} \frac{d\omega}{2\pi}.
\end{aligned} \tag{2.150}$$

The heat flux along the z -direction is searched for, so only the xy and yx -components of the matrices are needed. With the relations

$$\left(\mathbf{a}_s \otimes \mathbf{a}_p^{\text{vac}*}\right)_{xy} - \left(\mathbf{a}_s \otimes \mathbf{a}_p^{\text{vac}*}\right)_{yx} = -\frac{k_{\parallel}^{\text{vac}*}}{\omega/c}, \quad (2.151)$$

$$\left(\mathbf{a}_p^{\text{vac}} \otimes \mathbf{a}_s\right)_{xy} - \left(\mathbf{a}_p^{\text{vac}} \otimes \mathbf{a}_s\right)_{yx} = \frac{k_{\parallel}^{\text{vac}}}{\omega/c} \quad (2.152)$$

and Eq. (2.131) we obtain

$$\begin{aligned} \Phi_{\text{vac}} = & \Re \int_0^{\infty} \frac{\omega^3}{c^2} \mathcal{U}(\omega, T) \int_0^{\infty} \left(\Re[k_{\parallel}^{\text{o}}] \frac{c^2}{\omega^3} \frac{e^{-2\Im[k_{\parallel}^{\text{vac}}]z}}{|k_{\parallel}^{\text{o}}|^2} k_{\parallel}^{\text{vac}*} |t^{\text{s}}|^2 \right. \\ & + \frac{\Im[\epsilon_{\perp}]}{2\Im[k_{\parallel}^{\text{e}}]} \frac{c^2}{\omega^3} \frac{e^{-2\Im[k_{\parallel}^{\text{vac}}]z}}{|k_{\parallel}^{\text{e}}|^2} k_{\parallel}^{\text{vac}} |t^{\text{p}}|^2 \left[|k_{\parallel}^{\text{e}}|^2 + k_{\perp}^2 + Ck_{\perp}^2 \right. \\ & + C^*k_{\perp}^2 + |C|^2k_{\perp}^2 \left. \right] + \frac{\Im[\epsilon_{\parallel} - \epsilon_{\perp}]}{2\Im[k_{\parallel}^{\text{e}}]} \frac{c^2}{\omega^3} \frac{e^{-2\Im[k_{\parallel}^{\text{vac}}]z}}{|k_{\parallel}^{\text{e}}|^2} k_{\parallel}^{\text{vac}} \\ & \left. |t^{\text{p}}|^2 \left[k_{\perp}^2 + Ck_{\perp}^2 + C^*k_{\perp}^2 + |C|^2k_{\perp}^2 \right] \right) k_{\perp} \frac{dk_{\perp}}{2\pi} \frac{d\omega}{2\pi} \end{aligned}$$

$$\begin{aligned}
&= \int_0^\infty \mathcal{U}(\omega, T) \int_0^\infty \left(\frac{\Re[k_\parallel^o] \Re[k_\parallel^{\text{vac}}]}{|k_\parallel^o|^2} |t^s|^2 e^{-2\Im[k_\parallel^{\text{vac}}]z} \right. \\
&\quad \left. + \frac{\Im[\epsilon_\perp] \Re[k_\parallel^{\text{vac}}]}{2\Im[k_\parallel^e] |k_\parallel^e|^2} |t^p|^2 e^{-2\Im[k_\parallel^{\text{vac}}]z} \right. \\
&\quad \left[|k_\parallel^e|^2 + k_\perp^2 + 2\Re[C] k_\perp^2 + |C|^2 k_\perp^2 + \left(\frac{\Im[\epsilon_\parallel]}{\Im[\epsilon_\perp]} - 1 \right) \right. \\
&\quad \left. \left. \left\{ k_\perp^2 + 2\Re[C] k_\perp^2 + |C|^2 k_\perp^2 \right\} \right] \right) k_\perp \frac{dk_\perp}{2\pi} \frac{d\omega}{2\pi}.
\end{aligned} \tag{2.153}$$

As vacuum is non-dissipative we notice that evanescent modes do not contribute to the heat flux because $\Re[k_\parallel^{\text{vac}}] = 0$. So we can restrict the integration to modes propagating in vacuum and substitute the anisotropy coefficient C from (2.43)

$$\begin{aligned}
\Phi_{\text{vac}} &= \int_0^\infty \mathcal{U}(\omega, T) \int_{k_\parallel^{\text{vac}} \in \mathbb{R}} \left(\frac{\Re[k_\parallel^o] k_\parallel^{\text{vac}}}{|k_\parallel^o|^2} |t^s|^2 + \frac{\Im[\epsilon_\perp] k_\parallel^{\text{vac}}}{2\Im[k_\parallel^e] |k_\parallel^e|^2} |t^p|^2 \right. \\
&\quad \left. \left[|k_\parallel^e|^2 + \frac{\Im[\epsilon_\parallel]}{\Im[\epsilon_\perp]} \left\{ k_\perp^2 + 2\Re[C] k_\perp^2 + |C|^2 k_\perp^2 \right\} \right] \right) k_\perp \frac{dk_\perp}{2\pi} \frac{d\omega}{2\pi} \\
&= \int_0^\infty \mathcal{U}(\omega, T) \int_{k_\parallel^{\text{vac}} \in \mathbb{R}} \left(\frac{\Re[k_\parallel^o] k_\parallel^{\text{vac}}}{|k_\parallel^o|^2} |t^s|^2 + \frac{\Im[\epsilon_\perp] k_\parallel^{\text{vac}}}{2\Im[k_\parallel^e] |k_\parallel^e|^2} |t^p|^2 \right. \\
&\quad \left. \left[|k_\parallel^e|^2 + k_\perp^2 \frac{\Im[\epsilon_\parallel] |\epsilon_\perp|^2}{\Im[\epsilon_\perp] |\epsilon_\parallel|^2} \right] \right) k_\perp \frac{dk_\perp}{2\pi} \frac{d\omega}{2\pi}.
\end{aligned} \tag{2.154}$$

Substituting

$$\begin{aligned}
& \Im[\epsilon_{\perp}] \left(|k_{\parallel}^e|^2 + k_{\perp}^2 \frac{\Im[\epsilon_{\parallel}] |\epsilon_{\perp}|^2}{\Im[\epsilon_{\perp}] |\epsilon_{\parallel}|^2} \right) \\
&= |k_{\parallel}^e|^2 \Im[\epsilon_{\perp}] + k_{\perp}^2 \left(\Re \left[\frac{\epsilon_{\perp}}{\epsilon_{\parallel}} \right] \Im[\epsilon_{\perp}] - \Im \left[\frac{\epsilon_{\perp}}{\epsilon_{\parallel}} \right] \Re[\epsilon_{\perp}] \right) \quad (2.155) \\
&= |k_{\parallel}^e|^2 \Im[\epsilon_{\perp}] - \Re \left[k_{\parallel}^{e2} \right] \Im[\epsilon_{\perp}] + \Im \left[k_{\parallel}^{e2} \right] \Re[\epsilon_{\perp}] \\
&= 2\Im[k_{\parallel}^e]^2 \Im[\epsilon_{\perp}] + 2\Re[k_{\parallel}^e] \Im[k_{\parallel}^e] \Re[\epsilon_{\perp}] = 2\Im[k_{\parallel}^e] \Re \left[k_{\parallel}^e \epsilon_{\perp}^* \right]
\end{aligned}$$

gives us

$$\begin{aligned}
\Phi_{\text{vac}} &= \int_0^{\infty} \mathcal{U}(\omega, T) \int_{k_{\parallel}^{\text{vac}} \in \mathbb{R}} \left(\frac{\Re[k_{\parallel}^o] k_{\parallel}^{\text{vac}}}{|k_{\parallel}^o|^2} |t^s|^2 \right. \\
&\quad \left. + \frac{\Re \left[k_{\parallel}^e \epsilon_{\perp}^* \right] k_{\parallel}^{\text{vac}}}{|k_{\parallel}^e|^2} |t^p|^2 \right) k_{\perp} \frac{dk_{\perp}}{2\pi} \frac{d\omega}{2\pi}. \quad (2.156)
\end{aligned}$$

Now, we note that propagating modes in vacuum are characterized by $k_{\perp} \in [0, \frac{\omega}{c}]$. Further, the reflectivity at the vacuum–uniaxial medium interface

$$R^{s/p} = | -r^{s/p} |^2 = |r^{s/p}|^2 = 1 - \alpha^{s/p} \quad (2.157)$$

is independent of whether light is incident from vacuum or the medium. All the power which is not reflected is absorbed. $\alpha^{s/p}$ is the absorptivity.

Employing

$$\begin{aligned}
 \frac{\Re[k_{\parallel}^{\text{o}}]k_{\parallel}^{\text{vac}}}{|k_{\parallel}^{\text{o}}|^2} |t^{\text{s}}|^2 &= \frac{\Re[k_{\parallel}^{\text{o}}]k_{\parallel}^{\text{vac}}}{|k_{\parallel}^{\text{o}}|^2} \frac{|2k_{\parallel}^{\text{o}}|^2}{|k_{\parallel}^{\text{o}} + k_{\parallel}^{\text{vac}}|^2} \\
 &= \frac{|k_{\parallel}^{\text{o}} + k_{\parallel}^{\text{vac}}|^2 - |k_{\parallel}^{\text{o}} - k_{\parallel}^{\text{vac}}|^2}{|k_{\parallel}^{\text{o}} + k_{\parallel}^{\text{vac}}|^2} \quad (2.158) \\
 &= 1 - |r^{\text{s}}|^2 = 1 - R^{\text{s}} = \alpha^{\text{s}},
 \end{aligned}$$

$$\begin{aligned}
 \frac{\Re[k_{\parallel}^{\text{e}}\epsilon_{\perp}^*]k_{\parallel}^{\text{vac}}}{|k_{\parallel}^{\text{e}}|^2} |t^{\text{p}}|^2 &= \frac{\Re[k_{\parallel}^{\text{e}}\epsilon_{\perp}^*]k_{\parallel}^{\text{vac}}}{|k_{\parallel}^{\text{e}}|^2} \frac{|2k_{\parallel}^{\text{e}}|^2}{|k_{\parallel}^{\text{e}} + \epsilon_{\perp}k_{\parallel}^{\text{vac}}|^2} \\
 &= \frac{|k_{\parallel}^{\text{e}} + \epsilon_{\perp}k_{\parallel}^{\text{vac}}|^2 - |k_{\parallel}^{\text{e}} - \epsilon_{\perp}k_{\parallel}^{\text{vac}}|^2}{|k_{\parallel}^{\text{e}} + \epsilon_{\perp}k_{\parallel}^{\text{vac}}|^2} \quad (2.159) \\
 &= 1 - |r^{\text{p}}|^2 = 1 - R^{\text{p}} = \alpha^{\text{p}}
 \end{aligned}$$

the thermal power radiated into vacuum by a uniaxial medium becomes

$$\begin{aligned}
 \Phi_{\text{vac}} &= \sum_{j=\text{s,p}} \int_0^{\infty} \mathcal{U}(\omega, T) \int_0^{\frac{\omega}{c}} (1 - |r^j|^2) k_{\perp} \frac{dk_{\perp}}{2\pi} \frac{d\omega}{2\pi} \\
 &= \sum_{j=\text{s,p}} \int_0^{\infty} \mathcal{U}(\omega, T) \int_0^{\frac{\omega}{c}} \alpha^j k_{\perp} \frac{dk_{\perp}}{2\pi} \frac{d\omega}{2\pi}. \quad (2.160)
 \end{aligned}$$

(2.160) is a well-known result. It combines Planck's law of black-body radiation with Kirchhoff's law of thermal radiation which

says that emissivity of a body is equal to its absorptivity [10,11]. The equation (2.160) is even more general. It holds for any half-space which is homogeneous along the interface plane (xy -plane); although the integration over k_{\perp} should in general be replaced by a double integral over all \mathbf{k}_{\perp} . So it could e. g. be a layered halfspace.

The physics behind Kirchhoff's law is reciprocity [81]. Emission and absorption are reciprocal processes and should be similar in a system when this is reciprocal. Often derivations of Kirchhoff's law are based on thermodynamic balances instead of reciprocity. However, in non-reciprocal systems the laws of thermodynamics lead to violation of Kirchhoff's law [82]. Other, more general "Kirchhoff's laws" can be derived [83].

2.6.2 Radiative heat flux through vacuum gap

The last setup under investigation is shown in Fig. 2.6. A half-space 1 consisting of a uniaxial medium at temperature T is separated by a uniform vacuum gap from a halfspace 2 at 0 K. The gap size is l .

To calculate the heat flux across the vacuum gap we can follow the same procedure as in our two previous cases. In contrast to the emission into a vacuum halfspace, in the gap there is an additional backward "traveling" wave, as explained in Section 2.3.3. "Traveling" is put in quotation marks as the waves can be evanescent and not really traveling in that case. Alter-

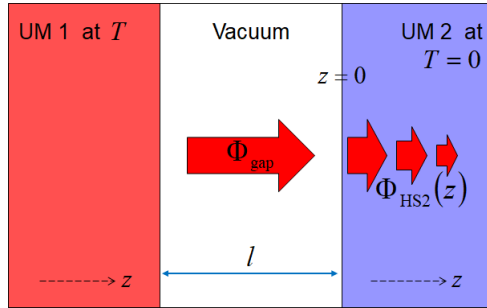


Figure 2.6: Illustration of the setup for which the thermal power flux through a vacuum gap Φ_{gap} is evaluated. Halfspace of uniaxial medium (UM) 1 at temperature T separated by a vacuum gap from a second halfspace of UM 2 at $T = 0$ K. The separation or gap size is l . In addition, the heat flux inside the second halfspace $\Phi_{\text{HS2}}(z)$ is displayed. The dashed arrows show the orientation of the optical axes of the UMs which are along the z -axis.

natively, one can calculate the heat flux in uniaxial medium 2 directly at the interface ($z = 0$). Since there are no surface currents or charges, the heat flux is continuous across material interfaces. Both approaches yield the same heat flux.

Let $r_i^{\text{s/p}}$ be the reflection coefficient at the vacuum–uniaxial medium i interface for s- or p-polarization respectively. The formulas required to calculate them are Eqs. (2.11) and (2.12).

The heat flux in the vacuum gap is [4, 5, 15]

$$\begin{aligned} \Phi_{\text{gap}} = & \sum_{j=\text{s,p}} \int_0^{\infty} \mathcal{U}(\omega, T) \left(\int_0^{\frac{\omega}{c}} \frac{(1 - |r_1^j|^2)(1 - |r_2^j|^2)}{|1 - r_1^j r_2^j e^{i2k_{\parallel}^{\text{vac}} l}|^2} k_{\perp} \frac{dk_{\perp}}{2\pi} \right. \\ & \left. + \int_{\frac{\omega}{c}}^{\infty} \frac{4\Im[r_1^j] \Im[r_2^j] e^{-2|k_{\parallel}^{\text{vac}}| l}}{|1 - r_1^j r_2^j e^{-2|k_{\parallel}^{\text{vac}}| l}|^2} k_{\perp} \frac{dk_{\perp}}{2\pi} \right) \frac{d\omega}{2\pi}. \end{aligned} \quad (2.161)$$

The heat flux has two contributions. First, the propagating modes, characterized by $k_{\perp} \in [0, \frac{\omega}{c}]$ and real $k_{\parallel}^{\text{vac}}$, contribute similarly as in the single interface case in Section 2.6.1. Half-space 1 emits with the emissivity $(1 - |r_1^j|^2)$ and halfspace 2 absorbs with absorptivity $(1 - |r_2^j|^2)$. The denominator accounts for Fabry-Pérot interferences in the gap.

Second, evanescent modes with $k_{\perp} > \frac{\omega}{c}$ and imaginary $k_{\parallel}^{\text{vac}}$ contribute too. As we learned in Section 2.6.1, evanescent modes usually don't transport energy in the direction of their exponential decay. Nonetheless, in the gap there are forward and backward "traveling" evanescent modes. Their interference causes power flows in the direction of decay. In quantum theory one says photons tunnel the gap. The smaller the gap l the more effective the tunneling and the larger the heat flux, exemplified by the term $e^{-2|k_{\parallel}^{\text{vac}}| l}$.

The exponential decay $e^{-2|k_{\parallel}^{\text{vac}}| l}$ introduces a cutoff which, for small l , is $k_{\perp}^{\text{cut}} \approx |k_{\parallel}^{\text{vac, cut}}| \propto \frac{1}{l}$. If there are no other, previous

cutoff mechanisms the spectral heat flux scales with $k_{\perp}^{\text{cut}^2} \propto \frac{1}{l^2}$. Eventually, the total heat flux also scales $\propto \frac{1}{l^2}$ [22].

Equation (2.161) is also not restricted to uniaxial media half-spaces but holds for any halfspaces which are homogeneous along the interface plane (xy -plane); although the integration over k_{\perp} should in general be replaced by a double integral over all \mathbf{k}_{\perp} . So we can calculate the radiative heat flux between e. g. layered halfspaces. The interaction of a halfspace to the outer vacuum, including its emission, is fully described by the reflection coefficients.

With the vacuum-homogeneous medium 2 interface at $z = 0$ the heat flux inside medium 2 reads

$$\begin{aligned} \Phi_{\text{HS}2} = & \sum_{j=\text{s,p}} \int_0^{\infty} \mathcal{U}(\omega, T) \left(\int_0^{\frac{\omega}{c}} \frac{(1 - |r_1^j|^2)(1 - |r_2^j|^2)}{|1 - r_1^j r_2^j e^{i2k_{\parallel}^{\text{vac}} l}|^2} e^{-2\Im[k_{\parallel}^j]z} k_{\perp} \frac{dk_{\perp}}{2\pi} \right. \\ & \left. + \int_{\frac{\omega}{c}}^{\infty} \frac{4\Im[r_1^j]\Im[r_2^j]e^{-2|k_{\parallel}^{\text{vac}}|l}}{|1 - r_1^j r_2^j e^{-2|k_{\parallel}^{\text{vac}}|l}|^2} e^{-2\Im[k_{\parallel}^j]z} k_{\perp} \frac{dk_{\perp}}{2\pi} \right) \frac{d\omega}{2\pi}. \end{aligned} \quad (2.162)$$

The normal wavevector components in medium 2 are

$$k_{\parallel}^{\text{s}} = \sqrt{\frac{\omega^2}{c^2} \epsilon_{\perp,2} - k_{\perp}^2} \quad (2.163)$$

for ordinary modes (s-polarized in the vacuum) and

$$k_{\parallel}^{\text{p}} = \sqrt{\frac{\omega^2}{c^2} \epsilon_{\perp,2} - k_{\perp}^2 \frac{\epsilon_{\perp,2}}{\epsilon_{\parallel,2}}} \quad (2.164)$$

for extraordinary modes (p-polarized in the vacuum).

The derivation of the heat flux formula (2.162) can be done the same way as before. A more skilful way is to note that the heat flux is continuous in the medium and at interfaces and that the fields of the plane waves we use as our basis exhibit a $\propto e^{ik_{\parallel}^{\text{s/p}}z}$ z -dependence. Consequently, at the $z = 0$ interface the heat flux is identical to the heat flux in the vacuum gap and the power afterwards decreases $\propto e^{-2\Im[k_{\parallel}^{\text{s/p}}]z}$.

Expressions for the heat flux in an arbitrary layered system consisting of isotropic materials can be found e. g. in Refs. [66, 74]. The extension to uniaxial media is straight forward.

The radiation channels for the heat are reciprocal because the systems we look at are so too. This can also be seen nicely from the gap heat flux expression (2.161). As a consequence, when the right halfspace 2 emits and the left one receives the direction of thermal radiation is reversed and the modes / channels are filled with photons according to $\mathcal{U}(\omega, T_2)$ not $\mathcal{U}(\omega, T_1)$.

Usually both halfspaces have non-zero temperatures and the effective heat flux is still calculated with the formulas (2.140), (2.161), (2.162), only $\mathcal{U}(\omega, T)$ is replaced by $\mathcal{U}(\omega, T_1) - \mathcal{U}(\omega, T_2)$. The heat transfer coefficient (HTC) H , and its spectral counter-

part $h(\omega)$, is defined as the effective heat flux normalized to the temperature difference

$$\begin{aligned} H &= \int_0^\infty h(\omega) d\omega \equiv \frac{d\Phi}{dT} = \int_0^\infty \frac{d\phi(\omega)}{dT} d\omega \\ &= \int_0^\infty \frac{d\mathcal{U}(\omega, T)}{dT} \dots \frac{d\omega}{2\pi}. \end{aligned} \quad (2.165)$$

The temperature difference dT is assumed to be small. The differentiated Bose–Einstein term reads

$$\frac{d\mathcal{U}(\omega, T)}{dT} = \frac{d}{dT} \frac{\hbar\omega}{e^{\frac{\hbar\omega}{k_B T}} - 1} = \frac{\hbar^2\omega^2}{k_B T^2} \frac{e^{\frac{\hbar\omega}{k_B T}}}{\left(e^{\frac{\hbar\omega}{k_B T}} - 1\right)^2}. \quad (2.166)$$

Chapter 3

Thermal radiation inside hyperbolic media

At the beginning of the 20th century Max Planck derived his famous law describing the spectral distribution of energy of a blackbody (BB) by introducing the concept of quantum of light, laying so the foundation of quantum physics [12]. Let us first summarize the properties of blackbody radiation which is the benchmark for any thermal radiation.

The internal energy density of blackbody radiation for both principal polarization states (abbreviated by s and p) is given

by [10, 11]

$$\begin{aligned}
 U_{\text{BB}}^{\text{s/p}} &= \int_0^{\infty} D_{\text{BB}}^{\text{s/p}}(\omega) \mathcal{U}(\omega, T) \, d\omega = \int_0^{\infty} \frac{\omega^2}{2\pi^2 c^3} \frac{\hbar\omega}{e^{\frac{\hbar\omega}{k_{\text{B}}T}} - 1} \, d\omega \\
 &= \frac{1}{2\pi^2} \frac{(k_{\text{B}}T)^4}{(\hbar c)^3} \int_0^{\infty} \frac{\Omega^3}{e^{\Omega} - 1} \, d\Omega = \frac{1}{2} \frac{\pi^2}{15} \frac{(k_{\text{B}}T)^4}{(\hbar c)^3}.
 \end{aligned} \tag{3.1}$$

The density of states (DOS) $D_{\text{BB}}^{\text{s/p}}$ was taken from Eq. (2.113). The spectral energy density is simply $u_{\text{BB}}^{\text{s/p}} = \mathcal{U} D_{\text{BB}}^{\text{s/p}}$. Appendix C.3 contains information on how this and upcoming integrations are carried out.

With the help of the DOS we can determine more thermodynamic potentials of the photon gas inside the material under investigation. E. g. the free energy [84] per unit volume is, for a blackbody, given by

$$\begin{aligned}
 F_{\text{BB}}^{\text{s/p}} &= \int_0^{\infty} D_{\text{BB}}^{\text{s/p}}(\omega) \mathcal{F}(\omega, T) \, d\omega \\
 &= \int_0^{\infty} \frac{\omega^2}{2\pi^2 c^3} k_{\text{B}}T \ln \left(1 - e^{-\frac{\hbar\omega}{k_{\text{B}}T}} \right) \, d\omega \\
 &= \frac{1}{2\pi^2} \frac{(k_{\text{B}}T)^4}{(\hbar c)^3} \int_0^{\infty} \Omega^2 \ln \left(1 - e^{-\Omega} \right) \, d\Omega
 \end{aligned}$$

$$\begin{aligned}
&= -\frac{1}{3} \frac{1}{2\pi^2} \frac{(k_B T)^4}{(\hbar c)^3} \int_0^\infty \frac{\Omega^3}{e^\Omega - 1} d\Omega \\
&= -\frac{1}{3} \frac{1}{2} \frac{\pi^2}{15} \frac{(k_B T)^4}{(\hbar c)^3} = -\frac{1}{3} U_{\text{BB}}^{s/p},
\end{aligned} \tag{3.2}$$

where $\mathcal{F}(\omega, T) = k_B T \ln \left(1 - e^{-\frac{\hbar\omega}{k_B T}} \right)$ is a direct result of the relation (assuming no change in volume) [84]

$$U = -T^2 \frac{\partial(F/T)}{\partial T} \quad \text{and thus} \quad \mathcal{U} = -T^2 \frac{\partial(\mathcal{F}/T)}{\partial T}. \tag{3.3}$$

Finally, from the internal and free energy we can also determine the entropy per unit volume by $S = \frac{U-F}{T}$ [84]. Clearly, by means of these expressions we can derive any thermodynamic property of the photon gas inside a large cavity as the pressure $P \propto U$, the photonic heat capacity (at constant volume) $C_V = \frac{\partial U}{\partial T}$, etc. [84].

Wien's displacement law [11] tells us the frequency ω_{max} , resp. wavelength λ_{max} , at which the energy distribution function has its maximum. The connection between frequency and wavelength dependence is $u(\omega)d\omega = u(\lambda)d\lambda$. A numerical calculation for which normalized frequency $\Omega = \frac{\hbar\omega}{k_B T}$ the integrand in (3.1) reaches its maximum reveals [10, 11]

$$\frac{\hbar\omega_{\text{max, BB}}}{k_B T} = \Omega_{\text{max, BB}} \approx 2.821 \quad \text{or} \quad \frac{2\pi l_c}{\lambda_{\text{max, BB}}} \approx 4.965. \tag{3.4}$$

Here, we have introduced the thermal coherence length [85]

$$l_c \equiv \frac{\hbar c}{k_B T}. \quad (3.5)$$

At a temperature of 300 K the coherence length is $l_c \approx 7.63 \mu\text{m}$, Wien's wavelength is $\lambda_{\text{max, BB}} \approx 9.66 \mu\text{m}$ and Wien's frequency $\omega_{\text{max, BB}} \approx 111 \cdot 10^{12} \text{ s}^{-1}$. The frequency / wavelength at which the blackbody heat flux has its maximum is the same as for the BB energy density. As the coherence length is on the order of one wavelength thermal blackbody radiation is said to be incoherent, meaning it does not show any interference effects.

Integrating Eq. (2.143) provides Stefan–Boltzmann's law [11]

$$\begin{aligned} \Phi_{\text{BB}}^{\text{s/p}} &= \int_0^\infty \frac{\omega^2}{8\pi^2 c^2} \mathcal{U}(\omega, T) d\omega = \frac{c}{4} \int_0^\infty \frac{\omega^2}{2\pi^2 c^3} \frac{\hbar\omega}{e^{\frac{\hbar\omega}{k_B T}} - 1} d\omega \\ &= \frac{c}{4} U_{\text{BB}}^{\text{s/p}} = \frac{1}{2} \frac{\pi^2}{60} \frac{(k_B T)^4}{\hbar^3 c^2} = \frac{1}{2} \sigma_B T^4. \end{aligned} \quad (3.6)$$

In this chapter we will first look at thermal radiation inside lossless, nondispersive hyperbolic media (HM). In such an idealized medium – a “hyperbolic blackbody” – all thermodynamic quantities can be calculated analytically. As will be shown, the radiation properties are fundamentally different from the “classical” blackbody properties. Then, a more realistic example of a dispersive HM is analyzed and its solid vs. radiative heat fluxes are compared. Finally, Section 3.2.3 outlines some thoughts on the radiative thermal conductivity of HMs.

Note that sometimes radiative heat flux inside HMs is referred to as a special kind of near-field heat flux. Usually this is incorrect. It is only correct if evanescent modes contribute to the heat flux which is only possible over very short distances.

Further note that blackbody radiation is not the radiation inside a black, thus (very) lossy, material or body. But it is the radiation inside a cavity (see Section 2.5.1) or emitted by a black, thus non-reflecting, body (see Section 2.5.2 or Section 2.6.1 with $\alpha^{s/p} = 1$). The “classical” blackbody assumes the cavity is evacuated or the black body emits into vacuum respectively. The “hyperbolic blackbody” assumes a cavity filled with a HM or emission into a HM.

Following Eqs. (2.11) and (2.12) lossy dielectric materials, which appear black to the human eye, partly reflect incident radiation. So they are rather gray (or imperfectly black) than perfectly black. Therefore, such a “black” body does not emit blackbody radiation but a little less depending on its emissivity. As we learned previously, determining the properties of thermal radiation inside lossy materials is very complicated. As a starting point one could look at the radiation inside lossless dielectrics.

3.1 Thermal radiation inside nondispersive hyperbolic media

An ideal HM is nondissipative and nondispersive. Although such materials cannot exist because they violate Kramers–Kronig relations [14, 44], their analysis is rather simple and they reveal important properties. Therefore, we look at such ideal HMs in this section. Analogous to the classical BB we call the ideal HMs “hyperbolic blackbodies”. The “classical” in classical BB does of course not refer to classical physics which, different from quantum physics, ignores quantization effects but simply refers to Planck’s theory which is nowadays more than 100 years old. The density of states and the heat flux inside uniaxial media have been derived in Section 2.5. These results are summarized and discussed. In addition, further thermal properties are studied.

3.1.1 Energy density and density of states

In dielectric anisotropic media the DOS D_D^o for the ordinary modes (OMs) and D_D^e for the extraordinary modes (EMs) are given by the expressions

$$D_D^o(\omega) = \frac{\omega^2}{\pi^2 c^3} \frac{\epsilon_{\perp} \sqrt{\epsilon_{\perp}}}{2} = D_{\text{BB}}^s \epsilon_{\perp} \sqrt{\epsilon_{\perp}}, \quad (3.7)$$

$$D_D^e(\omega) = \frac{\omega^2}{\pi^2 c^3} \frac{\epsilon_{\parallel} \sqrt{\epsilon_{\perp}}}{2} = D_{\text{BB}}^p \epsilon_{\parallel} \sqrt{\epsilon_{\perp}}, \quad (3.8)$$

which were already derived by Eckhardt [78], for instance. On the other hand, in the hyperbolic case we obtain

$$D_{\text{I}}^{\circ}(\omega) = \frac{\omega^2}{\pi^2 c^3} \frac{\epsilon_{\perp} \sqrt{\epsilon_{\perp}}}{2} = D_{\text{D}}^{\circ} = D_{\text{BB}}^{\text{s}} \epsilon_{\perp} \sqrt{\epsilon_{\perp}}, \quad (3.9)$$

$$\begin{aligned} D_{\text{I}}^{\text{e}}(\omega) &= \frac{\omega}{\pi^2 c^2} \frac{|\epsilon_{\parallel}|}{2} \left(k_{\parallel, \text{max}} - \frac{\omega}{c} \sqrt{\epsilon_{\perp}} \right) \\ &= \frac{\omega}{\pi^2 c^2} \frac{|\epsilon_{\parallel}|}{2} \left(\sqrt{k_{\perp, \text{max}}^2 \frac{\epsilon_{\perp}}{|\epsilon_{\parallel}|} + \frac{\omega^2}{c^2} \epsilon_{\perp}} - \frac{\omega}{c} \sqrt{\epsilon_{\perp}} \right) \end{aligned} \quad (3.10)$$

and

$$D_{\text{II}}^{\circ}(\omega) = 0, \quad (3.11)$$

$$\begin{aligned} D_{\text{II}}^{\text{e}}(\omega) &= \frac{\omega}{\pi^2 c^2} \frac{\epsilon_{\parallel}}{2} k_{\parallel, \text{max}} \\ &= \frac{\omega}{\pi^2 c^2} \frac{\epsilon_{\parallel}}{2} \sqrt{k_{\perp, \text{max}}^2 \frac{|\epsilon_{\perp}|}{\epsilon_{\parallel}} - \frac{\omega^2}{c^2} |\epsilon_{\perp}|}, \end{aligned} \quad (3.12)$$

for type I and type II HMs, respectively.

Note that we have introduced cutoff wavenumbers $k_{\parallel, \text{max}}$ and $k_{\perp, \text{max}}$ respectively, which are denoted by k_{max} whenever a differentiation is not necessary. k_{max} can be a function of frequency even for nondispersive media and is determined by the real (atomic or meta) structure of the medium. For an ideal HM k_{max} is infinite so that the DOS diverges as was pointed out previously [59, 60]. However, for any real structure k_{max} is a finite quantity (see Section 1.2). For hyperbolic metamaterials (HMMS) it is mainly determined by the unit-cell size of the meta structure. Note further that the DOS of the EMs of type

I and type II HMs coincide for $k_{\parallel,\max} \gg \frac{\omega}{c} \sqrt{|\epsilon_{\perp}|}$, respectively $k_{\perp,\max} \gg \frac{\omega}{c} \sqrt{|\epsilon_{\parallel}|}$, and are given by

$$D_{\text{I}}^{\text{e}} \approx D_{\text{II}}^{\text{e}} \approx \frac{\omega}{\pi^2 c^2} \frac{\epsilon_{\parallel}}{2} k_{\parallel,\max} \approx \frac{\omega}{\pi^2 c^2} \frac{\sqrt{|\epsilon_{\perp} \epsilon_{\parallel}|}}{2} k_{\perp,\max}. \quad (3.13)$$

Apparently, the DOS is linear in ω and linear in k_{\max} . If k_{\max} would be proportional to $\frac{\omega}{c}$ we would retrieve the usual quadratic behavior of the DOS with respect to frequency. We want to emphasize that the approximate expression of the DOS for a non-ideal dispersive material given in Refs. [59,60] is proportional to k_{\max}^3 , which is a consequence of the dispersive nature of the medium and is examined in the next section.

Let us first have a look at the expressions for the energy density inside an ordinary uniaxial material. In this case we obtain

$$U_{\text{D}}^{\text{o}} = \frac{\epsilon_{\perp} \sqrt{\epsilon_{\perp}}}{2} \frac{\pi^2}{15} \frac{(k_{\text{B}} T)^4}{(\hbar c)^3} = U_{\text{BB}}^{\text{s}} \epsilon_{\perp} \sqrt{\epsilon_{\perp}}, \quad (3.14)$$

$$U_{\text{D}}^{\text{e}} = \frac{\epsilon_{\parallel} \sqrt{\epsilon_{\perp}}}{2} \frac{\pi^2}{15} \frac{(k_{\text{B}} T)^4}{(\hbar c)^3} = U_{\text{BB}}^{\text{p}} \epsilon_{\parallel} \sqrt{\epsilon_{\perp}}. \quad (3.15)$$

Therefore, when $\epsilon_{\perp} = \epsilon_{\parallel} = 1$ we recover the classical BB result. The relations between the internal energy, the free energy and the entropy have the familiar forms

$$F_{\text{D}}^{\text{o/e}} = -\frac{1}{3} U_{\text{D}}^{\text{o/e}} \quad \text{and} \quad S_{\text{D}}^{\text{o/e}} = \frac{4}{3} \frac{U_{\text{D}}^{\text{o/e}}}{T}. \quad (3.16)$$

Note that these relations are the same as for a usual BB be-

cause the DOS of the field inside a dielectric uniaxial medium is proportional to ω^2 .

On the contrary, in type I and type II HMs we have seen that the DOS of the EMs is linear in ω as in a 2-dimensional photon gas in vacuum. It follows that the relations between the thermodynamic properties of the photon gas are radically different in that case. Indeed, we obtain (assuming no frequency dependence of k_{\max})

$$\begin{aligned}
 U_{\text{II}}^e &= \int_0^\infty D_{\text{II}}^e \mathcal{U} d\omega = \int_0^\infty \frac{\omega}{\pi^2 c^2} \frac{\epsilon_{\parallel}}{2} k_{\parallel, \max} \frac{\hbar \omega}{e^{\frac{\hbar \omega}{k_B T}} - 1} d\omega \\
 &= \frac{\epsilon_{\parallel}}{2\pi^2} k_{\parallel, \max} \frac{(k_B T)^3}{(\hbar c)^2} \int_0^\infty \frac{\Omega^2}{e^\Omega - 1} d\Omega \\
 &= \epsilon_{\parallel} \frac{\zeta(3)}{\pi^2} k_{\parallel, \max} \frac{(k_B T)^3}{(\hbar c)^2},
 \end{aligned} \tag{3.17}$$

$$\begin{aligned}
 U_{\text{I}}^e &= |U_{\text{II}}^e| - |U_{\text{D}}^e| \\
 &= |\epsilon_{\parallel}| \frac{\zeta(3)}{\pi^2} k_{\parallel, \max} \frac{(k_B T)^3}{(\hbar c)^2} - \frac{|\epsilon_{\parallel}| \sqrt{|\epsilon_{\perp}|}}{2} \frac{\pi^2}{15} \frac{(k_B T)^4}{(\hbar c)^3}
 \end{aligned} \tag{3.18}$$

and with $k_{\parallel, \max} \gg \frac{\omega}{c} \sqrt{|\epsilon_{\perp}|}$ ($k_{\perp, \max} \gg \frac{\omega}{c} \sqrt{|\epsilon_{\parallel}|}$) and $k_{\parallel, \max} \gg \frac{k_B T}{\hbar c} \sqrt{|\epsilon_{\perp}|}$ approximately

$$\begin{aligned}
 U_{\text{I}}^e &\approx U_{\text{II}}^e = |\epsilon_{\parallel}| \frac{\zeta(3)}{\pi^2} k_{\parallel, \max} \frac{(k_B T)^3}{(\hbar c)^2} \\
 &\approx \sqrt{|\epsilon_{\parallel} \epsilon_{\perp}|} \frac{\zeta(3)}{\pi^2} k_{\perp, \max} \frac{(k_B T)^3}{(\hbar c)^2}
 \end{aligned} \tag{3.19}$$

The zeta function value is $\zeta(3) \approx 1.202$. Furthermore, we find

$$F_{\text{I/II}}^e \approx -\frac{1}{2}U_{\text{I/II}}^e \quad \text{and} \quad S_{\text{I/II}}^e \approx \frac{3}{2}\frac{U_{\text{I/II}}^e}{T}. \quad (3.20)$$

Hence, U and F are proportional to T^3 and not anymore to T^4 . S is proportional to T^2 and not T^3 . This result is a direct consequence of the linear dependence of the electromagnetic DOS inside HMs with respect to ω .

Naturally, for the OMs we find

$$U_{\text{I}}^o = U_{\text{D}}^o \quad \text{and} \quad U_{\text{II}}^o = 0. \quad (3.21)$$

Note that for type II HMs the internal energy of the OMs is zero, since there are no OMs in such a material. The internal energy of the OMs in a type I HM is just the same as in a dielectric uniaxial medium. Hence, the relations between the thermodynamic potentials are the same as in a dielectric uniaxial medium. However, in typical HMs the maximal wavevector is much larger than the vacuum wavevector $k_{\text{max}} \gg \frac{\omega}{c}$ making the material properties dominated by EMs.

Another consequence of the linearity of the DOS with respect to ω inside a HM is a spectral shift of Wien's frequency ω_{max} (resp. wavelength λ_{max}) at which the energy distribution function has its maximum. For both type I and type II HMs we find after a straightforward analysis of the integrand in (3.17) that this

maximum is reached when (again assuming large k_{\max})

$$\frac{\hbar\omega_{\max, \text{HM}}}{k_{\text{B}}T} = \Omega_{\max, \text{HM}} \approx 1.595 \quad \text{or} \quad \frac{2\pi l_c}{\lambda_{\max, \text{HM}}} \approx 3.921 \quad (3.22)$$

whereas for a usual BB $\frac{\hbar\omega_{\max, \text{BB}}}{k_{\text{B}}T} \approx 2.821$ and $\frac{2\pi l_c}{\lambda_{\max, \text{BB}}} \approx 4.965$. Hence, we see that Wien's frequency is shifted toward smaller values and the vacuum wavelength to larger values.

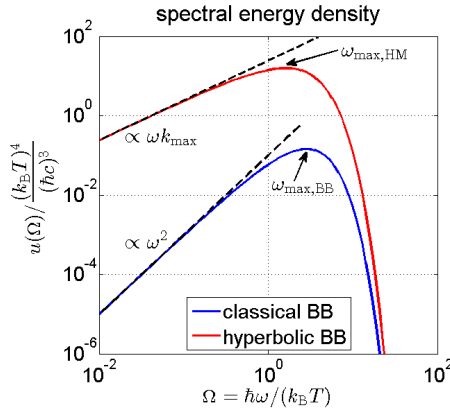


Figure 3.1: Comparison of the spectral energy density $u = u^o + u^e$ of a classical blackbody (BB) vs. a “hyperbolic blackbody”, assuming $|\epsilon_{\perp}\epsilon_{\parallel}| = 1$, $k_{\perp, \max} = \frac{\pi}{\Lambda}$ with $\Lambda = 50$ nm and $T = 300$ K. The hyperbolic BB energy density is completely dominated by extraordinary modes. The dashed straight lines show the asymptotic behavior in ω and ω^2 of the hyperbolic and classical BB spectrum. The arrows indicate Wien's frequencies ω_{\max} in both cases. [From Ref. [67], Copyright 2015 American Physical Society.]

In Fig. 3.1 the spectral energy densities $u(\omega) = D(\omega)\mathcal{U}(\omega, T)$ of a “classical” BB, as derived by Planck, and of an ideal HM (“hyperbolic blackbody”) are plotted. First, with reasonable assumptions the hyperbolic BB exhibits an orders of magnitude larger thermal energy density. How many orders depends on k_{\max} . The larger k_{\max} the larger $u(\omega)$. Second, at small frequencies where the quantization of light is irrelevant ($\hbar\omega \ll k_{\text{B}}T$), and thus the energy per mode $\mathcal{U}(\omega, T) \approx k_{\text{B}}T$, we see the linear vs. quadratic frequency dependence of the DOS. Once the quantization becomes significant ($\hbar\omega \gg k_{\text{B}}T$), $\mathcal{U}(\omega, T)$ and the energy density decline exponentially. Third, we see that indeed the frequency at which u is maximal is shifted towards smaller values for the hyperbolic BB.

Noticing the spectral properties, the temperature dependences of the total energy densities are easy to understand. The amplitude of the spectral energy density scales $\propto \mathcal{U}(\omega, T) \propto T$ at smaller frequencies. Then, the Bose–Einstein term $\mathcal{U}(\omega, T)$ introduces a (smooth) spectral cutoff, or in other words an effective integration limit, with a cutoff frequency $\propto T$. If the integration limit shifts $\propto T$ the integral of a linear function scales with T^2 (hyperbolic BB), of a square function with T^3 (classical BB). Together with the linearly scaling amplitude (at smaller frequencies) we get the T^3 vs. T^4 dependences.

It is now interesting to compare the internal energy of the EMs in a HM with that of a classical BB. From expressions (3.1) and

(3.19) we immediately get

$$\frac{U_{1/\Pi}^e}{U_{\text{BB}}^p} \approx \sqrt{|\epsilon_{\parallel}\epsilon_{\perp}|} \frac{30}{\pi^4} \zeta(3) k_{\perp,\text{max}} l_c. \quad (3.23)$$

If Λ denotes the unit-cell size of our HM then $k_{\parallel,\text{max}} = \frac{\pi}{\Lambda}$ or $k_{\perp,\text{max}} = \frac{\pi}{\Lambda}$ depending on the concrete structure. However, independent of the structure both maximum wavevectors are related by $k_{\perp,\text{max}} \approx \sqrt{\left|\frac{\epsilon_{\parallel}}{\epsilon_{\perp}}\right|} k_{\parallel,\text{max}}$ so that we generally have

$$\frac{U_{1/\Pi}^e}{U_{\text{BB}}^p} \propto \frac{l_c}{\Lambda}. \quad (3.24)$$

At a temperature of 300 K the coherence length is $l_c \approx 7.6 \mu\text{m}$, while the period of realistic HMMs is typically larger than $\Lambda \approx 10 \text{ nm}$ (see Refs. [50, 51] for instance). In natural HMs [47] the main length scale is determined by the interatomic spacing, i. e. $\Lambda \approx 1 \text{ \AA}$. Albeit, nonlocality can increase the length scale at which HMs exhibit metallic properties (in one or two directions) to the nanometer range [86, 87]. Nonlocality is a spatial dispersion manifesting itself in a \mathbf{k} -dependent permittivity ϵ [87] which approaches the vacuum value as the spatial variation k increases. Hence, the internal energy of thermal radiation inside a HM can be 3 ($\Lambda \approx 10 \text{ nm}$) to 5 ($\Lambda \approx 1 \text{ \AA}$) orders of magnitude larger than that of a perfect BB. The same is of course also true for the free energy and the entropy. This result suggests that the radiative heat flux inside a HM is dramatically enhanced compared to that of a classical BB.

3.1.2 Power flow

The expressions for the mean Poynting vector inside a dielectric uniaxial material are

$$\begin{aligned}\Phi_{\text{D}}^{\circ} &= \int_0^{\infty} \frac{\epsilon_{\perp}}{8\pi^2} \frac{\omega^2}{c^2} \mathcal{U}(\omega, T) d\omega \\ &= \frac{\epsilon_{\perp}}{2} \frac{\pi^2}{60} \frac{(k_{\text{B}}T)^4}{\hbar^3 c^2} = \frac{\epsilon_{\perp}}{2} \sigma_{\text{B}} T^4 = \Phi_{\text{BB}}^{\text{s}} \epsilon_{\perp},\end{aligned}\tag{3.25}$$

$$\begin{aligned}\Phi_{\text{D}}^{\text{e}} &= \int_0^{\infty} \frac{\epsilon_{\parallel}}{8\pi^2} \frac{\omega^2}{c^2} \mathcal{U}(\omega, T) d\omega \\ &= \frac{\epsilon_{\parallel}}{2} \frac{\pi^2}{60} \frac{(k_{\text{B}}T)^4}{\hbar^3 c^2} = \frac{\epsilon_{\parallel}}{2} \sigma_{\text{B}} T^4 = \Phi_{\text{BB}}^{\text{p}} \epsilon_{\parallel}.\end{aligned}\tag{3.26}$$

The underlying setup, depicted in Fig. 2.4a, is a halfspace at temperature T emitting into a second, identical halfspace at 0 K.

When $\epsilon_{\perp} = \epsilon_{\parallel} = 1$ we find again the usual BB result, i. e. Stefan–Boltzmann’s law. On the other hand, inside a uniaxial material (as inside an isotropic material) with $\epsilon_{\perp} > 1$ and $\epsilon_{\parallel} > 1$ the radiative heat flux is larger than the BB value, which is a well-known fact [88, 89].

In the case of HMs these results radically change. Before seeing this, let us first consider the OMs. For Φ_{I}° we find of course the same relation as for the dielectric anisotropic material $\Phi_{\text{I}}^{\circ} = \Phi_{\text{D}}^{\circ}$, whereas as a consequence that there do not exist any propagating OMs in a type II HM we find $\Phi_{\text{II}}^{\circ} = 0$.

On the contrary, for the EMs we find (assuming no frequency

dependence of $k_{\perp,\max}$)

$$\begin{aligned}\Phi_{\text{I}}^{\text{e}} &= \int_0^{\infty} \frac{k_{\perp,\max}^2}{8\pi^2} \mathcal{U}(\omega, T) \, d\omega \\ &= \frac{k_{\perp,\max}^2}{8\pi^2} \frac{(k_{\text{B}}T)^2}{\hbar} \int_0^{\infty} \frac{\Omega}{e^{\Omega} - 1} \, d\Omega = \frac{1}{48} k_{\perp,\max}^2 \frac{(k_{\text{B}}T)^2}{\hbar},\end{aligned}\quad (3.27)$$

$$\begin{aligned}\Phi_{\text{II}}^{\text{e}} &= \Phi_{\text{I}}^{\text{e}} - \Phi_{\text{D}}^{\text{e}} = \int_0^{\infty} \frac{1}{8\pi^2} \left(k_{\perp,\max}^2 - \frac{\omega^2}{c^2} \epsilon_{\parallel} \right) \mathcal{U}(\omega, T) \, d\omega \\ &= \frac{1}{48} k_{\perp,\max}^2 \frac{(k_{\text{B}}T)^2}{\hbar} - \frac{\epsilon_{\parallel}}{2} \frac{\pi^2}{60} \frac{(k_{\text{B}}T)^4}{\hbar^3 c^2}.\end{aligned}\quad (3.28)$$

Hence, when $k_{\perp,\max} \gg \frac{k_{\text{B}}T}{\hbar c} \sqrt{|\epsilon_{\parallel}|}$ we have

$$\Phi_{\text{II}}^{\text{e}} \approx \Phi_{\text{I}}^{\text{e}} = \frac{1}{48} k_{\perp,\max}^2 \frac{(k_{\text{B}}T)^2}{\hbar} \approx \frac{1}{48} \left| \frac{\epsilon_{\parallel}}{\epsilon_{\perp}} \right| k_{\parallel,\max}^2 \frac{(k_{\text{B}}T)^2}{\hbar}. \quad (3.29)$$

In this case, we see that the heat flux is proportional to T^2 and not anymore to T^4 as in the ‘‘classical’’ Stefan–Boltzmann law. The total and spectral heat flux are also proportional to $k_{\perp,\max}^2$, which is due to the fact that the heat flux scales like the area of the projection of the isofrequency surface in k -space [80] (see Appendix A.2), or like the number of transversal modes [22, 79], respectively. Note that the above limit is also the upper limit of heat radiation between two hyperbolic materials separated by a vacuum gap [18], when we assume the cutoff k_{\max} is caused by the finite gap size l , $k_{\max} \propto \frac{1}{l}$, and not by the (meta)material properties.

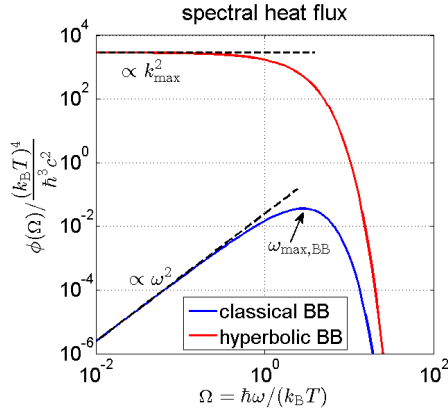


Figure 3.2: Comparison of the spectral heat flux $\phi = \phi^o + \phi^e$ of a classical blackbody (BB) vs. a “hyperbolic blackbody”, assuming $k_{\perp, \max} = \frac{\pi}{\Lambda}$ with $\Lambda = 50$ nm and $T = 300$ K. The hyperbolic BB heat flux is completely dominated by extraordinary modes. The dashed straight lines show the asymptotic behavior in 1 and ω^2 of the hyperbolic and classical BB spectrum.

In Fig. 3.2 we plot the spectral heat flux of a classical and a hyperbolic BB. The BB heat flux ϕ_{BB} resembles u_{BB} because $\phi_{\text{BB}} = \frac{c}{4} u_{\text{BB}}$. The hyperbolic BB heat flux $\phi_{\text{I/II}}$ is different from its energy density $u_{\text{I/II}}$. Again, with reasonable assumptions the hyperbolic BB exhibits an orders of magnitude larger thermal power flow. The difference between hyperbolic and classic BB is even larger than for the energy density and the dependence on k_{\max} stronger. At small frequencies where the quantization of light is irrelevant ($\hbar\omega \ll k_B T$) we see that $\phi_{\text{I/II}}$ is constant

over frequency whereas the classical BB shows the quadratic frequency dependence. Once the quantization becomes significant ($\hbar\omega \gg k_B T$), $\mathcal{U}(\omega, T)$ and the heat flux decline exponentially. The frequency at which ϕ is maximal is 0 for the hyperbolic BB, so shifted to an even smaller frequency than for u .

The T^4 temperature dependence of the total heat flux for the classical BB can be understood identically to its energy density. The T^2 dependence for the hyperbolic BB follows the same explanation. The integration limit shifts $\propto T$ and the integral of a constant function thus scales with T . Together with the linearly scaling amplitude we get the T^2 dependence.

Comparing the radiative heat fluxes, we find

$$\frac{\Phi_{1/\Pi}^e}{\Phi_{\text{BB}}^p} \approx \frac{5}{2\pi^2} (k_{\perp, \text{max}} l_c)^2 \propto \left(\frac{l_c}{\Lambda} \right)^2. \quad (3.30)$$

Thus, the normalized heat flux is proportional to $(k_{\perp, \text{max}} l_c)^2$. We have seen before in Eq. (3.23) that the ratio of the energy density of a HM and that of a BB is only linear in $k_{\perp, \text{max}} l_c$. This is quite astonishing, since for HMMs with a unit cell size Λ of 10 nm and for natural HMs with a unit-cell size $\Lambda \approx 1 \text{ \AA}$ we can now expect a hyperbolic BB heat flux 6 to 10 orders of magnitude larger than that of a usual BB at $T = 300 \text{ K}$. At cryogenic temperatures l_c becomes very large so that this ratio can become even much larger.

To summarize, Table 3.1 contrasts the important thermal radi-

ation properties of a classical BB and a hyperbolic BB.

	classical blackbody	“hyperbolic blackbody”
density of states $D(\omega)$	$\propto \left(\frac{\omega}{c}\right)^2$	$\propto \frac{\omega}{c} k_{\max}$
spectral heat flux $\phi(\omega)$	$\propto \left(\frac{\omega}{c}\right)^2 \mathcal{U}(\omega, T)$	$\propto k_{\perp, \max}^2 \mathcal{U}(\omega, T)$
energy density U	$\propto T^4$	$\propto k_{\max} T^3$
heat flux Φ	$\propto T^4$	$\propto k_{\perp, \max}^2 T^2$
$\frac{\hbar\omega_{\max}}{k_B T}$	≈ 2.821	≈ 1.595
$\frac{2\pi l_c}{\lambda_{\max}}$	≈ 4.965	≈ 3.921
entropy S	$= \frac{4}{3} \frac{U}{T} \propto T^3$	$\approx \frac{3}{2} \frac{U}{T} \propto k_{\max} T^2$

Table 3.1: Comparison of the thermal radiation properties of a classical blackbody (BB) vs. a “hyperbolic blackbody”. The classical BB has the properties described by Max Planck et al. The hyperbolic BB is an idealized (lossless, nondispersive) hyperbolic medium.

For dielectric anisotropic media we have seen that the thermodynamic properties of the photon gas inside such media are very similar to that of a classical BB. On the other hand, when these media are hyperbolic, the spectral energy distribution of radiation radically differs from that predicted by Planck and is shifted towards frequencies smaller than Wien’s frequency. We have also shown that in contrast to Stefan–Boltzmann’s law, the heat flux

radiated by these media depends quadratically on their temperature. Nevertheless, the magnitude of heat flux carried by these media can be several orders of magnitude larger than the flux radiated by a classical BB.

For completeness let us mention that dielectric and metallic materials also possess a k_{\max} beyond which they cannot be polarized and alter their properties (due to nonlocality they become vacuum-like [86]). But these k_{\max} correspond to atomic distances and have no effect on thermal radiation. Because of the Bose–Einstein cutoff the radiation is limited to a maximal frequency with a vacuum wavenumber corresponding to approximately Wien’s wavelength $\lambda_{\max, \text{BB}}$. So for wavenumbers on the scale of k_{\max} not to be spectrally cut off, the temperature has to be well above several 10 000 K. Under such extreme temperatures our assumption of a solid material is not justified any more and a different approach is needed. HMs, on the other hand, feature high- k modes even at low frequencies – below the Bose–Einstein cutoff – and hence, the radiation properties depend on k_{\max} .

3.2 Thermal radiation inside dispersive hyperbolic media

Before we look at the properties of thermal radiation inside more realistic, dispersive HMs, a few words should be mentioned on

anomalous dispersion.

The density of ordinary modes in the case $\epsilon_{\perp} > 0$ has been derived in Eq. (2.109). During the derivation one has to choose whether to take the positive or negative (real) values for k_{\parallel}° for the forward “propagating” or outgoing waves ($k_{\parallel}^{\circ} \in [0, \frac{\omega}{c}\sqrt{\epsilon_{\perp}}]$ or $k_{\parallel}^{\circ} \in [0, -\frac{\omega}{c}\sqrt{\epsilon_{\perp}}]$), as discussed in Section 2.3.1.

From the group velocity in \parallel -direction

$$\begin{aligned} c_{\text{g},\parallel}^{\circ}(\omega, k_{\parallel}^{\circ}) &= \frac{\partial\omega}{\partial k_{\parallel}^{\circ}} = \left(\frac{\partial k_{\parallel}^{\circ}}{\partial\omega}\right)^{-1} = \left(\frac{\partial}{\partial\omega}\sqrt{\frac{\omega^2}{c^2}\epsilon_{\perp} - k_{\perp}^2}\right)^{-1} \\ &= \frac{2\sqrt{\frac{\omega^2}{c^2}\epsilon_{\perp} - k_{\perp}^2}}{\frac{1}{c^2}\frac{d(\omega^2\epsilon_{\perp})}{d\omega}} = \frac{c^2 k_{\parallel}^{\circ}}{\omega\left(\epsilon_{\perp} + \frac{\omega}{2}\frac{d\epsilon_{\perp}}{d\omega}\right)}, \end{aligned} \quad (3.31)$$

we find that for a plane wave $\propto e^{ik_{\parallel}^{\circ}x_{\parallel}}$ to propagate in positive x_{\parallel} -direction, so $c_{\text{g},\parallel}^{\circ} > 0$, the sign of k_{\parallel}° must be chosen according to

$$\text{sgn}(k_{\parallel}^{\circ}) = \text{sgn}\left(\epsilon_{\perp} + \frac{\omega}{2}\frac{d\epsilon_{\perp}}{d\omega}\right). \quad (3.32)$$

On the other hand, starting with a plane ordinary wave with

$$\mathbf{E}^{\circ}(\omega, \mathbf{k}^{\circ}) = \hat{E}_0 \mathbf{a}_s e^{i\mathbf{k}_{\perp} \cdot \mathbf{x}_{\perp}} e^{ik_{\parallel}^{\circ}x_{\parallel}} \quad (3.33)$$

and

$$\begin{aligned}\mathbf{H}^o(\omega, \mathbf{k}^o) &= \frac{1}{i\omega\mu_0} \nabla \times \mathbf{E}^o = \frac{\hat{E}_0}{\omega\mu_0} \mathbf{k}^o \times \mathbf{a}_s e^{i\mathbf{k}_\perp \cdot \mathbf{x}_\perp} e^{ik_\parallel^o x_\parallel} \\ &= -\frac{\hat{E}_0}{\omega\mu_0} k_\parallel^o \mathbf{a}_p^o e^{i\mathbf{k}_\perp \cdot \mathbf{x}_\perp} e^{ik_\parallel^o x_\parallel}\end{aligned}\quad (3.34)$$

the Poynting vector is

$$\begin{aligned}\mathbf{S}^o(\omega, \mathbf{k}^o) &= \frac{1}{2} \Re(\mathbf{E}^o \times \mathbf{H}^{o*}) \\ &= \Re\left(-\frac{|\hat{E}_0|^2}{2\omega\mu_0} k_\parallel^{o*} \mathbf{a}_s \times \mathbf{a}_p^{o*} e^{-2\Im(k_\parallel^o) x_\parallel}\right) \\ &= \Re(\mathbf{k}^{o*}) \frac{|\hat{E}_0|^2}{2\omega\mu_0} e^{-2\Im(k_\parallel^o) x_\parallel}.\end{aligned}\quad (3.35)$$

Now, a wave $\propto e^{ik_\parallel^o x_\parallel}$ propagating in positive x_\parallel -direction must possess the property $S_\parallel^o > 0$ and the sign of k_\parallel^o is chosen by

$$\Re(k_\parallel^o) = \Re(k_\parallel^{o*}) > 0. \quad (3.36)$$

When $\epsilon_\perp + \frac{\omega}{2} \frac{d\epsilon_\perp}{d\omega} > 0$, particularly in the case of normal dispersion where $\frac{d\epsilon_\perp}{d\omega} > 0$, the results of both approaches are identical and the positive, real k_\parallel^o are chosen. However, for anomalous dispersion ($\frac{d\epsilon_\perp}{d\omega} < 0$) the sign can be unclear and the DOS of ordinary modes, indicated in Eq. (2.109), can become negative. Related phenomena that can occur in absorptive or gain media showing anomalous dispersion are superluminal and negative group velocities [90, 91]. The apparently controversy can

be resolved by noticing that anomalous dispersion is accompanied by absorption [14], typically a Drude–Lorentz peak, making losses non-negligible anymore. The theory must be adjusted to take into account the losses. When gain is used to compensate for the losses [90] non-thermal energy is supplied to the system, again making it necessary to adjust the theory. An analysis of extraordinary modes reveals similar features. We refrain from analyzing absorptive HMs with anomalous dispersion and focus our attention on lossless HMs with normal dispersion.

To analyze more realistic systems we select an exemplary HM and first assume both permittivity components to be describable by a single Drude–Lorentz resonance [44, 92]:

$$\begin{aligned}\epsilon_{\parallel/\perp}(\omega) &= \epsilon_{\infty,\parallel/\perp} \frac{\omega_{\text{LO},\parallel/\perp}^2 - \omega^2 - i\omega_{\text{col},\parallel/\perp}\omega}{\omega_{\text{TO},\parallel/\perp}^2 - \omega^2 - i\omega_{\text{col},\parallel/\perp}\omega} \\ &= \epsilon_{\infty,\parallel/\perp} + \epsilon_{\infty,\parallel/\perp} \frac{\omega_{\text{LO},\parallel/\perp}^2 - \omega_{\text{TO},\parallel/\perp}^2}{\omega_{\text{TO},\parallel/\perp}^2 - \omega^2 - i\omega_{\text{col},\parallel/\perp}\omega}.\end{aligned}\tag{3.37}$$

The Drude–Lorentz model is very general and resembles the Drude model by setting $\omega_{\text{TO}} = 0$ [44]. The permittivity of most materials can be described by a Drude–Lorentz model, at least in limited frequency ranges. A hyperbolic metamaterial consisting of a Drude–Lorentz medium and a simple dielectric (with constant permittivity) has effective Drude–Lorentz permittivities like (3.37) because the Drude–Lorentz characteristic is preserved under the mixing rule of effective medium theory (EMT).

Appendix C.1 provides the proof and the formulas.

We restrict our discussion to single resonances because multiple ones have no influence on the fundamental properties, only repeat them at different frequencies. The derivatives needed for the energy density calculations are

$$\begin{aligned}
 \frac{d\epsilon_{\parallel/\perp}}{d\omega} &= \epsilon_{\infty,\parallel/\perp} \frac{\left(\omega_{\text{LO},\parallel/\perp}^2 - \omega_{\text{TO},\parallel/\perp}^2\right) \left(2\omega + i\omega_{\text{col},\parallel/\perp}\right)}{\left(\omega_{\text{TO},\parallel/\perp}^2 - \omega^2 - i\omega_{\text{col},\parallel/\perp}\omega\right)^2} \\
 &= \frac{\left(\epsilon_{\parallel/\perp} - \epsilon_{\infty,\parallel/\perp}\right) \left(2\omega + i\omega_{\text{col},\parallel/\perp}\right)}{\omega_{\text{TO},\parallel/\perp}^2 - \omega^2 - i\omega_{\text{col},\parallel/\perp}\omega} \\
 &= \frac{\left(\epsilon_{\parallel/\perp} - \epsilon_{\infty,\parallel/\perp}\right)^2 \left(2\omega + i\omega_{\text{col},\parallel/\perp}\right)}{\epsilon_{\infty,\parallel/\perp} \left(\omega_{\text{LO},\parallel/\perp}^2 - \omega_{\text{TO},\parallel/\perp}^2\right)}.
 \end{aligned} \tag{3.38}$$

Fig. 3.3 shows the permittivities of the example under consideration. The corresponding parameters are $\epsilon_{\infty,\parallel} = 8$, $\omega_{\text{LO},\parallel} = 141 \cdot 10^{12} \text{ s}^{-1}$, $\omega_{\text{TO},\parallel} = 115.8 \cdot 10^{12} \text{ s}^{-1}$, $\omega_{\text{col},\parallel} = 1.52 \cdot 10^{12} \text{ s}^{-1}$, $\epsilon_{\infty,\perp} = 10.7$, $\omega_{\text{LO},\perp} = 115.8 \cdot 10^{12} \text{ s}^{-1}$, $\omega_{\text{TO},\perp} = 106 \cdot 10^{12} \text{ s}^{-1}$ and $\omega_{\text{col},\perp} = 1.52 \cdot 10^{12} \text{ s}^{-1}$. Without losses ω_{TO} is a pole of the permittivity. Losses ($\omega_{\text{col}} > 0$) smear out this pole. The real part of the permittivity still changes its sign from + to - in a pole-like manner, while the imaginary part features a peak around ω_{TO} . ω_{LO} is a zero, respectively the frequency at which the real part becomes positive again.

This exemplary material corresponds to a layered metamaterial consisting of gallium nitride (GaN) and germanium (Ge) with

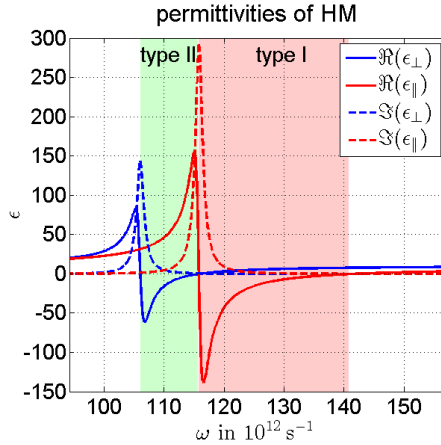


Figure 3.3: Effective permittivities of layered GaN–Ge hyperbolic metamaterial. A filling factor of 50% is assumed. Both permittivities, parallel and orthogonal to the metamaterial’s optical axis, feature a Drude–Lorentz resonance. The spectral ranges with type I or II hyperbolic dispersion are highlighted in color.

50% filling factor. The optical response of GaN is in the infrared dominated by optical phonons so that the relative permittivity of GaN can be described by a Drude–Lorentz model with $\epsilon_{\infty}^{\text{GaN}} = 5.35$, $\omega_{\text{LO}}^{\text{GaN}} = 141 \cdot 10^{12} \text{ s}^{-1}$, $\omega_{\text{TO}}^{\text{GaN}} = 106 \cdot 10^{12} \text{ s}^{-1}$, $\omega_{\text{col}}^{\text{GaN}} = 1.52 \cdot 10^{12} \text{ s}^{-1}$ [45]. It is important to notice that inside the reststrahlen band of GaN ($\omega_{\text{TO}} < \omega < \omega_{\text{LO}}$) the (real part of the) permittivity is negative. The permittivity of Ge is in the infrared to very good approximation dispersionless having a value of $\epsilon_{\text{Ge}} = 16$ [93]. The 50% filling factor ensures that type I and type II hyperbolic frequency ranges are adjacent to each

other (cf. Fig. 3.3) and not separated by a dielectric or metallic region in between. The optical axis of the effective HM is perpendicular to the layer interfaces. Both materials as well as the HM are nonmagnetic.

Our HM has one spectral range with type I and one with type II hyperbolic dispersion, highlighted in color in Fig. 3.3. Frequencies with anomalous dispersion at which, moreover, the losses are large ($\Im(\epsilon)$ even larger than $|\Re(\epsilon)|$) are not considered in the calculations. At the remaining frequencies the small imaginary part of the permittivities is ignored.

To assess the effect of the dispersion we compare the dispersive HM with two nondispersive HMs. A type I HM with $\epsilon_{\perp} = 5.41$, $\epsilon_{\parallel} = -25.13$ and a type II HM with $\epsilon_{\perp} = -18.45$, $\epsilon_{\parallel} = 66.19$. These are the mean values of the dispersive permittivities in the type I hyperbolic spectral range or type II hyperbolic spectral range, respectively. In all cases, the maximal wavevector is $k_{\parallel, \max} = \frac{\pi}{50 \text{ nm}}$, representing a layered structure with a 50 nm periodicity. $k_{\perp, \max}$ is calculated via Eq. (1.9) for each HM individually.

In the following, we will normalize the quantities under consideration to the respective classical BB values. The classical BB is well understood and its properties have been discussed in the previous section. The idea is to see how differently the HM behaves w. r. t. the BB. Assuming no temperature dependence of the optical properties, the normalized spectral properties are even independent of T because the T dependence cancels out

during the normalization. Whenever we simply talk about black-body we of course mean the classical BB.

Whenever the integration over frequency cannot be performed analytically we perform it numerically in MATLAB (by Math-Works).

3.2.1 Energy density and density of states

As we have seen in Section 2.5.1, dispersion adds further terms to the DOS. E. g. for OMs the DOS is

$$D_D^o(\omega) = D_I^o(\omega) = \frac{\omega^2}{\pi^2 c^3} \frac{\epsilon_{\perp} \sqrt{\epsilon_{\perp}}}{2} + \frac{\omega^2}{\pi^2 c^3} \frac{\sqrt{\epsilon_{\perp}}}{2} \frac{\omega}{2} \frac{d\epsilon_{\perp}}{d\omega}. \quad (3.39)$$

So we cannot only distinguish contributions from ordinary and extraordinary modes but also “nondispersive” (only implicitly dispersive terms in DOS without $\frac{d\epsilon}{d\omega}$) and “dispersive” (explicitly dispersive $\frac{d\epsilon}{d\omega}$ terms) contributions. The nondispersive contributions are still subject to permittivity changes over frequency, so strictly speaking also (implicitly) dispersive. “Nondispersive contributions” should be viewed as just a name for the DOS parts without $\frac{d\epsilon}{d\omega}$.

The DOS for all the different uniaxial materials can be found in Section 2.5.1. We just want to emphasize that the DOS of HMs

has a dispersive extraordinary contribution

$$\begin{aligned}
 D_{\text{I}}^{\text{e}} \approx D_{\text{II}}^{\text{e}} &\approx \frac{k_{\parallel, \text{max}}^3}{12\pi^2} \left| \frac{\epsilon_{\parallel}}{\epsilon_{\perp}} \right| \left(\frac{1}{|\epsilon_{\parallel}|} \frac{d\epsilon_{\parallel}}{d\omega} + \frac{1}{|\epsilon_{\perp}|} \frac{d\epsilon_{\perp}}{d\omega} \right) \\
 &\approx \frac{k_{\perp, \text{max}}^3}{12\pi^2} \sqrt{\left| \frac{\epsilon_{\perp}}{\epsilon_{\parallel}} \right|} \left(\frac{1}{|\epsilon_{\parallel}|} \frac{d\epsilon_{\parallel}}{d\omega} + \frac{1}{|\epsilon_{\perp}|} \frac{d\epsilon_{\perp}}{d\omega} \right), \tag{3.40}
 \end{aligned}$$

which is assumed to dominate the DOS $D_{\text{I}}(\omega)$ and $D_{\text{II}}(\omega)$ because k_{max} is large. Consequently, the total density of states is proportional to k_{max}^3 [59, 60].

Fig. 3.4 illustrates that in the hyperbolic frequency ranges the nondispersive extraordinary DOS contribution is already stronger than the OM contributions. It is also larger than the DOS at non-hyperbolic frequencies. But dispersion further increases the DOS by several orders of magnitude, making the dispersive extraordinary part the dominant one. The approximation (3.40) which takes only this part into account is agreeing very well with the exact calculations. Because k_{max} is so large, the k_{max}^3 proportionality of the dispersive part makes it so much larger than the nondispersive part $\propto k_{\text{max}}$.

The DOS inside the nondispersive HMs is around the mean value of the nondispersive extraordinary contribution inside the dispersive HM in the hyperbolic bands. The DOS inside nondispersive HMs is $\propto \omega$, the (classical) blackbody DOS $\propto \omega^2$, such that the ratio is decreasing with $\propto \frac{1}{\omega}$.

The total thermal energy density U is obtained by multiplying

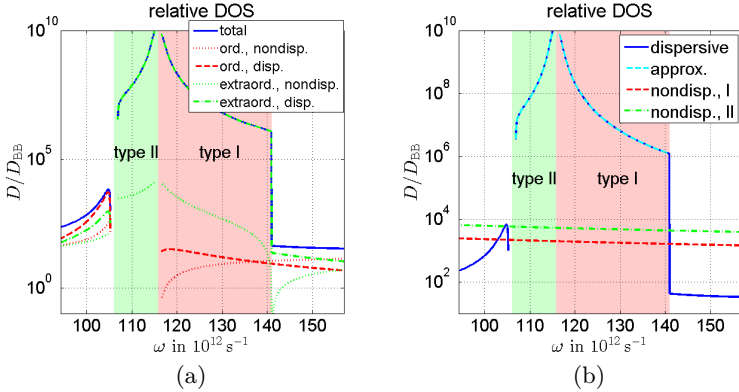


Figure 3.4: Density of states (DOS) D inside exemplary HM, with $k_{\parallel, \text{max}} = \frac{\pi}{50 \text{ nm}}$, normalized to blackbody. (a) shows the contributions of ordinary and extraordinary modes to the DOS inside the dispersive HM. Further, nondispersive and dispersive contributions are distinguished. Although the nondispersive hyperbolic (extraordinary) part already dominates over the ordinary parts dispersion significantly increases the DOS in the hyperbolic bands. (b) compares the three materials: dispersive HM, type I and type II nondispersive HMs. In addition, the approximation (3.40) for the dispersive case is also plotted, agreeing very well with the exact curve. The dispersive HM has a much larger DOS in the hyperbolic bands than the nondispersive HMs.

the DOS by $\mathcal{U}(\omega, T)$ and integrating over frequency. As shown in Fig. 3.5, the thermal energy density is dominated by extraordinary modes, more precisely the dispersive part of them, because

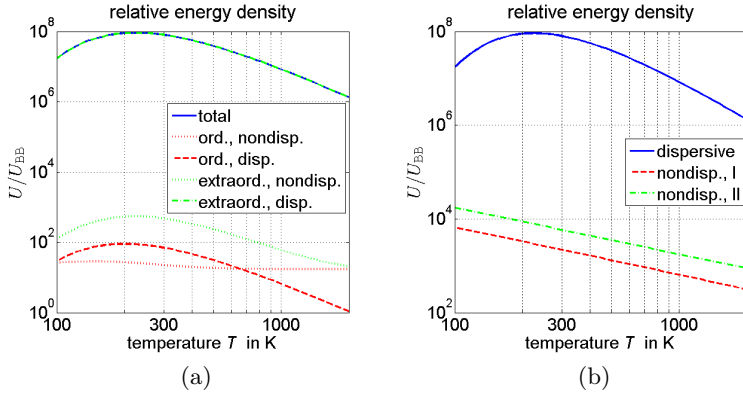


Figure 3.5: Thermal energy density U inside exemplary HM, with $k_{\parallel, \text{max}} = \frac{\pi}{50 \text{ nm}}$, normalized to blackbody for different temperatures. (a) shows the contributions of ordinary and extraordinary modes to the energy density inside the dispersive HM. Further, nondispersive and dispersive contributions are distinguished. The energy density is dominated by the dispersive extraordinary part. (b) compares the three materials: dispersive HM, type I and type II nondispersive HMs. The dispersive HM features an energy density orders of magnitude larger.

the DOS and thus the spectral energy density are much larger in the hyperbolic bands than at other frequencies. Even at high temperatures T at which the BB energy density has its maximum at a significantly larger frequency, where the HM is not hyperbolic anymore, the energy density is still dominated by the dispersive hyperbolic modes.

However, with higher temperatures the increase above the BB

value becomes smaller. The hyperbolic bands are just populated by more photons $\propto \mathcal{U}(\omega, T) \propto T$, whereas the blackbody does not only populate the smaller frequency modes more $\propto T$, but also populates before unpopulated higher frequency modes because the cutoff of the Bose–Einstein statistic $\mathcal{U}(\omega, T)$ shifts, yielding the known T^4 dependence explained in the previous section. The normalized energy density decreases almost $\propto \frac{1}{T^3}$, actually a little bit less fast because the HM not only gains energy due to stronger occupation of hyperbolic modes but also some due to the shifted cutoff.

Towards smaller temperatures the normalized energy density reaches a maximum and decreases afterwards. The decrease is caused by the Bose–Einstein cutoff cutting a part of the hyperbolic region and therefore reducing the enormous amount of hyperbolic energy.

For nondispersive HMs we know the temperature dependence to be $\propto T^3$. The ratio is decreasing $\propto \frac{1}{T}$ as seen in Fig. 3.5b. The nondispersive HMs feature an overall thermal energy density close to the sum of nondispersive parts of the dispersive HM. The extraordinary and ordinary nondispersive parts of energy density inside the dispersive HM are not many orders of magnitude apart. In the hyperbolic regions the EMs possess much more energy than the OMs, but in the dielectric regions both types of modes are contributing similarly and quite much since the permittivities are high. So nondispersive extraordinary modes are not outranking the ordinary ones so much.

3.2.2 Power flow

The radiative heat flux has no $\frac{d\epsilon}{d\omega}$ terms. So dispersion only manifests itself as spectrally dependent optical properties. A simple explanation can be deduced from the formulas in Appendix A.2. The DOS and thus the spectral energy density is proportional to the area of the isofrequency contour divided by the group velocity c_g . Frequency derivatives are part of c_g . In particular, normal dispersion $\frac{d\epsilon}{d\omega} > 0$ decreases c_g and thus increases the DOS. The spectral heat flux is then obtained by multiplying the energy density by c_g (more precisely the \mathbf{c}_g -component in the heat flux direction) [10]. This way, the frequency derivatives cancel out and the heat flux becomes proportional to the (projected) isofrequency area [80, 94].

As in the dispersionless case, the spectral heat flux supported by EMs with hyperbolic dispersion is

$$\phi_{\text{II}}^e(\omega) \approx \phi_{\text{I}}^e(\omega) = \frac{k_{\perp, \text{max}}^2}{8\pi^2} \mathcal{U}(\omega, T) \approx \left| \frac{\epsilon_{\parallel}}{\epsilon_{\perp}} \right| \frac{k_{\parallel, \text{max}}^2}{8\pi^2} \mathcal{U}(\omega, T). \quad (3.41)$$

$k_{\perp, \text{max}}$ generally depends on ω . The respective spectral heat transfer coefficient (sHTC) is

$$\begin{aligned} h_{\text{II}}^e(\omega) \approx h_{\text{I}}^e(\omega) &= \frac{d\phi_{\text{I}}^e}{dT} = \frac{k_{\perp, \text{max}}^2}{8\pi^2} \frac{d\mathcal{U}(\omega, T)}{dT} \\ &\approx \left| \frac{\epsilon_{\parallel}}{\epsilon_{\perp}} \right| \frac{k_{\parallel, \text{max}}^2}{8\pi^2} \frac{d\mathcal{U}(\omega, T)}{dT}. \end{aligned} \quad (3.42)$$

In the previous section we have looked at the heat flux inside HMs and have made the comparison to blackbody radiation. The commonly known properties of BB radiation are for a setup where a black (perfectly absorbing) body thermally emits into free space. The hyperbolic counterpart is a black body emitting into a HM / a free hyperbolic space. (Among non-transmitting, “black” means non-reflecting. To realize perfect optical matching and avoid reflections we assumed the emitting bodies / half-spaces to consist of the same material as the space into which is emitted; cf. Fig. 2.4a.) Alternatively, two black reservoirs, one of which at 0 K, exchanging heat resemble the emission into free space. The reservoir at 0 K basically mirrors a free space.

For real hyperbolic materials a setup of two matched reservoirs of (slightly) different temperatures separated by the HM (cf. Fig. 3.8) is more interesting. The heat flux can be normalized by the temperature difference leaving a quantity characteristic of the heat transport capability of the HM at a mean temperature T . Hence, we now switch from (spectral) heat fluxes to the transfer coefficients sHTC and HTC instead.

The sHTC h inside our exemplary media are shown in Fig. 3.6. In the hyperbolic bands the spectral heat flux is orders of magnitude larger compared to the dielectric bands. Furthermore, in these bands the heat flux is entirely dominated by the extraordinary modes, which exhibit the hyperbolic isofrequency contours. The ordinary modes feature dielectric or metallic behavior and are irrelevant. The approximation (3.42) which takes only the

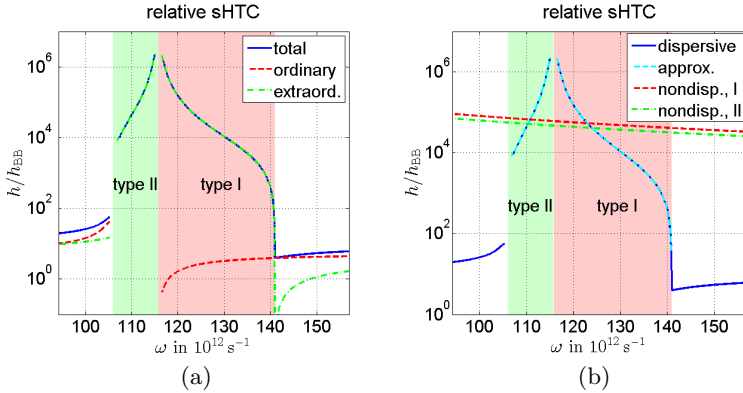


Figure 3.6: Spectral heat transfer coefficient (sHTC) h inside exemplary HM, with $k_{\parallel, \text{max}} = \frac{\pi}{50 \text{ nm}}$, normalized to blackbody. (a) shows the contributions of ordinary and extraordinary modes to the heat flux inside the dispersive HM. In the hyperbolic bands the heat flux is dominated by extraordinary hyperbolic modes. (b) compares the three materials: dispersive HM, type I and type II nondispersive HMs. In addition, the approximation (3.42) for the dispersive case is also plotted, agreeing very well with the exact curve. The nondispersive HMs feature a heat flux close to the mean value of the dispersive HM in the hyperbolic bands.

EMs into account is agreeing very well with the exact calculations.

The heat flux inside the nondispersive HMs is around the mean value inside the dispersive HM in the hyperbolic bands. The spectral heat flux inside nondispersive HMs is $\propto \mathcal{U}(\omega, T)$, the BB heat flux $\propto \omega^2 \mathcal{U}(\omega, T)$, such that the ratio is decreasing

with $\propto \frac{1}{\omega^2}$. Same holds for the sHTC.

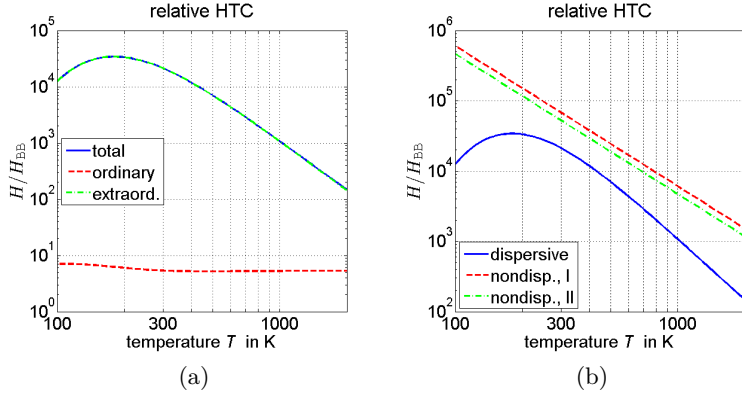


Figure 3.7: Heat transfer coefficient (HTC) H inside exemplary HM, with $k_{\parallel, \text{max}} = \frac{\pi}{50 \text{ nm}}$, normalized to blackbody for different temperatures. (a) shows the contributions of ordinary and extraordinary modes to the heat flux inside the dispersive HM. The heat flux is dominated by extraordinary modes because they exhibit hyperbolic dispersion at which the heat flux is orders of magnitude larger than in non-hyperbolic frequency ranges. (b) compares the three materials: dispersive HM, type I and type II nondispersive HMs. The nondispersive HMs feature a larger heat flux because they are hyperbolic throughout the whole spectral region.

Since the spectral heat flux in the hyperbolic bands is much larger than at other frequencies, the total heat flux H is expected to be dominated by extraordinary modes. Fig. 3.7 confirms this conclusion. Even at high temperatures at which the

BB heat flux has its maximum at a significantly larger frequency, where the HM is not hyperbolic anymore, the heat flux is still dominated by the hyperbolic modes. This is because the spectral heat flux in the hyperbolic region is increased from $\propto \omega^2$ in BB to $\propto k_{\max}^2$, whereas the DOS is only increased from $\propto \omega^2$ to $\propto \omega k_{\max}$. So extraordinary modes are outranking the ordinary ones much more than the nondispersive EMs outrank the nondispersive OMs in the energy density. Comparing Fig. 3.6a to Fig. 3.4a clearly demonstrates this.

With higher temperatures the increase above the blackbody value becomes smaller. Similar to the energy density, the hyperbolic bands are just populated by more photons $\propto \mathcal{U}(\omega, T) \propto T$, whereas the BB does not only populate the smaller frequency modes more, but also populates before unpopulated higher frequency modes giving the T^4 dependence. The normalized heat flux decreases almost $\propto \frac{1}{T^3}$. Same $\frac{1}{T^3}$ proportionality holds for the normalized heat transfer coefficient (HTC).

Towards smaller temperatures the normalized heat flux reaches a maximum and decreases afterwards. The decrease is caused by the Bose–Einstein cutoff cutting a part of the hyperbolic region and therefore reducing the enormous amount of hyperbolic energy flow, again similar to the energy density.

For nondispersive HMs we even know the temperature dependence to be $\propto T^2$ ($\propto T$ for the HTC), for blackbodies it's $\propto T^4$ ($\propto T^3$ for the HTC). The ratio is decreasing $\propto \frac{1}{T^2}$ as seen in Fig. 3.7b. The nondispersive HMs feature an overall larger heat

flux because their hyperbolic bands are infinite throughout the whole spectral range and not limited to some frequencies.

Note, that our results on thermal radiation inside HMs are quite different from the results obtained in Ref. [95]. There, the heat flux was found to be $\propto k_{\max}^4$ and very sensitive to the dispersion in the HM, $\frac{d\epsilon}{d\omega}$. A derivation is missing. Ref. [96] calculates a radiative thermal conductivity of a layered HMM at which we take a brief look in the next section.

In summary, although, just like a hyperbolic BB, realistic HMs contain a huge amount of thermal radiation they show somewhat different behavior. The DOS and energy density are strongly increased over the hyperbolic BB because of the dispersion. But this does not apply for the heat flux. A realistic HM conducts less heat due to the limited hyperbolic frequency range. To maximize the heat flux one has to maximize the spectral region with hyperbolic dispersion.

Let us now consider a numerical example for the heat flux between two reservoirs connected by our exemplary HM, as shown in Fig. 3.8. The reservoirs have the temperatures $T = 300$ K and $T + \Delta T$ with a small temperature difference $\Delta T \ll T$ and consist of the same HM. Similar configurations were studied in Refs. [95–97]. Here, we want to determine the radiative heat flux by using our theory for HMs. As there is only a single HM involved and therefore both reservoir–layer interfaces are optically non-existent, we can directly use our derived formulas,

neglecting absorption in the middle layer.

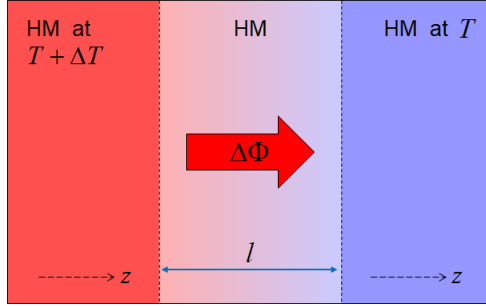


Figure 3.8: Illustration of setup for which radiative heat transfer between two hyperbolic reservoirs $\Delta\Phi$ separated by an intermediate hyperbolic layer of thickness l is evaluated. In order to have a perfect coupling between the reservoirs and the intermediate layer we assume that the reservoirs consist of the same HM as the intermediate layer. One reservoir is at temperature $T + \Delta T$, the other one at T with $\Delta T \ll T$. The dashed arrows show the orientation of the optical axes of the HMs which are along the z -axis.

The blackbody HTC is

$$H_{\text{BB}} = \frac{d\Phi_{\text{BB}}}{dT} = \frac{d}{dT}\sigma_{\text{B}}T^4 = 4\sigma_{\text{B}}T^3 = 4\frac{\Phi_{\text{BB}}}{T}. \quad (3.43)$$

At 300 K it is $H_{\text{BB}} \approx 6.124 \text{ W m}^{-2} \text{ K}^{-1}$.

The normalized HTC of the HM is shown in Fig. 3.7. Its absolute

value at 300 K (and $k_{\parallel, \max} = \frac{\pi}{50 \text{ nm}}$) is

$$\frac{\Delta\Phi_{\text{HM}}}{\Delta T} \approx \frac{d\Phi_{\text{HM}}}{dT} = H_{\text{HM}} \approx 1.29 \cdot 10^5 \frac{\text{W}}{\text{m}^2 \text{K}}. \quad (3.44)$$

With our hyperbolic BB we can easily estimate a maximal heat transfer coefficient of

$$H_{\text{I}}^e \approx H_{\text{II}}^e \approx \frac{d}{dT} \frac{k_{\perp, \max}^2}{48\hbar} (k_{\text{B}}T)^2 = \frac{k_{\perp, \max}^2}{24\hbar} k_{\text{B}}^2 T \quad (3.45)$$

for hyperbolic materials. Assuming for convenience that on average $\sqrt{\left| \frac{\epsilon_{\parallel}}{\epsilon_{\perp}} \right|} \approx 1$ we have $k_{\perp, \max} \approx k_{\parallel, \max}$. Then

$$H_{\text{I}}^e \approx H_{\text{II}}^e \approx 8.9 \cdot 10^4 \frac{\text{W}}{\text{m}^2 \text{K}} \quad (3.46)$$

at $T = 300 \text{ K}$. The HTC for our dispersive HM is larger just because $\left| \frac{\epsilon_{\parallel}}{\epsilon_{\perp}} \right| > 1$. With average permittivities the hyperbolic BB (nondispersive HM) features a larger HTC than the dispersive HM (cf. Fig. 3.7).

Of course, if one used a normal dielectric material instead of a hyperbolic material as the intermediate structure, the corresponding Stefan–Boltzmann law for normal dielectrics should be used to determine the maximum contribution of the radiative modes. Furthermore, since in such a case there is a mismatch between the reservoirs and the intermediate structure there can also be a contribution by evanescent waves which has to be added (like in the case of near-field heat flux through a vacuum gap,

see Section 4.2).

It is interesting to compare the radiative heat flux to the solid heat conduction by phonons and electrons inside the hyperbolic multilayer structure. At ambient temperature, the thermal conductivity of each unit layer is $\kappa_{\text{GaN}} \approx 120 \text{ W m}^{-1} \text{ K}^{-1}$ and $\kappa_{\text{Ge}} \approx 60 \text{ W m}^{-1} \text{ K}^{-1}$ [45, 46]. The inverse of the effective thermal conductivity of the HM (along the optical axis / perpendicular to the layer interfaces) is the weighted sum of inverse conductivities of both materials. This is due to the fact that the multilayer structure represents a series connection of thermal resistances and, as a consequence, the effective resistance is the weighted sum of the resistances of both materials. The weighting factors are the filling factors, here 0.5. The effective conductivity is $\kappa_{\text{HM}} \approx 80 \text{ W m}^{-1} \text{ K}^{-1}$. Interfacial thermal resistances (Kapitza resistances) are neglected and would make the overall conductance smaller [98].

Now, let us assume that the thickness of the intermediate hyperbolic multilayer is $l = 200 \text{ nm}$ so that we have four periods with periodicity $\Lambda = 50 \text{ nm}$. The choice of l is crucial. On the one hand, radiative heat flux is independent of the distance between the reservoirs, expect for interference and tunneling (near-field) effects which we excluded via our setup. Conduction, on the other hand, depends on the temperature gradient and thus on the distance l . $l = 200 \text{ nm}$ ensures that the intermediate HMM consists of several layers but its absorption is not too large to completely invalidate our no dissipation assumption.

The heat transfer coefficient by heat conduction through our hyperbolic multilayer structure of $l = 200$ nm is about

$$H_{\text{cond}} = \frac{\kappa_{\text{HM}}}{l} \approx 4 \cdot 10^8 \frac{\text{W}}{\text{m}^2 \text{K}}. \quad (3.47)$$

The conduction dominates the heat flux by three orders of magnitude but radiation is very strong compared to a blackbody and makes a non-vanishing contribution.

If less conductive materials like silicon dioxide (SiO_2) are chosen and interface resistances are non-negligible, the effective solid conductivity can become $< 1 \text{ W m}^{-1} \text{ K}^{-1}$ [96]. The solid HTC is then on the order of $H_{\text{cond}} \approx 10^6 \text{ W m}^{-2} \text{ K}^{-1}$. With a reduced HMM periodicity of $\Lambda = 10$ nm we get a radiative HTC on the same order of magnitude, $H_{\text{HM}} \approx 10^6 \text{ W m}^{-2} \text{ K}^{-1}$. Therefore, a hyperbolic material can theoretically have a radiative heat flux very close to heat conduction or even larger, even at ambient temperatures, depending on the material system and the thickness l of the intermediate layer.

We want to emphasize that in Ref. [96] a radiative conductivity of about $0.03 \text{ W m}^{-1} \text{ K}^{-1}$ was found for a doped InGaAs–AlInAs HMM and $0.004 \text{ W m}^{-1} \text{ K}^{-1}$ for a doped Si– SiO_2 HMM. These values are similar to our estimation for GaN–Ge which is about $0.026 \text{ W m}^{-1} \text{ K}^{-1}$.

To recapitulate, our analysis revealed that the magnitude of radiative heat flux carried by hyperbolic media can be several orders of magnitude larger than the flux radiated by a classical

BB or dielectric and may even exceed the heat flux carried by conduction in superlattices.

An application of this remarkable property could be to place a HM / HMM between emitter and photovoltaic cell in a TPV system. Similar to near-field TPV such TPV would utilize the increased radiative heat flux to increase output power or decrease operation temperature. The HMM provides also additional spectral control. The solid heat flux is parasitic and a drawback of this concept.

3.2.3 Thermal conductivity in hyperbolic materials

Let's look back at a situation like in Fig. 3.8. Two thermal reservoirs at different temperatures separated by a distance l are connected by a medium. When the intermediate medium is (approximately) lossless it acts as a radiation channel. The optical properties of medium and reservoirs determine how well the channel allows heat to go from one reservoir to the other. For larger l near-field and interference effects vanish, the reservoirs "see" each other over arbitrary distances and the radiative heat flux depends on the reservoir temperatures but not on l .

In practical situations, however, hyperbolic media or metamaterials are always accompanied by losses. Radiation cannot transport heat over arbitrary distances but is emitted, absorbed and re-emitted. Consequently, the heat flux does not only depend on the temperature difference between two reservoir but also on

their distance, or in other words on the temperature gradient. The microscopic explanation is identical to the one for solid heat conduction. Electrons and phonons can only move a short distance, the mean free path d [10, 44], between interactions with the lattice or each other, typically few 10 nm. Same holds for photons in an absorptive medium. They travel a distance d before they are absorbed, although, depending on the absorption, the distance can be much larger. The heat flux is governed by the temperature difference between two points separated by d , and therefore by the temperature gradient.

So the question arises: What is the radiative thermal conductivity of (lossy) HMs [95, 96]?

The previous discussion leads on to the idea that the conductivity is obtained by simply multiplying the HTC with the mean free path d . If d depends on frequency or k -vector, which it generally does, the multiplication must be performed before the integration. If we assume the losses are so weak that they only lead to a damping but otherwise do not (significantly) change the electromagnetic modes, we can take our equation for the heat flux in lossless uniaxial media (2.140) and expand it by the mean propagation distance of photons d . We obtain the radia-

tive thermal conductivity

$$\begin{aligned} \kappa = \int_0^\infty \frac{d\mathcal{U}(\omega, T)}{dT} & \left(\int_{\text{prop. ord. modes}} d^o(\omega, k_\perp) k_\perp \frac{dk_\perp}{2\pi} \right. \\ & \left. + \int_{\text{prop. extraord. modes}} d^e(\omega, k_\perp) k_\perp \frac{dk_\perp}{2\pi} \right) \frac{d\omega}{2\pi}. \end{aligned} \quad (3.48)$$

The integration boundaries basically remain the same as in the lossless case, but because strictly speaking propagating as well as evanescent modes now have a complex k_\parallel we renamed them. The idea is that photons are transporting the thermal energy by the distance d . Or for a given temperature gradient, the temperature difference determining the heat flux is the product of the gradient and d .

The equation (3.48) is identical with one derived via Boltzmann transport theory in Ref. [96] for a layered HMM consisting of a Drude metal and a dielectric with constant permittivity. Only the mean propagation distance d is expressed there as $v_g\tau$, group velocity times mean photon lifetime. Remembering that the power flow scales $\propto e^{-2\Im(k_\parallel)z}$, we propose the more simple ansatz

$$d^{e/o} = \frac{1}{2\Im(k_\parallel^{e/o})}. \quad (3.49)$$

It fits into the mathematical expression, thus requiring no additional computation effort, and is not limited to materials with particular optical properties like in Ref. [96]. There, the con-

ductivity is also found to be proportional to the inverse of the structure period and accordingly $\propto k_{\max}$. In HMMs $d^e \propto \frac{1}{k_{\perp}}$ for large k_{\perp} (hyperbolic) modes and the conductivity (3.48) indeed becomes $\propto k_{\max}$ when hyperbolic modes dominate the heat flux.

However, there is a problem with the proposed radiative thermal conductivity, in particular when dissipation is weak. Eqs. (2.140) and (3.48) assume a halfspace at homogeneous temperature. With losses included the radiation at an observation point is effectively emitted from a slab of thickness d . The assumption of weak material dissipation implies that the propagation distance of photons d is large. It means for the formula (3.48) to be correct the temperature of the thick slab must be (almost) homogeneous. But due to solid conduction it is unlikely to obtain a situation with an (almost) homogeneous temperature over a large distance d .

A possible resolution can be the utilization of a numerical approach. There is a distinct interaction of radiative and conductive heat transfer. An analytic solution of the coupled equations governing radiation and conduction does not exist. So a numerical approach could be to divide the material into small layers of homogeneous temperature. Conductive heat flux is approximated by taking the quotients of temperature difference and layer thickness as the needed gradients. Radiative heat flux can be calculated as presented in Chapter 2 but with emitting slabs instead of a halfspace [74]. The location of the heat flux z , which similar to Eq. (2.138) is in the heat flux equations, allows de-

termining how much radiative energy is going into which layer. Iterative calculations will lead to a steady state, for which a radiative conductivity can then be defined.

It will be interesting to see whether experiments can confirm the prediction that in HMs radiative heat flux can be as large as solid heat flux. Experimentally distinguishing the contributions may unfortunately be complicated. The HTC of dispersive HMs is (in first order) independent of mean temperature (see discussion in Section 3.2.2), so is the solid heat flux. Thus, a differentiation via the temperature dependence will probably not be possible. Other techniques must be thought of. E.g. if properties can be changed in a way that one contribution, radiation or solid conduction, is effected but not the other one it will be possible to extract the properties from a series of measurements.

Chapter 4

Near-field radiative heat flux and its penetration depth in hyperbolic media

Theoretically, it is well-known for a long time that heat radiation at the nanoscale can surpass the blackbody limit by orders of magnitude [4, 5, 15]. More recently, this super-Planckian property has been confirmed experimentally [9, 20, 21]. The underlying mechanisms resulting in elevated radiative heat fluxes are nowadays well understood. In particular, surface phonon polaritons can enhance the radiative heat flux by several orders

of magnitude [16] due to the very large number of contributing modes [22]. However, it has been shown very recently that also hyperbolic modes can lead to an enormous increase in the radiative heat flux [17, 18, 97] which can be even larger than that caused by surface modes [18].

This effect of enhanced near-field thermal radiation has several possible applications [4, 5] such as touchless cooling [26, 27] and near-field imaging [20, 23, 24] for instance. But probably one of the most discussed is near-field thermophotovoltaics (nTPV) which exploits the near-field enhancement effect for increasing the output power and the efficiency of thermophotovoltaics (TPV) devices [7, 34, 35, 37]. Structures using hyperbolic materials for nTPV were proposed recently [97, 99].

Surface modes are supported by many different materials, like metals and polar materials. On the other hand, hyperbolic modes only exist in very few natural materials like calcite and tetradymites [3, 47]. But it is possible to fabricate hyperbolic metamaterials (HMMs) which support hyperbolic modes. These HMMs can be constructed by combining metals or metal-like materials with dielectrics in subwavelength structures [1, 2]. The main advantage of the hyperbolic modes with respect to the surface modes is that they are propagating inside the hyperbolic medium [2], whereas the surface modes are bound to the surface of the material which is one of the bottlenecks of nTPV [37].

In Section 4.2 the near-field radiative heat transfer due to sur-

face and hyperbolic modes is analyzed and explained. It should provide a foundation for the reader for the later discussion.

The purpose of Section 4.3 is to analyze the penetration depth (PD) of thermal photons [100, 101] resulting from the heat exchange between two bodies close to each other. This quantity is very important for possible nTPV applications. It defines the effective thickness of the layer in which electron-hole pairs can be generated. As we shall see later, for surface mode dominated heat fluxes the PD is well below the gap width l and scales linearly with l [100]. It is e. g. only a few ten nanometers for $l = 100$ nm and mostly independent of the strength of material losses. But also for cooling applications larger PDs are preferable because photons transport heat much faster than phonons. Furthermore, it is better to have a larger volume where the heat is absorbed to avoid local overheating.

But before we come to the near field we have a brief look at the far-field thermal emission of hyperbolic metamaterials in the first section of this chapter. It turns out that HMM structures can have a band-edge emission characteristic which is desirable for (far-field) TPV; albeit the hyperbolicity itself is irrelevant here.

Different from the previous chapter, we now look at the heat flux in vacuum (and its penetration into materials), not inside HMs. In this chapter, we do not impose any restrictions to the emitting bodies / materials, especially no assumption of vanishing dissipation. In principle, some dissipation is even required for thermal radiation to be emitted. But because our emitting bodies

are halfspaces infinitely small losses are sufficient. So whenever lossless materials are discussed it is assumed that their non-zero losses approach 0.

4.1 Far-field thermal emission from hyperbolic media

Despite their fascinating properties concerning internal as well as near-field thermal radiation, HMMs can have a band-edge like far-field emission [41, 102]. The origin and consequences of this emission characteristic are summarized in this section.

The characteristics are depicted in Fig. 4.1. The analyzed HMM is a stack of alternating tungsten (W) and hafnium dioxide (HfO_2) layers, as illustrated in the inset of Fig. 4.1a. The tungsten permittivity is taken from Ref. [93] and resembles the permittivity of a Drude model [44]. The hafnia permittivity is well approximated by $\epsilon_{\text{HfO}_2} = 3.88$ [41]. The layer thicknesses are $\Lambda_{\text{W}} = 20$ nm and $\Lambda_{\text{HfO}_2} = 100$ nm.

The effective permittivity in Fig. 4.1a shows a transition from positive (real part of) ϵ_{\perp} at shorter wavelengths to negative ϵ_{\perp} at longer wavelengths. The wavelength of the transition is the epsilon-near-zero (ENZ) wavelength [102]. So the W– HfO_2 HMM has a transition from dielectric to metallic optical behavior in the near infrared. Actually, at longer wavelengths the metamaterial is hyperbolic but as we will see the hyperbolicity

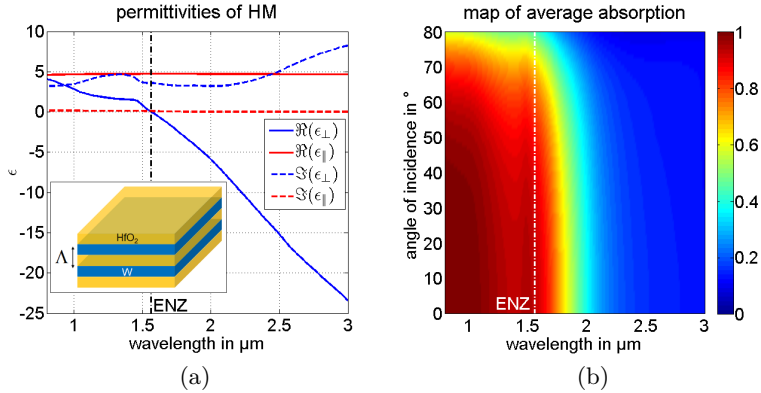


Figure 4.1: Effective permittivities and absorptivity of W–HfO₂ hyperbolic metamaterial. The tungsten filling factor is $\frac{1}{6}$ and the periodicity $\Lambda = 120$ nm. (a) shows the effective permittivities together with the epsilon-near-zero (ENZ) wavelength. The inset is a schematic image of the metamaterial. (b) is a map of the absorptivity for different wavelengths and angles of incidence. It is the absorptivity averaged over s- and p-polarization and assumes the top layer is HfO₂. [(b) adapted from Ref. [41].]

is irrelevant.

The behavior translates to the absorptivity of the metamaterial. Metallic optical properties are characterized by high reflectivity and thus low absorptivity. A lossy dielectric, on the other side, typically reflects little and absorbs a lot. Exactly these features are observed in Fig. 4.1b. The calculations are performed using the transfer-matrix method and assuming the top layer to be

HfO₂. The medium from which light impinge on the HMM is vacuum and the HMM is thick enough to ensure no transmission. The band-edge is approximately at the ENZ wavelength. Although the HMM is anisotropic the absorption is mainly determined by the optical constant along the layers ϵ_{\perp} . S-polarized light does not sense the anisotropy at all but a medium with permittivity ϵ_{\perp} . P-polarized light does sense the anisotropy but (especially for smaller incidence angles) the electric field in the vacuum is oriented mainly in the \perp -direction. However, the anisotropy flattens the angular dependence and keeps the absorptivity high in the dielectric region till about 70°. Hyperbolic modes are irrelevant here because they have such large k_{\perp} that they are mismatched to the small k_{\perp} modes in vacuum and therefore cannot be excited from the outside nor radiated into vacuum.

Kirchhoff's law of thermal radiation says that emissivity of a body is equal to its absorptivity [10, 11] (see Section 2.6.1). So we can expect the HMM to have a band-edge emissivity. Such a characteristic is very interesting for thermophotovoltaics [6]. The TPV cell, the receiver in a TPV system, employs a semiconductor. Wavelengths above the semiconductor band gap are not absorbed. To increase efficiency such wavelengths should not be emitted at all [41, 102]. Hence, a HMM could efficiently act as the selective thermal emitter.

It has also the advantage of being tunable. The ENZ wavelength can be adjusted to the semiconductor band gap via the filling

factors. After all, metamaterials can exhibit optical resonances or special features in the near infrared where most natural materials do not do that [41].

Experiments have confirmed the expected properties [41, 103] but high temperature stability of the nanostructures remains a critical issue.

4.2 Near-field heat flux between hyperbolic media

Let us consider two halfspaces at slightly different temperatures $T + \Delta T$ and T with $\Delta T \ll T$ separated by a homogeneous vacuum gap with the width l , as illustrated in Fig. 4.2. The halfspaces consist of homogeneous, isotropic or uniaxial materials, or multilayer structures with optical axes parallel to the surface normal.

The assumption of homogeneous temperatures in the two halfspaces is well justified because even the increased near-field heat conduction through the gap is much smaller than the solid conduction inside the halfspaces.

In some cases, like in a TPV setup, the assumption $\Delta T \ll T$ is not justified. Then, the heat flux for the concrete temperatures instead of the HTC at a mean temperature T has to be calculated. The difference between heat flux and HTC is minimal and we will work with the normalized quantity, the HTC, as it

is less dependent on adjustable parameters like the temperature difference.

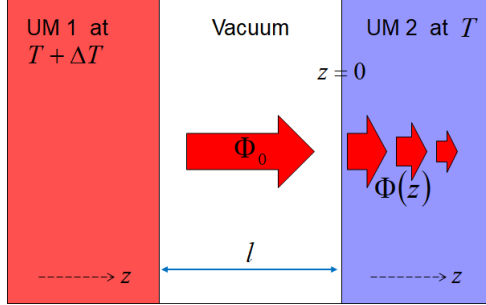


Figure 4.2: Illustration of setup for which radiative heat transfer between two reservoirs Φ_0 separated by a vacuum gap of thickness l is evaluated. One reservoir is at temperature $T + \Delta T$, the other one at T with $\Delta T \ll T$. The reservoirs can be uniaxial media (UM) but also multilayer structures. In addition, the heat flux inside the second halfspace $\Phi(z)$ is displayed. The dashed arrows show the orientation of the optical axes of the UMs which are along the z -axis.

Then the radiative heat flux through the gap is, according to Eq. (2.161), given by $\Phi_0 = H_0 \Delta T$ where the heat transfer coefficient (HTC) is

$$H_0 = \sum_{j=s,p} \int_0^{\infty} h_0^j(\omega) \frac{d\omega}{2\pi}, \quad (4.1)$$

introducing the spectral heat transfer coefficient (sHTC)

$$h_0^j(\omega) = \frac{d\mathcal{U}(\omega, T)}{dT} \int_0^\infty \mathcal{T}^j(\omega, k_\perp) k_\perp \frac{dk_\perp}{2\pi}. \quad (4.2)$$

The energy transmission coefficient \mathcal{T}^j for s- and p-polarized waves is given by

$$\mathcal{T}^j(\omega, k_\perp; l) = \begin{cases} \frac{(1-|r_1^j|^2)(1-|r_2^j|^2)}{\left|1-r_1^j r_2^j e^{i2k_\parallel^{\text{vac}} l}\right|^2} & k_\perp < \frac{\omega}{c} \\ \frac{4\Im[r_1^j]\Im[r_2^j]e^{-2|k_\parallel^{\text{vac}}|l}}{\left|1-r_1^j r_2^j e^{-2|k_\parallel^{\text{vac}}|l}\right|^2} & k_\perp > \frac{\omega}{c} \end{cases}, \quad (4.3)$$

where r_i^s and r_i^p are the Fresnel coefficients for reflection of s- and p-polarized light at the halfspace i . For more information please refer to Section 2.6.2. \mathcal{T} is a unitless number between 0 and 1 representing the quality of the radiation channel from one halfspace to the other [18, 22, 79]. Its expressions are different for propagating and evanescent waves in the vacuum.

In the following, we consider the heat exchange by thermal radiation for the three different fundamental structures depicted in Fig. 4.3: (a) two halfspaces consisting of a bulk material, (b) two multilayer HMM (mHMM) halfspaces, and (c) two nanowire HMM (wHMM) halfspaces.

Let us first have a look at the radiative heat flux in the gap and the near-field effect. We consider four systems where hot and cold halfspaces are always identical: (i) bulk germanium

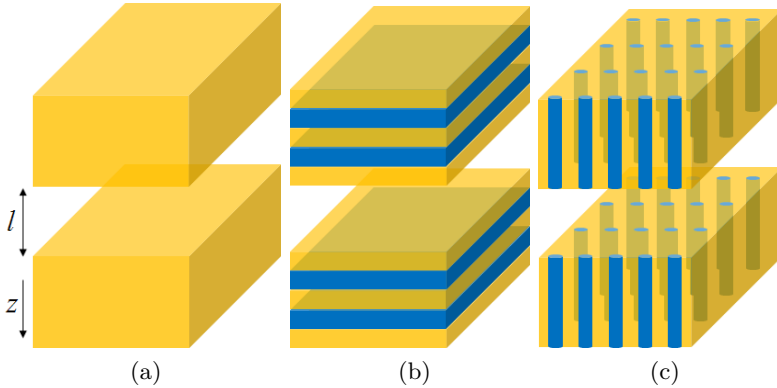


Figure 4.3: Systems to be analyzed. Two identical halfspaces of (a) bulk materials, of (b) layer HMMs and of (c) wire HMMs separated by a vacuum gap. The layer HMMs are modeled as effective media or full multilayers, the wire HMMs as effective media. The gap width is l .

(Ge), (ii) bulk gallium nitride (GaN) both resembling case (a), (iii) multilayer HMM (mHMM) composed of GaN–Ge bilayers and treated as an effective medium, and (iv) mHMM composed of GaN–Ge bilayers with the top layer being Ge. The last two systems have a period of $\Lambda = 5$ nm with a filling factor of 50% and correspond to case (b). The fundamental features of wire HMMs (wHMMs) are identical to those of mHMMs. For a better overview we skip the wHMMs in this section but return to them when studying the penetration depth.

Ge is a lossless dielectric with a permittivity of $\epsilon_{\text{Ge}} = 16$ in the

mid infrared [93]. The relative permittivity of GaN can be described by a Drude–Lorentz model and features a negative (real part of the) permittivity in the angular frequency spectral range $106 - 141 \cdot 10^{12} \text{ s}^{-1}$. The resulting HMM is hyperbolic in the same spectral range with one type I and one type II hyperbolic range. Check Section 3.2 for the parameters and the effective permittivity. Both materials as well as the HMM are nonmagnetic.

The HTC at $T = 300 \text{ K}$ are presented in Fig. 4.4a. They are normalized to the blackbody HTC $H_{\text{BB}} \approx 6.124 \text{ W m}^{-2} \text{ K}^{-1}$ which is independent of the gap l . The integrations are performed numerically in MATLAB (by MathWorks). Fig. 4.4b illustrates the contributions of the different modes to the heat flux [22].

In the far-field regime, so for large l , only modes propagating in the gap can contribute. They are limited to $k_{\perp} < \frac{\omega}{c}$. For blackbodies the transmission coefficient \mathcal{T} is 1 for all propagating modes (and 0 for all other modes). For real systems \mathcal{T} is smaller because of reflections at the interfaces. The heat flux is thus below the blackbody heat flux and cannot surpass it.

Towards smaller gaps Ge shows an increase to a value 16 times above the blackbody value. This behavior is well explained remembering the radiative heat flux inside (approximately) lossless materials. It is supported by propagating modes solely. Those modes propagating inside Ge are characterized by $k_{\perp} < \frac{\omega}{c} \sqrt{\epsilon_{\text{Ge}}}$. At the gap frustrated total internal reflection occurs [22]. So, different from total internal reflection [14], a part of the energy

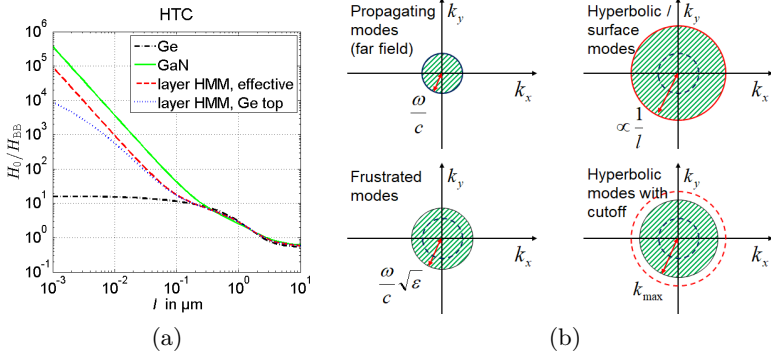


Figure 4.4: (a) Heat transfer coefficient (HTC) H_0 in the vacuum gap at $T = 300$ K for the systems: bulk Ge, bulk GaN, GaN–Ge layer HMM treated as effective medium, GaN–Ge multilayer HMM with Ge top layer. The period of the HMMs is $\Lambda = 5$ nm and the filling factor 50%. The HTC is normalized to the HTC between blackbodies H_{BB} . (b) Illustration of contributions of different modes to the heat flux. The plane of k -vectors parallel to the interfaces, \mathbf{k}_\perp -plane, is shown. The shaded area shows the modes contributing to the heat flux. The red arrow and its value constitute the radius of the shaded area. For better visualization the drawings are not to scale.

is not reflected back into the halfspace where it comes from but is transmitted across the gap. Ideally, all propagating and frustrated modes exhibit a transmission coefficient of 1, which is indeed the case for $l \rightarrow 0$. The spectral heat flux is increased by $\sqrt{\epsilon_{\text{Ge}}^2} = \epsilon_{\text{Ge}} = 16$ above the blackbody [22] and, in lack of dispersion, so is the total heat flux.

For a uniaxial dielectric the radius shown in Fig. 4.4b is either $\frac{\omega}{c}\sqrt{\epsilon_{\perp}}$ or $\frac{\omega}{c}\sqrt{\epsilon_{\parallel}}$ depending on the polarization. Hyperbolic dispersion as well as surface modes are only observed for p-polarized light.

The effective HMM and the GaN show an increase towards smaller gaps proportional to $\frac{1}{l^2}$ [22]. The HMM supports hyperbolic modes and GaN surface modes. We will soon take a closer look at these modes. But we already know that they are modes with very large wavevectors. Only the non-zero gap size introduces a k_{\perp} cutoff $\propto \frac{1}{l}$, see Section 2.6.2, hence the $\frac{1}{l^2}$ heat flux dependence.

Effective medium theory (EMT) gives reliable results if the unit-cell size of the underlying structure is much smaller than the wavelength. In the far-field regime the dominant wavelength is the thermal wavelength which is about $10\ \mu\text{m}$ at 300 K. In the near-field regime, the contribution of the evanescent waves sets another constraint to the applicability of the effective description. As a rule of thumb, the effective description gives reliable results for distances l larger than the unit-cell size Λ [57, 104]. For smaller distances, it tends to overestimate the hyperbolic heat flux contribution [104, 105].

Eventually, as expected, the real multilayer HMM resembles the effective HMM for larger gaps but for very small l starts to deviate from the $\frac{1}{l^2}$ dependence and to saturate. For large k -vectors the dispersion relations of effective and real HMM differ and in particular the multilayer has a cutoff k_{max} for modes propagat-

ing inside the HMM. When the gap becomes too small the factor limiting the modal contributions to heat flux is not the cutoff due to the gap size but due to k_{\max} . Although we neglected a possible k_{\max} for the effective HMM, it should be noted that, as discussed in Section 1.2, all HMMs and also natural HMs will show a k_{\max} . And even surface modes cannot take on arbitrary large k -vectors e. g. due to nonlocal effects [86, 87]. The k -values can be too large for a material to be polarized and thus to sustain metallic properties which are, on the other side, a requirement for surface modes. However, these k_{\max} correspond to atomic distances and are hardly visible for gaps larger than a few nanometers [86].

A deeper understanding of surface and hyperbolic mode mediated heat flux can be obtained from Figs. 4.5 and 4.6. They show the energy transmission coefficient \mathcal{T} and the sHTC for bulk GaN and the GaN–Ge layer HMM at a gap of $l = 10$ nm when surface and hyperbolic modes dominate the heat flux.

Inside the reststrahlen band ($\omega_{\text{TO}} < \omega < \omega_{\text{LO}}$) $106 - 141 \cdot 10^{12} \text{ s}^{-1}$ where GaN has a negative (real part of the) permittivity it supports surface modes, more precisely surface phonon polaritons. The resonance is around $136 \cdot 10^{12} \text{ s}^{-1}$ where $\Re(\epsilon_{\text{GaN}}) = -1$. Appendix C.2 derives the dispersion relation of surface modes and provides more insight.

The heat flux is caused by surface modes on both sides of the gap coupling and thus creating an efficient radiation channel through the gap [16, 106]. The coupling can be symmetric or antisym-

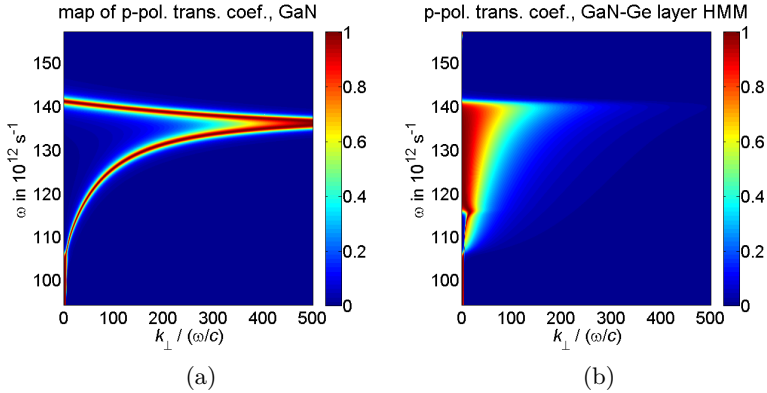


Figure 4.5: Energy transmission coefficient \mathcal{T} of p-polarized radiation through the vacuum gap for the systems: (a) bulk GaN and (b) a GaN–Ge layer HMM treated as effective medium. The filling factor of the HMM is 50%. The gap size is $l = 10$ nm.

metric, depending on the permittivity value. For permittivities (with real part) smaller -1 , i. e. for the lower-frequency branch, the coupling is symmetric; for permittivities between -1 and 0 , i. e. for the higher-frequency branch, the coupling is antisymmetric [4, 5]. The red, large heat flux lines in Fig. 4.5a coincide with the dispersion relation of coupled surface modes. The heat flux is maximal at the resonance around $136 \cdot 10^{12} \text{ s}^{-1}$, see Fig. 4.6a, because it features the highest k_{\perp} -values and therefore the largest area of contributing modes in the \mathbf{k}_{\perp} -plane. Surface modes are only observed in p-polarization (see Appendix C.2). For s-polarization, as they do not support any bulk or surface

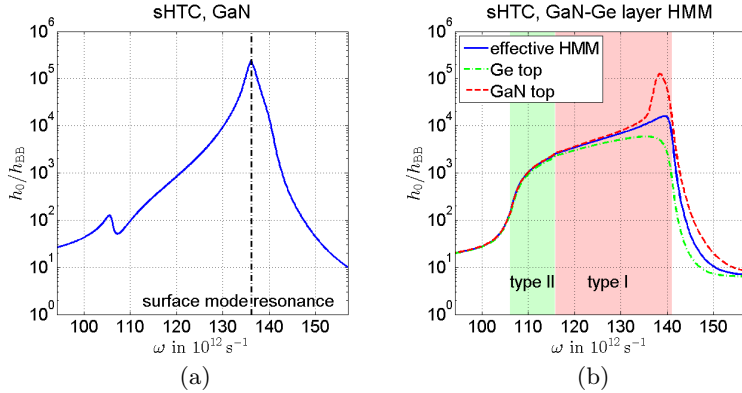


Figure 4.6: Spectral heat transfer coefficient (sHTC) in the vacuum gap h_0 for the systems: (a) bulk GaN and (b) a GaN–Ge layer HMM. The period of the HMM is $\Lambda = 5$ nm and the filling factor 50%. The gap size is $l = 10$ nm. Results for the effective HMM and the real multilayers are plotted. The sHTC is normalized to the sHTC between blackbodies h_{BB} .

modes, metallic properties (negative permittivity) lead to very small heat fluxes.

Surface modes allow heat transfer with extremely large k_{\perp} . This may be surprising since, as discussed in Section 2.6.2, the $e^{-2|k_{\parallel}^{\text{vac}}|l}$ term in the transmission coefficient (4.3) introduces a cutoff. This is indeed the case but surface modes are characterized by the denominator of \mathcal{T} approaching 0, a kind of a resonant behavior [107]. Hence, the exponential damping can be partly compensated for and the cutoff sets in only at very large k_{\perp} . The

cutoff towards high wavenumbers is always smooth, not sharp.

Hyperbolic modes, on the other side, are broadband w. r. t. the wavevectors. They are not thin lines in the ω - k_{\perp} -plane but whole areas. Thermal photons propagating inside the HMM tunnel the vacuum gap where they cannot propagate due to their large k_{\perp} [18, 38, 108]. Hyperbolic modes are, in fact, frustrated total internal reflection modes; however, with much larger k_{\perp} than the frustrated modes of dielectric media.

Type II hyperbolic modes feature a region of small k_{\perp} with no propagating modes. This translates into a small \mathcal{T} there. In the type I range all modes with k_{\perp} from 0 till the cutoff contribute to the heat flux. Different from surface modes hyperbolic modes do not exhibit the behavior of the denominator of \mathcal{T} approaching 0 and are cut off at smaller k_{\perp} .

We already discussed the heat flux between real HMMs with Ge top layer in comparison to effective HMMs, seen in Fig. 4.6b. The multilayer displays a smaller heat flux. How much smaller depends on the ration of gap size l and HMM periodicity Λ . When GaN is the top layer things change. Concerning the hyperbolic modes actually nothing changes. But because GaN supports surface modes the HMM with GaN top layer does so too [57, 104]. Hyperbolic and surface modes overlap making it impossible to clearly distinguish them. But the peak in Fig. 4.6b around $138 \cdot 10^{12} \text{ s}^{-1}$ is clearly caused by surface modes. Note that because the top layer has a finite thickness the dispersion relation of these surface modes is different from the one for bulk

GaN [107].

If only one of the two bodies exchanging heat support high- k modes the near-field heat flux is significantly reduced and also its spectral distribution altered [35, 105]. Only if both sides support modes at the same frequency ω and the same tangential wavevector k_{\perp} those modes will couple across the gap efficiently and transport a lot of heat via radiation [36, 105]. These high- k modes don't have to have the same physical origin, although same kinds of modes (e.g. surface modes) match the best [36, 105].

4.3 Penetration depth of near-field heat flux in hyperbolic media

After discussing the near-field heat flux through the vacuum gap we turn to its penetration into the colder halfspace, as depicted in Fig. 4.2.

In the following, we consider the heat exchange by thermal radiation for the three different structures depicted in Fig. 4.3: (a) two gallium nitride (GaN) halfspaces, (b) two multilayer HMM (mHMM) halfspaces composed of GaN–Ge bilayers, and (c) two nanowire HMM (wHMM) halfspaces consisting of GaN nanowires immersed in a Ge host.

In order to describe the optical response of the structures (b) and (c) we use effective medium theory (EMT), more precisely

Eqs. (1.5)–(1.8). We choose $f_{\text{GaN}} = 50\%$ for the mHMM and $f_{\text{GaN}} = 30\%$ for the wHMM filling factor. The 50% for the mHMM ensure that type I and type II hyperbolic spectral ranges are adjacent to each other (cf. Fig. 3.3) – not separated by a dielectric or metallic region in between – and as wide as possible. The 30% for the wHMM also maximize the width of the hyperbolic regions while remaining small enough for the EMT to be applicable [54]. z is the direction perpendicular to the surfaces. Note that although we call the structures (b) and (c) HMMs, they are hyperbolic only in certain frequency ranges. For the mHMM the range is $106 - 141 \cdot 10^{12} \text{ s}^{-1}$ and for the wHMM it is $106 - 121 \cdot 10^{12} \text{ s}^{-1}$ (with a small non-hyperbolic region from $111 - 112 \cdot 10^{12} \text{ s}^{-1}$).

Now, we want to define the penetration depth (PD) or attenuation length δ of the thermal radiation into the colder medium. To this end, we need to determine the heat flux or the heat transfer coefficient inside the colder medium. It is already clear that due to the rotational symmetry of the problem the heat flux is along the z -direction (\parallel -direction) only. Furthermore, the components of the electric and magnetic fields parallel to the interfaces are continuous which implies that the z -component of the Poynting vector is continuous at the interface as well. Finally, we know that the intensity of a plane wave with a given frequency ω and tangential wavevector k_{\perp} impinging on a semi-infinite uniaxial medium (with the optical axis along the surface normal) is damped by a factor $e^{-2\Im(k_{\parallel}^j)z}$, where k_{\parallel}^j is the polariza-

tion dependent wavevector component along z -direction, i. e. the direction of propagation of the heat flux. Hence, from Eq. (4.2) giving the spectral heat transfer coefficient inside the vacuum gap and in particular at the interface of the absorbing medium, we can easily deduce the sHTC inside the colder medium. We obtain

$$h^j(\omega; z) = \frac{d\mathcal{U}(\omega, T)}{dT} \int_0^\infty \mathcal{T}^j(\omega, k_\perp) e^{-2\Im(k_\parallel^j)z} k_\perp \frac{dk_\perp}{2\pi} \quad (4.4)$$

assuming the vacuum–cold medium interface is located at $z = 0$ (see Fig. 4.2). More information on the derivation is given in Section 2.6.2. By replacing h_0^j by h^j in Eq. (4.1) we obtain the heat transfer coefficient $H(z)$ inside the colder medium. The z -component of the wavevector is in our case given by

$$k_\parallel^s = \sqrt{\frac{\omega^2}{c^2} \epsilon_\perp - k_\perp^2} \quad (4.5)$$

for s-polarized waves (ordinary waves) and by

$$k_\parallel^p = \sqrt{\frac{\omega^2}{c^2} \epsilon_\perp - k_\perp^2 \frac{\epsilon_\perp}{\epsilon_\parallel}} \quad (4.6)$$

for p-polarized waves (extraordinary waves). The $\epsilon_{\perp/\parallel}$ are the (effective) permittivities of the halfspace. Obviously, the anisotropy makes itself felt through the p-polarized waves.

The PD δ is now defined such that it determines the distance at

which the heat transfer coefficient H has dropped to $1/e$ of its value inside the vacuum gap, i. e.

$$H(\delta) = \frac{H(0)}{e} = \frac{H_0}{e}. \quad (4.7)$$

In a similar way we define the spectral PD $\delta(\omega)$ as the distance at which the spectral heat transfer coefficient $h = h^s + h^p$ drops to $1/e$, i. e.

$$h(\omega; \delta(\omega)) = \frac{h(\omega; 0)}{e} = \frac{h_0(\omega)}{e} = \frac{h_0^s(\omega) + h_0^p(\omega)}{e}. \quad (4.8)$$

It is worth noting that the penetration depth of radiative heat flux is naturally related to the PD of the intensity of electromagnetic plane waves $\delta^j(\omega, k_\perp) = \frac{1}{2\Im(k_\parallel^j)}$ ($j = s, p$).

Before discussing the total PD for the different systems (a)–(c), we present in Fig. 4.7 the sHTC $h_0(\omega)$ and the spectral PD $\delta(\omega)$ for the different structures choosing $l = 10$ nm and $T = 300$ K. It can be seen in Fig. 4.7a that the heat flux between bulk GaN has a large, narrow peak at the surface mode frequencies as expected in this case [16]. For the two HMMs in Figs. 4.7b and 4.7c, the heat flux is strong in the broad frequency bands where hyperbolic modes exist. For the mHMM in Fig. 4.7b both bands touch each other which is due to the choice of $f_{\text{GaN}} = 0.5$ resulting in a broad plateau for the sHTC and the spectral PD. For the wHMM in Fig. 4.7c both bands are separated by a small, non-hyperbolic region (when choosing $f_{\text{GaN}} = \frac{1}{3}$ instead of $f_{\text{GaN}} = 0.3$ both

bands would touch as well). That is the reason for the small dip in the middle of the plateau of the sHTC.

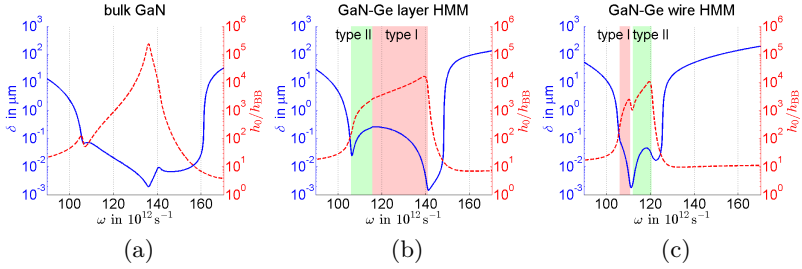


Figure 4.7: Spectral thermal penetration depth $\delta(\omega)$ (solid lines) and spectral heat transfer coefficients (sHTC) in the vacuum gap h_0 (dashed lines) for (a) bulk GaN, (b) GaN–Ge layer HMMs and (c) GaN–Ge wire HMMs. The sHTC is normalized to the sHTC between blackbodies h_{BB} . The gap width is $l = 10 \text{ nm}$. For the HMMs the spectral ranges with type I or II hyperbolic dispersion are highlighted in color. [From Ref. [65], Copyright 2014 AIP Publishing LLC.]

For all structures, the spectral PD decreases when the sHTC increases [100, 101, 109]. This is not surprising if Eq. (4.6) is recalled. The larger k_{\perp} the larger is the imaginary part of (assuming $k_{\perp} \gg \frac{\omega}{c}$)

$$k_{\parallel}^{\text{p}} \approx ik_{\perp} \sqrt{\frac{\epsilon_{\perp}}{\epsilon_{\parallel}}}, \quad (4.9)$$

namely

$$\begin{aligned} \Im(k_{\parallel}^{\text{p}}) &\approx k_{\perp} \Re\left(\sqrt{\frac{\epsilon_{\perp}}{\epsilon_{\parallel}}}\right) \\ &\approx k_{\perp} \sqrt{\frac{|\epsilon_{\perp}|}{|\epsilon_{\parallel}|}} \cos\left(\frac{\arg(\epsilon_{\perp}) - \arg(\epsilon_{\parallel})}{2}\right). \end{aligned} \quad (4.10)$$

And the large heat fluxes are caused by p-polarized, high k_{\perp} modes. Note that the opposite behavior in sHTC and spectral PD is a general trend we observe, not a strict monotonicity.

We have small damping inside the anisotropic material if $\arg(\epsilon_{\perp}) - \arg(\epsilon_{\parallel}) \approx \pm\pi$ or if $|\epsilon_{\perp}| \ll |\epsilon_{\parallel}|$. In particular, inside a hyperbolic material where $\Re(\epsilon_{\perp})\Re(\epsilon_{\parallel}) < 0$ the condition on the phases can be fulfilled if the imaginary parts of the permittivities perpendicular and parallel to the optical axis are small, i. e. if $\Im(\epsilon_{\perp}) \ll |\Re(\epsilon_{\perp})|$ and $\Im(\epsilon_{\parallel}) \ll |\Re(\epsilon_{\parallel})|$. In a lossless case the term $\sqrt{\frac{\epsilon_{\perp}}{\epsilon_{\parallel}}}$ is just an imaginary number and the modes are not damped at all.

But for GaN $\Im(k_{\parallel}^{\text{p}}) \approx k_{\perp}$ and damping is always observed independent of losses. So the thermal photons are absorbed at the surface even when the dissipation is very weak. This comes from the fact that surface mode photons can propagate long distances along the surface and be eventually absorbed without penetrating deep into the material.

Comparing the results in Fig. 4.7 for the different structures (a)–(c) it becomes apparent that the PD in the HMMs can have values as small as the PD in GaN at the peak frequency of the

sHTC. However, considering the whole hyperbolic region $\delta(\omega)$ can for the HMMs also have values which are one or even two orders of magnitude larger than the corresponding value for bulk GaN. By optimizing the HMMs to have smaller absorption this difference in PD can be made even larger.

In Fig. 4.8a the total HTC for the three systems and additionally between two bulk Ge halfspaces is shown. It is normalized to the HTC between two blackbodies. In accordance with the last Section 4.2, the HMMs and GaN show the well-known $\frac{1}{r^2}$ dependence in the near field. The relative heat flux of Ge approaches the value $\epsilon_{\text{Ge}} = 16$, because the heat transfer is sustained only by frustrated total internal reflection modes which contribute by photon tunneling. Since we have neglected losses for Ge, its PD is infinite. Of course, real Ge has losses due to imperfections but the PD δ can still be very large. As can be observed in Fig. 4.8a, the wHMM has a relatively weak heat transfer coefficient compared to bulk GaN and the mHMM. However, we have checked that by replacing Ge with some dielectric having a lower refraction index one can make the hyperbolic band much broader and thus enhance the near-field heat flux significantly [18].

Finally, the total PD δ is depicted in Fig. 4.8b. In the far field and the intermediate region it is more or less constant for all materials. The higher the filling factor of GaN, the more lossy is the effective material and the shorter the penetration. To get an approximate boundary between the region dominated by hyperbolic modes and the region dominated by propagating and

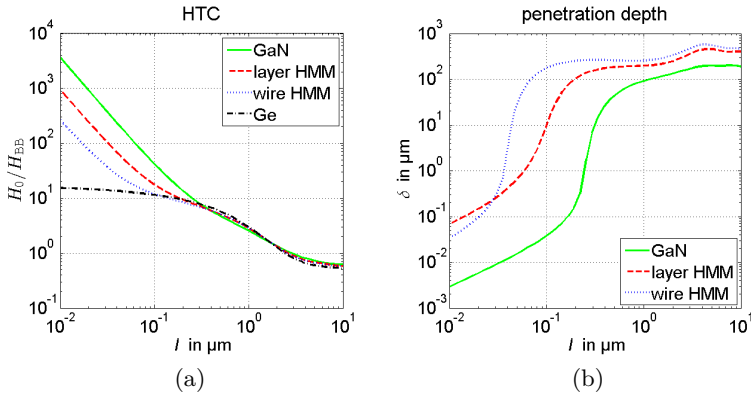


Figure 4.8: (a) Heat transfer coefficient (HTC) in the vacuum gap H_0 and (b) thermal penetration depth δ at $T = 300$ K for the systems: bulk GaN, GaN–Ge layer HMM, GaN–Ge wire HMM, and bulk Ge. The HTC is normalized to the HTC between blackbodies H_{BB} . [From Ref. [65], Copyright 2014 AIP Publishing LLC.]

normal frustrated modes we calculated the distance l at which 50% of the total heat flux is due to hyperbolic modes. This distance is 115 nm for the mHMM and 44 nm for the wHMM – so approximately given by the start of the $\frac{1}{l^2}$ dependence of the HTC. The spectral heat flux is generally much broader (e.g. the full width at half maximum range is $46 - 212 \cdot 10^{12} \text{ s}^{-1}$ for blackbody heat flux at 300 K) than the hyperbolic bands such that they only dominate in the near field on which our focus lies. In this strong near-field regime where the surface or hyperbolic

modes dominate the heat flux for GaN and the HMMs, δ drops dramatically. This behavior can be understood by the fact that with smaller l modes with k_{\perp} on the order of $\frac{1}{7}$ dominate the thermal radiation, so that $\Im(k_{\parallel}^p) \propto k_{\perp} \propto \frac{1}{7}$ and hence the PD becomes approximately proportional to l . Most importantly, in the intermediate regime the PD in the HMMs can be two to three orders of magnitude larger than in GaN and in the strong near-field regime it can be more than one order of magnitude larger than in GaN. Hence, our numerical results suggest that hyperbolic materials are preferable to phonon-polaritonic media when larger near-field PDs are needed as in the case of nTPV [37].

In a real GaN–Ge multilayer the extinction of the heat flux is not uniform. In the lossless Ge layers the heat flux is constant. In the lossy GaN layers the absorption is so strong that the absorption averaged over GaN and Ge layers equals the absorption of the effective HMM [66]. This is true as long as the EMT is applicable.

Following Section 4.2, as the EMT fails it overestimates the heat flux because it assumes the existence of high k_{\perp} modes which are actually cut off. For the PD the effect is reverse. Smaller k_{\perp} modes means smaller heat flux but larger penetration depths for the real structure. There is a tendency of opposite trends for the thermal heat flux and the attenuation length, i. e. large attenuation lengths are accompanied by relatively small heat fluxes and vice versa.

When GaN is the top HMM layer hyperbolic and surface modes

mix. The surface-mode mediated heat flux decays very rapidly, as typical for surface modes. The hyperbolic-mode mediated heat flux behaves as explained previously. Depending on the strengths of both fluxes the PD of the total flux can be smaller or larger.

A deeper discussion on the penetration of radiative heat flux into real multilayers is presented in Ref. [66].

It should be mentioned that the structures presented here are not directly applicable to nTPV systems. Here, we report on the general property of hyperbolic modes supporting large penetration depths of near-field heat flux. For nTPV applications, the materials should produce hyperbolic regions in the near-infrared where photovoltaic cells are available. Furthermore, the hyperbolicity and the cell functionality – separation of created free charges resulting in a usable voltage – must be combined. The ratio of photons creating free charges and photons absorbed in the metal just heating the receiver is crucial for the system efficiency. Concrete systems and the variety of nTPV aspects are left for further studies.

In conclusion, we have shown with concrete examples that the PD of thermal photons in the near-field regime can be much larger for materials or systems supporting hyperbolic modes than for materials supporting surface modes. The reason is the different nature of those modes. In addition, there is a trade-off between large heat fluxes and large PDs. It seems achieving both simultaneously is very complicated.

Although having a broad frequency band for nanoscale heat radiation seems to be disadvantageous for nTPV, this disadvantage is compensated by a striking property of hyperbolic modes: Hyperbolic modes are propagating modes inside the hyperbolic metamaterials and therefore the penetration depth is much larger than for surface modes. Hence, the effective layer on which electron-hole pairs are generated can be orders of magnitude larger than for surface-mode driven heat transfer. And thus, HMMs could be used to overcome the tricky problem of the saturation in hole-electron pair concentration close to the surface in nTPV devices. They could also be exploited to develop efficient heat removal systems which are able to extract the huge density of energy confined at the surface of hot bodies.

Chapter 5

Dynamic measurement of near-field radiative heat transfer

As we previously learned, in the far field the electromagnetic radiation emitted by a hot body is limited to the well-known blackbody distribution. However, the blackbody theory is only valid when the characteristic dimensions of the body are significantly greater than the wavelength of maximal thermal radiation, $\approx 10\ \mu\text{m}$ at 300 K. When bodies at different temperatures do not satisfy this criterion, then the radiative heat flux may display drastically different characteristics. Particularly, if the separation distance is smaller than the maximum wavelength

the radiative heat flux can be orders of magnitude greater than the blackbody limit. We discussed this phenomenon, known as near-field radiative heat transfer [4, 5, 15], in Chapter 4.

Given its importance as a generalization of Kirchhoff's law of thermal radiation, near-field radiative heat transfer has garnered considerable scientific interest, spanning computational aspects [15, 19, 22], the effect of surface [16, 100] and hyperbolic modes [17, 18, 65, 97, 99], and potential applications [5, 7, 20, 26, 28]. A number of experiments demonstrating the near-field effect in different geometries have also been reported, each with their own merits and drawbacks. Tip-plane [8, 20, 23, 25, 110–112] and sphere-plane [9, 27, 108, 113–116] geometries allow for surface mapping and precise distance control, but suffer from complicated data analysis. Plane-plane experiments offer the advantage of simple interpretation and large, easily detectable, heat fluxes [7, 21, 26, 117–123], however, these experiments are complicated by the need to create uniform sub-micrometer gaps. Other geometries combine advantages of these geometries, but suffer from their own challenges, such as elaborate microfabrication of samples [124, 125].

While the details of these experiments are widely varied, they are tied by a single, dominant, operational paradigm: One side is heated with constant power, and the other is kept at constant lower temperature. The temperatures on hot and cold sides, along with heat power flux, are then measured once the system has reached a steady (stationary) state, and from these

quantities the near-field heat conductance – radiative heat power flux normalized to the temperature difference – is determined. That is, these experiments are all performed under stationary or steady-state conditions, where by “stationary” we refer to non-time-varying systems. “Steady-state” measurement techniques allow variations at one frequency (and its harmonics), thus include “stationary” measurements, but forbid the measurement of any transient effects. In other words, “stationary” and “steady-state” measurement signals have a discrete, not continuous, frequency spectrum. In some of the near-field experiments the gap size [7, 20, 25, 110, 116, 122] or the heating power [111, 116, 122] is modulated to improve sensitivity. Yet even in these cases, measurements are conducted only once steady-state conditions have been achieved, and the measured quantities directly determine the gap conductance.

In theory, this is the simplest (most straight forward and indisputable) method of measuring the power transferred by thermal radiation. However in practice, there is a number of drawbacks:

- (I) All other resistances and losses between the sensors must be carefully approximated or eliminated before the radiative gap conductance can be measured.
- (II) The sensors and heaters / coolers must be built into the system. This requires sample accessibility from both sides of the gap where thermal heat transfer is taking place, and good contacting. Often, additional micro- / nanofabrication steps are utilized for that.

- (III) The time for an object to thermalize is proportional to $\frac{D^2}{\alpha}$, with D standing for the largest characteristic length, and α the thermal diffusivity. If a sample has any characteristic dimensions on the centimeter scale then it can quickly become very time consuming – several minutes to several tens of minutes to even hours – to wait for thermal transients to decay substantially.

In this chapter, we report a dynamic near-field radiative heat transfer measurement procedure based on the transient plane source (TPS) technique [126, 127] that substantially alleviates these functional concerns. Notably, the approach requires no specialized sample preparation or microfabrication steps. We present experimental data showing the viability of our method using centimeter sized samples consisting of two optical glass disks separated by gaps varying from 7 μm down to 150 nm.

This data agrees well with expected theoretical values and marks the highest radiative thermal conductance enhancement – up to 16 times greater than the blackbody limit – reported for such macroscopic samples. Further, our method requires only one side of the sample to be contacted, and provides additional information about the thermal dynamics of the sample not measurable with stationary approaches. Conceivably, it also allows for the resolution of thermal conductance at multiple gaps; and provides a vital step towards analyzing and implementing systems making use of dynamic thermal effects in the near field.

5.1 Sample preparation and characterization

5.1.1 Sample preparation

For our near-field measurements we have used interferometric quality disks (double surface polished optical flats from Laser 2000) with 20 mm diameter and 5 mm thickness as samples. Two types of optical flats were tested: BK7 glass with a specified surface flatness of $\lambda/10$ and fused silica glass with $\lambda/20$ peak-to-valley flatness for smaller gaps ($\lambda = 633$ nm).

The gap between the lower disk (substrate) and upper disk (superstrate) is maintained by silica spheres serving as spacers, similar to Ref. [21]. The particles (monodisperse particles for research purposes from microParticles GmbH) with mean diameters of 7.38 μm , 4.64 μm , 2.79 μm , 1.3 μm , 755 nm, 500 nm, 304 nm, 143 nm and polydispersity less than 5% ensure sufficiently uniform gaps. Silica is chosen for its good mechanical and thermal stability.

Gaps were created using the following procedure: First, the glass disks are thoroughly cleaned. After ultrasonication in acetone, and then isopropanol, the flats are rinsed with deionized water. Next, the disks are placed in a 60 °C bath of water and 2% glass cleaning concentrate (Hellmanex III from Hellma Analytics) and rinsed again. Finally, the disks are blown dry with nitrogen.

An aqueous suspension is then prepared with the micro particles

such that in statistical average three 1 μl drops will contain the desired amount of particles. Three such drops are placed on one disk (the substrate). Using a hot plate the water then is evaporated leaving only the particles on the upper surface. Finally, the second disk (the superstrate) is carefully placed on top of the substrate.

The particles cover approximately $10^{-3}\%$ of the $\approx 314\text{mm}^2$ gap area. Tables B.1 and B.2 in Appendix B.1 present the expected number of particles for each measurement. The actual number is subject to statistical variations. Assuming mechanical properties of bulk fused silica, the deformation of the spheres is calculated to be less than 1%. Even with reduced mechanical properties, as expected for untreated as-synthesized particles [128], sphere deformation is likely limited to a few percent of the radius.

The smaller, 300 nm and 150 nm gaps pose a particular challenge for realization and measurement. One of problems is clustering of the particles, the number of which increases with decreasing gap size (cf. Table B.1) making clustering more likely. Hence, clustering is a small gaps problem. Although our general approach for smaller gaps is the same as for larger gaps, additional measures must have been taken which are listed in Appendix B.3.

As we will see, the substrate–gap–superstrate setup must be contacted only on the lower side. Thus, the spacer concentration can be reduced compared to conventional steady-state techniques as the upper load is less and the probability to destroy the spacers during setting up is lower. Additionally, the open upper disk

allows e. g. simple, optical in-situ gap measurements without access difficulties [119, 120].

5.1.2 Gap size measurement

To verify the existence and determine the size of the gap between the disks we measure the reflectivity of the substrate–gap–superstrate setup with a UV/Vis/NIR spectrometer (LAMBDA 1050 spectrophotometer + URA module from PerkinElmer). The reflectivity features result from Fabry–Pérot interference in the gap, with a periodicity characteristic of the gap size. This allows the gap size to be determined to high precision [119, 120]. The spectral range is limited to the near ultraviolet, visible and near infrared where the glasses are transparent. The concrete wavelength range depends on the gap size and the glass type. We used a wavelength resolution of 5 nm.

Measured and simulated reflectivity are plotted in Fig. 5.1. The calculation is based on a simple, multiple reflections assumption and given by

$$R_{\text{gap setup}} = R + T^2 R_{\text{gap}} + T^2 R R_{\text{gap}}^2 + T^2 R T_{\text{gap}}^2. \quad (5.1)$$

R and $T = 1 - R$ are the reflectivity and transmission at the air–glass interfaces. Reflectivity is obtained by taking the absolute values squared of the reflection coefficients provided by equations (2.11) and (2.12) or the well-known Fresnel equations. Note that

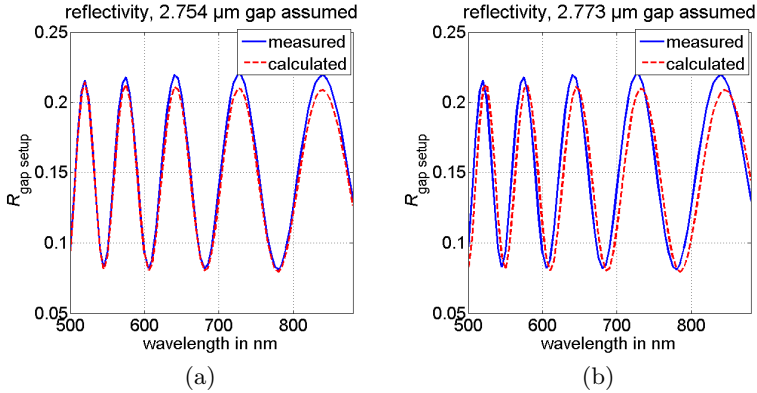


Figure 5.1: Reflectivity of substrate–gap–superstrate setup $R_{\text{gap setup}}$ with BK7 disks and $2.79\ \mu\text{m}$ particles used as gap spacers. Besides the measured reflectivity also the calculated one is shown assuming (a) a gap size of $2.754\ \mu\text{m}$ fitting the reflectivity the best and (b) a gap size representing the upper limit of the gap size error margin which turns out to be $\pm 19\ \text{nm}$. The angle of incidence is 8° , the light is unpolarized. The periodicity of the Fabry–Pérot interference in the gap is very sensitive to the gap size leading to very precise gap size determination. [From Ref. [68].]

reflectivity and transmission of light coming from the air at an angle of incidence of $\varphi = 8^\circ$ and of light coming from the glass at the respective, refracted angle of incidence are identical. Gap reflectivity and transmission are given by $R_{\text{gap}} = 1 - T_{\text{gap}}$ and

the Fabry–Pérot expression

$$T_{\text{gap}} = \frac{T^2}{1 + R^2 - 2R \cos\left(\frac{\omega}{c} 2l \cos \varphi\right)}. \quad (5.2)$$

l is the gap size. There is no Fabry–Pérot interference observed from the disk due to the large disk thickness of 5 mm. As directly seen from (5.1) the reflectivity of the gap setup takes into account up to two light interactions with the gap. We checked that taking into account more interactions has practically no more effect on the calculated $R_{\text{gap setup}}$.

To determine the gap size we first define the fitting error as the sum (over discrete measurement wavelengths) of squared differences between measured and calculated reflectivity. The fitted gap size is the one minimizing the error. The uncertainty region is the gap size range which yields errors smaller than two times the minimal error. The factor two is chosen by us to ensure a reliable but not too large error margin.

Fig. 5.1 shows the measured reflectivity for a gap created with 2.79 μm particles and two calculated reflectivities, one assuming the fitted gap size and one assuming the gap size corresponding to the upper uncertainty limit. As the figure depicts, the Fabry–Pérot features are very sensitive to the gap size. Even small deviations from the optimal value make measured and simulated reflectivities different, and therefore, the gap size fitting uncertainty is small. As the gap size is measured within a small area at one position, an additional deviation of two times $\lambda/10$

or $\lambda/20$ (peak-to-valley deviation of glass disks at $\lambda = 633$ nm) is always included in the gap uncertainty to account for possible sample non-planarity.

Small variations in the gap size across the 5×5 mm² measurement area result in locally different Fabry–Pérot patterns. These different patterns have slightly different periodicities proportional to the inverse of the gap size (remember R vs. wavenumber $\frac{\omega}{c}$ shows a unique period whereas R vs. wavelength shows an increasing period). The averaging over the measurement area results in an averaging over the Fabry–Pérot periods and thus, in an averaging over the inverse of the gap size. So $(1 / \text{obtained gap size})$ equals the average of $(1 / \text{gap size})$. In the transition region from far-field to strong near-field heat transfer, where most of our measurement points lie, the heat flux approximately scales with the inverse of the gap size (cf. Section 4.2). Consequently, the measured average heat flux is the heat flux at average inverse gap size; these are both quantities that we measure [121].

Any significant non-uniformity of the gap, and thus locally shifted interference patterns, results in the disappearance of the pattern in the measurement. Strongly non-uniform gaps can even be identified with the naked eye because they show an interference color line pattern. Furthermore, the upper disk is floating on the lower one because there is almost no friction, especially at larger gaps. If there are locations where the two samples are touching, e. g. because the spacers were destroyed there, we will

easily identify them since they cause friction and thus, lose their floating property. This and the interference color line patterns moreover allow us to make sure that after mounting the samples the gap is still intact.

5.2 Dynamic measuring technique

The basis of our measurement technique is the transient plane source (TPS) method, commonly used in the determination of bulk thermal parameters [126,127]. In this approach, a thin disk consisting of a nickel double spiral embedded in Kapton [129] insulation, acts both as a heat source and temperature sensor. To perform a measurement, the sensor/heater is brought into contact with the material under investigation, and a step power input function is applied. The temperature transient is then recorded by measuring the changing resistive load of the sensor/heater which is a function of temperature. The transient depends on the heat conductance of the environment with which the sensor/heater is in contact.

The thermal properties, including any potential boundary effects, of the surrounding material influence the shape of this temperature transient. As each bulk thermal characteristic affects heat transport in a distinct way, the transient contains enough information to simultaneously extract thermal conductivity and diffusivity without knowledge of the specific heat capacity [126,127]. (Our measurements have been conducted using

a commercially available TPS 2500 S from Hot Disk AB, and a Kapton sensor/heater of 19.8 mm diameter provided by this same company.) To our knowledge, the here presented work is the first extension of the TPS technique to near-field measurements.

Once the gap setup is prepared and the gap size measured, the setup is placed onto the TPS sensor/heater. To improve the thermal contact 1 ml of a vacuum suitable thermal paste (Apiezon L Grease from M&I Materials Ltd) is applied between sensor/heater and substrate. The setup is lying on a thermal insulator (Vacupor from Morgan Advanced Materials Porextherm, conductivity at 1 mbar $\approx 5 \text{ mW m}^{-1} \text{ K}^{-1}$) and a piece of aluminum foil is placed between sensor/heater and insulator to reduce thermal losses via conduction and radiation. The setting is visualized in Fig. 5.2.

To mitigate both convective and conductive heat flow from the boundaries, the whole setup is then placed in a vacuum chamber reaching a pressure of approximately 10^{-5} mbar. The glass disks lie freely on the sensor/heater, with only the upper disk touching two nylon screws of a sample holder. (Without the holder the upper disk would slide away as friction is extremely low.) The thermal conduction through the screws adds to the side radiation losses. But since nylon is low conducting and due to the very small contact force the contact resistance is high, the effect of the screws is assumed to be negligible.

Two measurements are performed. First, the temperature tran-

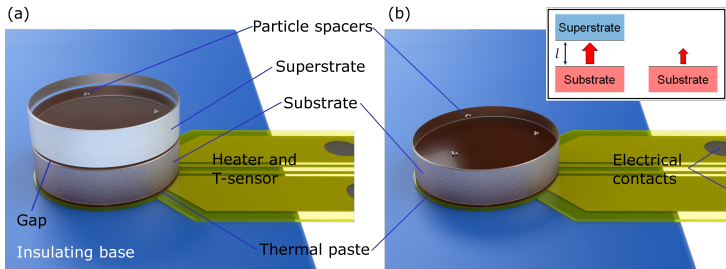


Figure 5.2: Schematic of experimental setup. (a) Two optical glass disks 20 mm in diameter (substrate and superstrate), separated by micro/nano particle spacers, are placed on the TPS sensor/heater. After the transient has been recorded the upper disk is removed, keeping the remaining setup unchanged, and a reference measurement (b) is made. For easier visualization particles size and TPS sensor/heater thickness are shown not to scale. The inset illustrates the situations at the gap / substrate top. The heat flux from hot substrate to cold superstrate through a gap with small size l (left) is larger than far-field radiation from the substrate top (right). For thermal radiation around room temperature the glass disks are opaque. [From Ref. [68].]

sient of the gap setup is measured without modification. This setup is called the gap sample. Next, the superstrate is carefully taken away such that the rest of the setup remains otherwise unchanged, Fig. 5.2. This second measurement serves as a reference, thus, this setup is called the reference sample. For both measurements, a power input of 40 mW is applied to the sensor/heater for 640 s. In Fig. 5.4 two examples of measured gap

transients for gap sizes of 315 nm and 2.75 μm are shown for BK7 and for fused silica along with their reference transients. When the glass superstrate is present, near-field radiative heat transfer allows additional heat to escape the substrate, lowering its temperature at constant heating power (Fig. 5.2 inset). The smaller the gap the stronger this effect is. Note that the transients begin to differ significantly only once the heat front originating from the sensor/heater has reached the upper surface of the substrate, confirming the validity of the reference.

5.3 Modeling and fitting

As the measurement is dynamic, the thermal conductance of the gap cannot be read out directly. Rather, this information must be extracted from the shape of the transient by a fitting procedure. To accomplish this fitting, we utilize two models: a simple 1-dimensional (1D) stack and a more comprehensive, hence complex, 2-dimensional (2D) finite-difference-time-domain (FDTD) gaped cylinder [130, 131]. The underlying assumptions of the 1D model, 1-dimensionality and linear response, are verified by the 2D FDTD model.

5.3.1 1-dimensional model

The framework of the 1D model is illustrated in Fig. 5.3. The glass disks serving as substrates and superstrates are divided into

N layers, each with a thermal capacity $mc_{1/2,j}$, and a relative temperature $\Delta T_{1/2,j}$ with respect to the thermal equilibrium temperature $T_0 = 294\text{ K}$ ($\pm 1\text{ K}$). $N - 1$ resistances $R_{1/2,j}$ separate these layers, comprising the thermal resistivity of the disks. Additionally, the TPS sensor/heater has a capacity mc_{sen} and temperature ΔT_{sen} and the gap as well as the sensor/heater-substrate contact are represented as resistances R_{gap} and R_c .

At $t = 0$ heat with a power of $P_{\text{in}} = 40\text{ mW}$ is applied to the sensor/heater. As time progresses, this input power to the sensor/heater is countered by conductive and radiative losses to the base and radiative losses to free space. We model these additional effects as the conductance h_{sen} and emissivities ε , assuming linear dependence on ΔT . The validity of this assumption rests on the fact that ΔT is small compared to T_0 , and is one of the reasons a small input power is used. The sensor/heater is only a few tens of microns thick in total, and so losses to its sides are neglected.

The 1D model provides an analytic solution for the layer temperatures as a function of time, including the sensor/heater temperature. To obtain the temperatures, we first consider the heat equation for each individual layer (heat capacity mc). Each equation has the form

$$\frac{d\Delta T}{dt} = \frac{1}{mc} \frac{d\Delta Q}{dt} = \frac{1}{mc} P_{\text{in,total}} \quad (5.3)$$

where ΔQ is the thermal energy of the layer relative to the initial

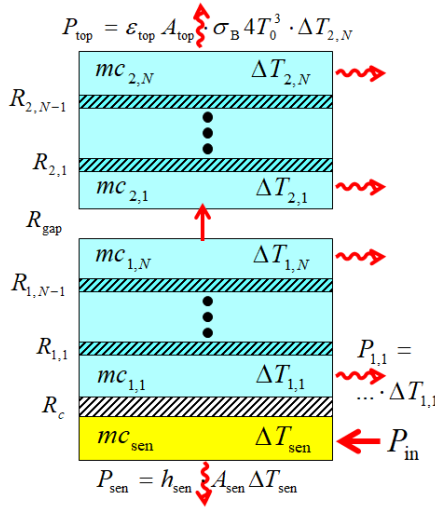


Figure 5.3: Illustration of the 1-dimensional (1D) model. The model consists of alternating layers of thermal capacities mc at absolute temperature $\Delta T + T_0$ and thermal resistances R . The system is initially in thermal equilibrium at temperature T_0 ($\Delta T = 0$). At time $t = 0$ a thermal power of $P_{\text{in}} = 40 \text{ mW}$ is applied to the TPS sensor/heater. The system loses energy via conduction and radiation to the bottom P_{sen} and via radiation to the top P_{top} and the sides $P_{1/2,j}$. [From Ref. [68].]

equilibrium. For a layer j in the middle of the sample, the total

input power is

$$P_{\text{in,total } 1/2,j} = \frac{\Delta T_{1/2,j-1} - \Delta T_{1/2,j}}{R_{1/2,j-1}} + \frac{\Delta T_{1/2,j+1} - \Delta T_{1/2,j}}{R_{1/2,j}} - \varepsilon_{1/2,j} A_{1/2,j} \sigma_B 4T_0^3 \Delta T_{1/2,j}. \quad (5.4)$$

Similar expressions can be found for the outer sample layers and the sensor/heater layer. The equations (5.3) for all capacity layers, combined with the expressions for the input power (5.4), yield a system of linear differential equations

$$\frac{d}{dt} \Delta \mathbf{T}(t) = \mathbf{M} \cdot \Delta \mathbf{T}(t) + \mathbf{P}_{\text{in}}, \quad (5.5)$$

with initial condition

$$\Delta \mathbf{T}(t = 0) = 0. \quad (5.6)$$

We collected all temperatures in one vector

$$\Delta \mathbf{T} = \left(\Delta T_{\text{sen}} \quad \Delta T_{1,1} \quad \cdots \quad \Delta T_{2,N} \right)^T. \quad (5.7)$$

The \mathbf{P}_{in} vector is

$$\mathbf{P}_{\text{in}} = \left(\frac{P_{\text{in}}}{mc_{\text{sen}}} \quad 0 \quad \cdots \quad 0 \right)^T \quad (5.8)$$

and the tridiagonal \mathbf{M} matrix has the entries

$$\begin{aligned}
 M_{1,1} &= -\frac{1 + h_{\text{sen}}A_{\text{sen}}R_c}{R_c mc_{\text{sen}}}, \\
 M_{1,2} &= \frac{1}{R_c mc_{\text{sen}}}, \\
 M_{2,1} &= \frac{1}{R_c mc_{1,1}}, \\
 M_{2,2} &= -\frac{R_c + R_{1,1} + \varepsilon_{1,1}A_{1,1}\sigma_B 4T_0^3 R_c R_{1,1}}{R_c R_{1,1} mc_{1,1}}, \\
 M_{2,3} &= \frac{1}{R_{1,1} mc_{1,1}}, \\
 M_{j+1,j} &= \frac{1}{R_{1,j-1} mc_{1,j}}, \\
 M_{j+1,j+1} &= -\frac{R_{1,j-1} + R_{1,j} + \varepsilon_{1,j}A_{1,j}\sigma_B 4T_0^3 R_{1,j-1}R_{1,j}}{R_{1,j-1}R_{1,j} mc_{1,j}}, \\
 M_{j+1,j+2} &= \frac{1}{R_{1,j} mc_{1,j}}, \\
 M_{N+1,N} &= \frac{1}{R_{1,N-1} mc_{1,N}}, \\
 M_{N+1,N+1} &= -\frac{R_{1,N-1} + R_{\text{gap}} + \varepsilon_{1,N}A_{1,N}\sigma_B 4T_0^3 R_{1,N-1}R_{\text{gap}}}{R_{1,N-1}R_{\text{gap}} mc_{1,N}}, \\
 M_{N+1,N+2} &= \frac{1}{R_{\text{gap}} mc_{1,N}}, \\
 M_{N+2,N+1} &= \frac{1}{R_{\text{gap}} mc_{2,1}}, \\
 M_{N+2,N+2} &= -\frac{R_{\text{gap}} + R_{2,1} + \varepsilon_{2,1}A_{2,1}\sigma_B 4T_0^3 R_{\text{gap}}R_{2,1}}{R_{\text{gap}}R_{2,1} mc_{2,1}},
 \end{aligned}$$

$$\begin{aligned}
M_{N+2,N+3} &= \frac{1}{R_{2,1}mc_{2,1}}, \\
M_{N+j+1,N+j} &= \frac{1}{R_{2,j-1}mc_{2,j}}, \\
M_{N+j+1,N+j+1} &= -\frac{R_{2,j-1} + R_{2,j} + \varepsilon_{2,j}A_{2,j}\sigma_B 4T_0^3 R_{2,j-1}R_{2,j}}{R_{2,j-1}R_{2,j}mc_{2,j}}, \\
M_{N+j+1,N+j+2} &= \frac{1}{R_{2,j}mc_{2,j}}, \\
M_{2N+1,2N} &= \frac{1}{R_{2,N-1}mc_{2,N}}, \\
M_{2N+1,2N+1} &= -\frac{1 + (\varepsilon_{2,N}A_{2,N} + \varepsilon_{\text{top}}A_{\text{top}})\sigma_B 4T_0^3 R_{2,N-1}}{R_{2,N-1}mc_{2,N}}.
\end{aligned} \tag{5.9}$$

The solution to this system of linear differential equations is

$$\Delta \mathbf{T}(t) = \text{expm}(\mathbf{M}t) \mathbf{M}^{-1} \mathbf{P}_{\text{in}} - \mathbf{M}^{-1} \mathbf{P}_{\text{in}}. \tag{5.10}$$

Here $\text{expm}(\circ)$ is the matrix exponential. The model and the corresponding equations for the reference measurements with only one glass flat are analog to the gap model.

We divided the total thermal capacity of one glass disk into $N = 10$ equal capacity layers and the total thermal resistance into $N - 1 = 9$ equal resistance layers. Accordingly, the lateral surface area is also divided into $N = 10$ equal areas $A_{1/2,j}$. Finer discretization, accompanied by larger N , does not further improve the accuracy of simulation results, however, would increase computation time.

Glass disks and TPS sensor/heater have a diameter of 20 mm.

The disks are 5 mm thick. One BK7 disk weighs $m_{\text{BK7}} = 3.92$ g and fused silica disk $m_{\text{FS}} = 3.46$ g. For our modeling we employ a specific capacity of $c_{\text{BK7}} = 0.82 \text{ J g}^{-1} \text{ K}^{-1}$ and a conductivity of $\lambda_{\text{BK7}} = 1.11 \text{ W m}^{-1} \text{ K}^{-1}$ for BK7. For fused silica the values are $c_{\text{FS}} = 0.755 \text{ J g}^{-1} \text{ K}^{-1}$ and $\lambda_{\text{FS}} = 1.38 \text{ W m}^{-1} \text{ K}^{-1}$. They are taken from the respective datasheets [132, 133] and agree with independent measurements (performed with TPS 2500 S from Hot Disk AB). Only the specific capacities are slightly modified by a few percent compared to the datasheets to improve fitting. Such variations are not unusual and depend on manufacturing procedures, glass composition, etc. Resistances are calculated via $R_{1/2,j} = \frac{5 \text{ mm}}{(N-1)\lambda\pi(10 \text{ mm})^2}$. The sensor/heater capacity is $mc_{\text{sen}} = 85 \text{ mJ K}^{-1}$ which is increased above the value provided by the sensor/heater manufacturer to account for the thermal paste.

The fitting procedure proceeds as follows: First, we fit the reference sample measurements; determining the contact resistance R_c , top emissivity ε_{top} , side emissivity $\varepsilon_{\text{side}}$ (we assume all side emissivities to be equal $\varepsilon_{1/2,j} = \varepsilon_{\text{side}}(\forall j)$), and sensor/heater loss conductance h_{sen} . ε_{top} and $\varepsilon_{\text{side}}$ are identical for all BK7 references and all fused silica references. R_c and h_{sen} vary from measurement to measurement as the sensor/heater–substrate contact is intrinsically variable due to varying thickness and morphology of the thermal paste layer used to contact the sensor/heater to the glass disk and due to small differences in the position where the sensor/heater lies on the insulator.

The fitted figures are $\varepsilon_{\text{top}} = \varepsilon_{\text{side}} = 0.85$ for BK7 and $\varepsilon_{\text{top}} = \varepsilon_{\text{side}} = 0.89$ for fused silica. Note that these fits were compared against absorptivity measurements from a Fourier Transform Spectrometer (FTIR) (VERTEX 70 from Bruker) and found to be in agreement, see Fig. B.2 in Appendix B.2. (In principle the top and side emissivities can be different due to different roughness.) Fitted R_c values were found to range from 5 to 11 K W^{-1} , while sensor/heater loss conductance h_{sen} was found to vary from 0.3 to 5.5 $\text{W m}^{-2} \text{K}^{-1}$ (below the blackbody heat flux of 5.76 $\text{W m}^{-2} \text{K}^{-1}$ at 294 K). Considering all the possible variations from measurement to measurement, some mentioned above, the large ranges of R_c and h_{sen} are reasonable. These fluctuations pose no problem to the measuring technique as their influence is taken into account. Only changes from gap to reference measurement are problematic and will be discussed next.

Next, the gap sample measurement is fit using only one parameter, the gap resistance R_{gap} . Fitted R_{gap} values ranged from 35.2 K W^{-1} for the smallest gap to 605 K W^{-1} for the largest gap. Fitted curves together with the measured ones are shown exemplarily for a 315 nm and a 2.75 μm gap in Fig. 5.4. Fits and measurements agree very well.

We note that the two step fitting procedure for this model is well justified by the similarity of the reference and gap measurements; which ensures no changes of other parameters between gap and reference measurement. Only the sensor/heater loss parameter h_{sen} might vary due to the change in weight. We estimated from

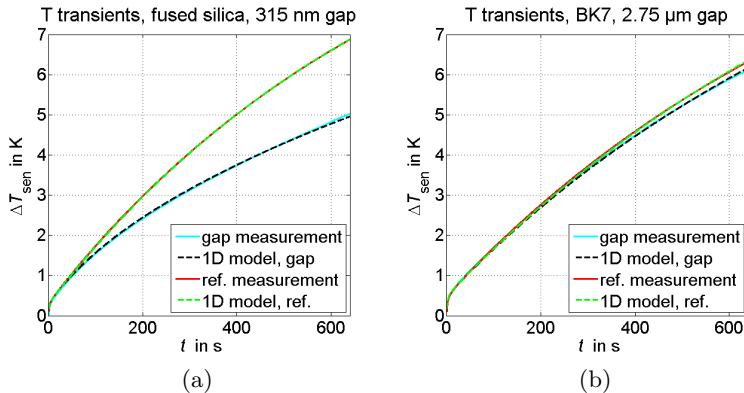


Figure 5.4: Measured and fitted temperature transients. Sensor/heater temperatures ΔT_{sen} over time for an input power $P_{\text{in}} = 40 \text{ mW}$ switched on at $t = 0$. Before ($t < 0$), the system was in thermal equilibrium at $T_0 = 294 \text{ K}$. The samples are composed of (a) fused silica and (b) BK7 glass disks. The measured gap is (a) 315 nm or (b) 2.75 μm , respectively. When near-field heat transfer is present (gap sample measurement) additional heat escapes the substrate, lowering its temperature relative to the reference sample measurement, during which only far-field radiation is present. The smaller the gap the stronger the cooling of the substrate and the larger the separation of gap and reference transients. The optical properties of the glasses are only minorly different, see Appendix B.2, such that they do not significantly influence the heat flux. The fitted 1D model curves agree very well with the measured ones. [From Ref. [68].]

the largest gap measurement – where gap heat flux and far-field emission are almost identical – that h_{sen} does not change by more

than 10% of the blackbody heat flux. R_c could theoretically also vary due to the change in weight but it is proportional to the initial temperature increase of the sensor/heater during the first few seconds which turned out to be stable. So changes in R_c are negligible.

Qualitatively, the transient behavior can be described as follows: In the first few seconds the sensor/heater heats up to few hundred millikelvin above the ambient environment. This increased temperature is necessary for the heat to begin to mainly flow into the substrate (or the insulating base) instead of increasing the sensor/heater temperature. It looks like a temperature needed to bridge the contact resistance R_c , although the behavior is of course linear and the temperature increase scales with the input power. Because the thermal mass of the sensor/heater, mc_{sen} , is small the temperature increases quickly. The larger R_c is, the larger this initial temperature increase of the sensor/heater needs to be such that almost all the input power flows into the substrate. Note that as $R_c \ll \frac{1}{h_{\text{sen}}A_{\text{sen}}}$ sensor/heater losses are irrelevant for these dynamics.

After this initial heating has occurred, the heat front begins moving from the bottom to the top of the substrate. This middle time span captures the bulk thermal properties of the sample. Separation between the two measurements begins as soon as the heat front has reached the top of the substrate. For reference sample measurements and gap sample measurements employing large gaps, in which case the upper disk practically keeps its

initial temperature, the remaining dynamic is then governed by the sensor/heater and substrate heating up together while losing heat at the sensor/heater, the substrate side and the top / gap. The large thermal mass of the disks makes this dynamic significantly slower. Any changes to the top emissivity or gap conductance alter the shape of this portion of the transient. For smaller gaps, the near-field heat flux is large enough to allow the superstrate disk to heat up significantly, producing dramatic alterations to the shape of the transient curve.

In principle, all the variables can be obtained directly from the gap measurement without the need for a reference. Following the above description, unique identification is possible as each parameter influence the transient in a different way. E.g. R_c is proportional to the initial steep temperature increase in the first few seconds, whereas R_{gap} start to influence the transient only after some time, the time the two curves in Fig. 5.4 start to deviate.

However, in our particular setup, the sensor/heater losses h_{sen} and gap conductance $\frac{1}{R_{\text{gap}}}$ have a similar effect on the transient; and while differentiation is theoretically possible, due to the delayed influence of the gap conductance vs. the non-delayed influence of the sensor/heater losses, it is not practical. An improved design with a better, e.g. active, thermal insulation may reduce h_{sen} to negligibly small values and render the problem void. Similarly, sensor/heater losses h_{sen} and side losses $\varepsilon_{\text{side}}$ have a combined effect, not distinguishable in practice. However, a dif-

ferentiation is not needed to obtain the gap heat flux. Nevertheless, the two-step gap-reference measurement procedure outlined above provides extra information without introducing new unknowns, and increases both the certainty and accuracy of the fitted results.

5.3.2 2-dimensional model

The 1D model makes two major simplifications, the applicability of which must be checked. Namely, the model neglects any radial temperature gradients / heat fluxes, and linearizes emitted radiation with respect to ΔT . To check that the effect of these assumptions is small, we utilized a 2-dimensional (2D) finite-difference time-domain (FDTD) model [130]. A 3rd dimension is not necessary as the system is rotationally symmetric.

The 2D model consists of three material domains stacked vertically, with identical diameters but possibly different heights. The lowest material domain represents the TPS sensor/heater. Its diffusivity and conductivity are adjusted to yield a low heat capacity and negligible inner temperature gradients. The upper two domains represent the substrate and superstrate. Separating the three regions are two thermal resistances / conductances representing possible gaps (linear in temperature difference). The lower inter-block resistance determines the contact resistance of the substrate and sensor/heater, and the upper resistance the conductivity of the gap. The reference setup is modeled by ad-

justing the upper block heights and shorting the upper inter-block resistance, such that the upper two blocks appear as a single domain.

Heat flux is applied uniformly at bottom boundary of the lowest domain. At exterior boundaries, each domain is assumed to radiate based on its emissivity. The thermal radiation is modeled properly proportional to $(\Delta T + T_0)^4 - T_0^4$ or linearized proportional to $4T_0^3\Delta T$. Inside the material domains the FDTD scheme is employed following the Crank–Nicholson method [130] in cylindrical coordinates. The cell equations are analogues to those given by Dawson et al. [131] except for the added radiative heat loss at boundary elements.

Thermal transients simulated with the 2D model show only minor differences compared with the 1-dimensional method. In Fig. 5.5 calculated temperature profiles for both the gap and reference sample setups are displayed. Two things are observed. First, although small radial changes are visible, the heat is mainly flowing in axial direction, resembling a 1-dimensional situation. Second, the temperature differences between the hotter core and cooler exterior boundary amounts to only few 100 mK even for long simulation times. It means the inner sample resistance overall has no big influence on the thermal dynamics. The reason for this agreement comes from the nearly 1-dimensional character of the system we have considered. The sensor/heater covers the whole sample cross section, and so heat flows mainly in axial direction.

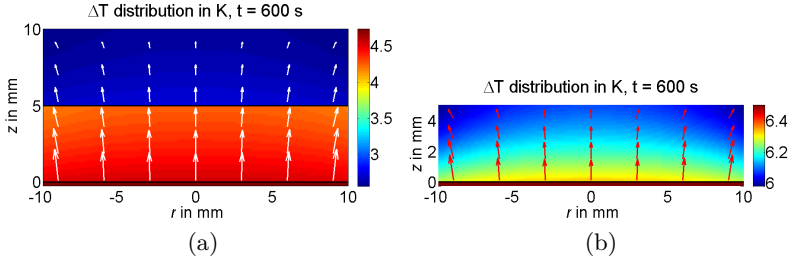


Figure 5.5: Temperature distribution (ΔT distribution) in (a) the gap sample setup and (b) the reference sample setup at $t = 600$ s. Both setups are rotationally symmetric and thus, simulations and illustrations show only the axial and radial dimensions. The sensor/heater, seen as the low homogeneously colored slab, is assumed to be 0.25 mm thick and have negligible inner resistance. These 2-dimensional simulations are based on the parameters obtained from the fit of the 300 nm gap measurements. The white and respectively red arrows indicate the direction and strength of the heat flux, which is proportional to the negative temperature gradient. Despite the large side emissivity of $\epsilon_{\text{side}} = 0.89$ the heat flows predominantly in axial direction. [From Ref. [68].]

Slightly larger differences are observed in the switch from linear to non-linear emission, but these too are found to be mostly inconsequential. Specifically, the introduction of non-linearity is found to increase the emitted power and, thus, decrease the sensor/heater temperature, check Fig. 5.6. This effect is most pronounced at larger temperatures. Yet, overall linearization has also only a weak influence on the transients. Although the

2D model is slightly more accurate, we generate our results with the 1D model because of its exact (analytic) solution and its advantageous computation time.

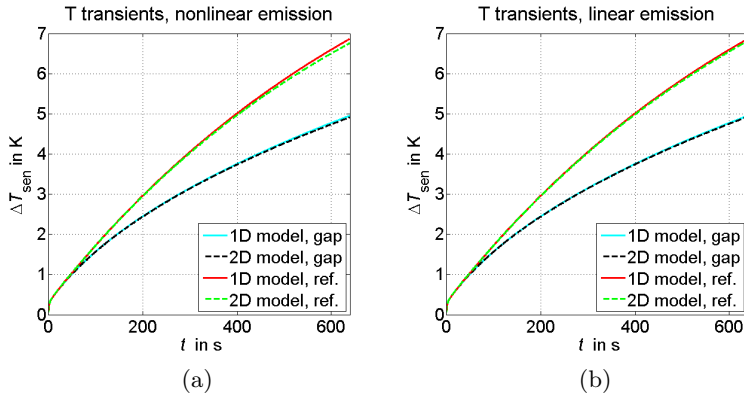


Figure 5.6: Simulated temperature transients. The simulations are based on the parameters obtained from the fit of the 300 nm gap measurements. For both, 1- and 2-dimensional models, the same parameters are used. The 2D model simulations assume (a) a nonlinear, T^4 emission (including nonlinear sensor/heater losses) and (b) a linearized emission as in the 1D model. In the linearized emission case (b) both models agree very well. Accounting for the radial inner sample resistance practically does not change the transients. The nonlinear emission is stronger than the linearized one leading to slightly weaker heating up, as seen in (a). [From Ref. [68].]

5.4 Measurement results

Fig. 5.7 shows the heat transfer coefficient (HTC) H normalized to the blackbody HTC $H_{\text{BB}} = 5.76 \text{ W m}^{-2} \text{ K}^{-1}$ (at 294 K) for different gap sizes. Each of the points corresponds to one measurement where $H = \frac{1}{R_{\text{gap}}\pi(1 \text{ cm})^2}$. The error margin in the horizontal axis corresponds to the error in the determination of the gap size (see Section 5.1.2). The relative gap size error increases for the smaller gaps.

The vertical error margins in Fig. 5.7 represent our measurement inaccuracy and combine the effects from fitting procedure and parameter changes between gap and reference measurements. The uncertainty for each measurement is the quadrature of an up to 8% fitting uncertainty, and a 10% variation accounting for possible changes in the sensor/heater losses h_{sen} between gap and reference measurement. The individual contributions are not summed up but the square root of the sum of their squares is taken (root sum square). This leads to an estimated inaccuracy of up to $\pm 13\%$.

For the 150 nm gap the resistance between the substrate and superstrate becomes comparable to the disks' inner resistance. Consequently, the influence of this variable on the transient is weaker than for larger gaps and the variation accounting for possible changes in sensor/heater losses becomes 20% instead of 10%. Additional details are provided in Appendix B.3.

To confirm the reproducibility of the measured results we re-

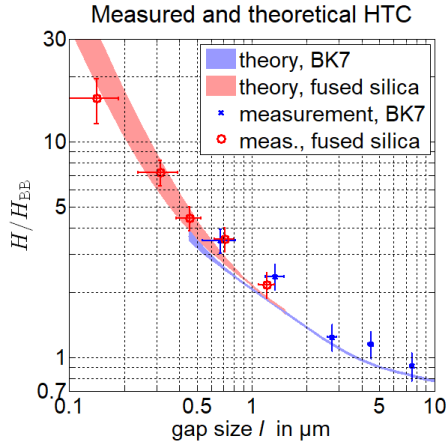


Figure 5.7: Gap dependent heat flux. Comparison of theoretical and measured radiative heat transfer coefficients (HTC) H versus gap size, normalized by the blackbody result H_{BB} . Colored areas represent the possible range of theoretical heat flux due to uncertainties in the samples' optical properties. All measurements contain a small contribution by solid thermal conduction through the spacers; check the text and Appendix B.1. Gap size error margins (horizontal) are small for large gaps and thus hardly visible underneath the symbols. Overall strong agreement is observed between theory and experiment. [From Ref. [68].]

peated measurements for the fused silica optical flats with $1.3\ \mu\text{m}$ gap. In addition, the number of deposited microspheres (spacers) was systematically decreased in five measurements to determine the influence of the heat conduction through the microspheres on the apparent radiative HTC. Also, the measurement with the

smallest number of particles was repeated four times to check the reproducibility. For additional details see Appendix B.1. These series of measurements exhibited no clear trend of the heat flux and a standard deviation of 7.5% which is within the measurement accuracy.

The theoretical areas are calculated using the well-known integral expression for the near-field heat flux between two half-spaces, as derived in Section 2.6.2 and discussed in Section 4.2. Since transmission through our disks is zero (in the mid infrared), we can utilize this simple, two homogeneous halfspaces setup for our calculations and don't need to worry about the finite thickness of the disks. All media are nonmagnetic. The thermal transients with their seconds-range or even minutes-range dynamics are slow and we can utilize the stationary theory of near-field heat transfer.

As the optical properties of our samples are known only within a given margin of uncertainty the theoretical HTC is represented as an area, rather than single line. The optical properties used are examined in Appendix B.2. Independent of the inaccuracy, we find both glasses to have a spectral region in the mid infrared with negative (real part of the) permittivity and thus supporting surface modes which we discussed in the context of near-field heat transfer in Section 4.2.

The measured HTCs are observed to be in good agreement with the theoretically predicted range of near-field heat transfer. With decreasing gap size the HTC predictably increases due to the

increasing contribution of evanescent modes [4, 5]. Besides confirming our dynamic measurement approach, the measurements themselves are notable. The recorded near-field heat flux ≈ 16 times above the blackbody for the 150 nm gap is presently the largest recorded radiative enhancement for centimeter sized samples at ambient temperatures. At the smallest gap size the surface modes [16, 100], supported by our fused silica samples, create a significantly larger enhancement of the heat flux as compared to purely dielectric samples [123]. Employing the mean optical properties from Appendix B.2, at the smallest gap surface modes are calculated to sustain around 77% of the total radiative heat flux. We also note that the creation of a gap as small as 150 nm over macroscopic cross sections has previously been reported in only one other experiment [123], where only an 8.4 heat flux enhancement over blackbody was demonstrated.

For larger gaps a small systematic overestimation of the HTC is observed. We attribute this $\approx 20\%$ offset to the solid conduction through the supporting microspheres. Their contribution to the total gap conductance consists of a series of resistances, namely the inner sphere resistance and the two contact resistances. While the inner resistance decreases towards zero the smaller the spheres become, the contact resistances may vary but will not vanish. Therefore, the particles' contribution is reduced at smaller gap sizes because the solid conductance approaches a constant value, the contact conductance, and the radiative conductance approaches square of inverse gap size dependency.

However, it should be noted that the HTC is unequivocally dominated by radiation for all investigated gap sizes. Appendix B.1 details the solid thermal conduction through the spacers.

5.5 Discussion of new dynamic technique

The additional information contained in any dynamic or transient approach is both a strength and weakness compared to steady-state measurement techniques. Fundamentally, the measurement is not direct, and the desired parameters are only obtained by iteratively solving an inverse problem. Even for a relatively simple system, like the one we have considered, this introduces the need to carefully consider issues like numerical accuracy, initial values for system parameters, and generally increases the complexity of data analysis.

In return, the strict conditions that are required for a stationary measurement are relaxed. Steady-state measurements require at least three sensors: one sensor for measuring the temperature on each side of the gap, and additional flux sensor for measuring either the heating or cooling power. (Note that the flux sensor may be incorporated as part of the temperature sensor as it is in the TPS method.) Crucially, there must be only one undetermined thermal resistance between these sensors. If it is not possible to isolate the near-field radiative heat transfer in this way, then prior to measurement all other heat conduction pathways must be properly modeled before any measurements can

be made.

Comparatively, in a transient approach the influence of a resistance varies relative to its position from the sensor/heater. The further away from the sensor/heater it is, the later its influence starts. This segregation of effects based on their temporal influence range has three primary benefits. First, it allows the gap resistance to be distinguished from other (parasitic) resistances in the system from collected data (a posteriori). Second, it allows the sensor/heater to be moved away from gap, separating and protecting the gap which is probed from (influences of) the measuring setup. Third, it allows for the simultaneous determination of solid state thermal characteristics that must be assumed in steady-state measurements, and would allow for more than one gap resistance to be determined in a possible multi-gap setup [31]. As mentioned in the chapter introduction, there may also be significant differences in the time needed to perform an individual measurement. For a dynamic measurement the characteristic duration is determined by the distance that must be traveled by the thermal wave front before the influence of the unknown parameter begins to affect the shape of the transient.

In some experiments, to isolate the near-field heat flux from other parasitic heat fluxes, the gap size has been modulated with a constant frequency and only the heat flux varying with the same frequency has been analyzed [7, 20, 25, 110, 116, 122]. Further, analogues of 3ω measuring method have also been pursued [111, 116, 122]. These are certainly counterparts to the re-

ported technique, but they are not dynamic in sense that measurement remains steady-state. At present, no analogues of the dynamic laser flash, transient line or plane source methods used routinely in measuring solid thermal properties exist for near-field heat transfer measurements.

For academic settings, particularly if all the other thermal characteristics of a given sample are known, these advantages are clearly minimized. Generally, samples are very small and can be carefully designed with multiple micro- / nanofabrication steps. Nevertheless, as near-field technologies develop it is highly likely that this will not remain the case. Under even slightly different circumstances, the comparative ability of a dynamic approach to quickly and reliably characterize a variety of samples and reduce design complexity could become critically important. These considerations extend to any transient technique, and the method we have presented here could, for example, be adjusted to a laser flash system. It is also worth noting that dynamic measurements are a vital step towards analyzing and implementing systems which make use of dynamic effects which, by definition, cannot be investigated by steady-state measurements.

In summary, we have developed a new, dynamic near-field radiative heat transfer measuring method, the first of its kind for this application. Using gap and reference sample types employing two different glass materials and gaps varying from 7 μm to 150 nm we have experimentally confirmed the ability of the approach to accurately measure near-field thermal radiative heat

transfer. For the 150 nm gap the measured heat flux is as large as ≈ 16 times above the blackbody. Advantages of this method include simple and precise referencing, the lack of required micro- / nanofabrication, and the ability to temporally resolve the influence of various thermal parameters; which helps to distinguish the gap conduction from other effects like interface resistances. The method can also easily be modified and extended. Our results bring to light so far neglected transient measurement techniques, and open the door for the investigation of dynamic radiative effects.

Chapter 6

Conclusions and outlook

The broader topic of this thesis is thermal radiation. In particular, we have looked at the phenomenon of near-field radiative heat transfer and at the effects of hyperbolic metamaterials on thermal radiation.

The near-field effect is scientifically interesting because it can feature characteristics which are very unusual for thermal radiation. The heat fluxes can be orders of magnitude larger than the blackbody heat flux. Furthermore, it can be spectrally narrowband. But also practically the effect takes on greater significance. It may allow new applications or increase application efficiencies, like spectral imaging or thermal rectification. Near-field heat transfer is also something that must be handled in the miniaturization of electronics, sensors etc.

Metamaterials can possess unique optical properties which be-

come attractive in theory and for utilization. HMMs are extremely anisotropic leading to negative refraction and lensing applications. For thermal radiation the gigantic density of electromagnetic states of HMMs is the crucial aspect.

First, we observed that thermal radiation inside hyperbolic media has very different properties compared to a blackbody emitting into vacuum or more generally into a dielectric. In the ideal “hyperbolic blackbody” the spectral heat flux scales proportional to the maximal wavevector squared k_{\max}^2 instead of the free space wavevector squared $(\frac{\omega}{c})^2$, as for the normal blackbody. Consequently, the total heat flux scales $\propto k_{\max}^2 T^2$ instead of $\propto T^4$.

A dispersive HM has only a limited hyperbolic spectral range. The heat flux depends on the position of the Bose–Einstein cut-off which prevents modes at frequencies above a cutoff frequency ($\propto T$) to be thermally populated. However, as long as the hyperbolic range is not completely cut off properties remain very different from a blackbody. Nevertheless, in both cases the heat flux inside HMs is orders of magnitude higher than blackbody heat flux. Similar characteristics hold for other thermal quantities like the energy density.

Because the radiative heat flux is so large inside HMs it can theoretically even at room temperature surpass the solid heat flux. This is rarely observed and when done so the realization is typically based on strongly reducing the solid flux rather than increasing the radiation. Whenever large radiative heat fluxes are required HMs / HMMs could be the right choice.

Experimental verification of the theoretical predictions is still missing. Besides, the impact of dissipation on the heat flux and the radiative heat conductivity must be looked at in detail. Once these issues are understood studies could focus on applying the characteristics e. g. in TPV systems.

The second issue we looked at is the penetration depth of near-field heat fluxes into HMMs. Near-field radiative heat fluxes are particularly large when the bodies exchanging heat support many high- k modes. These modes can be surface or hyperbolic modes. When it comes to the penetration into the bodies, surface and hyperbolic modes behave very differently due to their different nature. Surface modes are bound to the surface whereas hyperbolic modes are propagating in the bulk. Therefore, along with large near-field heat fluxes HMs and HMMs provide large penetration depths of the same.

This is potentially important for nTPV systems. On the one hand, a photovoltaic cell which does not support high- k modes deteriorates the performance improvement due to the near-field effect. On the other hand, a photovoltaic cell that supports high- k modes must convert the huge radiation into electricity. Otherwise the whole idea of near-field TPV makes no sense. And a deep penetration into the cell is essential for the conversion.

Our investigation is just the first step towards a potential hyperbolic photovoltaic cell. A concrete concept how to combine hyperbolicity with photovoltaic effect must be developed before a cell can be realized.

The above two topics, heat transfer inside HMs and penetration depth of near-field heat flux into HMs, are closely related. Both deal with radiative heat fluxes inside HMs. Only the origins of the heat fluxes are different. So scientific results in one topic could benefit the other one, or efforts can be combined to further investigate the physics and applications of thermal radiation in HMs / HMMs.

Moreover, we have had a brief look at the far-field thermal emission characteristics of HMMs. If designed properly they can exhibit a band-edge emissivity and thus serve as a selective emitter in a high-efficiency TPV system. This characteristic has already been demonstrated experimentally. However, for high-efficiency TPV operation temperatures above 1500 K are required. Thermal stability of HMMs at such high temperatures remains an unsolved challenge.

On the one hand, smaller HMM periods better satisfy the effective medium approach, increase the cutoff wavenumber k_{\max} and are beneficial for realizing large heat fluxes. On the other hand, when layers or wires become too small the optical properties of the constituent media can change, especially of metals [51]. Such changes must be taken into account when designing HMMs for whatever purpose.

The physical principles limiting the density of propagating modes inside natural HMs (by a k_{\max} ?) are not clearly understood yet. Although it is known that material cannot be polarized when the spatial oscillation period is smaller than an atom – so without

doubt there is a limitation – it is not known which mechanisms exactly lead to it and how it can be described. Spatial dispersion (nonlocality) is one possibility. Whether the cutoff is hard or rather smooth and which values it assumes must be studied.

Finally, we developed a dynamic near-field radiative heat transfer measurement technique. We measured heat fluxes up to 16 times larger than blackbody radiation across cm^2 -sized cross sections. The gaps ranged from above $7\ \mu\text{m}$ down to around $150\ \text{nm}$. Measured heat fluxes agree with theoretical predictions, confirming the validity of our technique.

The main advantage of our measurement method in comparison with conventional steady-state methods is its practicability. A measurement is fast and easy to setup up. It also provides additional information e. g. about parasitic resistances which would otherwise needed to be identified or treated separately.

The dynamic method can be used in the future to measure near-field heat fluxes between different materials or structures. Although the number of near-field experiments has increased in the past few years, many theoretical predictions still lack an experimental verification.

Measuring the dynamic properties of near-field radiative heat transfer is another possible continuation. The samples will probably be miniaturized to reduce thermal mass and our technique has to be adjusted to that. But there are no fundamental problems within sight. In the spirit of this work, more adaptations of dynamic thermal measurement techniques like laser flash to

near-field measurements are desirable.

The fundamental understanding of thermal radiation – Planck’s blackbody theory – is now more than 100 years old. Yet, we have seen that there are many phenomena which are not understood or verified up to the present. Our increasing use of nanostructures make it necessary to consider or even utilize effects like near-field radiative heat transfer. New optical properties realized by metamaterials are reflected in unique thermal radiation properties. This thesis should make a contribution to the progress towards near-field based thermal systems.

Appendix A

Thermal properties derived from mode counting

A.1 Density of states and heat flux

Similar to the derivation of the mode density in vacuum [10], we consider a cubic volume $V = L^3$ filled with the lossless material to investigate. Taking periodic boundary conditions (perfect electric or magnetic boundaries can be taken as well), only discrete k -vectors fulfill them. The components of these discrete k -vectors differ by $\frac{2\pi}{L}$, such that one mode occupies the volume $V_{k,\text{mode}} = (\frac{2\pi}{L})^3$ in k -space.

The number of modes in the frequency interval $[\omega, \omega + d\omega]$ is given by the k -space volume enclosed between the two isofrequency ($\omega = \text{const.}$) contours at ω and $\omega + d\omega$, $|dV_k|$ (Fig. A.1b), divided by $V_{k,\text{mode}}$. The same result is obtained by calculating the k -space volume enclosed by the isofrequency contour at ω , V_k (Fig. A.1a), and taking the derivative w. r. t. ω (and dividing by $V_{k,\text{mode}}$):

$$D(\omega)Vd\omega = \frac{|dV_k|}{V_{k,\text{mode}}} = \frac{1}{V_{k,\text{mode}}} \left| \frac{dV_k}{d\omega} \right| d\omega. \quad (\text{A.1})$$

The spectral mode density $D(\omega)$ is then given by

$$D(\omega) = \frac{1}{V} \frac{1}{V_{k,\text{mode}}} \left| \frac{dV_k}{d\omega} \right| = \frac{1}{(2\pi)^3} \left| \frac{dV_k}{d\omega} \right|. \quad (\text{A.2})$$

The dispersion relation of extraordinary modes [42] is according to Eq. (2.33)

$$\frac{k_{\perp}^2}{\epsilon_{\parallel}} + \frac{k_{\parallel}^2}{\epsilon_{\perp}} = \frac{\omega^2}{c^2}. \quad (\text{A.3})$$

It describes different isofrequency curves in k -space. Here, we exemplarily consider the hyperbolic type II case with $\epsilon_{\parallel} > 0$ and $\epsilon_{\perp} < 0$. The results for the other two cases $\{\epsilon_{\parallel} > 0 \text{ and } \epsilon_{\perp} > 0\}$ and $\{\epsilon_{\parallel} < 0 \text{ and } \epsilon_{\perp} > 0\}$, as well as for the ordinary modes which behave like in an isotropic medium with permittivity ϵ_{\perp} , can be found with the same procedure. In the anisotropic metal case ($\epsilon_{\parallel} < 0$ and $\epsilon_{\perp} < 0$) no propagating modes exist and mode density and heat flux are 0.

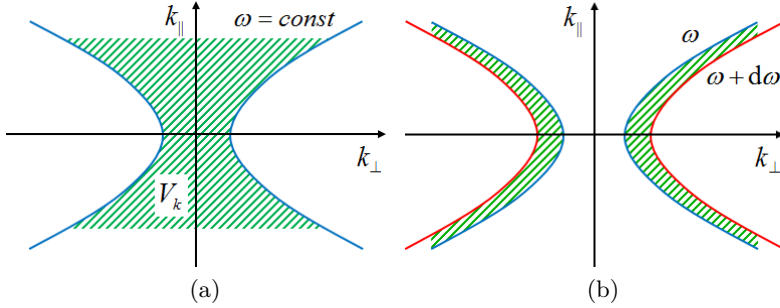


Figure A.1: Isofrequency contours in k -space of a type II hyperbolic medium. (a) shows a contour at ω and the enclosed volume V_k . (b) shows two contour at ω and $\omega + d\omega$ and the volume dV_k between them. Both volumes can be used to calculate the density of states $D(\omega)$.

Fig. A.1 shows the isofrequency curve for the case under consideration. The k -space volume enclosed by the contour is infinite. However, in reality the k -vectors of propagating modes are always limited [2] limiting the volume to a finite value. If the maximal parallel k -vector component is given by $k_{\parallel, \text{max}} = \sqrt{\frac{\omega^2}{c^2} \epsilon_{\perp} - k_{\perp, \text{max}}^2 \frac{\epsilon_{\perp}}{\epsilon_{\parallel}}}$ the mode density is

$$D_{\text{II}}^e(\omega) = \frac{1}{(2\pi)^3} \left| \frac{dV_k}{d\omega} \right| = \frac{1}{(2\pi)^3} \left| \frac{d}{d\omega} \int_{-k_{\parallel, \text{max}}}^{k_{\parallel, \text{max}}} \pi k_{\perp}^2 dk_{\parallel}^e \right|$$

$$\begin{aligned}
&= \int_0^{k_{\parallel, \max}} \left| \frac{d}{d\omega} \left(\frac{\omega^2}{c^2} \epsilon_{\parallel} - k_{\parallel}^{e2} \frac{\epsilon_{\parallel}}{\epsilon_{\perp}} \right) \right| \frac{dk_{\parallel}^e}{(2\pi)^2} \\
&= \int_0^{k_{\parallel, \max}} \left| \frac{1}{c^2} \frac{d(\epsilon_{\parallel} \omega^2)}{d\omega} - k_{\parallel}^{e2} \frac{d(\epsilon_{\parallel}/\epsilon_{\perp})}{d\omega} \right| \frac{dk_{\parallel}^e}{(2\pi)^2} \\
&= \int_0^{k_{\parallel, \max}} \left| \frac{2\omega}{c^2} \epsilon_{\parallel} + \frac{\omega^2}{c^2} \frac{d\epsilon_{\parallel}}{d\omega} - k_{\parallel}^{e2} \frac{1}{\epsilon_{\perp}} \frac{d\epsilon_{\parallel}}{d\omega} \right. \\
&\quad \left. + k_{\parallel}^{e2} \frac{\epsilon_{\parallel}}{\epsilon_{\perp}^2} \frac{d\epsilon_{\perp}}{d\omega} \right| \frac{dk_{\parallel}^e}{(2\pi)^2} \equiv \int_0^{k_{\parallel, \max}} D_{\Pi}^e(\omega, k_{\parallel}^e) dk_{\parallel}^e,
\end{aligned} \tag{A.4}$$

where we introduced the wavevector resolved spectral mode density $D(\omega, k_{\parallel})$. Similarly, the energy density is $u(\omega, k_{\parallel}) = \mathcal{U}(\omega, T) \cdot D(\omega, k_{\parallel})$.

Note that mathematically the change of the mode volume with respect to frequency can be positive or negative. However, it is the absolute value that provides the mode density. This holds even for every k_{\parallel} making it necessary to take the absolute value of the integrand not the whole integral.

With normal dispersion ($\frac{d\epsilon_{\perp}}{d\omega} > 0$, $\frac{d\epsilon_{\parallel}}{d\omega} > 0$) the integration yields for the spectral density of states

$$\begin{aligned}
D_{\Pi}^e(\omega) &= \frac{\omega}{\pi^2 c^2} \left[\frac{\epsilon_{\parallel}}{2} + \frac{\omega}{12} \frac{d\epsilon_{\parallel}}{d\omega} \left(\frac{k_{\parallel, \max}^2}{|\epsilon_{\perp}| \omega^2 / c^2} + 3 \right) \right. \\
&\quad \left. + \frac{\epsilon_{\parallel}}{|\epsilon_{\perp}|} \frac{\omega}{12} \frac{d\epsilon_{\perp}}{d\omega} \frac{k_{\parallel, \max}^2}{|\epsilon_{\perp}| \omega^2 / c^2} \right] k_{\parallel, \max},
\end{aligned} \tag{A.5}$$

consistent with Eq. (2.121) which has been derived via fluctuational electrodynamics.

To determine the energy flux the group velocity is needed. It is calculated from the gradient of the frequency w. r. t. the wavevector [14]

$$\mathbf{c}_g = \nabla_{\mathbf{k}}\omega(\mathbf{k}). \quad (\text{A.6})$$

For the energy flux along the optical axis only the corresponding component of the group velocity is required. It is

$$\begin{aligned} c_{g,\parallel}^e(\omega, k_{\parallel}^e) &= \frac{\partial\omega}{\partial k_{\parallel}^e} = \left(\frac{\partial k_{\parallel}^e}{\partial\omega}\right)^{-1} = \left(\frac{\partial}{\partial\omega}\sqrt{\frac{\omega^2}{c^2}\epsilon_{\perp} - k_{\perp}^2\frac{\epsilon_{\perp}}{\epsilon_{\parallel}}}\right)^{-1} \\ &= \frac{2\sqrt{\frac{\omega^2}{c^2}\epsilon_{\perp} - k_{\perp}^2\frac{\epsilon_{\perp}}{\epsilon_{\parallel}}}}{\frac{1}{c^2}\frac{d(\epsilon_{\perp}\omega^2)}{d\omega} - k_{\perp}^2\frac{d(\epsilon_{\perp}/\epsilon_{\parallel})}{d\omega}} \\ &= \frac{2k_{\parallel}^e}{\frac{2\omega}{c^2}\epsilon_{\perp} + \frac{\omega^2}{c^2}\frac{d\epsilon_{\perp}}{d\omega} - \left(\frac{\omega^2}{c^2}\epsilon_{\parallel} - k_{\parallel}^{e2}\frac{\epsilon_{\parallel}}{\epsilon_{\perp}}\right)\left(\frac{1}{\epsilon_{\parallel}}\frac{d\epsilon_{\perp}}{d\omega} - \frac{\epsilon_{\perp}}{\epsilon_{\parallel}^2}\frac{d\epsilon_{\parallel}}{d\omega}\right)} \\ &= \frac{\epsilon_{\parallel}}{\epsilon_{\perp}\frac{2\omega}{c^2}\epsilon_{\parallel} + \frac{\omega^2}{c^2}\frac{d\epsilon_{\parallel}}{d\omega} - k_{\parallel}^{e2}\frac{1}{\epsilon_{\perp}}\frac{d\epsilon_{\parallel}}{d\omega} + k_{\parallel}^{e2}\frac{\epsilon_{\parallel}}{\epsilon_{\perp}^2}\frac{d\epsilon_{\perp}}{d\omega}}. \end{aligned} \quad (\text{A.7})$$

The thermal energy flux of each mode is connected to its energy density via \mathbf{c}_g [10, 13]. To get the spectral flux along the optical

axis one has to integrate over the modes

$$\begin{aligned}\phi(\omega) &= \frac{1}{2} \int u(\omega, k_{\parallel}) |c_{g,\parallel}(\omega, k_{\parallel})| dk_{\parallel} \\ &= \frac{1}{2} \mathcal{U}(\omega, T) \int D(\omega, k_{\parallel}) |c_{g,\parallel}(\omega, k_{\parallel})| dk_{\parallel}\end{aligned}\tag{A.8}$$

The factor $\frac{1}{2}$ comes from the fact that for every mode there exists another mode that propagates exactly in the opposite direction, such that only half of the modes contribute to the energy flux in the particular direction. For the same reason we take the absolute value of $c_{g,\parallel}(\omega, k_{\parallel})$ thus guaranteeing a positive value of $\phi(\omega)$.

Finally, the heat flux of extraordinary modes for the hyperbolic type II case thus is

$$\begin{aligned}\phi_{\text{II}}^e(\omega) &= \frac{1}{2} \mathcal{U}(\omega, T) \int_0^{k_{\parallel,\text{max}}} \frac{2k_{\parallel}^e}{(2\pi)^2} \frac{\epsilon_{\parallel}}{|\epsilon_{\perp}|} dk_{\parallel}^e \\ &= \mathcal{U}(\omega, T) \frac{1}{8\pi^2} \frac{\epsilon_{\parallel}}{|\epsilon_{\perp}|} k_{\parallel,\text{max}}^2 \\ &= \mathcal{U}(\omega, T) \frac{1}{8\pi^2} \left(k_{\perp,\text{max}}^2 - \frac{\omega^2}{c^2} \epsilon_{\parallel} \right).\end{aligned}\tag{A.9}$$

Our previous result in Eq. (2.148) indicates the same.

It can be seen that the results obtained from simple mode counting are the same as derived with fluctuational electrodynamics. The mode counting approach is certainly much simpler and can be nicely visualized in k -space. Nonetheless, fluctuational elec-

trodynamics is more general and allows treating effects by evanescent modes, interfaces and basically all non-quantum effects.

A.2 Graphical derivation of heat flux formula

There exists a simple, graphical way to derive the heat flux inside a lossless medium. The way is presented in this section. Required quantities are illustrated in Fig. A.2. The shape of the isofrequency contours can be arbitrary, Fig. A.2 exemplarily employs the isofrequency contours of type I hyperbolic modes.

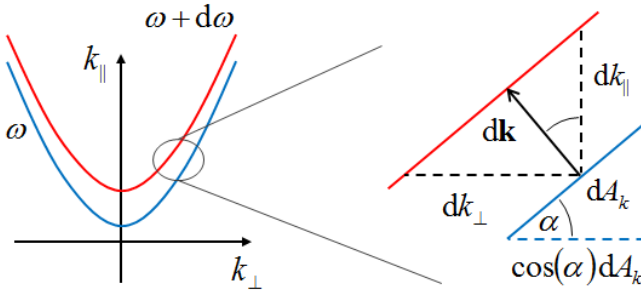


Figure A.2: Two exemplary isofrequency contours in k -space, one at frequency ω , one at $\omega + d\omega$. A zoom shows a region where the two curves are quasi linear and parallel. In addition, the displacements $d\mathbf{k}$, dk_{\perp} , dk_{\parallel} , the angle α and the area dA_k are introduced.

First, we rewrite the wavevector resolved spectral mode density

$$\begin{aligned} D(\omega, k_{\perp}) = D(\omega, k_{\parallel}) &= \frac{1}{(2\pi)^3} \left| \frac{dV_k}{d\omega} \right| = \frac{1}{(2\pi)^3} \frac{dA_k |d\mathbf{k}|}{d\omega} \\ &= \frac{1}{(2\pi)^3} \frac{dA_k}{|\mathbf{c}_g|}. \end{aligned} \quad (\text{A.10})$$

Then, we rewrite the wavevector resolved spectral heat flux

$$\begin{aligned} \phi(\omega, k_{\perp}) &= \mathcal{U}(\omega, T) D(\omega, k_{\perp}) |c_{g,\parallel}(\omega, k_{\perp})| \\ &= \frac{\mathcal{U}(\omega, T)}{(2\pi)^3} dA_k \frac{|c_{g,\parallel}|}{|\mathbf{c}_g|} = \frac{\mathcal{U}(\omega, T)}{(2\pi)^3} \frac{dA_k |d\mathbf{k}|}{d\omega} \frac{d\omega}{dk_{\parallel}} \\ &= \frac{\mathcal{U}(\omega, T)}{(2\pi)^3} dA_k \frac{|d\mathbf{k}|}{dk_{\parallel}} = \frac{\mathcal{U}(\omega, T)}{(2\pi)^3} \cos(\alpha) dA_k. \end{aligned} \quad (\text{A.11})$$

The term $\cos(\alpha) dA_k$ is the projection of the isofrequency contour area dA_k onto the plane normal to the direction of heat flux (\parallel -direction). The spectral heat flux

$$\begin{aligned} \phi(\omega) &= \frac{\mathcal{U}(\omega, T)}{2\pi} \iint_{\mathbf{k}(\omega)} \frac{\cos(\alpha) dA_k}{(2\pi)^2} = \frac{\mathcal{U}(\omega, T)}{2\pi} \frac{A_k^{\text{proj}}}{(2\pi)^2} \\ &= \frac{\mathcal{U}(\omega, T)}{2\pi} \iint_{k_{\parallel} \in \mathbb{R}} \frac{d^2 k_{\perp}}{(2\pi)^2} \end{aligned} \quad (\text{A.12})$$

is the integration over the whole isofrequency contour area and proportional to the area of the projected isofrequency curve A_k^{proj} [80, 94]. The last representation in (A.12) makes the connection to Eq. (2.140) which has been derived via fluctuational

electrodynamics.

Note that here dk_{\perp} , dk_{\parallel} are not the components of $d\mathbf{k}$ but they are connected via the norm of the group velocity

$$|\mathbf{c}_g| = \frac{d\omega}{|d\mathbf{k}|} = \left| \left(\begin{array}{c} \frac{d\omega}{dk_{\perp}} \\ \frac{d\omega}{dk_{\parallel}} \end{array} \right) \right|. \quad (\text{A.13})$$

The presented approach can be extended to 2- and 1-dimensional systems and the proportionality to the projected isofrequency contour holds for arbitrary shaped contours. On the downside, this approach is limited to homogeneous materials and not applicable e. g. for the heat flux in a vacuum gap.

Appendix B

Additional information on the near-field measurements

B.1 Number of spacers and their contribution to the heat flux

To create and maintain the vacuum gaps between glass disks we utilize silica particles as spacers. Although this is a rather simple and stable method, it has the disadvantage of introducing solid thermal conduction through the spacers which adds up to the radiative heat flux. This effect is estimated in this section.

Tables B.1 and B.2 display the expected numbers of particles used for the experiments. The given number of particles is the value expected from amount and concentration of the particle suspension used. The actual number is subject to statistical variations. The particle coverage or surface coverage of the $\approx 314 \text{ mm}^2$ large gap area, defined as $N_{\text{particle}} \frac{d_{\text{particle}}^2}{d_{\text{disk}}^2}$ with the disk diameter $d_{\text{disk}} = 20 \text{ mm}$, is slightly below 10^{-5} . Since the silica disks are a bit lighter than the BK7 ones less particles are used when working with the silica disks, proportional to the sample weights.

To estimate an upper limit on the heat flux via solid conduction we assumed silica cylinders instead of spheres with conductivity $\lambda_{\text{SiO}_2} = 1.3 \text{ W m}^{-1} \text{ K}^{-1}$ and neglected contact resistances. The conduction through the cylinders is given in Tables B.1 and B.2 in absolute values as well as normalized to the theoretical radiative heat flux. Table B.1 shows the data of the measurements presented in Section 5.4 in Fig. 5.7. Table B.2 shows the data of the repetitive measurements with a $1.3 \mu\text{m}$ gap. Besides varying the number of particles we also performed four measurement with 400 particles to check not only the influence of particles and but also the reproducibility of our measurements.

Although the solid conduction seems relatively high, the cylinder assumption is definitely overestimating the effect. Spheres are conducting less than cylinders due to smaller contact area. Additionally, there are contact resistances at the particle–disk interfaces adding to the total thermal resistance [98]. And be-

Type	Nominal gap size: d_{particle} [μm]	Number of particles: N_{particle}	Surface coverage [in 10^{-6}]	Conduction through particles assuming cylinders [$\text{W m}^{-2} \text{K}^{-1}$]	Theoretical radiation [$\text{W m}^{-2} \text{K}^{-1}$]	Conduction / radiation
BK7	7.38	56	8	1.35	4.75	28%
	4.64	142	8	2.15	5.33	40%
	2.79	394	8	3.57	6.63	54%
	1.3	1814	8	7.66	10.2	75%
	0.755	5377	8	13.19	14.27	92%
Fused silica	1.3	1601	7	6.76	10.42	65%
	0.755	4746	7	11.65	15.42	76%
	0.5	10822	7	17.59	22.56	78%
	0.304	9758	2	9.64	41.52	23%
	0.143	138250	7	64.25	141.35	45%

Table B.1: Number of particles used as spacers and their maximal contribution to the heat flux via solid conduction. The table represents the measurements with different gaps. To estimate an upper limit on the heat flux via solid conduction we assumed silica cylinders instead of spheres and neglected contact resistances. [From Ref. [68].]

cause the particles are not perfectly monodisperse and the disks not perfectly flat, the number of particles actually being in contact with the superstrate is less than the total number. Overall,

Type	Nominal gap size: d_{particle} [μm]	Number of particles: N_{particle}	Surface coverage [in 10^{-6}]	Conduction through particles assuming cylinders [$\text{W m}^{-2} \text{K}^{-1}$]	Theoretical radia- tion [$\text{W m}^{-2} \text{K}^{-1}$]	Conduction / radiation
Fused silica	1.3	1601	6.8	6.76	10.42	65%
		1300	5.5	5.49		53%
		1000	4.2	4.23		41%
		700	3	2.96		28%
		400	1.7	1.69		16%

Table B.2: Number of particles used as spacers and their maximal contribution to the heat flux via solid conduction. Same as Table B.1 but for the repetitive measurements with a $1.3 \mu\text{m}$ gap. [From Ref. [68].]

we can be certain that the thermal conduction through the gap which we measure is dominated by radiation. The effect of solid conduction can be also estimated from heat flux measurements. The solid conduction through spacers is a reasonable explanation for the small, positive offset of the measured, larger gaps HTC's w. r. t. the theoretical, purely radiative HTC's, seen in Fig. 5.7 (Section 5.4).

The repetitive measurements with decreasing number of spacers, presented in Fig. B.1, show no clear trend. This, together with

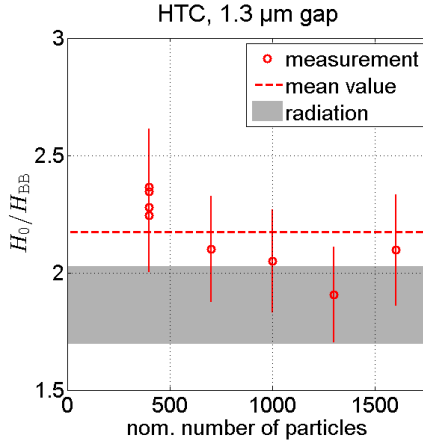


Figure B.1: Particle dependent heat flux. Heat transfer coefficient (HTC) H_0 from thermal radiation theory and from experiments versus nominal number of particles for repetitive measurements with fused silica and a $1.3\ \mu\text{m}$ gap. The HTC H_0 is normalized to the HTC between blackbodies H_{BB} . The grey band representing the theoretical radiative HTC includes fluctuations and measurement uncertainties of the gap size, as well as the uncertainty of the optical properties of our fused silica. The error bars contain the fitting uncertainty (for these measurements up to 5%) and possible changes of sensor/heater losses (leading up to a 10% error). The dashed line is the mean value of the 8 measurements. The standard deviation is $\approx 7.5\%$. The slightly higher measured values are probably caused by conduction through the spheres used as spacers for the gap. [From Ref. [68].]

the fact that the gap setup is still mechanically stable even with

much less particles, indicates that indeed the number of particles in contact with lower and upper disks, or in other word actually holding the superstrate, is less than the total number and not varying too much while we varied the total number. Only these particles increase the heat flux by solid conduction.

All in all, the mean gap conductivities of the eight measurements with fused silica and a $1.3\ \mu\text{m}$ gap vary by $\pm 7.5\%$ around the mean value. This is our measurement reproducibility. The variation is probably mainly due to the measurement inaccuracy and due to real variations of the gap heat flux. The gap heat flux fluctuations come from variations in gap size, and thus in radiative heat flux ($\approx 9\%$), and from variations of solid heat flux through the spacers. The number of particles in contact with both glass disks varies statistically, as properties like contact resistances do, too. Consequently, the solid conduction through them changes. Further reasons can be small variations in gap uniformity and small variations in equilibrium temperature T_0 .

The uncertainty of the fitting procedure is typically around $\pm 2\%$ but can go up to 8% . Finally, the variation in sensor/heater losses from gap to reference measurement (we estimated a maximum of 10% of blackbody HTC) translates into an error up to 10% . Similar to the standard deviation of the sum of stochastic variables, the individual contributions are not summed up but the square root of the sum of their squares is taken (root sum square). This leads to an inaccuracy of up to $\pm 13\%$ which we take as our error margin.

The mean gap conductivity of the eight measurements with fused silica and a $1.3\ \mu\text{m}$ gap is offset by $\approx 20\%$ above the expected value from thermal radiation only. We attribute this offset to solid conductivity through the spacers. The solid conductance is inversely proportional to the sum of a constant term, representing the contact resistances between spheres and disks, and a term proportional to the gap size, representing the resistance through spheres (the surface coverage is independent of gap size). At small gap sizes the solid conductance should approach a constant value. Thus, the relative effect of solid conductivity should diminish as soon as the thermal radiation contribution starts to increase at smaller gap sizes, and consequently the relative share of solid conduction in the total heat flux decreases. Exactly this behavior is observed in Fig. 5.7 (Section 5.4).

Moreover, the measured HTC's are normalized to the blackbody HTC at the initial equilibrium temperature T_0 . In the experiment, the mean temperature at the gap will be fractionally higher, so that the true blackbody normalization factor should correspondingly be slightly larger. The smaller the HTC is, the larger this effect will be. Note that the normalized theory curves are rather insensitive to changes in T_0 .

B.2 Optical properties of BK7 and fused silica glass

Since we measure the radiative heat flux at room temperature most of the thermal radiation is in the mid infrared (MIR), around 10 μm free space wavelength. To obtain the optical properties of our BK7 and fused silica samples in the MIR, we first looked at literature values for fused silica [93]. The frequency dependent relative permittivity of fused silica can be well described by a Drude–Lorentz model [44, 92] with three resonances

$$\epsilon(\omega) = \epsilon_\infty + \sum_{j=1}^3 \frac{A_j (2\pi f_j)^2}{(2\pi f_j)^2 - \omega^2 - i2\pi f_{\text{col},j}\omega}. \quad (\text{B.1})$$

The parameters are: $\epsilon_\infty = 2.01$, $A_1 = 1.071$, $A_2 = 0.113$, $A_3 = 0.77$, $f_1 = 13.52$ THz, $f_2 = 23.83$ THz, $f_3 = 31.92$ THz, $f_{\text{col},1} = 1.43$ THz, $f_{\text{col},2} = 2$ THz, $f_{\text{col},3} = 2$ THz. The permittivity is plotted in Fig. B.3b (“literature”).

Second, we adjusted the parameters to better fit the reflectivity measured with a Fourier transform infrared spectrometer (FTIR) (VERTEX 70 from Bruker). For BK7 we also assumed the same Drude–Lorentz model because there are no literature data for the MIR. Fig. B.2 depicts measured and fitted reflectivities which coincide fairly well.

The parameters obtained from fitting the reflectivity are for BK7: $\epsilon_\infty = 2.25$ (± 0.18), $A_1 = 0.796$ (± 0.122), $A_2 = 0.028$,

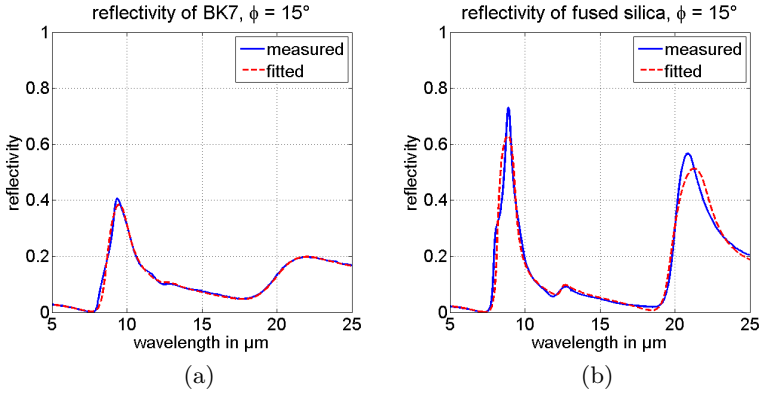


Figure B.2: Measured and fitted reflectivity of (a) BK7 and (b) fused silica samples. The angle of incidence is 15° , the light is unpolarized. For the permittivity of BK7 and of fused silica we assumed a Drude–Lorentz model with three resonances causing the three peaks in reflection; the middle peak is very weak. [From Ref. [68].]

$A_3 = 0.741 (\pm 0.076)$, $f_1 = 13.9 \text{ THz} (\pm 0.6 \text{ THz})$, $f_2 = 23.8 \text{ THz}$,
 $f_3 = 30.2 \text{ THz} (\pm 0.6 \text{ THz})$, $f_{\text{col},1} = 2.9 \text{ THz} (\pm 0.7 \text{ THz})$, $f_{\text{col},2} = 2 \text{ THz}$,
 $f_{\text{col},3} = 3 \text{ THz} (\pm 0.5 \text{ THz})$.

And for fused silica: $\epsilon_\infty = 2.1 (\pm 0.36)$, $A_1 = 0.805 (\pm 0.169)$,
 $A_2 = 0.063$, $A_3 = 0.575 (\pm 0.134)$, $f_1 = 13.6 \text{ THz} (\pm 0.5 \text{ THz})$,
 $f_2 = 24 \text{ THz}$, $f_3 = 32.3 \text{ THz} (\pm 1 \text{ THz})$, $f_{\text{col},1} = 0.8 \text{ THz} (\pm 0.5 \text{ THz})$,
 $f_{\text{col},2} = 1.4 \text{ THz}$, $f_{\text{col},3} = 1.2 \text{ THz} (\pm 0.9 \text{ THz})$.

The corresponding relative permittivities can be seen in Fig. B.3. The values in brackets represent the uncertainty margins of the

fits. The second of the three resonances is very weak and reasonable changes in its parameters have practically no effect. For this reason we skip the corresponding uncertainty margins.

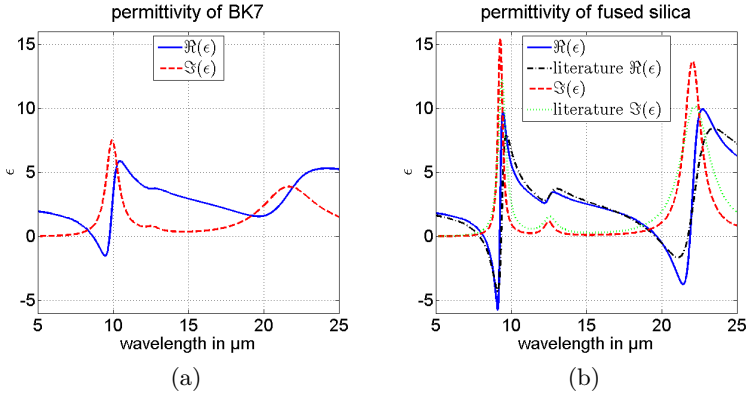


Figure B.3: Relative permittivity of (a) BK7 and (b) fused silica obtained from fitting the reflectivity. In both cases a Drude–Lorentz model with three resonances is applied. Fused silica shows the stronger resonances. Additionally, literature values [93] approximated by a Drude–Lorentz model with three resonances are plotted for fused silica. Our measurements indicate that the resonances of our silica disks are stronger than expected. Both glasses have at least one region with negative (real part of the) permittivity. [From Ref. [68].]

The silica resonances are stronger than expected from literature, and much stronger than the BK7 resonances. However, both materials feature at least one region with negative (real part of the) permittivity and thus support surface modes in a spectral

range where they significantly contribute to the near-field heat flux [16, 100]. Both theory and measurements exhibit negligibly small transmission. It can therefore not be used to characterize the materials.

B.3 300 nm and 150 nm gaps

The deep sub-micrometer small gaps pose a particular challenge. Realizing as well as confirming them is accompanied by additional effort. Here, we provide the important aspects associated with our experiments with 300 nm and 150 nm gaps. 150 nm gaps are the smallest gaps realized in a macroscopic plane–plane geometry up to now [123].

The main issues for realizing small gaps by the spacer method are to overcome clustering of particles and to avoid larger dust / grime particles in the gap. The clustering tends to form multi-layers of particles and, therefore, increases the gap by approximately an integer multiple of the particle size. Additionally, this clustering may also induce inclined gaps, if the numbers of layers are unequal between the supporting points. Remember, we place three drops of particle solution on our disks. On the other hand, a large number of spacer particles is required to mechanically hold the superstrate. Unwanted dust or grime will lead to unpredictable and uncontrollable gaps.

For avoiding the unwanted dust / grime particles in the gap, we performed the cleaning procedure twice. Furthermore, we

used fresh samples to ensure there are no surface damages due to previous experiments.

We solved the clustering problem by two separate approaches. First, we reduced the particle concentration, and thus the possibility of cluster formation. For the 300 nm gap the total number of particles is three times less than usual (cf. Table B.1). Also, we used three 2.5 μl instead of 1 μl drops which allowed us to further reduce the concentration of particles in the suspension. Second, for the 150 nm gap we accepted the clustering in the first place and reduced the gap distance by applying a small vertical force while rotating the upper disk, to destroy the clusters but not the particles. For the second approach the gap distance is measured at six different spots, aligned in a cross, with the UV/Vis/NIR spectrometer and a wavelength range from 195 nm to 1500 nm. After the first three spots we turned the sample by 90° horizontally around its center point for measuring the last three spots. With the six spots, we were able to capture the inclination of the plane–plane geometry and provide a gap size averaged over the whole sample area. This is of particular importance for creating the 150 nm gap, since an inclination cannot be identified by a visible interference pattern, as it is the case for gap sizes larger than 300 nm.

The inclination is reduced by applying a small vertical force at the largest gap spot and rotating the superstrate, resulting in a shear force which separates the cluster. Applying a force to destroy the cluster only seems convenient, as long as the amount

of particles forming the clusters is low compared to the total amount of particles, because otherwise many particles would be destroyed, due to the high necessary force. We confirmed this by investigating the particle distribution with a scanning electron microscope (SEM). For that, we prepared object slides with particles on it, under the same conditions as we prepared the sample disks, but omitting the upper disk. As a matter of fact, for the particle concentrations we used, the amount of particles forming a multilayer cluster is low compared to the total amount of particles.

Finally, we want to discuss the uncertainty of the 150 nm gap HTC measurement. It is larger than all other uncertainties. The reason for that is illustrated in Fig. B.4. The figure shows simulated transients for different gap conductances. Whereas for smaller gap conductances a change by a factor of two significantly alters the temperature transient, for larger gap HTCs above $16H_{\text{BB}}$ the transient becomes less sensitive and finally saturates to a curve independent of the gap heat flux. This happens when the gap resistance gets in the range of the disk resistance (fused silica disk conductance corresponds to $\approx 48H_{\text{BB}}$). It's clear that a very small disk resistance practically doesn't influence the total system resistance and hence the system behavior. With an expected gap heat flux of approx. 18 to 32 times the blackbody value, the 150 nm gap is our only measurement in the saturating region.

This measurement difficulty is not particular to our transient

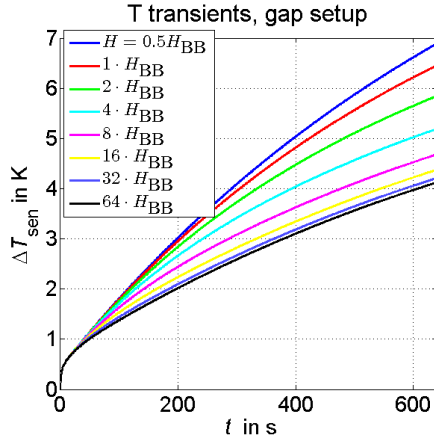


Figure B.4: Simulated temperature transients for different gap conductances. The simulations are based on the fused silica parameters and $R_c = 8 \text{ K W}^{-1}$, $h_{\text{sen}} = 2.88 \text{ W m}^{-2} \text{ K}^{-1}$. The gap conductance H is varied from 50% of the HTC between two blackbodies, $H_{\text{BB}} = 5.76 \text{ W m}^{-2} \text{ K}^{-1}$, to 64 times the value. Transients of the reference setup are not shown. Whereas for smaller gap conductances a change by a factor of two significantly alters the temperature transient, for larger gap HTCs above $16H_{\text{BB}}$ the transient becomes less sensitive and finally saturates to a curve independent of the gap heat flux. [From Ref. [68].]

method. In steady state one measures the total resistance. The smaller the portion of gap resistance in total resistance, the less accurate the measurements become, till the gap resistance completely disappears in the resistance measurement inaccuracy. The problem can be avoided by employing thinner and better

conducting samples.

Appendix C

Physical and mathematical relations

C.1 Effective permittivity of layered structures

Assume a periodically layered metamaterial consists of two materials 1 and 2. Further assume the permittivity of material 1, ϵ_1 , is given by a Drude–Lorentz model [44, 92]

$$\begin{aligned}\epsilon_1(\omega) &= \epsilon_{\infty,1} \frac{\omega_{\text{LO},1}^2 - \omega^2 - i\omega_{\text{col},1}\omega}{\omega_{\text{TO},1}^2 - \omega^2 - i\omega_{\text{col},1}\omega} \\ &= \epsilon_{\infty,1} + \epsilon_{\infty,1} \frac{\omega_{\text{LO},1}^2 - \omega_{\text{TO},1}^2}{\omega_{\text{TO},1}^2 - \omega^2 - i\omega_{\text{col},1}\omega}\end{aligned}\tag{C.1}$$

and the permittivity of material 2, ϵ_2 , is constant, as for many dielectrics. The filling factors are f_1 and $f_2 = 1 - f_1$.

The effective permittivities of the metamaterial are [42] (see Eqs. (1.5) and (1.6))

$$\begin{aligned}
 \epsilon_{\perp}(\omega) &= f_1\epsilon_1 + f_2\epsilon_2 \\
 &= f_2\epsilon_2 + f_1\epsilon_{\infty,1} + f_1\epsilon_{\infty,1} \frac{\omega_{\text{LO},1}^2 - \omega_{\text{TO},1}^2}{\omega_{\text{TO},1}^2 - \omega^2 - i\omega_{\text{col},1}\omega} \quad (\text{C.2}) \\
 &\stackrel{!}{=} \epsilon_{\infty,\perp} + \epsilon_{\infty,\perp} \frac{\omega_{\text{LO},\perp}^2 - \omega_{\text{TO},\perp}^2}{\omega_{\text{TO},\perp}^2 - \omega^2 - i\omega_{\text{col},\perp}\omega}
 \end{aligned}$$

and

$$\begin{aligned}
 \epsilon_{\parallel}(\omega) &= \frac{1}{f_1/\epsilon_1 + f_2/\epsilon_2} = \frac{\epsilon_1\epsilon_2}{f_1\epsilon_2 + f_2\epsilon_1} \\
 &= \frac{\epsilon_2\epsilon_{\infty,1} (\omega_{\text{LO},1}^2 - \omega^2 - i\omega_{\text{col},1}\omega)}{f_1\epsilon_2 (\omega_{\text{TO},1}^2 - \omega^2 - i\omega_{\text{col},1}\omega) + f_2\epsilon_{\infty,1} (\omega_{\text{LO},1}^2 - \omega^2 - i\omega_{\text{col},1}\omega)} \quad (\text{C.3}) \\
 &= \frac{\frac{\epsilon_2\epsilon_{\infty,1}}{f_1\epsilon_2 + f_2\epsilon_{\infty,1}} (\omega_{\text{LO},1}^2 - \omega^2 - i\omega_{\text{col},1}\omega)}{\frac{f_1\epsilon_2\omega_{\text{TO},1}^2 + f_2\epsilon_{\infty,1}\omega_{\text{LO},1}^2}{f_1\epsilon_2 + f_2\epsilon_{\infty,1}} - \omega^2 - i\omega_{\text{col},1}\omega} \\
 &\stackrel{!}{=} \epsilon_{\infty,\parallel} \frac{\omega_{\text{LO},\parallel}^2 - \omega^2 - i\omega_{\text{col},\parallel}\omega}{\omega_{\text{TO},\parallel}^2 - \omega^2 - i\omega_{\text{col},\parallel}\omega},
 \end{aligned}$$

so again Drude–Lorentz permittivities with the effective param-

eters

$$\epsilon_{\infty,\perp} = f_1\epsilon_{\infty,1} + f_2\epsilon_2, \quad (\text{C.4})$$

$$\omega_{\text{LO},\perp} = \sqrt{\frac{f_1\epsilon_{\infty,1}\omega_{\text{LO},1}^2 + f_2\epsilon_2\omega_{\text{TO},1}^2}{f_1\epsilon_{\infty,1} + f_2\epsilon_2}}, \quad (\text{C.5})$$

$$\omega_{\text{TO},\perp} = \omega_{\text{TO},1}, \quad (\text{C.6})$$

$$\omega_{\text{col},\perp} = \omega_{\text{col},1}, \quad (\text{C.7})$$

$$\epsilon_{\infty,\parallel} = \frac{\epsilon_2\epsilon_{\infty,1}}{f_1\epsilon_2 + f_2\epsilon_{\infty,1}}, \quad (\text{C.8})$$

$$\omega_{\text{LO},\parallel} = \omega_{\text{LO},1}, \quad (\text{C.9})$$

$$\omega_{\text{TO},\parallel} = \sqrt{\frac{f_1\epsilon_2\omega_{\text{TO},1}^2 + f_2\epsilon_{\infty,1}\omega_{\text{LO},1}^2}{f_1\epsilon_2 + f_2\epsilon_{\infty,1}}}, \quad (\text{C.10})$$

$$\omega_{\text{col},\parallel} = \omega_{\text{col},1}. \quad (\text{C.11})$$

C.2 Dispersion relation of surface waves

Surface waves are particular solutions of Maxwell's equations at an interface between two materials [134]. We want to derive the dispersion relation of surface waves. To do so, we assume an interface at $z = 0$ separating two isotropic halfspaces, one dielectric with permittivity ϵ_d at $z > 0$ and one metallic with permittivity ϵ_m at $z < 0$.

The magnetic field of p-polarized surface waves is

$$\mathbf{H}^p(\omega, \mathbf{k}) = \begin{cases} \hat{H}_0 \mathbf{a}_s e^{i\mathbf{k}_\perp \cdot \mathbf{r}_\perp} e^{-ik_\parallel^m z} & z < 0 \\ \hat{H}_0 \mathbf{a}_s e^{i\mathbf{k}_\perp \cdot \mathbf{r}_\perp} e^{ik_\parallel^d z} & z \geq 0 \end{cases}. \quad (\text{C.12})$$

Amplitude \hat{H}_0 , tangential wavevector \mathbf{k}_\perp and polarization \mathbf{a}_s are identical on both sides of the interface to ensure continuity of the magnetic field. It looks like plane waves propagating away from the interface. But surface waves are characterized by propagation along the interface and exponential decay away from it. So we look for solutions with $\Re(\mathbf{k}_\perp) \gg \Im(\mathbf{k}_\perp)$ and $\Im(k_\parallel) \gg \Re(k_\parallel)$. In the lossless case \mathbf{k}_\perp is real and both k_\parallel imaginary.

The electric field is

$$\begin{aligned} \mathbf{E}^p(\omega, \mathbf{k}) &= -\frac{1}{i\omega\epsilon_0\epsilon} \nabla \times \mathbf{H}^p \\ &= \begin{cases} \frac{\hat{H}_0}{\omega\epsilon_0\epsilon_m} k^m \mathbf{a}_p^m e^{i\mathbf{k}_\perp \cdot \mathbf{r}_\perp} e^{-ik_\parallel^m z} & z < 0 \\ \frac{\hat{H}_0}{\omega\epsilon_0\epsilon_d} k^d \mathbf{a}_p^d e^{i\mathbf{k}_\perp \cdot \mathbf{r}_\perp} e^{ik_\parallel^d z} & z > 0 \end{cases} \end{aligned} \quad (\text{C.13})$$

with

$$\mathbf{a}_p^m = \frac{1}{k^m} \mathbf{a}_s \times \begin{pmatrix} \mathbf{k}_\perp \\ -k_\parallel^m \end{pmatrix} = \frac{1}{k_\perp k^m} \begin{pmatrix} k_x k_\parallel^m \\ k_y k_\parallel^m \\ k_\perp^2 \end{pmatrix}, \quad (\text{C.14})$$

$$\mathbf{a}_p^d = \frac{1}{k^d} \mathbf{a}_s \times \begin{pmatrix} \mathbf{k}_\perp \\ k_\parallel^d \end{pmatrix} = \frac{1}{k_\perp k^d} \begin{pmatrix} -k_x k_\parallel^d \\ -k_y k_\parallel^d \\ k_\perp^2 \end{pmatrix} \quad (\text{C.15})$$

and $k^{m/d^2} = k_{\parallel}^{m/d^2} + k_{\perp}^2$. Continuity of tangential E -field implies

$$\frac{k_{\parallel}^m}{\epsilon_m} = -\frac{k_{\parallel}^d}{\epsilon_d}. \quad (\text{C.16})$$

Because both $k_{\parallel}^{m/d}$ represent the \parallel wavevector component of a plane wave “traveling” in positive \parallel -direction (cf. Section 2.3.1), Eq. (C.16) can only be fulfilled if the (real parts of the) permittivities have opposite signs. For that reason we talked about a metal and a dielectric from the beginning, although the metal can be any material showing optically metallic behavior (negative permittivity). S-polarized surface waves require permeabilities with opposite signs which is rarely the case and not considered here.

Together with the dispersion relations inside the two materials

$$k^{m/d^2} = k_{\parallel}^{m/d^2} + k_{\perp}^2 = \frac{\omega^2}{c^2} \epsilon_{m/d}, \quad (\text{C.17})$$

we obtain the dispersion relation of surface modes [134]

$$\begin{aligned} \frac{k_{\parallel}^{m^2}}{\epsilon_m^2} = \frac{k_{\parallel}^{d^2}}{\epsilon_d^2} &\iff \epsilon_d^2 \frac{\omega^2}{c^2} \epsilon_m - \epsilon_d^2 k_{\perp}^2 = \epsilon_m^2 \frac{\omega^2}{c^2} \epsilon_d - \epsilon_m^2 k_{\perp}^2 \\ &\implies k_{\perp}^2 = \frac{\omega^2}{c^2} \frac{\epsilon_m \epsilon_d}{\epsilon_m + \epsilon_d}. \end{aligned} \quad (\text{C.18})$$

Surface modes exist as long as $\epsilon_m \leq -\epsilon_d$. At the frequency at which $\epsilon_m = -\epsilon_d$ – if the dielectric halfspace is vacuum at which

$\epsilon_m = -1$ – the surface wave is resonant and $k_\perp \rightarrow \infty$. Losses make k_\perp complex and finite. Then, the resonance frequency is the frequency at which the real parts of the permittivities cancel each other.

C.3 Mathematical relations

When integrating the spectral energy density or spectral heat flux to obtain the total quantities, the following relation is utilized ($\Re(n) > 0$)

$$\int_0^\infty \frac{\Omega^n}{e^\Omega - 1} d\Omega = \Gamma(n+1)\zeta(n+1), \quad (\text{C.19})$$

where $\Gamma(z)$ is the gamma function and $\zeta(z)$ the Riemann zeta function. For $n \in \mathbb{N}$ the relation simplifies to

$$\int_0^\infty \frac{\Omega^n}{e^\Omega - 1} d\Omega = n!\zeta(n+1). \quad (\text{C.20})$$

Furthermore, certain values of the zeta function are known:

$$\zeta(2) = \frac{\pi^2}{6} \quad \text{and} \quad \zeta(4) = \frac{\pi^4}{90}. \quad (\text{C.21})$$

Bibliography

- [1] W. Cai and V. Shalaev, *Optical Metamaterials*. Springer, 2010.
- [2] A. Poddubny, I. Iorsh, P. Belov, and Y. Kivshar, “Hyperbolic metamaterials,” *Nat. Photon.*, vol. 7, pp. 948–957, 2013.
- [3] V. P. Drachev, V. A. Podolskiy, and A. V. Kildishev, “Hyperbolic metamaterials: new physics behind a classical problem,” *Opt. Express*, vol. 21, pp. 15048–15064, 2013.
- [4] S. Basu, Z. M. Zhang, and C. J. Fu, “Review of near-field thermal radiation and its application to energy conversion,” *Int. J. Energy Res.*, vol. 33, pp. 1203–1232, 2009.
- [5] K. Park and Z. Zhang, “Fundamentals and Applications of Near-Field Radiative Energy Transfer,” *Front. Heat Mass Transfer*, vol. 4, p. 013001, 2013.

-
- [6] T. Bauer, *Thermophotovoltaics*. Green Energy and Technology, Springer, 2011.
- [7] R. S. DiMatteo, P. Greiff, S. L. Finberg, K. A. Young-Waithe, H. K. H. Choy, M. M. Masaki, and C. G. Fonstad, “Enhanced photogeneration of carriers in a semiconductor via coupling across a nonisothermal nanoscale vacuum gap,” *Appl. Phys. Lett.*, vol. 79, p. 1894, 2001.
- [8] A. Kittel, W. Müller-Hirsch, J. Parisi, S.-A. Biehs, D. Reddig, and M. Holthaus, “Near-Field Heat Transfer in a Scanning Thermal Microscope,” *Phys. Rev. Lett.*, vol. 95, p. 224301, 2005.
- [9] E. Rousseau, A. Siria, G. Jourdan, S. Volz, F. Comin, J. Chevrier, and J.-J. Greffet, “Radiative heat transfer at the nanoscale,” *Nat. Photon.*, vol. 3, pp. 514–517, 2009.
- [10] C. Kittel and H. Kroemer, *Thermal Physics*. W. H. Freeman and Company, 2 ed., 1980.
- [11] J. R. Howell, M. P. Mengüç, and R. Siegel, *Thermal Radiation Heat Transfer*. CRC Press, 6 ed., 2015.
- [12] M. Planck, “Ueber das Gesetz der Energieverteilung im Normalspectrum,” *Ann. Phys.*, vol. 309, pp. 553–563, 1901.
- [13] J. D. Jackson, *Classical Electrodynamics*. John Wiley & Sons, 3 ed., 1999.

-
- [14] L. D. Landau and E. M. Lifshitz, *Electrodynamics of Continuous Media*, vol. 8 of *Course of Theoretical Physics*. Pergamon Press, 1 ed., 1960.
- [15] D. Polder and M. Van Hove, “Theory of Radiative Heat Transfer between Closely Spaced Bodies,” *Phys. Rev. B*, vol. 4, pp. 3303–3314, 1971.
- [16] K. Joulain, J.-P. Mulet, F. Marquier, R. Carminati, and J.-J. Greffet, “Surface electromagnetic waves thermally excited: Radiative heat transfer, coherence properties and Casimir forces revisited in the near field,” *Surf. Sci. Rep.*, vol. 57, pp. 59–112, 2005.
- [17] Y. Guo, C. L. Cortes, S. Molesky, and Z. Jacob, “Broadband super-Planckian thermal emission from hyperbolic metamaterials,” *Appl. Phys. Lett.*, vol. 101, p. 131106, 2012.
- [18] S.-A. Biehs, M. Tschikin, and P. Ben-Abdallah, “Hyperbolic Metamaterials as an Analog of a Blackbody in the Near Field,” *Phys. Rev. Lett.*, vol. 109, p. 104301, 2012.
- [19] C. R. Otey, L. Zhu, S. Sandhu, and S. Fan, “Fluctuational electrodynamic calculations of near-field heat transfer in non-planar geometries: A brief overview,” *J. Quant. Spectrosc. Radiat. Transfer*, vol. 132, pp. 3–11, 2014.
- [20] Y. De Wilde, F. Formanek, R. Carminati, B. Gralak, P.-A. Lemoine, K. Joulain, J.-P. Mulet, Y. Chen, and J.-J. Greff-

- fet, “Thermal radiation scanning tunnelling microscopy,” *Nature*, vol. 444, pp. 740–743, 2006.
- [21] L. Hu, A. Narayanaswamy, X. Chen, and G. Chen, “Near-field thermal radiation between two closely spaced glass plates exceeding Planck’s blackbody radiation law,” *Appl. Phys. Lett.*, vol. 92, p. 133106, 2008.
- [22] S.-A. Biehs, E. Rousseau, and J.-J. Greffet, “Mesoscopic Description of Radiative Heat Transfer at the Nanoscale,” *Phys. Rev. Lett.*, vol. 105, p. 234301, 2010.
- [23] A. Kittel, U. F. Wischnath, J. Welker, O. Huth, F. Rütting, and S.-A. Biehs, “Near-field thermal imaging of nanostructured surfaces,” *Appl. Phys. Lett.*, vol. 93, p. 193109, 2008.
- [24] F. Huth, M. Schnell, J. Wittborn, N. Ocelic, and R. Hillenbrand, “Infrared-spectroscopic nanoimaging with a thermal source,” *Nat. Mater.*, vol. 10, pp. 352–356, 2011.
- [25] A. C. Jones and M. B. Raschke, “Thermal Infrared Near-Field Spectroscopy,” *Nano Lett.*, vol. 12, pp. 1475–1481, 2012.
- [26] R. S. Ottens, V. Quetschke, S. Wise, A. A. Alemi, R. Lundock, G. Mueller, D. H. Reitze, D. B. Tanner, and B. F. Whiting, “Near-Field Radiative Heat Transfer between Macroscopic Planar Surfaces,” *Phys. Rev. Lett.*, vol. 107, p. 014301, 2011.

- [27] B. Guha, C. Otey, C. B. Poitras, S. Fan, and M. Lipson, “Near-Field Radiative Cooling of Nanostructures,” *Nano Lett.*, vol. 12, pp. 4546–4550, 2012.
- [28] C. R. Otey, W. T. Lau, and S. Fan, “Thermal Rectification through Vacuum,” *Phys. Rev. Lett.*, vol. 104, p. 154301, 2010.
- [29] P. Ben-Abdallah and S.-A. Biehs, “Phase-change radiative thermal diode,” *Appl. Phys. Lett.*, vol. 103, p. 191907, 2013.
- [30] J. Huang, Q. Li, Z. Zheng, and Y. Xuan, “Thermal rectification based on thermochromic materials,” *Int. J. Heat Mass Transfer*, vol. 67, pp. 575–580, 2013.
- [31] P. Ben-Abdallah and S.-A. Biehs, “Near-Field Thermal Transistor,” *Phys. Rev. Lett.*, vol. 112, p. 044301, 2014.
- [32] V. Kubytzkyi, S.-A. Biehs, and P. Ben-Abdallah, “Radiative Bistability and Thermal Memory,” *Phys. Rev. Lett.*, vol. 113, p. 074301, 2014.
- [33] S. A. Dyakov, J. Dai, M. Yan, and M. Qiu, “Near field thermal memory based on radiative phase bistability of VO_2 ,” *J. Phys. D: Appl. Phys.*, vol. 48, no. 30, p. 305104, 2015.

-
- [34] A. Narayanaswamy and G. Chen, “Surface modes for near field thermophotovoltaics,” *Appl. Phys. Lett.*, vol. 82, p. 3544, 2003.
- [35] M. Laroche, R. Carminati, and J.-J. Greffet, “Near-field thermophotovoltaic energy conversion,” *J. Appl. Phys.*, vol. 100, p. 063704, 2006.
- [36] A. Karalis and J. D. Joannopoulos, “‘Squeezing’ near-field thermal emission for ultra-efficient high-power thermophotovoltaic conversion,” *Sci. Rep.*, vol. 6, p. 28472, 2016.
- [37] K. Park, S. Basu, W. P. King, and Z. M. Zhang, “Performance analysis of near-field thermophotovoltaic devices considering absorption distribution,” *J. Quant. Spectrosc. Radiat. Transfer*, vol. 109, pp. 305–316, 2008.
- [38] Y. Guo and Z. Jacob, “Thermal hyperbolic metamaterials,” *Opt. Express*, vol. 21, pp. 15014–15019, 2013.
- [39] S. Fan, “Photovoltaics: An alternative ‘sun’ for solar cells,” *Nat. Nanotechnol.*, vol. 9, pp. 92–93, 2014.
- [40] W. Shockley and H. J. Queisser, “Detailed Balance Limit of Efficiency of p-n Junction Solar Cells,” *J. Appl. Phys.*, vol. 32, p. 510, 1961.
- [41] P. N. Dyachenko, S. Molesky, A. Y. Petrov, M. Störmer, T. Krekeler, S. Lang, M. Ritter, Z. Jacob, and M. Eich,

- “Controlling thermal emission with refractory epsilon-near-zero metamaterials via topological transitions,” *Nat. Commun.*, vol. 7, p. 11809, 2016.
- [42] P. Yeh, *Optical Waves in Layered Media*. John Wiley & Sons, 2005.
- [43] D. R. Smith and D. Schurig, “Electromagnetic Wave Propagation in Media with Indefinite Permittivity and Permeability Tensors,” *Phys. Rev. Lett.*, vol. 90, p. 077405, 2003.
- [44] M. Dressel and G. Grüner, *Electrodynamics of Solids*. Cambridge University Press, 2002.
- [45] S. Adachi, *III-V Compound Semiconductors*, vol. 2 of *Handbook on Physical Properties of Semiconductors*. Kluwer Academic Publishers, 2004.
- [46] S. Adachi, *Group-IV Semiconductors*, vol. 1 of *Handbook on Physical Properties of Semiconductors*. Kluwer Academic Publishers, 2004.
- [47] E. E. Narimanov and A. V. Kildishev, “Metamaterials: Naturally hyperbolic,” *Nat. Photon.*, vol. 9, pp. 214–216, 2015.
- [48] M. Esslinger, R. Vogelgesang, N. Talebi, W. Khunsin, P. Gehring, S. de Zuani, B. Gompf, and K. Kern, “Tetradymites as Natural Hyperbolic Materials for the

- Near-Infrared to Visible,” *ACS Photon.*, vol. 1, pp. 1285–1289, 2014.
- [49] A. J. Hoffman, L. Alekseyev, S. S. Howard, K. J. Franz, D. Wasserman, V. A. Podolskiy, E. E. Narimanov, D. L. Sivco, and C. Gmachl, “Negative refraction in semiconductor metamaterials,” *Nat. Mater.*, vol. 6, pp. 946–950, 2007.
- [50] H. N. S. Krishnamoorthy, Z. Jacob, E. Narimanov, I. Kretzschmar, and V. M. Menon, “Topological Transitions in Metamaterials,” *Science*, vol. 336, pp. 205–209, 2012.
- [51] S. Lang, H. S. Lee, A. Y. Petrov, M. Störmer, M. Ritter, and M. Eich, “Gold-silicon metamaterial with hyperbolic transition in near infrared,” *Appl. Phys. Lett.*, vol. 103, p. 021905, 2013.
- [52] J. Yao, Z. Liu, Y. Liu, Y. Wang, C. Sun, G. Bartal, A. M. Stacy, and X. Zhang, “Optical Negative Refraction in Bulk Metamaterials of Nanowires,” *Science*, vol. 321, p. 930, 2008.
- [53] M. A. Noginov, Y. A. Barnakov, G. Zhu, T. Tumkur, H. Li, and E. E. Narimanov, “Bulk photonic metamaterial with hyperbolic dispersion,” *Appl. Phys. Lett.*, vol. 94, p. 151105, 2009.
- [54] R. Wangberg, J. Elser, E. E. Narimanov, and V. A. Podolskiy, “Nonmagnetic nanocomposites for optical and in-

- frared negative-refractive-index media,” *J. Opt. Soc. Am. B*, vol. 23, pp. 498–505, 2006.
- [55] O. Kidwai, S. V. Zhukovsky, and J. E. Sipe, “Effective-medium approach to planar multilayer hyperbolic metamaterials: Strengths and limitations,” *Phys. Rev. A*, vol. 85, p. 053842, 2012.
- [56] O. Kidwai, S. V. Zhukovsky, and J. E. Sipe, “Dipole radiation near hyperbolic metamaterials: applicability of effective-medium approximation,” *Opt. Lett.*, vol. 36, pp. 2530–2532, 2011.
- [57] M. Tschikin, S.-A. Biehs, R. Messina, and P. Ben-Abdallah, “On the limits of the effective description of hyperbolic materials in the presence of surface waves,” *J. Opt.*, vol. 15, no. 10, p. 105101, 2013.
- [58] S. Lang, “Transfer-Matrix Method for the Modeling of Metamaterials,” master thesis, Technische Universität Hamburg-Harburg (TUHH), 2013.
- [59] Z. Jacob, J.-Y. Kim, G. V. Naik, A. Boltasseva, E. E. Narimanov, and V. M. Shalaev, “Engineering photonic density of states using metamaterials,” *Appl. Phys. B*, vol. 100, pp. 215–218, 2010.
- [60] I. I. Smolyaninov and E. E. Narimanov, “Metric Signature Transitions in Optical Metamaterials,” *Phys. Rev. Lett.*, vol. 105, p. 067402, 2010.

-
- [61] Z. Liu, H. Lee, Y. Xiong, C. Sun, and X. Zhang, “Far-Field Optical Hyperlens Magnifying Sub-Diffraction-Limited Objects,” *Science*, vol. 315, p. 1686, 2007.
- [62] S. M. Rytov, Y. A. Kravtsov, and V. I. Tatarskii, *Principles of Statistical Radiophysics 3*, vol. 3. Springer, 1989.
- [63] G. S. Agarwal, “Quantum electrodynamics in the presence of dielectrics and conductors. I. Electromagnetic-field response functions and black-body fluctuations in finite geometries,” *Phys. Lett. A*, vol. 11, p. 230, 1975.
- [64] C.-T. Tai, *Dyadic Green’s functions in electromagnetic theory*. Intext Educational Publishers, 1 ed., 1971.
- [65] S. Lang, M. Tschikin, S.-A. Biehs, A. Y. Petrov, and M. Eich, “Large penetration depth of near-field heat flux in hyperbolic media,” *Appl. Phys. Lett.*, vol. 104, p. 121903, 2014.
- [66] M. Tschikin, S.-A. Biehs, P. Ben-Abdallah, S. Lang, A. Y. Petrov, and M. Eich, “Radiative heat flux predictions in hyperbolic metamaterials,” *J. Quant. Spectrosc. Radiat. Transfer*, vol. 158, pp. 17–26, 2015.
- [67] S.-A. Biehs, S. Lang, A. Y. Petrov, M. Eich, and P. Ben-Abdallah, “Blackbody Theory for Hyperbolic Materials,” *Phys. Rev. Lett.*, vol. 115, p. 174301, 2015.

- [68] S. Lang, G. Sharma, S. Molesky, P. U. Kränzien, T. Jalas, Z. Jacob, A. Y. Petrov, and M. Eich, “Dynamic measurement of near-field radiative heat transfer,” *Sci. Rep.*, vol. 7, p. 13916, 2017.
- [69] A. Einstein and O. Stern, “Einige Argumente für die Annahme einer molekularen Agitation beim absoluten Nullpunkt,” *Ann. Phys.*, vol. 345, pp. 551–560, 1913.
- [70] A. Narayanaswamy and Y. Zheng, “A Green’s function formalism of energy and momentum transfer in fluctuational electrodynamics,” *J. Quant. Spectrosc. Radiat. Transfer*, vol. 132, pp. 12–21, 2014.
- [71] E. E. Narimanov, “Photonic Hypercrystals,” *Phys. Rev. X*, vol. 4, p. 041014, 2014.
- [72] W. S. Weiglhofer, “Dyadic Green’s functions for general uniaxial media,” *IEE Proc. H*, vol. 137, pp. 5–10, 1990.
- [73] A. S. Potemkin, A. N. Poddubny, P. A. Belov, and Y. S. Kivshar, “Green function for hyperbolic media,” *Phys. Rev. A*, vol. 86, p. 023848, 2012.
- [74] M. Francoeur, M. P. Mengüç, and R. Vaillon, “Solution of near-field thermal radiation in one-dimensional layered media using dyadic Green’s functions and the scattering matrix method,” *J. Quant. Spectrosc. Radiat. Transfer*, vol. 110, pp. 2002–2018, 2009.

- [75] F. S. S. Rosa, D. A. R. Dalvit, and P. W. Milonni, “Electromagnetic energy, absorption, and Casimir forces: Uniform dielectric media in thermal equilibrium,” *Phys. Rev. A*, vol. 81, p. 033812, 2010.
- [76] W. Eckhardt, “Radiation laws in the vicinity of metallic boundaries,” *Z. Phys. B*, vol. 46, pp. 85–94, 1982.
- [77] Y. S. Barash and V. L. Ginzburg, “Expressions for the energy density and evolved heat in the electrodynamics of a dispersive and absorptive medium,” *Sov. Phys. Usp.*, vol. 19, pp. 263–270, 1976.
- [78] W. Eckhardt, “Electromagnetic fluctuations in anisotropic dielectric crystals,” *Opt. Commun.*, vol. 27, pp. 299–302, 1978.
- [79] P. Ben-Abdallah and K. Joulain, “Fundamental limits for noncontact transfers between two bodies,” *Phys. Rev. B*, vol. 82, p. 121419(R), 2010.
- [80] M. Florescu, K. Busch, and J. P. Dowling, “Thermal radiation in photonic crystals,” *Phys. Rev. B*, vol. 75, p. 201101(R), 2007.
- [81] J.-J. Greffet and M. Nieto-Vesperinas, “Field theory for generalized bidirectional reflectivity: derivation of Helmholtz’s reciprocity principle and Kirchhoff’s law,” *J. Opt. Soc. Am. A*, vol. 15, pp. 2735–2744, 1998.

- [82] L. Zhu and S. Fan, “Near-complete violation of detailed balance in thermal radiation,” *Phys. Rev. B*, vol. 90, p. 220301(R), 2014.
- [83] D. A. B. Miller, L. Zhu, and S. Fan, “Universal modal radiation laws for all thermal emitters,” *Proc. Natl. Acad. Sci. U.S.A.*, vol. 114, no. 17, pp. 4336–4341, 2017.
- [84] L. D. Landau and E. M. Lifshitz, *Statistical Physics*, vol. 5 of *Course of Theoretical Physics*. Pergamon Press, 2 ed., 1969.
- [85] L. Mandel and E. Wolf, *Optical Coherence and Quantum Optics*. Cambridge University Press, 1 ed., 1995.
- [86] P.-O. Chapuis, S. Volz, C. Henkel, K. Joulain, and J.-J. Greffet, “Effects of spatial dispersion in near-field radiative heat transfer between two parallel metallic surfaces,” *Phys. Rev. B*, vol. 77, p. 035431, 2008.
- [87] A. A. Rukhadze and V. P. Silin, “Electrodynamics of Media with Spatial Dispersion,” *Sov. Phys. Usp.*, vol. 4, no. 3, pp. 459–484, 1961.
- [88] Z. Yu, N. P. Sergeant, T. Skauli, G. Zhang, H. Wang, and S. Fan, “Enhancing far-field thermal emission with thermal extraction,” *Nat. Commun.*, vol. 4, p. 1730, 2013.

-
- [89] M. Mirmoosa, S.-A. Biehs, and C. Simovski, “Super-Planckian Thermophotovoltaics Without Vacuum Gaps,” *Phys. Rev. Applied*, vol. 8, p. 054020, 2017.
- [90] L. J. Wang, A. Kuzmich, and A. Dogariu, “Gain-assisted superluminal light propagation,” *Nature*, vol. 406, pp. 277–279, 2000.
- [91] M. D. Stenner, D. J. Gauthier, and M. A. Neifeld, “The speed of information in a ‘fast-light’ optical medium,” *Nature*, vol. 425, pp. 695–698, 2003.
- [92] P. R. West, S. Ishii, G. V. Naik, N. K. Emani, V. M. Shalaev, and A. Boltasseva, “Searching for better plasmonic materials,” *Laser Photonics Rev.*, vol. 4, pp. 795–808, 2010.
- [93] E. D. Palik, ed., *Handbook of Optical Constants of Solids*, vol. 1. Academic Press, 1997.
- [94] M. Florescu and K. Busch, “Properties of thermal radiation in photonic crystals,” *J. Opt. A*, vol. 11, no. 11, p. 114005, 2009.
- [95] E. E. Narimanov and I. I. Smolyaninov, “Beyond Stefan-Boltzmann Law: Thermal Hyper-Conductivity,” *arXiv*, p. 1109.5444, 2011.

- [96] J. Liu and E. Narimanov, “Thermal hyperconductivity: Radiative energy transport in hyperbolic media,” *Phys. Rev. B*, vol. 91, p. 041403(R), 2015.
- [97] I. S. Nefedov and C. R. Simovski, “Giant radiation heat transfer through micron gaps,” *Phys. Rev. B*, vol. 84, p. 195459, 2011.
- [98] C. V. Madhusudana, *Thermal Contact Conductance*. Mechanical Engineering Series, Springer, 2 ed., 2014.
- [99] C. Simovski, S. Maslovski, I. Nefedov, and S. Tretyakov, “Optimization of radiative heat transfer in hyperbolic metamaterials for thermophotovoltaic applications,” *Opt. Express*, vol. 21, pp. 14988–15013, 2013.
- [100] S. Basu and Z. M. Zhang, “Ultrascale penetration depth in nanoscale thermal radiation,” *Appl. Phys. Lett.*, vol. 95, p. 133104, 2009.
- [101] S. Basu and M. Francoeur, “Penetration depth in near-field radiative heat transfer between metamaterials,” *Appl. Phys. Lett.*, vol. 99, p. 143107, 2011.
- [102] S. Molesky, C. J. Dewalt, and Z. Jacob, “High temperature epsilon-near-zero and epsilon-near-pole metamaterial emitters for thermophotovoltaics,” *Opt. Express*, vol. 21, pp. A96–A110, 2013.

- [103] J. H. Kim, S. M. Jung, and M. W. Shin, “High-temperature degradation of one-dimensional metallodielectric (W/SiO₂) photonic crystal as selective thermal emitter for thermophotovoltaic system,” *Opt. Mater.*, vol. 72, pp. 45–51, 2017.
- [104] S.-A. Biehs, M. Tschikin, R. Messina, and P. Ben-Abdallah, “Super-Planckian near-field thermal emission with phonon-polaritonic hyperbolic metamaterials,” *Appl. Phys. Lett.*, vol. 102, p. 131106, 2013.
- [105] B. Liu and S. Shen, “Broadband near-field radiative thermal emitter/absorber based on hyperbolic metamaterials: Direct numerical simulation by the Wiener chaos expansion method,” *Phys. Rev. B*, vol. 87, p. 115403, 2013.
- [106] A. I. Volokitin and B. N. J. Persson, “Resonant photon tunneling enhancement of the radiative heat transfer,” *Phys. Rev. B*, vol. 69, p. 045417, 2004.
- [107] M. Francoeur, M. P. Mengüç, and R. Vaillon, “Spectral tuning of near-field radiative heat flux between two thin silicon carbide films,” *J. Phys. D: Appl. Phys.*, vol. 43, no. 7, p. 075501, 2010.
- [108] J. Shi, B. Liu, P. Li, L. Yen Ng, and S. Shen, “Near-Field Energy Extraction with Hyperbolic Metamaterials,” *Nano Lett.*, vol. 15, pp. 1217–1221, 2015.

- [109] T. J. Bright, X. L. Liu, and Z. M. Zhang, “Energy streamlines in near-field radiative heat transfer between hyperbolic metamaterials,” *Opt. Express*, vol. 22, pp. A1112–A1127, 2014.
- [110] A. Babuty, K. Joulain, P.-O. Chapuis, J.-J. Greffet, and Y. De Wilde, “Blackbody Spectrum Revisited in the Near Field,” *Phys. Rev. Lett.*, vol. 110, p. 146103, 2013.
- [111] K. Kim, B. Song, V. Fernández-Hurtado, W. Lee, W. Jeong, L. Cui, D. Thompson, J. Feist, M. T. H. Reid, F. J. García-Vidal, J. C. Cuevas, E. Meyhofer, and P. Reddy, “Radiative heat transfer in the extreme near field,” *Nature*, vol. 528, pp. 387–391, 2015.
- [112] K. Kloppstech, N. Köhne, S.-A. Biehs, A. W. Rodriguez, L. Worbes, D. Hellmann, and A. Kittel, “Giant heat transfer in the crossover regime between conduction and radiation,” *Nat. Commun.*, vol. 8, p. 14475, 2017.
- [113] A. Narayanaswamy, S. Shen, and G. Chen, “Near-field radiative heat transfer between a sphere and a substrate,” *Phys. Rev. B*, vol. 78, p. 115303, 2008.
- [114] S. Shen, A. Narayanaswamy, and G. Chen, “Surface Phonon Polaritons Mediated Energy Transfer between Nanoscale Gaps,” *Nano Lett.*, vol. 9, pp. 2909–2913, 2009.
- [115] P. J. van Zwol, L. Ranno, and J. Chevrier, “Tuning Near Field Radiative Heat Flux through Surface Excita-

- tions with a Metal Insulator Transition,” *Phys. Rev. Lett.*, vol. 108, p. 234301, 2012.
- [116] B. Song, Y. Ganjeh, S. Sadat, D. Thompson, A. Fiorino, V. Fernández-Hurtado, J. Feist, F. J. Garcia-Vidal, J. C. Cuevas, P. Reddy, and E. Meyhofer, “Enhancement of near-field radiative heat transfer using polar dielectric thin films,” *Nat. Nanotechnol.*, vol. 10, pp. 253–258, 2015.
- [117] C. M. Hargreaves, “Anomalous radiative transfer between closely-spaced bodies,” *Phys. Lett.*, vol. 30A, pp. 491–492, 1969.
- [118] T. Kralik, P. Hanzelka, M. Zobac, V. Musilova, T. Fort, and M. Horak, “Strong Near-Field Enhancement of Radiative Heat Transfer between Metallic Surfaces,” *Phys. Rev. Lett.*, vol. 109, p. 224302, 2012.
- [119] T. Ijro and N. Yamada, “Near-field radiative heat transfer between two parallel SiO₂ plates with and without microcavities,” *Appl. Phys. Lett.*, vol. 106, p. 023103, 2015.
- [120] K. Ito, A. Miura, H. Iizuka, and H. Toshiyoshi, “Parallel-plate submicron gap formed by micromachined low-density pillars for near-field radiative heat transfer,” *Appl. Phys. Lett.*, vol. 106, p. 083504, 2015.
- [121] M. Lim, S. S. Lee, and B. J. Lee, “Near-field thermal radiation between doped silicon plates at nanoscale gaps,” *Phys. Rev. B*, vol. 91, p. 195136, 2015.

- [122] B. Song, D. Thompson, A. Fiorino, Y. Ganjeh, P. Reddy, and E. Meyhofer, “Radiative heat conductances between dielectric and metallic parallel plates with nanoscale gaps,” *Nat. Nanotechnol.*, vol. 11, pp. 509–514, 2016.
- [123] M. P. Bernardi, D. Milovich, and M. Francoeur, “Radiative heat transfer exceeding the blackbody limit between macroscale planar surfaces separated by a nanosize vacuum gap,” *Nat. Commun.*, vol. 7, p. 12900, 2016.
- [124] R. St-Gelais, B. Guha, L. Zhu, S. Fan, and M. Lipson, “Demonstration of Strong Near-Field Radiative Heat Transfer between Integrated Nanostructures,” *Nano Lett.*, vol. 14, pp. 6971–6975, 2014.
- [125] R. St-Gelais, L. Zhu, S. Fan, and M. Lipson, “Near-field radiative heat transfer between parallel structures in the deep subwavelength regime,” *Nat. Nanotechnol.*, vol. 11, pp. 515–519, 2016.
- [126] S. E. Gustafsson, “Transient plane source techniques for thermal conductivity and thermal diffusivity measurements of solid materials,” *Rev. Sci. Instrum.*, vol. 62, p. 797, 1991.
- [127] M. Gustavsson, E. Karawacki, and S. E. Gustafsson, “Thermal conductivity, thermal diffusivity, and specific heat of thin samples from transient measurements with hot disk sensors,” *Rev. Sci. Instrum.*, vol. 65, p. 3856, 1994.

-
- [128] S. Romeis, J. Paul, P. Herre, M. Hanisch, R. N. Klupp Taylor, J. Schmidt, and W. Peukert, “In Situ Deformation and Breakage of Silica Particles Inside a SEM,” *Procedia Eng.*, vol. 102, pp. 201–210, 2015.
- [129] D. J. Benford, T. J. Powers, and S. H. Moseley, “Thermal conductivity of Kapton tape,” *Cryogenics*, vol. 39, pp. 93–95, 1999.
- [130] J. Crank and P. Nicolson, “A practical method for numerical evaluation of solutions of partial differential equations of the heat-conduction type,” *Math. Proc. Cambridge Philos. Soc.*, vol. 43, pp. 50–67, 1947.
- [131] C. N. Dawson, Q. Du, and T. F. Dupont, “A finite difference domain decomposition algorithm for numerical solution of the heat equation,” *Math. Comp.*, vol. 57, no. 195, pp. 63–71, 1991.
- [132] SCHOTT AG, *Optical Glass – Collection Datasheets*. downloadable at www.schott.com.
- [133] Heraeus Quarzglas GmbH & Co. KG, *Data sheet: Fused silica for Optics - Data and Properties*. downloadable at www.heraeus.com.
- [134] H. Raether, *Surface Plasmons on Smooth and Rough Surfaces and on Gratings*, vol. 111 of *Springer Tracts in Modern Physics*. Springer, 1988.

List of Figures

1.1	Radiative heat transfer in the near field.	4
1.2	Isofrequency contours of extraordinary modes in uniaxial media.	10
1.3	Hyperbolic metamaterials and their isofrequency contours.	13
2.1	Visualization of transfer-matrix method (TMM).	27
2.2	Illustration of setups for which Green's functions are evaluated.	32
2.3	Illustration of setups for which energy density inside uniaxial media is evaluated.	60
2.4	Illustration of setups for which thermal power flux inside uniaxial media is evaluated.	74
2.5	Illustration of setup for which thermal power flux into vacuum is evaluated.	89

2.6	Illustration of setup for which thermal power flux through vacuum gap is evaluated.	96
3.1	Spectral energy density of classical blackbody vs. “hyperbolic blackbody”.	111
3.2	Spectral heat flux of classical blackbody vs. “hyperbolic blackbody”.	116
3.3	Effective permittivities of layered GaN–Ge HMM.	124
3.4	Density of states (DOS) inside exemplary HM. .	128
3.5	Thermal energy density inside exemplary HM. .	129
3.6	Spectral heat transfer coefficient (sHTC) inside exemplary HM.	133
3.7	Heat transfer coefficient (HTC) inside exemplary HM.	134
3.8	Illustration of setup for which radiative heat transfer through hyperbolic medium is evaluated. . . .	137
4.1	Effective permittivities and absorptivity of W–HfO ₂ HMM.	150
4.2	Illustration of setup for which radiative heat transfer through vacuum gap is evaluated.	153
4.3	Systems to be analyzed.	155
4.4	HTC in vacuum gap and illustration of mode contributions.	157

4.5	Energy transmission coefficient in vacuum gap. . .	160
4.6	sHTC in vacuum gap.	161
4.7	Spectral thermal PD and spectral HTC in vacuum gap.	167
4.8	HTC in vacuum gap and thermal PD.	170
5.1	Reflectivity of substrate–gap–superstrate setup. . .	181
5.2	Schematic of experimental setup.	186
5.3	Illustration of 1D model.	189
5.4	Measured and fitted temperature transients. . . .	195
5.5	Temperature distribution in samples.	200
5.6	Temperature transients simulated with 1D and 2D model.	201
5.7	Measured and theoretical gap dependent heat flux.	203
A.1	Isofrequency contours of type II hyperbolic medium and enclosed volumes.	218
A.2	Illustration of quantities used in graphical heat flux derivation.	222
B.1	Particle dependent heat flux.	229
B.2	Measured and fitted reflectivities of samples. . .	233
B.3	Relative permittivities of samples.	234

B.4 Simulated temperature transients for different gap conductances.	238
---	-----

List of Tables

3.1	Comparison of thermal radiation properties of classical blackbody vs. “hyperbolic blackbody”. . . .	118
B.1	Number of particles used as spacers and their maximal contribution to the heat flux I.	227
B.2	Number of particles used as spacers and their maximal contribution to the heat flux II.	228

List of publications

S. Lang, H. S. Lee, A. Yu. Petrov, M. Störmer, M. Ritter, and M. Eich, “Gold-silicon metamaterial with hyperbolic transition in near infrared,” *Appl. Phys. Lett.* **103**, 021905 (2013).

DOI: 10.1063/1.4813499

S. Lang, M. Tschikin, S.-A. Biehs, A. Yu. Petrov, and M. Eich, “Large penetration depth of near-field heat flux in hyperbolic media,” *Appl. Phys. Lett.* **104**, 121903 (2014).

DOI: 10.1063/1.4869490

E. A. Ulchenko, D. Jalas, A. Yu. Petrov, M. Castellanos Muñoz, S. Lang, and M. Eich, “Pulse compression and broadening by reflection from a moving front of a photonic crystal,” *Opt. Express* **22**, 13280 (2014).

DOI: 10.1364/OE.22.013280

D. Jalas, R. Canchi, A. Yu. Petrov, S. Lang, L. Shao, J. Weissmüller, and M. Eich, “Effective medium model for the spectral properties of nanoporous gold in the visible,” *Appl. Phys. Lett.* **105**, 241906 (2014).

DOI: 10.1063/1.4904714

M. Tschikin, S.-A. Biehs, P. Ben-Abdallah, S. Lang, A. Yu. Petrov, and M. Eich, “Radiative heat flux predictions in hyperbolic metamaterials,” *J. Quant. Spectrosc. Radiat. Transf.* **158**, 17 (2015).

DOI: 10.1016/j.jqsrt.2014.11.013

L. S. Fohrmann, A. Yu. Petrov, S. Lang, D. Jalas, T. F. Krauss, and M. Eich, “Single mode thermal emission,” *Opt. Express* **23**, 27672 (2015).

DOI: 10.1364/OE.23.027672

S.-A. Biehs, S. Lang, A. Yu. Petrov, M. Eich, and P. Ben-Abdallah, “Blackbody Theory for Hyperbolic Materials,” *Phys. Rev. Lett.* **115**, 174301 (2015).

DOI: 10.1103/PhysRevLett.115.174301

P. N. Dyachenko, S. Molesky, A. Yu. Petrov, M. Störmer, T. Krekeler, S. Lang, M. Ritter, Z. Jacob, and M. Eich, “Controlling thermal emission with refractory epsilon-near-zero metamaterials via topological transitions,” *Nat. Commun.* **7**, 11809 (2016).

DOI: 10.1038/ncomms11809

D. Jalas, L.-H. Shao, R. Canchi, T. Okuma, S. Lang, A. Petrov, J. Weissmüller, and M. Eich, “Electrochemical tuning of the optical properties of nanoporous gold,” *Sci. Rep.* **7**, 44139 (2017).
DOI: 10.1038/srep44139

S. Lang, G. Sharma, S. Molesky, P. U. Kränzien, T. Jalas, Z. Jacob, A. Yu. Petrov, and M. Eich, “Dynamic measurement of near-field radiative heat transfer,” *Sci. Rep.* **7**, 13916 (2017).
DOI: 10.1038/s41598-017-14242-x

L. Maiwald, S. Lang, D. Jalas, H. Renner, A. Yu. Petrov, and M. Eich, “Ewald sphere construction for structural colors,” *Opt. Express* **26**, 11352 (2018).
DOI: 10.1364/OE.26.011352

List of conference contributions

The underlined author has been the presenting author.

S. Lang, A. Petrov, M. Störmer, and M. Eich, “Layered Au-Si hyperbolic metamaterial for near infrared,” Nanoscale Radiative Heat Transfer, Physics School Les Houches 2013, Les Houches, France (2013)

A. Petrov, S. Lang, and M. Eich, “Near infrared hyperbolic metamaterial with thin gold layers,” Days on Diffraction 2013, Saint Petersburg, Russia (2013)

S. Lang, A. Petrov, M. Störmer, and M. Eich, “Near Infrared Metamaterial Containing a Metal,” 7th International Congress on Advanced Electromagnetic Materials in Microwaves and Optics (Metamaterials 2013), Bordeaux, France (2013)

M. Störmer, S. Lang, H. S. Lee, A. Petrov, M. Ritter, and M. Eich, “Preparation and characterization of thin film hyperbolic metamaterials,” The 5th International Conference on Metamaterials, Photonic Crystals and Plasmonics (META’14), Singapore (2014)

S. Lang, M. Tschikin, S.-A. Biehs, A. Petrov, and M. Eich, “Large penetration depth of near-field heat flux in hyperbolic media,” Days on Diffraction 2014, Saint Petersburg, Russia (2014)

S. Lang, M. Tschikin, S.-A. Biehs, A. Petrov, and M. Eich, “Thermal near-field penetration depth into materials supporting hyperbolic or surface modes,” 2nd International Workshop on Nano-Micro Thermal Radiation (NanoRad2014), Shanghai, China (2014)

M. Tschikin, S.-A. Biehs, P. Ben-Abdallah, S. Lang, A. Petrov, and M. Eich, “Exact calculation of heat flux and attenuation length in multilayer hyperbolic metamaterials,” 2nd International Workshop on Nano-Micro Thermal Radiation (NanoRad2014), Shanghai, China (2014)

D. Jalas, A. Yu. Petrov, S. Lang, R. Canchi, L. Shao, J. Weissmüller, and M. Eich, “Qualitative explanation of the spectral properties of nanoporous gold,” 8th International Congress on Advanced Electromagnetic Materials in Microwaves and Optics (Metamaterials 2014), Copenhagen, Denmark (2014)

S. Lang, P. Dyachenko, A. Petrov, M. Eich, M. Störmer, S.-A. Biehs, M. Tschikin, and Z. Jacob, “Anisotropic metamaterials for thermal photonics,” Materials Science and Engineering (MSE), Darmstadt, Germany (2014)

P. Dyachenko, S. Lang, A. Yu. Petrov, M. Störmer, M. Eich, H. Hu, S. Molesky, and Z. Jacob, “New frontier for plasmonics and metamaterials: Thermophotovoltaics,” 11th World Conference on Thermophotovoltaic Generation of Electricity, Amsterdam, Netherlands (2014)

S. Lang, M. Tschikin, S.-A. Biehs, P. Ben-Abdallah, A. Petrov, and M. Eich, “Large penetration depth in hyperbolic metamaterials,” Eurotherm 103, Nanoscale and Microscale Heat Transfer IV, Lyon, France (2014)

M. Waleczek, E. M. Hildyard, J. J. do Rosario, S. Lang, J. M. Montero Moreno, R. Zierold, M. Eich, G. Schneider, and K. Nielsch, “Template Guided Self-Assembly: Influence of Lithographic Patterning on the Crystallization of Opal Structures,” 2015 MRS Spring Meeting & Exhibit, San Francisco, USA (2015)

M. Waleczek, J. J. do Rosario, J. M. Montero Moreno, R. Zierold, S. Lang, A. Petrov, M. Eich, G. Schneider, and K. Nielsch, “Pattern Guided Assembly and Inversion of Synthetic Opals,” DPG Jahrestagung 2015, Berlin, Germany (2015)

S.-A. Biehs, S. Lang, A. Yu. Petrov, M. Eich, and P. Ben-Abdallah, “Hyperbolic blackbody,” Electromagnetic & Light Scattering XV 2015 (ELS-XV), Leipzig, Germany (2015)

S.-A. Biehs, S. Lang, A. Yu. Petrov, M. Eich, and P. Ben-Abdallah, “Thermal Emission of a Hyperbolic Blackbody,” Progress In Electromagnetics Research Symposium (PIERS), Prague, Czech Republic (2015)

S. Lang, A. Yu. Petrov, M. Eich, P. Ben-Abdallah, and S.-A. Biehs, “Hyperbolic blackbody,” The 6th International Conference on Metamaterials, Photonic Crystals and Plasmonics (META’15), New York, USA (2015)

S.-A. Biehs, S. Lang, A. Yu. Petrov, M. Eich, and P. Ben-Abdallah, “Blackbody Theory for Hyperbolic Materials,” Micro/Nanoscale Heat & Mass Transfer International Conference (MNHMT), Singapore (2016)

M. Eich, P. N. Dyachenko, S. Molesky, M. Störmer, A. Yu. Petrov, T. Krekeler, S. Lang, M. Ritter, and Z. Jacob, “Tailored thermal emission from refractory metamaterials,” ICNP 2016, The 9th International Conference on Nanophotonics, Taipei, Taiwan (2016)

P. N. Dyachenko, S. J. Molesky, A. Yu. Petrov, M. Störmer, T. Krekeler, S. Lang, M. Ritter, Z. Jacob, M. Eich, and L. S. Fohrmann, “Radiative engineering with refractory epsilon-near-zero metamaterials,” SPIE Photonics Europe 2016, Brussels, Belgium (2016)

S. Lang, S. Molesky, G. Sharma, A. Petrov, Z. Jacob, and M. Eich, “Near-field radiative heat transfer measurements with the transient Hot Disk technique,” 613. WE-Heraeus-Seminar: Heat Transfer and Heat Conduction on the Nanoscale, Bad Honnef, Germany (2016)

A. Yu. Petrov, P. N. Dyachenko, S. Lang, E. W. Leib, J. do Rosario, S. Molesky, Z. Jacob, T. Krekeler, M. Ritter, M. Störmer, T. Vossmeier, H. Weller, G. Schneider, and M. Eich, “Tungsten based metamaterials and photonic crystals for selective thermal emitters,” Days on Diffraction 2016, Saint Petersburg, Russia (2016)

P. N. Dyachenko, S. Lang, E. W. Leib, J. do Rosario, S. Molesky, J. Zubin, T. Krekeler, M. Ritter, M. Störmer, T. Vossmeier, H. Weller, G. Schneider, A. Yu. Petrov, and M. Eich, “Tungsten based selective thermal emitters at 1000 °C,” PECS-XII, The 12th International Symposium on Photonic and Electromagnetic Crystal Structures, York, UK (2016)

L. Maiwald, D. Jalas, S. Lang, A. Yu. Petrov, and M. Eich, “Application of the Ewald sphere approach to structural colors,” DoKDoK 2016, Oppurg, Germany (2016)

A. Yu. Petrov, P. N. Dyachenko, S. Molesky, S. Lang, M. Störmer, T. Krekeler, M. Ritter, J. Zubin, and M. Eich, “High Temperature Hyperbolic Metamaterial for Selective Thermal Emission,” Progress In Electromagnetics Research Symposium (PIERS), Saint Petersburg, Russia (2017)

A. Petrov, K. Knopp, S. Lang, E. Leib, J. do Rosario, S. Molesky, Z. Jacob, T. Krekeler, M. Ritter, M. Störmer, T. Vossmeier, H. Weller, G. Schneider, and M. Eich, “Tungsten based metamaterials and photonic crystals for selective thermal emitters,” The 8th International Conference on Metamaterials, Photonic Crystals and Plasmonics (META’17), Incheon, South Korea (2017)

L. Maiwald, S. Lang, D. Jalas, H. Renner, A. Petrov, and M. Eich, “Ewald Sphere Construction for Light Scattering in Disordered Media,” 2018 MRS Fall Meeting & Exhibit, Boston, USA (2018)

Curriculum vitae

Last name Lang
First name Slawa
Date of birth June 6, 1988
Place of birth Pavlodar
Citizenship German

08/1994 - 07/1998 Luther-Schule in Lübeck,
elementary school

08/1998 - 06/2007 Oberschule zum Dom in Lübeck,
Gymnasium

10/2007 - 08/2010 Study at Hamburg University of Tech-
nology (TUHH) in Hamburg
Degree: Bachelor of Science in electrical
engineering

10/2010 - 01/2013 Study at Hamburg University of Tech-
nology (TUHH) in Hamburg
Degree: Master of Science in electrical
engineering

- 01/2013 - 04/2017** Research assistant at Institute of Optical and Electronic Materials, Hamburg University of Technology (TUHH) in Hamburg
- since 06/2018** Development engineer in systems engineering at Siemens Mobility in Braunschweig